THE EFFECT OF JOINT COMPLIANCE WITHIN RIGID WHOLE-BODY COMPUTER SIMULATIONS OF IMPACTS

By

Stuart Antony McErlain-Naylor

A Doctoral Thesis

Submitted in partial fulfilment of the requirements for the award of Doctor of Philosophy of Loughborough University

September 2017

ABSTRACT

In high impact human activities, much of the impact shock wave is dissipated through internal body structures, preventing excessive accelerations from reaching vital organs. Mechanisms responsible for this attenuation, including lower limb joint compression and spinal compression have been neglected in existing whole-body simulation models. Accelerometer data on one male subject during drop landings and drop jumps from four heights revealed that peak resultant acceleration tended to decrease with increasing height in the body. Power spectra contained two major components, corresponding to the active voluntary movement (2 Hz – 14 Hz) and the impact shock wave (16 Hz – 26 Hz). Transfer functions demonstrated progressive attenuation from the MTP joint towards the C6 vertebra within the 16 Hz – 26 Hz component. This observed attenuation within the spine and lower-limb joint structures was considered within a rigid body, nine-segment planar torque-driven computer simulation model of drop jumping. Joints at the ankle, knee, hip, shoulder, and mid-trunk were modelled as non-linear spring-dampers. Wobbling masses were included at the shank, thigh, and trunk, with subject-specific biarticular torque generators for ankle plantar flexion, and knee and hip flexion and extension. The overall root mean square difference in kinetic and kinematic time-histories between the model and experimental drop jump performance was 3.7%, including ground reaction force root mean square differences of 5.1%. All viscoelastic displacements were within realistic bounds determined experimentally or from the literature. For an equivalent rigid model representative of traditional frictionless pin joint simulation models but with realistic wobbling mass and foot-ground compliance, the overall kinetic and kinematic difference was 11.0%, including ground reaction force root mean square differences of 12.1%. Thus, the incorporation of viscoelastic elements at key joints enables accurate replication of experimentally recorded ground reaction forces within realistic whole-body kinematics and removes the previous need for excessively compliant wobbling masses and/or foot-ground interfaces. This is also necessary in cases where shock wave transmission within the simulation model must be non-instantaneous.

PUBLICATIONS

Journal Articles

McErlain-Naylor, S., King, M., & Pain, M.T.G. (2014). Determinants of countermovement jump performance: a kinetic and kinematic analysis. *Journal of Sports Sciences*, **32**, 1805-1812.

Peploe, C., McErlain-Naylor, S.A., Harland, A.R., Yeadon, M.R., & King, M. (2017). A curve fitting methodology to determine impact location, timing, and instantaneous post-impact ball velocity in cricket batting. *Proceedings of the Institution of Mechanical Engineers, Part P: Journal of Sports Engineering and Technology*.

Peploe, C., McErlain-Naylor, S.A., Harland, A.R., & King, M.A. (2017). The relationships between impact location and post-impact ball speed, bat twist, and ball direction in cricket batting. Journal of Sports Sciences, **36**, 1407-1414.

Book Chapters

McErlain-Naylor, S., Miller, R., King, M., & Yeadon, M.R. (2017). Determining instantaneous shuttlecock velocity: Overcoming the effects of a low ballistic coefficient. In Kondrič, M., Zhang, X., & Xiao, D (Eds.), *Science and Racket Sports V* (pp. 203-212). Suzhou, China: Soochow University Press.

Miller, R., Felton, P., McErlain-Naylor, S., Towler, H., & King, M. (2017). Relationship between technique and speed in the badminton jump smash. In Kondrič, M., Zhang, X., & Xiao, D (Eds.), *Science and Racket Sports V* (pp. 240-248). Suzhou, China: Soochow University Press.

Conference proceedings

King, M.A., McErlain-Naylor, S.A., Yeadon, M.R., & Caldwell, G.E. Effects of drop height and ground contact time constraints on optimum drop jumping technique. *Proceedings of the XVI International Symposium on Computer Simulation in Biomechanics,* Gold Coast, Australia, 2017, pp. 7-8.

McErlain-Naylor, S.A., King, M.A., & Pain, M.T.G. Determinants of countermovement jump performance: a kinetic and kinematic analysis. *Proceedings*

of the Biomechanics Interest Group of the British Association of Sports and Exercise Sciences, 29, Manchester Metropolitan University, 2014, pp.16.

McErlain-Naylor, S., Allen, S., & King, M. A spectral analysis of impact shock attenuation in single leg drop landings. Poster presentation, SSEHS Postgraduate Research Student Conference, 4, Loughborough University, 2015.

McErlain-Naylor, S., Allen, S., & King, M. A spectral analysis of impact shock attenuation in single leg drop landings. *Proceedings of the Biomechanics Interest Group of the British Association of Sports and Exercise Sciences,* 30, University of Roehampton, 2015, pp.25.

McErlain-Naylor, S.A., Yeadon, M.R., & King, M.A. The effect of drop height on optimum technique in drop jumping. *Proceedings of the 25th Congress of the International Society of Biomechanics,* Glasgow, 2015.

McErlain-Naylor, S., Allen, S., & King, M. Acceleration attenuation in drop landing and drop jumping: a spectral analysis. *Proceedings of the XXVI Congress of the International Society of Biomechanics,* Brisbane, Australia, 2017, pp. 437.

McErlain-Naylor, S.A., Allen, S.J., & King, M.A. Incorporating joint compliance within a rigid body simulation model of drop jumping. *Proceedings of the XVI International Symposium on Computer Simulation in Biomechanics,* Gold Coast, Australia, 2017, pp. 17-18.

Miller, R., Felton, P., McErlain-Naylor, S., Towler, H., & King, M. Relationship between technique and speed in the badminton jump smash. *Proceedings of the 14th ITTF Sports Science Congress and 5th World Racquet Sports Congress,* Suzhou, 2015.

Peploe, C., McErlain-Naylor, S., & King, M. Identifying cricket bat-ball impact characteristics: a curve fitting technique. *Proceedings of the 5th International Conference on Mathematics in Sport*, Loughborough University, 2015.

Peploe, C., McErlain-Naylor, S., Yeadon, F., Harland, A., & King, M. Determining instantaneous impact characteristics in cricket batting. *Proceedings of the XXVI Congress of the International Society of Biomechanics,* Brisbane, Australia, 2017, pp. 311.

Peploe, C., McErlain-Naylor, S., Harland, A., & King, M. Relationships between hitting technique and ball carry distance in cricket. *Proceedings of the 35th International Society of Biomechanics in Sport Conference, Cologne, Germany, 2017.*

Prizes Awarded

Best poster presentation:

McErlain-Naylor, S., Allen, S., & King, M. A spectral analysis of impact shock attenuation in single leg drop landings. *Proceedings of the Biomechanics Interest Group of the British Association of Sports and Exercise Sciences,* 30, University of Roehampton, 2015, pp.25.

Positions Held

Student Board Member:

International Society of Biomechanics Technical Group on Computer Simulation 2014-2017.

Organising Committee:

The XVI International Symposium on Computer Simulation in Biomechanics, Gold Coast, Australia, 2017.

ACKNOWLEDGEMENTS

I am extremely grateful for the support and guidance of my supervisors, Dr Mark King and Dr Sam Allen, throughout this project. A special mention must also go to Prof. Fred Yeadon for his immense knowledge and helpful insights. I would like to acknowledge the financial support of Lord Glendonbrook through the Glendonbrook Doctoral Fellowship, as well as expressing my gratitude to the subject who kindly volunteered his time to take part in this study. Finally, I wish to thank everybody in the Sports Biomechanics and Motor Control Research Group at Loughborough University during my time here, especially my longest serving office mates Paul Felton, Romanda Miller, Jon Knight, Chris Peploe, Idrees Afzal, Pete Alway, and Dimitrios Voukelatos for their ongoing friendship and support.

DEDICATION

To Emma-Jane and my family.

Thank you for your ongoing support in everything I do.

TABLE OF CONTENTS

LIST OF FIGURES

LIST OF TABLES

CHAPTER 1

INTRODUCTION

1.1 CHAPTER OVERVIEW

This chapter introduces computer simulation of human performance. Previous literature relating to forward-dynamics computer simulation modelling (particularly impact ground reaction forces) and jumping (particularly drop jumping) is outlined prior to the posing and description of the research questions. Finally, a structural overview of the thesis is presented with a brief description of each chapter.

1.2 PREVIOUS RESEARCH

Due to a lack of control, experimental studies are unable to wholly understand the effects of complex relationships between various kinetic and kinematic factors on optimal performance. To understand the relationships in detail requires a theoretical analysis using computer simulation so that individual factors can be perturbed and the effect on performance observed through simulation (Yeadon & King, 2008). Such computer simulation studies have been instrumental in furthering our understanding of the mechanical principles governing human sporting movements. Unlike experimental studies, a theoretical analysis allows complete control of the testing environment, in which individual factors can be systematically isolated and perturbed independently of potentially confounding variables. Additionally, a whole-body simulation model can perform repeated simulations without being subjected to the performance limiting effects of fatigue. Nonetheless, forward-dynamics simulations do not function independently of the experimental approach since the model input parameters depend upon experimental measurement protocols (Pandy, 2001).

The complexity of whole-body simulation models should be appropriate for the research question being answered. Accordingly, a relatively simple planar two segment and single muscle model (Alexander, 1990) was sufficient to estimate

optimum touchdown conditions for the plant leg in running jumps that were in close agreement with competitive performances. Contrastingly, the realistic replication of muscular control during jump performances has required three-dimensional models consisting of ten segments and 54 muscle actuators (Anderson & Pandy, 1999) or 17 segments and 46 muscle actuators (Hatze, 1981).

The Sports Biomechanics and Motor Control Research Group at Loughborough University has developed a progressive series of PhD theses on optimal performance using whole-body forward-dynamics simulation modelling of jumping activities comprising tumbling (King, 1998), running jumps (Wilson, 2003), diving (Kong, 2005), triple jumping (Allen, 2010) and squat jumping (Lewis, 2011). The whole-body simulation models are generally driven using joint torque generators and have developed to incorporate independent arm and leg movement, wobbling mass motion, and biarticular torque generators. Subject-specific strength and inertia parameters have been determined for each simulation model from isovelocity dynamometer and anthropometric measurements, constraining techniques within realistic limits whilst seeking to determine model parameters, recreate experimentally observed performances, or maximise performances.

A general assumption of the existing forward-dynamics whole-body simulation models has been the simplistic modelling of frictionless pin joints and fixed segment lengths. This approach has been consistent throughout the literature for both angle-driven and torque-driven forward-dynamics simulation models of jumping and other activities, despite impact forces of up to 13 times bodyweight (Allen et al., 2012). However, it has long been accepted that the human skeletal system is capable of damping impact shock waves and avoiding direct transmission of kinetic energy to internal structures (Coventry et al., 2006; Gross & Nelson, 1988; Hoshino & Wallace, 1987; Radin et al., 1970; Zhang et al., 1998). The mechanisms responsible for this attenuation, including foot arch and heel pad compliance; lower extremity joint compression; and spinal compliance (Boocock et al., 1990; Camosso & Marotti, 1962; Gross & Nelson, 1988; Helliwell et al., 1989; Radin et al., 1970; Simkin et al., 1989), have previously been overlooked in aid of simplifying models. Pin joint representations have therefore resulted in unrealistic dissipation of energy and transmission of accelerations throughout the body following impact and hence

difficulty in accurately reproducing experimentally measured ground reaction forces (Allen et al., 2012).

This limitation is especially problematic in movements such as drop jumping (Figure 1.1) where the attenuation of impact accelerations affects the kinetics and kinematics being investigated in the subsequent propulsion phase of the jump (Arampatzis et al., 2001; Bobbert et al., 1987a; Marshall & Moran, 2013). Previous studies have attempted to overcome this limitation by modelling excessive wobbling mass movement or excessive compression at the foot-ground interface to compensate for the lack of compression and thus force dissipation within the joint structures (Allen et al., 2012). Allen et al. (2012) stated that whilst unrestricted foot-ground compression was appropriate for simulating performance, accurate internal force replication would require compliance elsewhere within the rigid link system.

1.3 STATEMENT OF PURPOSE

The purpose of this thesis is to investigate the effect of incorporating joint compliance on the ability of a subject-specific computer simulation model to accurately predict ground reaction forces during dynamic jumping activities. The thesis will aim to answer the following two questions:

1.4 RESEARCH QUESTIONS

Q1. What contribution does spinal and joint compression make to the attenuation of impact-related accelerations following landings?

Experimental data collection during a series of drop landings and drop jumps from a range of heights will enable the passive dissipation of impact accelerations through the human body to be quantified. The relationship between the magnitude of ground reaction force and these acceleration reductions will also be calculated. Accelerometers strapped tightly over areas with relatively little soft tissue movement, combined with a power spectral analysis, will enable calculation of the

impact acceleration attenuation across major joints. Voluntary joint flexion will be accounted for, isolating the transmission of accelerations due to the foot-ground impact. Conclusions will be drawn regarding the magnitude of the limitations associated with using pin joints in models of human body following a large impact force.

Q2. Is it necessary to represent compression within the spinal column and ankle, knee, hip and shoulder joints in planar whole-body simulation models of drop jumping?

A subject-specific two-dimensional torque-driven simulation model of drop jumping, incorporating biarticular torque generators and compressive joint representations, will be compared with an equivalent model without joint compression, representative of traditional frictionless pin joint models. Subject-specific viscoelastic parameters will be determined separately for each model by matching the model to experimental performance data using an optimisation algorithm. The simulation models will then be evaluated against the recorded performances to quantify how closely the modelled activity is represented. Conclusions will be drawn regarding the importance of compressive joint structures and the appropriate level of complexity required to match experimental kinematics and ground reaction forces whilst utilising realistic foot-ground interface compliance and wobbling mass displacements.

1.5 RELEVANCE OF THE WORK

Existing forward-dynamics whole-body simulation models in sports biomechanics can be utilised to investigate the optimum technique for the performance of a specific individual. Likewise, through varying parameters including segment anthropometry or joint torque parameters, researchers can use these models to investigate the performance effects of potential changes in body size or shape, or increases in muscle strength due to resistance training.

However, researchers currently using these methodologies are unable to accurately predict the forces acting at the foot-ground interface, and much less so the forces acting at joints in the body. Consequently, previous simulation research has found it difficult to address questions relating specifically to ground reaction forces or joint reaction forces during sporting movements. The cause of this limitation has been identified as likely due to inaccurate internal transmission of energy within the modelled human body system. A thorough investigation into post-impact energy dissipation and shock wave attenuation in humans can highlight the areas in which existing forward-dynamics whole-body simulation models are failing to accurately replicate in vivo mechanics.

Inclusion of the identified, currently neglected, features within a simulation model may address the above internal energy transmission limitations. If so, this presents the possibility for future forward-dynamics whole-body simulation research to estimate more accurate joint reaction forces. The relationships between technique factors and injury risk could then be investigated theoretically without the need for potentially injurious experimental procedures. Likewise, the likelihood of acute or chronic musculoskeletal injuries could be considered alongside performance measures when determining the optimum technique for a specific individual through subject-specific modelling approaches.

1.6 CHAPTER ORGANISATION

Chapter 2 comprises a critical review of the literature related to forward-dynamics simulation models. A review of the literature relating to impact shock wave attenuation features within the human body and the important considerations when modelling high impact activities follows.

Chapter 3 describes the general experimental methods employed in this research to obtain the required kinematic and kinetic measurements for a subject performing drop jumps and drop landings from various drop heights.

Chapter 4 quantifies the post-impact attenuation in acceleration up the body during drop landing and drop jumping, including a discussion of the results. Conclusions

are drawn regarding the magnitude of the limitations associated with modelling pin joints in the human body following a large impact force.

Chapter 5 details the development of a planar, nine-segment, torque-driven whole-body simulation model of drop jumping.

Chapter 6 describes the derivation of subject-specific torque-generator parameters for monoarticular and biarticular representations of torque actuators in the whole-body simulation model utilising isovelocity dynamometer measurements. Subject-specific segmental inertia parameters are also determined from anthropometric measurements.

Chapter 7 includes an evaluation of the compressive joint, torque-driven, simulation model of drop jumping against experimental performance data, as well as a comparison with a similar process for an equivalent model without compression at joints.

Chapter 8 provides a discussion of the thesis in summary. This includes the discussion of results from the evaluation of the simulation model and answering of research questions posed in Chapter 1. Finally, the implications and potential limitations of the findings are discussed, and conclusions are stated.

CHAPTER 2

REVIEW OF THE LITERATURE

2.1 CHAPTER OVERVIEW

The following chapter contains a critical review of the literature related to forward-dynamics simulation models relevant to the construction of a simulation model of drop jumping. Literature relating to other specific areas of the thesis, including experimental methodology and evaluation of simulation models, will be included within the relevant chapters. In this chapter, an overview of computer simulation modelling and the construction of previous vertical jumping simulation models will be reviewed. This will be followed by a review of other relevant areas of the literature including muscle models, biarticular torque generators, and ground contact models. Finally, the chapter includes a review of the human body's internal impact attenuation mechanisms and limitations of previous simulation models in representing these features.

2.2 COMPUTER SIMULATION MODELS

Any whole-body simulation model will necessarily be a simplified representation of the over 200 bones and 500 muscles of the human musculoskeletal system, although the complexity should be appropriate for the research question being addressed. As such a single model cannot be utilised to answer all possible research questions in sports biomechanics and so specific models must be tailored to the research question and the activity being investigated. A general guideline to researchers is that the model should remain as simplistic as possible whilst comprising sufficient complexity to answer the proposed research questions (Yeadon & King, 2008). Each component of the model is based on physiological and biomechanical systems within the human body. Assumptions within these systems are stated, and the various interactions between these systems are prescribed. This allows the researcher a far greater level of control than a more traditional experimental or statistical analysis of human movement, as well as

enabling an unlimited number of simulations to be performed to the same degree of accuracy without succumbing to the performance limiting effects of fatigue.

Simulation models can follow either an inverse or a forward-dynamics approach. In inverse dynamics approaches the joint kinematic time histories and the external forces acting upon the model are defined as inputs to the model, with the required net torques at each joint then calculated as outputs from the model. This approach offers a novel technique for quantifying the intrinsic properties required to generate specific performance outputs but is not well suited to determining optimal technique or identifying the relationships between strength and performance. These tasks require a forward-dynamics approach to computer simulation modelling.

Forward-dynamics simulation models can either be angle-driven or torque/force-driven. Angle-driven models utilise the joint angle time histories as inputs to the model and compute the resulting whole-body orientation and mass centre position. These have typically modelled activities that are not limited by the strength of an individual, such as the aerial phases of diving (Miller, 1971), high jumping (Dapena, 1981), or trampolining (Yeadon et al., 1990). When used elsewhere (e.g. long swings on rings or high bar circling in gymnastics) joint torques have been limited to prevent unrealistic movements (Brewin et al., 2000; Yeadon & Hiley, 2000). Angle-driven models benefit from ease of control and superior computational speed when compared with torque-driven models.

In contrast, torque/force-driven simulation models require joint torque or muscle force time histories as inputs to calculate the resulting kinematics. With a few notable exceptions (Hatze, 1981; Anderson & Pandy, 1999) these have typically represented relatively simple planar movements such as the drop jumping movement under investigation in the present thesis. Movements such as bilateral vertical jumps can easily be represented as a two-dimensional movement, with relatively little error introduced by the assumptions of planar movement or bilateral symmetry. The muscle forces or joint torques used as inputs to the model are themselves often calculated from activation levels and known capabilities of the relevant musculature given the angle and angular velocity of the joint at that instant. This approach enables both activation patterns and muscle capabilities to be varied systematically, investigating the resulting effects on performance. This is the most appropriate approach for answering the second research question posed in Section

1.4 and so the following review of the literature will focus mainly on existing forward-dynamics simulation models.

2.3 CONSTRUCTION OF JUMPING MODELS

Most existing whole-body simulation models are based on a system of linked rigid bodies representing body segments, each requiring a segmental length, mass, mass centre location, and moment of inertia. As with most elements of the model, the number of segments depends upon the specific activity being represented and the aims of the study. A relatively simple planar two segment and single muscle model (Alexander, 1990) was sufficient to predict optimum touchdown conditions for the plant leg in running jumps that were in close agreement with competitive performances. Several assumptions were present in the simplistic model. The model consisted of two rigid massless leg segments of equal length and the body mass concentrated at the hip (Figure 2.1). The foot was treated as a point at the distal end of distal leg segment. During ground contact the muscle exerted a sole extensor torque at the knee joint, with no ankle or hip joint included in the model. Despite this simplistic replication of a human jumping movement, the model incorporated both a contractile component and a series elastic component within the knee extensor musculature, with a Hill-type relationship between torque and rate of shortening of the contractile component. The muscle was assumed to be fully activated throughout the period of ground contact. A similar model also consisting of two massless leg segments and a point mass at the hip has been used by the same author to investigate a standing vertical jump (Alexander, 1989).

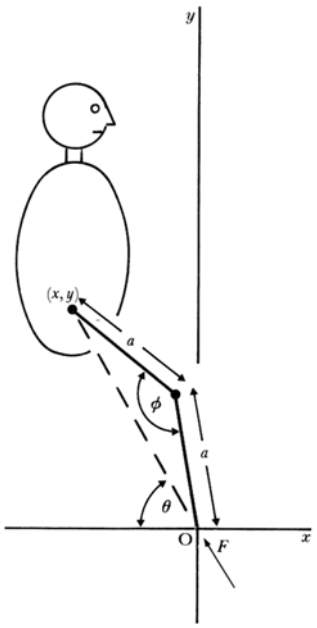

Figure 2.1. A simplistic two-segment model of running jumps, adapted from Alexander (1990)

This simple model was adapted by Dapena (1999), who added a piston-like ring to model the action of the arms in vertical jumping. The initial and final velocities of these arms were variable, enabling the arm action to be manipulated and investigated. Dapena discovered that a constant velocity of 3 $m \cdot s^{-1}$ optimised jump height. This piston-like representation, however, has its disadvantages in that arms moving with constant velocity cannot accelerate the torque generator to a greater extent than if they had been static. The beneficial effect of this piston-like arm movement was therefore not to apply a force to the trunk but to produce favourable conditions for the knee extensors to generate greater torques at the beginning of the simulation.

Perhaps more realistically, Ashby and Delp (2006) investigated the effects of an arm swing on jumping performance, albeit in the standing long jump, through the addition of a one-segment arm driven by a shoulder torque generator incorporating torque-angle-angular velocity relationships as well as passive ligamentous torques to a typical four-segment model. Rather than modelling separate antagonistic flexion and extension torques, a net joint torque activation was determined for each joint by nodes at 50 ms intervals, taking values from -1.0 to 1.0 with the signs denoting flexor or extensor torques. Inertia and torque parameters were taken from the literature and so the model was not specific to any individual.

A more detailed analysis of optimum whole-body technique would require complex multi-joint movement. Furthermore, subject-specific anthropometry and strength profiles would be necessary for the general results to be applied to a specific individual. Indeed, optimisation of vertical jump control to maximise jump height has required a slightly more complex four-segment planar model driven by eight musculotendon actuators (Pandy et al., 1990). These actuators were driven by Hill-type contractile components (Hill, 1938) containing series and parallel elastic components. The properties of the elastic tendons were defined by a stress-strain curve, with the model driven by a first-order activation dynamics representation. It was noted, however, that whilst the determined optimum technique was qualitatively similar to experimental jumping data, it was not similar enough to be considered a reasonable optimum technique to be employed by humans. For example, the optimum technique exhibited less than 5° trunk countermovement prior to upward propulsion whereas experimental studies have reported values of up to 25° (Pandy et al., 1988). This discrepancy was explained by the inability of the model to exert a large enough torque at the hip joint, as well as the unrealistic and simplistic one-segment representation of the trunk (Pandy & Zajac, 1991). Similarly, the optimal solution generated segmental angular velocities that were increasing at take off rather than decreasing, as observed experimentally (Bobbert & van Ingen Schenau, 1988). The authors were therefore unable to draw conclusions regarding the features of optimum vertical jumping technique. To do so would likely require a more complex representation of the human musculoskeletal system.

The authors noted that their model was particularly sensitive to activation timings of the vastii muscles and that it could be utilised in future studies to perturb various physiological factors in order to gain an enhanced understanding of their effects on vertical jumping performance when compared with experimental studies alone. This model was subsequently evaluated against experimentally collected data (Pandy & Zajac, 1991) and determined to be sufficiently accurate to justify a detailed analysis of the optimal control system, even if not the optimum technique. The identified optimal control strategy comprised a proximodistal sequencing of muscle activations, with the vasti and gluteus maximus muscles as the major energy producers of the lower extremity. The complexity within the muscle model used did enable the researchers to investigate the dependence of jumping performance on biarticular muscle function, via the removal from the model of any biarticular

muscles. Jumping performance was found to be similar when the gastrocnemius was replaced with a monoarticular ankle plantar flexor.

In contrast, van Soest et al. (1993) found that jump height decreased by 10 mm when the biarticular gastrocnemius was converted to a monoarticular muscle. As with the model of Pandy et al (1990), the model of van Soest et al. (1993) comprised four rigid segments. The distal end of the foot segment was connected to the floor by a frictionless hinge joint, thus preventing translational movement at this point. As with many other models of vertical jumping, the six muscles were Hill-type muscles consisting of a series elastic element (SEE), a parallel elastic (PE) element, and a contractile element (CE; Figure 2.2; see Section 2.3.1). The authors explained the difference in results between their study and that of Pandy and Zajac (1991) through the differing representation of biarticular moment arms. Pandy and Zajac's (1991) moment arm of the biarticular gastrocnemius approached zero as the knee approached full extension, resulting in the muscle acting similarly to a monoarticular muscle in this range.

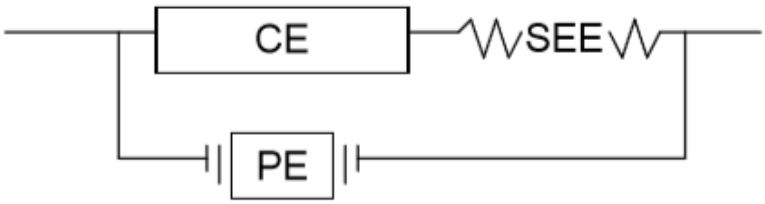

Figure 2.2. Representation of the muscle-tendon complex

Further fundamental issues relating to the application of computer simulation modelling to vertical jumping were subsequently investigated using the model of van Soest et al (1993) (Bobbert, 2001; Bobbert & Casius, 2005; Bobbert & van Soest, 1994; Bobbert & van Soest, 2001; Bobbert and van Zandwijk, 1999; Bobbert et al., 1996; Bobbert et al., 2008; van Soest & Bobbert, 1993; Vanrenterghem et al., 2008). The first of these studies (van Soest & Bobbert, 1993) concluded that the force-length-velocity relationship in muscle acts as an immediate feedback mechanism enabling humans to maintain consistent technique despite perturbations to initial kinematic conditions. It is therefore important that these muscle characteristics are represented within forward-dynamics simulation models of vertical jumping. The sensitivity of optimal jumping performance to changes in strength capabilities of the

musculature (Bobbert & van Soest, 1994) highlights the need for subject-specific strength measurements to be included within a model if the optimal technique is to be applied practically to an individual.

A later study by the same group demonstrated the sensitivity of vertical jump performance to muscle stimulation onset times, with jump height decreasing with increasing rise times (Bobbert & van Zandwijk, 1999). Thus, it is important that muscle activation dynamics are realistic if the capabilities of a particular technique are not to be overestimated. Indeed, it was stated that the use of instantaneous changes in stimulation in simulation models of vertical jumping (Levine et al., 1983; Pandy et al., 1990; van Soest et al., 1993; Zajac et al., 1984) may lead to unrealistically fast force development. Their model was also more robust with increases in rise times, likely due to a slower development of errors. Similarly, it is important that elastic compliance is realistic in simulation model representations of tendon structures, with vertical jump performance sensitive to changes in this compliance (Bobbert, 2001).

Whereas the models discussed above have utilised muscle actuators, a similar four-segment planar model by Selbie and Caldwell (1996) was driven by three joint torque generators. These incorporated joint torque-angle-angular velocity relationships as well as an activation parameter to control the rate of torque development. As with van Soest et al. (1993), the distal point of the foot was connected to the floor by a frictionless hinge joint. Heel-ground contact was modelled using a rotational spring damper. This model enabled both joint torque activation timings and model initial conditions to be varied to optimise vertical jumping performance. However, the model did not incorporate antagonistic joint torques or biarticular muscles and hence was unable to reproduce the proximodistal sequencing of joint coordination that has been reported experimentally and in other theoretical studies.

In contrast to these simple planar models, the realistic replication of muscular control during jump performances has required three-dimensional models consisting of ten segments and 54 muscle actuators (Anderson & Pandy, 1999) or 17 segments and 46 muscle actuators (Hatze, 1981). The model of Anderson and Pandy (1999) comprised a head-arms-torso (HAT) segment, a pelvis, two thighs, two shanks, two hindfeet, and two forefeet. A unique feature of this model is the three degrees of

freedom ball-and-socket joint between the pelvis segment and the HAT segment. The hindfoot articulates with the shank via a two degrees of freedom universal joint, whilst each knee and toe-hindfoot joint comprises a single degree of freedom hinge joint. Each leg contained a complex system of 24 muscle actuators (Figure 2.3), with a further six in the upper body. The foot-ground interface was modelled using a series of five spring-damper units distributed over the sole of each foot, with the force varying exponentially with displacement: four at the corners of each hindfoot, and one at the distal end of the toes.

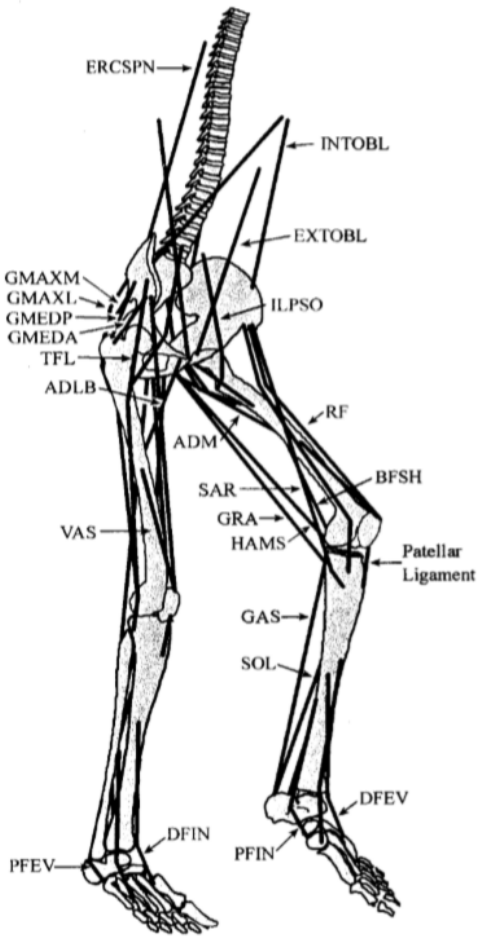

Figure 2.3. Geometry of Anderson and Pandy's (1999) 54 muscle actuators

Similarly to Pandy et al. (1990), the muscles in the model of Anderson and Pandy (1999) comprised a contractile element and series and parallel elastic elements, all in series with a tendon (Figure 2.4; see Section 2.3.1). To prevent the joint angles

from reaching physically impossible values, passive ligament torques were applied as the sum of two exponential terms. A first order differential equation relating the rate of change of muscle activation to muscle excitation governed the excitation-contraction dynamics. Musculoskeletal geometries were taken from the literature, with maximal isometric torques matched to the average values measured on a dynamometer for the five subjects in the study. Segmental inertia parameters were similarly calculated as the average of the subject-specific parameters determined from anthropometric measurements according to the methods of McConville et al. (1980).

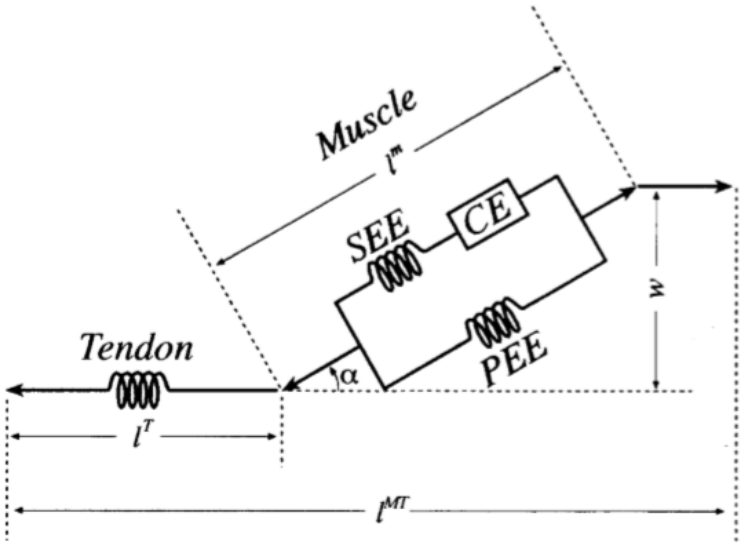

Figure 2.4. Schematic of Anderson and Pandy's (1999) musculotendon model

This complex model (Anderson & Pandy, 1999) showed quantitative agreement with experimentally collected performance data although the model exhibited considerably shorter ground contact times and was unable to reproduce the kinematics of the jump near to take-off. This difference was attributed to the short rise time of muscle activation (20 ms) in the model, determined from single muscle fibres rather than whole muscles. The earlier long jumping model of Hatze (1981) is a similarly complex muscle model, with the added complexity of 17 segments and 46 muscle actuators required to not only model the kinematics of the technique but also account for the internal excitation and contraction dynamics of the human muscular subsystem.

A simpler muscle model of squat jumping comprising ten rigid segments and seven muscles has been used to investigate the influence of lumbar spine extension on

vertical jump height (Blache & Monteil, 2014). The model included separate pelvis, lumbar vertebrae (five), and thorax-head-arms segments, as well as the erector spinae muscle. Jump height was optimised for five different erector spinae maximal isometric strengths (± 10% and 20%), with the reference value taken from the literature (Andersson et al., 1988). Vertical jump height decreased by 14.4% if the erector spinae was not taken into consideration in the model and increased progressively with increases in the strength of this muscle.

2.3.1 MUSCLE MODELS

Many of the computer simulation models described in Section 2.3 used muscle forces to generate motion around joints. These are typically based upon the work of A.V. Hill, referred to as Hill-type muscle models, where the force generating capabilities of the muscle are divided into contractile components and elastic elements (lumped parameter models). The most commonly used in sports biomechanics has been the three-component Hill model (Caldwell, 2004). These muscle models comprise a contractile component, a series elastic element, and a parallel elastic element (Figure 2.2). Mathematical relationships for each component enable the force exerted by the muscle to be defined throughout a simulated movement. The force generated by the contractile component is typically expressed as a function of the muscle length, muscle velocity, and muscle activation. The series elastic component represents the connective tissue (tendon and aponeurosis) in series with the contractile component and the force generated by this component is usually expressed as an increasing function of its length, with no force generated below a fixed slack length. The parallel elastic element, however, has often been ignored in sporting simulation models as within the normal functional range of joints it does not generate high forces (Chapman, 1985). The relationships determining force in each of these components are discussed in more detail in Section 5.4.8.

2.3.2 JOINT TORQUE GENERATORS

For muscle models in which more than one muscle is active for a given joint action, it can be difficult to determine subject-specific strength parameters. Individual parameters must be determined for each component of each muscle and these cannot easily be determined non-invasively in an experimental approach unless all muscles for a given joint action are combined into one 'lumped muscle'. Relying on data from the literature results in parameters that are not specific to any individual being represented in a simulation model and so an alternative to muscle models – joint torque generators – has often been used, especially when building subject-specific models. Joint torque generators represent the net effect of all muscles acting at a joint (King & Yeadon, 2002). Unlike the parameters for individual muscles, this net joint torque can be measured experimentally on an isovelocity dynamometer. Additional complexity can be incorporated through the modelling of separate extensor and flexor torque generators (King et al., 2006), enabling antagonistic joint torques and co-contraction (Yeadon et al., 2010). Similar to the components of a muscle model, each torque generator comprises rotational contractile and elastic elements (Section 5.4.8). The mathematical functions describing these components are similar to those in a muscle model, with the maximal voluntary torque of the contractile component expressed as a function of the muscle angle and muscle angular velocity (Yeadon et al., 2006).

2.3.3 BIARTICULAR TORQUE GENERATORS

Most existing forward-dynamics computer simulation models incorporating joint torque generators, as opposed to muscle models, have represented the torque at a joint based solely on the kinematics of that primary joint, assuming a negligible effect of the kinematics at secondary proximal or distal joints. This ignores any effect of biarticular muscles, which have been shown in muscle models to influence vertical jump performance (van Soest et al., 1993). Attempts have recently been made to quantify the errors associated with these assumptions. Indeed, Lewis et al. (2012) found a 19 parameter two-joint function expressing maximal voluntary ankle plantar flexor torques as a function of the kinematics at this joint and the knee to be a more accurate representation than an existing single-joint function, with differences of

19% reported for maximum torque. The authors concluded that a two-joint representation of ankle plantar flexor torque is necessary in torque-driven simulation models where the knee is flexed by more than 40°.

A further study by the same group (King et al., 2012) expressed knee flexor and knee extensor torques as a function of kinematics at both the knee and the hip. Comparing this biarticular function to a traditional monoarticular function, they found a difference of 9% of maximum torque for both knee flexion and knee extension. The two-joint representation was more accurate at hip angles other than that used on the dynamometer to calculate the single-joint function parameters. The differences between the two alternative methods were greatest for both flexion and extension at the most extended hip angle. It was concluded that the use of biarticular joint torque generators has the potential to improve the biofidelity of whole-body subject-specific torque-driven simulation models.

A further guideline offered by Lewis (2011) is that for ankle plantar flexion, knee flexion, and knee extension torques, a biarticular representation offers better agreement with torques measured on an isovelocity dynamometer than a monoarticular representation when the joint angle of a secondary joint changes by 37° or more. He also stated that a two-joint representation should account for the biarticular knee flexor and extensor contributions to hip joint torques. The details of the biarticular torque generator functions and parameter determination are discussed further in Chapter 6.

When these two alternative approaches (single- or two-joint representations) were incorporated within a subject-specific model of squat jumping, Lewis (2011) found better agreement with experimentally collected performance data when the biarticular functions were used. The author went on to suggest that the simulation of a maximal effort human movement should include two-joint torque representations when the following characteristics are present in the simulated movement:

- initial whole-body momentum is not large;
- multiple joint kinematics with a large biarticular muscle contribution are involved.

If, however, the simulated activity involves similar kinematics at both joints then a single-joint representation may be sufficient (Lewis, 2011).

2.3.4 GROUND CONTACT MODELS

The simplest solution for modelling an interaction between a body segment and an external surface such as the ground or sports equipment has been to use a hinge joint, enabling rotational but not translational movement, as in the vertical jumping model of Bobbert et al. (2002). This method cannot facilitate the non-zero initial velocity in an impact with the external surface and so is inappropriate for drop jumping.

A slightly more complex alternative has been to apply forces at a finite number of locations through visco-elastic elements. The forces are determined from the displacements and velocities of the contact points. These visco-elastic contact points have previously been used to model specific elastic structures including the heel pad, which is known to compress following an impact (Pain & Challis, 2001), as well as sports equipment such as a gymnastics high bar (Hiley & Yeadon, 2003) or tumble track (King & Yeadon, 2004).

As with all aspects of simulation modelling, the visco-elastic contact points used in previous literature have varied in number and complexity according to the task being modelled and the specific research questions being answered. This has resulted in a range from simple damped linear springs (King & Yeadon, 2004) to the use of highly non-linear equations (Wright et al., 1998), and from less than three contact points (Yeadon & King, 2002) to as many as 66 during heel-toe running (Wright et al., 1998). One adaptation of note is that expressing the horizontal force in visco-elastic springs as a function of the vertical force ensures both directional force vectors decay to zero at the same time point (Wilson et al., 2006).

When horizontal ground reaction forces are being modelled, an alternative to visco-elastic springs (Yeadon & King, 2002) has been to use a model of frictional forces, expressing the horizontal force as a function of the vertical force and the horizontal velocity of the contact point (Gerritsen et al., 1995). In a simulation of handspring straight somersault vaulting in gymnastics, Jackson et al. (2011) modelled the hand-

vaulting table tangential contact force using both dynamic and static friction. When the gymnast contacted the table, sliding friction was applied. Once the tangential velocity dropped below 0.01 ms^{-1} the implementation was switched to a model of static friction with constrained zero tangential velocity. This was continued until such a time that the frictional force became greater than limiting friction, at which point the implementation was switched back to sliding friction and the hands once again translated tangentially to the vaulting table. The authors compared this two-state model to a more complex pseudo-Coulomb friction implementation and found similar results alongside faster simulation and optimisation times. Such a representation when applied to horizontal foot-ground interactions has the potential to facilitate translation or 'sliding' of the foot prior to 'sticking' the foot once its horizontal velocity drops below a threshold value.

2.4 IMPACT DISSIPATION IN HUMANS

Impacts form an inevitable aspect of many human sporting activities, including the drop jump. The initial point of contact between the human body and an external surface following a drop landing impact is the feet, which experience large ground reaction forces and hence high accelerations. During the impact, kinetic energy of the body is dissipated as heat due to negative muscle work and damping associated with deformation of internal body structures. Compliance in the form of joint motions and tissue deformation enables mass superior to the site of compliance to continue moving downwards momentarily, thus reducing accelerations of segments in an inferior to superior pattern. This prevents excessive accelerations at the brain and other vital organs, thus ensuring the stability of the head, maintenance of consistent vestibular and visual function, and reduced likelihood of acute or chronic musculoskeletal injuries (Hamill et al., 1995; Owen & Lee, 1986; Pozzo et al., 1991).

Ground reaction forces as great as 10 and 22 times bodyweight have been reported during a drop landing (Edwards et al., 2010) and during the single leg step phase of a triple jump (Amadio, 1985) respectively. These large forces experienced during sporting activities result in high accelerations being transferred through the various tissues of the human musculoskeletal system as an impact acceleration, or shock wave, of kinetic energy from the foot to the head (Derrick, 2004; Lafortune et al.,

1996; Mercer et al., 2003; Mizrahi et al., 2000; Moran & Marshall, 2006). These accelerations, as well as their dissipation, can have important effects on the subsequent kinetics and kinematics within the human body and so may contribute to the determination of optimal sporting technique and the accurate replication of human movement.

2.4.1 IN VIVO DISSIPATION

The human body's internal structures provide several mechanisms for the passive dissipation of the impact shock wave, many of which are of direct relevance to drop landing and drop jumping biomechanics. Major contributors to this dissipation of energy include foot arch compliance, heel pad deformation, compliance within joint structures, spinal compression, and soft tissue movement, as well as voluntary joint actions.

Accelerometers have been utilised to gain an indication of shock wave dissipation through the human body. As the impact-related kinetic energy is dissipated, thus the measured accelerations would be expected to progressively decrease at sites more superior on the human body. Zhang et al. (2008) positioned accelerometers at the tibia and head, showing that following drop landings, tibial accelerations were greater than those at the head and that these accelerations increased with increases in drop height. However, drop height had no effect on the acceleration signal attenuation between the tibia and the forehead, calculated as the average of the transfer function from 21 to 50 Hz between the two acceleration signals. Thus, it can be said that various mechanisms contribute to the dissipation of kinetic energy between these two sites but that there may be a maximal capacity to attenuate the accelerations, with no increase in attenuation with further increases in ground reaction force and foot acceleration. This study offers no quantification, however, of acceleration attenuation below the tibia, or any progressive attenuation throughout the body from foot to head.

A sophisticated study by Shorten and Winslow (1992) again utilised accelerometers at the shank and the head, as they investigated shock wave attenuation during treadmill running. This study has the same disadvantages as Zhang et al. (2008)

due to the lack of information at other sites on the body but succeeded in conducting a thorough analysis of the acceleration signals. The typical shank acceleration power spectrum contained two major components, corresponding to the active (5-8 Hz) and impact (12-20 Hz) phases of the time-domain ground reaction force. This distinction leads to the possibility of future studies removing the active component from an acceleration signal to isolate the effects of various passive measures on impact attenuation. Both the amplitude and frequency of shank accelerations increased with increasing running speed, with the greatest attenuation between the two sites occurring in the range of 15-50 Hz. Unlike with increasing drop heights in Zhang et al. (2008), impact attenuation increased with increasing running speeds. Transmission of kinetic energy to the head was therefore limited despite the increases in ground reaction force. It is important for future studies to utilise these novel methods to isolate the effects of passive energy dissipation in progressive stages up the body to quantify the contribution of various mechanisms. The following sub-sections will discuss these in vivo dissipation mechanisms in more detail with reference to previous literature.

Foot Arch Compliance

The medial longitudinal arch is the highest of three foot arches and is composed of the calcaneus, talus, navicular, cuneiforms, and the first three metatarsals (Figure 2.5). This arch is supported by ligaments (e.g. the plantar calcaneonavicular ligament) as well as muscles (e.g. the small muscles in the sole of the foot) and tendons (e.g. that of the tibialis posterior). The joint between the talus and navicular is braced by the plantar calcaneonavicular ligament, which is also known as the spring ligament due to its elastic nature and ability to deform under pressure and quickly restore the arch to its original position once the force is removed. This arch thus provides compliance and demonstrates an ability to attenuate the accelerations experienced superior to this site shortly after a dynamic foot-ground collision (Hageman et al., 2011).

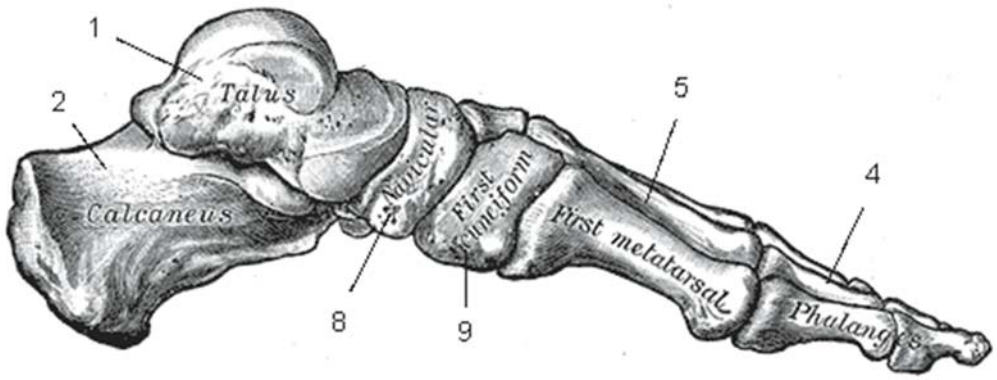

Figure 2.5 Medial longitudinal arch (medial view). Gray (1918).

The negative vertical displacement of the navicular tuberosity under deformation of the medial longitudinal arch has been proposed as a method of quantifying this deformation (Brody, 1982). Experimental studies have reported values for this navicular drop ranging from 5 mm to 11 mm when subjects transition from a seated posture to two-footed standing (Bandholm et al., 2008; Brody, 1982; Fiolkowski et al., 2003; Headlee et al., 2008; Snook, 2001). The value of the navicular drop is known to be dependent upon the magnitude of the ground reaction force experienced at the foot (Huang et al., 1993), increasing by 4.5 mm when standing on one leg when compared with two-legged standing (Billis et al., 2007). Concurrently with a negative vertical displacement of the navicular tuberosity, medial longitudinal arch deformation under impact also results in a lengthening of the arch. Even during the relatively low impact activity of walking arch length has been shown to increase by almost 2% when compared with a seated posture (Cashmere et al., 1999).

A more sophisticated experimental study by Hageman et al. (2011) investigated medial longitudinal arch deformation during the stance phases of walking, stair ascent, and stair descent both unloaded and with added weights to the front or back of 13.6 kg. Arch length was defined as the three-dimensional distance from a medial calcaneus marker to a first metatarsal head marker, with lengthening expressed relative to an unloaded standing trial. Navicular height was the three-dimensional, perpendicular distance from a navicular tuberosity marker to the line defined by the arch length (Figure 2.6), again relative to the static trial. These values were also summed to give an overall value for arch collapse.

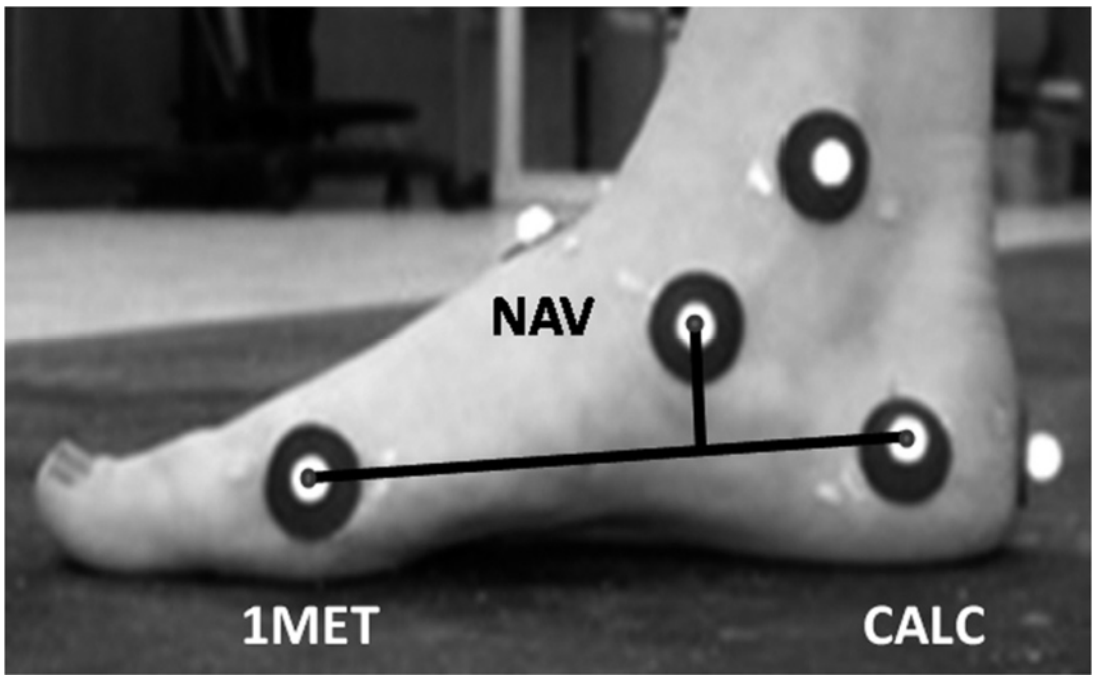

Figure 2.6 Navicular height and arch length definitions (Hageman et al., 2011)

This investigation highlighted the change in arch deformation over time, showing that for each activity, navicular displacement increased upon impact beyond the value of the unloaded static trial before recoiling back to the initial position or further (Figure 2.7). This visco-elastic nature of arch deformation suggests an ability to dissipate kinetic energy from the impact shock wave and therefore reduce the accelerations of the shank. Arch lengthening was greatest during walking and stair descent, with navicular displacement greatest during stair descent. The addition of a 13.6 kg external load did not affect medial longitudinal arch deformation during walking or stair ambulation and so it is possible that either this extra load was distributed in other ways and/or that the activities investigated resulted in maximal arch deformation. Medial longitudinal arch deformation is yet to be investigated during landings from a drop and so it is not known whether the changes in navicular height and arch length would be of greater magnitude to those discussed above or whether these values do indeed represent maximal arch deformation.

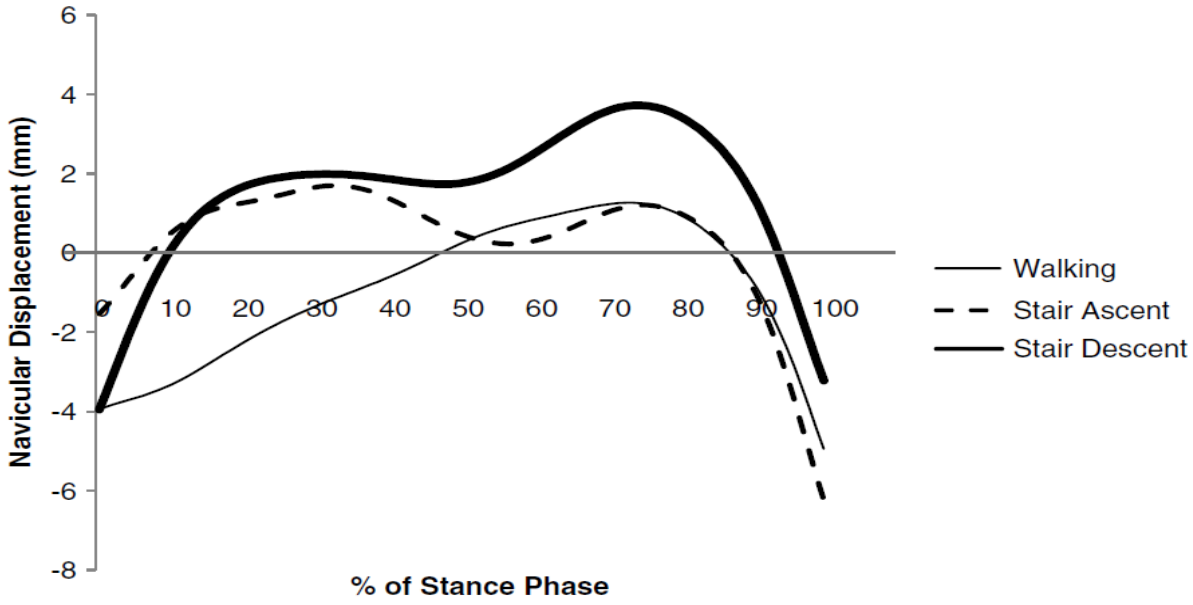

Figure 2.7 Representative navicular displacement during the stance phase of walking, stair ascent, and stair descent for one trial by one subject. Zero displacement represents the navicular height during a static standing trial. A positive displacement represents a lower navicular height than standing. Adapted from Hageman et al. (2011).

One point of note is that expressing navicular drop relative to standing, as in Hageman et al. (2011) fails to quantify any displacement that occurs due to the increase in loading in a transition from an entirely unloaded condition to a bodyweight stance condition. Figure 2.7 implies that including this initial displacement could increase navicular drop measures by as much as 4 mm. Indeed, Nielsen et al. (2009), whilst investigating the mean of 20 consecutive walking steps, calculated navicular displacement in the same way as Hageman et al. (2011) but expressed navicular drop as the maximal displacement from heel strike to when the navicular tuberosity was closest vertically to the floor. This dynamic navicular drop ranged from 1.3 mm to 13.4 mm. Ninety-five percent of the population had a navicular drop of less than 8.7 mm and greater than 1.7 mm.

Two previous studies had recorded navicular drop values of greater than the 13.4 mm of Nielsen et al. (2009). Billis et al. (2007) reported 15.5 ± 3.6 mm of navicular drop during single-leg stance, whilst subjects in the study of Headlee et al. (2008) exhibited 10.0 ± 3.8 mm and 11.8 ± 3.8 mm of drop pre- and post-fatigue respectively during sit-to-stand. Both studies, however, measured navicular drop

as the change in height of the navicular tuberosity relative to the ground, thus including heel pad compression and so failing to isolate the effects of the medial longitudinal arch. Therefore, the available literature suggests a maximal reported navicular drop of 13.4 mm (Nielsen et al., 2009) when compression of the heel pad is isolated and considered separately.

Heel Pad

The heel pad constitutes a further energy dissipating structure within the human foot, and dependent upon technique may represent one of the first points of contact during a foot-ground impact. The heel pad is a thick pad of fat and connective tissue between the skin and the calcaneus with viscoelastic properties and has been identified as having the ability to attenuate shock wave accelerations following an impact (Paul et al., 1978; Pain & Challis, 2001). A typical heel pad is between 10 mm and 20 mm in thickness (Jorgensen & Bojsen-Moller, 1989; Ker et al., 1989; Noe et al., 1993; Valiant, 1990) and can compress upon impact (Aerts & De Clerq, 1993; Light et al., 1980; Valiant, 1990). The fat in the pad is compartmentalised, restricting its displacement under compressive loading (Bennett & Ker, 1990).

The striking of a ballistic pendulum against the heel to imitate heel contact with the ground initially indicated that between 85% and 95% of energy is dissipated during heel pad deformation, with a small proportion recovered via elastic recoil (Cavanagh et al., 1984; Denoth & Nigg, 1981; Nigg & Denoth, 1980; Valiant & Cavanagh, 1984). In contrast, Alexander et al. (1986) later reported, following the investigation of non-human mammal heel pads considered akin to those of humans, that roughly 70% of energy is recovered due to elastic recoil following heel pad deformation. The approximate 30% energy dissipation value is much lower than reported in earlier pendulum experiments. This lower value is supported, however, by Bennett & Ker's (1990) subsequent human heel pad cadaver study and so it may be that the results of the pendulum studies represent the energy attenuating features of the lower leg as a whole. Additionally, it is possible that the pendulum studies failed to replicate human locomotion conditions, as subjects reported pain when forces greater than one bodyweight were applied, a phenomenon not observed during running or walking.

A further consideration with increasing drop heights is that with the heel pad rapidly stiffening under compression, only limited protection to the foot from impact forces is provided (Bennett & Ker, 1990). Thus, it is likely that voluntary movements are made at the lower limb joints to reduce the possibility of the heel being subjected to high ground reaction forces upon impact (Frederick, 1986). Experimentally, it has been noted that heel contact with the ground may be inevitable during drops from heights above a certain level and that heel pad compression is of importance when this contact does occur. It was observed by Bobbert et al. (1987b) that whilst subjects could voluntarily reduce the angular velocity of the feet to zero prior to heel contact following drops from 0.20 m and 0.40 m, this was not the case from 0.60 m, resulting in a sharp peak in vertical ground reaction force. These results were for short ground contact duration 'bounce drop jumps' and are supported by Young et al. (1995)'s increase in heel contact occurrence with increases in drop height when subjects were asked to minimise the ground contact time or maximise the jump height–contact time ratio. This increase was also present when jumping to maximise height using jumps closer to a 'countermovement drop jump' with longer ground contact durations than a bounce drop jump.

Numerous researchers have sought to quantify the magnitude of heel pad compression under varying loads and conditions. Whilst addressing the differences in previous heel pad energy dissipation results (attributed to the incorporation of dissipation due to the lower leg) discussed above, Aerts et al. (1995) reported non-linear heel pad stiffness with a peak observed deformation of 6.3 mm during pendulum and pendulum mimicking impacts. The results of this study were later compared with a theoretical model of energy dissipation following pendulum-heel impacts with the inclusion of lower leg soft tissue that could translate relative to the underlying bone (Pain & Challis, 2001). The model predicted maximum heel pad deformations of 7.1 mm. One of the earlier pendulum studies measuring energy dissipation of the lower leg as a whole had recorded heel pad deformations of 8.8 mm and 10.9 mm following application of forces between 338 and 676 N at 1.03 ms^{-1} and 1.44 ms^{-1} respectively (Cavanagh et al., 1984). This is similar to maximum observed deformations of 9.9 mm, 10.0 mm, and 12.7 mm in impacts with peak forces of up to 437 N, double bodyweight, and one bodyweight (569 N) respectively (Valiant & Cavanagh, 1985; Denoth, 1986; Kinoshita et al., 1993).

Despite the relatively low magnitudes of these impact forces when compared with those experienced in sporting impacts, peak heel pad deformations seem to vary little when studied in higher impact activities. For example, De Clercq et al. (1994) utilised x-ray film to record peak deformations of 9.0 ± 0.5 mm for two subjects during barefoot running. Thus, it appears likely that this range of deformation values represent a physiological maximum, with further increases in impact force resulting in little extra compression of the human heel pad. Indeed, Verdejo and Mills (2004) stated that in their finite element simulation of foot-shoe-interactions most of the deformation at forces less than 200 N occurs by the flattening of the lower surface of the heel pad, and the increase of the contact area with the shoe foam but that at higher forces, the deformed heel pad does not decrease much in thickness.

Shoe Compression

When investigating or modelling foot-ground interactions following an impact, it would be remiss to neglect the influence of compliance within the shoe. Indeed, the foam of sports shoes exhibits viscoelastic properties, compressing under impact. One of the heel pad deformation studies discussed above also investigated the mechanical properties of a running shoe sole (Kinoshita et al., 1993). The sole consisted of a 25 mm thick ethyl vinyl acetate (EVA) foam midsole, 7 mm thick rubber sponge outer sole, and 4 mm thick soft EVA foam inner sole, for a combined thickness of 36 mm. Under free-fall impact testing at the centre of the heel portion for five cycles, the sole deformed 9.3 mm and 11.5 mm from 30 mm and 50 mm drop height conditions respectively. With a 67% increase in drop height resulting in only a 24% increase in deformation, it can be assumed that the shoe sole exhibits non-linear stiffness and that further increases in drop height would be unlikely to result in much more than 11.5 mm of deformation.

Foot-Shoe Horizontal Displacement

Interactions between the foot and shoe are not limited to vertical deformations. Indeed, it is possible for the foot to translate horizontally inside the shoe following an impact with the ground and thus this must be added to any representation of

realistic shoe-ground translation when modelling the overall displacement between the human foot and the ground. For example, a 3D finite element model simulating the foot-sock-insole contact interactions has been used to demonstrate that regardless of sock-skin frictional properties, slippage displacement within the shoe of 3.7 mm was possible during walking (Dai et al., 2006). This value reduced to 2.0 mm for sockless shod walking. It remains possible that for higher impact and higher velocity activities a sockless foot could displace further than 2.0 mm within a shoe, although the value of around 3.7 mm predicted in two different conditions likely represents an upper limit for the displacement possible within the constraints of a shoe.

Lower Limb Joint Compression

Whilst compliance within the shoe, medial longitudinal arch, and heel pad can initiate the process of shock wave energy dissipation, they are unable to entirely prevent the kinetic energy and associated accelerations from reaching the ankle and other lower limb joints and body segments. Other mechanisms and structures must then continue to dissipate energy as it is transmitted through the human body from the feet towards the head. The three main lower limb joints of the ankle, knee, and hip contribute to the dissipative process, protecting the internal structures of the joints (Edwards, 1966; Radin et al., 1970).

Previous literature has tended to focus on the negative consequences of the degeneration of various joint structures over time. For example, it has been shown that degeneration of articular cartilage, the hyaline cartilage on the articulating surfaces of bones, can lead to pain within the joint (Radin et al., 1970; Roughley & White, 1980). Thus, it can be expected that the articular cartilage within a joint has compliant properties and is the cause of the energy dissipating properties within a joint (Camasso & Marotti, 1962; Edwards, 1966; Hirsch, 1944; McCutchen, 1962).

Subchondral bone, lying under articular cartilage towards the ends of a bone and containing marrow, is a compliant material, albeit with a much greater stiffness than articular cartilage (Radin et al., 1970). This type of bone has also been found to exhibit energy dissipating features. Both subchondral bone and articular cartilage

have been found to deform under high loads and can dissipate the kinetic energy transmitted through the lower body following a landing, resulting in lower accelerations at sites superior to this compliance (Camosso & Marotti, 1962; Gross & Nelson, 1988; Radin et al., 1970).

The dissipative properties of each of these features were investigated by Hoshino and Wallace (1987) in twenty cadaveric knees. They applied an impact load to the proximal femur and measured the force transmitted through the knee to a transducer at the distal tibia. Removal or damage of the meniscus, articular cartilage, and subchondral bone resulted in sequential increases in the measured force at the distal tibia (Figure 2.8). Indeed, that in an implanted total knee replacement was on average 180% of the recorded peak force in the intact knee

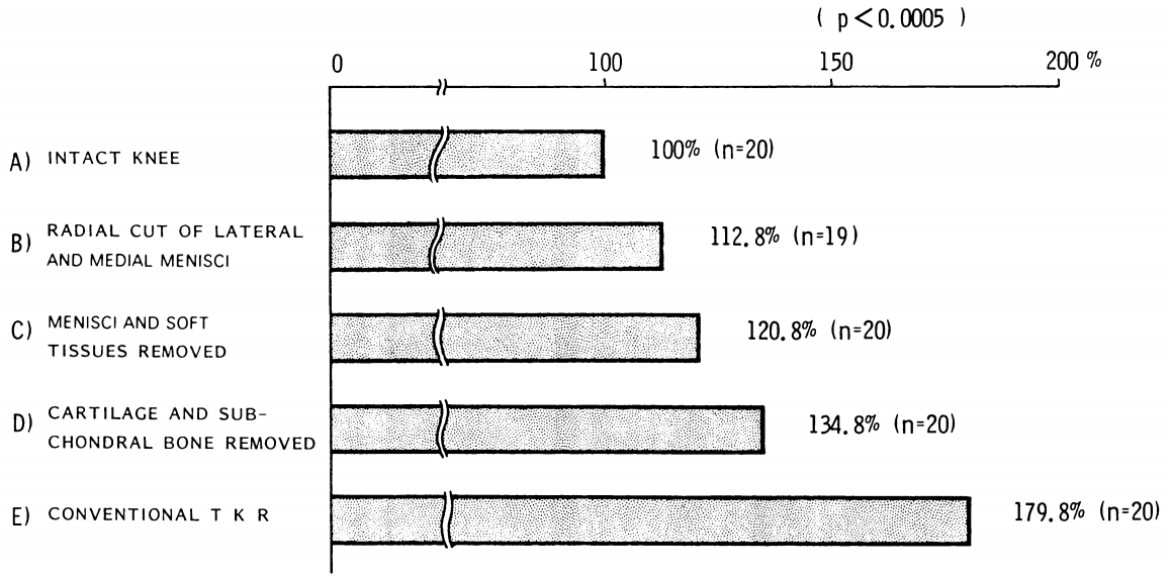

Figure 2.8. Peak force transmitted through the knee joint relative to that in an intact knee. TKR: total knee replacement. Adapted from Hoshino and Wallace (1987).

In addition to compliant joint structures and bone close to the joint, it was originally believed that long bones such as the femur and the tibia in the lower extremities would bend under loading (Huiskes, 1990; Prendergast & Taylor, 1990; Tensi & Gese, 1989; Verdonschot et al., 1993). This research was mainly based upon simplistic loading of the femur, which failed to represent typical loading during

dynamic human activities. The surrounding musculature and their interactions with the long bones were generally neglected and more recent research has identified that the muscle forces generated in the thigh and hip region are great enough to create equilibrium with the impact forces acting upon the femur, leading to minimal subsequent bending (Duda et al., 1997; Taylor et al., 1996). Whilst it is unlikely that long bone bending accounts for shock wave dissipation, the femur and tibia have greater volumes of subchondral bone than other bones and so exhibit a greater capacity to dissipate energy as it is transmitted through the lower extremity (Camosso & Marotti, 1962; Gross & Nelson, 1988; Radin et al., 1970; Yamada et al., 2002).

Whilst there has been little research to quantify compression within joint structures following an impact, relevant information can be gained from studies into joint spaces and joint unloading procedures. One cadaveric study by Fragomen et al. (2014) sought to discover the minimum distraction gap needed to ensure that the tibiotalar joint surfaces at the ankle would not contact each other with full weight-bearing while under distraction. For an unloaded leg, an average of 4.9 mm of distraction was required for the nine specimens to provide total unloading during full weight-bearing (700 N). The maximum required for any of the specimens was 7.0 mm, although it was acknowledged by the authors that in vivo, the dynamic load placed on the ankle joint by the tendons, including ankle dorsi flexors and plantar flexors, may increase the load and require greater distraction to unload the joint. The same could be said for greater loads during activities other than ambulation. Further information with regards to the maximum possible deformation within joint structures can be gained from literature relating to joint spaces. It has been shown that the mean medial tibiofemoral joint space in 22 knees was 6.04 mm (range 3 to 7 mm) in full extension, and 5.54 mm (range 3 to 7 mm) in 30° of flexion (Deep et al., 2003). The height of the lateral tibiofemoral joint space was measured in 20 knees and had a mean of 5.9 (3 – 8) mm in full extension and 5.2 (3 – 8) mm in 30° flexion. There is a shortage of available literature with regards to joint spaces and minimum distraction gaps at other joints such as the hip, although the mechanical responses to loading are likely to be similar.

Soft Tissue Movement

Soft tissue surrounding the skeleton makes up approximately 80% of a typical human's body mass. Most of this soft tissue is situated in the shank, thigh, and torso. Each has substantial inertia, affecting the magnitude of accelerations at the respective body segments. Following an impact soft tissue displaces relative to the underlying bone and thus provides an important energy dissipation mechanism (Gruber et al., 1987; 1998).

After Aerts et al. (1995) had concluded that the difference between in vivo and in vitro heel pad studies was attributable to contributions of the rest of the lower leg, Pain and Challis (2001) sought to resolve this heel pad paradox. They developed a computer simulation model replicating a pendulum impact experiment and were able to exclude aspects of the model to investigate their effects on energy dissipation. The authors reported a significant role of the wobbling mass of the shank, with peak forces over 100% greater in a heel pad linked to a solid shank than one attached to a shank with a wobbling mass. This therefore supports the suggestion that soft tissue plays a role in damping the kinetic energy being transmitted through the lower extremity following an impact with the ground. Indeed, it was recently stated that soft tissue deformation dissipates mechanical energy during running, performing net negative work, with magnitude increasing linearly with speed (Riddick & Kuo, 2016). Further recent work has quantified shank soft tissue mass centre displacement during drop landings from 0.30 m and 0.45 m (Furlong et al., 2016). These authors found group average absolute displacements (maximum observed displacements in brackets) in the anteroposterior, mediolateral, and vertical directions of 8 (16) mm, 7 (13) mm, and 21 (30) mm from 0.30 m, and 10 (33) mm, 5 (16) mm, and 20 (38) mm from 0.45 m. It should be remembered that the direction-specific maximum displacements did not necessarily coincide in time, trial, or subject, and so maximum absolute resultant displacement of the shank mass centre was likely less than the combined 53 mm.

A large proportion of the soft tissue in the shank, thigh, and torso is skeletal muscle with the capacity to rapidly change its physical properties. Skeletal muscle stiffness varies in accordance with its activation, being much stiffer when contracting than when relaxed. Indeed, intra-segmental motion in an arm during a repetitive hand-

striking action was reduced by 50% when the arm was tensed (Pain and Challis, 2002). Whilst simplistic representations remain desirable, researchers modelling the effects of soft tissue upon shock wave energy dissipation should consider including the effects of local skeletal muscle activation.

Post-impact segmental mass centre displacement in the trunk includes displacement of skeletal muscle and adipose tissue as well as internal trunk viscera. The viscera have a mass of approximately 0.14 x unshod body mass (Ciba Geigy, Scientific Tables; Minetti & Belli, 1994) and a vertical displacement within the range of 5 – 8 cm (Minetti & Belli, 1994) recorded during a hopping task. However, it must be remembered that a viscera displacement of up to 8 cm will not displace the entire trunk internal non-rigid mass by that amount and will likely be out of synchronisation with muscle and adipose displacement, thus resulting in an overall trunk wobbling mass displacement not equal to and likely less than that of the viscera. Furthermore, it remains unlikely that greater impact forces could result in viscera displacements of greater than 8 cm due to physiological constraints within the human anatomy.

Spinal Compression

The 24 articulating vertebrae within the spinal column coupled with the natural curvature of the spine provide an amount of compliance, with the spine able to vary shape in three planes. The individual vertebrae are connected by an intervertebral joint, with an intervertebral disc between the two articulating vertebrae enabling a small range of movement between the bony structures (Figure 2.9). Research has shown these intervertebral discs to be too stiff to provide any direct damping effect (Smeathers, 1984; 1988) and so any benefit in force attenuation is likely as part of a more complex system.

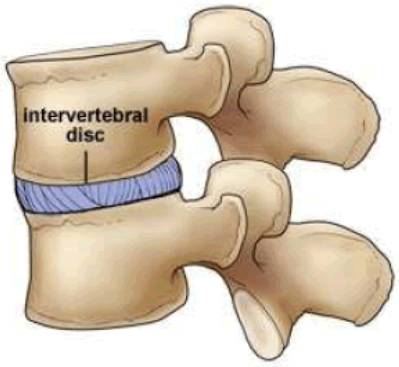

Figure 2.9 An intervertebral disc between two vertebrae. Jaiganesh et al. (2015).

Indeed, Helliwell et al. (1989) suggested that the intervertebral joints may act as flexible links, lowering the resonant frequency of the whole spine as forces pass through the spinal column. They compared a control group of subjects to a group who were diagnosed with ankylosing spondylitis, a condition involving fusion of the spine and thus minimal spinal compliance. Accelerometer analysis showed that the control group, but not the ankylosing spondylitis group, exhibited the ability to attenuate shock at frequencies above 15 Hz. The curvature of the spine has also been shown to contribute to energy dissipation, enabling the spinal column to have a non-linear, biphasic and viscoelastic behaviour during stress (Oliver & Middleditch, 1991). Thus, the entire spinal structure may have the ability to change shape following an impact, flattening and then recoiling, as seen with the medial longitudinal arch and the heel pad. The final phase of shock wave attenuation prior to the kinetic energy reaching the head is spinal column compliance and as such this dissipative ability is of high importance.

One study to investigate compliance within the overall spinal structure considered resultant vector length changes between the C7 and L5 vertebra following drop landings of up to 0.74 m (Bostock, 2009). The greatest mean compression of 14.6 mm was less than the combined compression of spinal subsections due to squashing the ‘S-shape’ of the spine. The compression magnitudes recorded in this study may have been influenced by retroreflective marker skin movement artefact and so this average of five trials is possibly slightly more representative than the greatest individual value, although it may still be an overestimate. On the other hand, length changes were determined relative to a standing trial, in which there

was likely already a certain amount of compression compared with a truly unloaded condition. Therefore, resultant vector length changes relative to zero spinal loading may be greater than those presented in this study.

Voluntary Movement

Technique during landing tasks has been investigated with respect to the magnitude of ground reaction forces experienced. It has been shown that landings in which a greater range of active ankle dorsiflexion and knee and hip flexion are exhibited result in lower ground reaction forces (DeVita & Skelly, 1992; Zhang et al., 1998). DeVita and Skelly (1992) concluded that a 'soft' technique absorbed 19% more kinetic energy in comparison to a 'stiff' landing technique. Unlike the mechanisms discussed above, this is not a passive impact attenuation mechanism, with the ankle plantar flexors, knee extensors, and hip extensors all active in dissipating energy. It is therefore important to account for differences in voluntary joint motion when comparing shock wave transmission in differing conditions, for example through an identification of the appropriate frequency content within an acceleration or force-time signal (Shorten & Winslow, 1992).

2.4.2 REPRESENTATION IN COMPUTER SIMULATION MODELS

Wobbling Masses

When modelling activities involving an impact, it has become increasingly common to incorporate wobbling mass elements alongside the rigid segments in the model (Gruber et al., 1998). This represents an attempt to replicate soft tissue displacement following an impact by enabling the mass incorporated in the wobbling element to displace relative to the rigid segment (bone). This is highly important when modelling an impact as the inclusion of wobbling masses has been shown to result in a loading on the system that is up to 50% lower than an equivalent rigid model (Pain & Challis, 2006). The wobbling element is commonly attached to the rigid segment at the proximal and distal end via damped non-linear passive springs of force F:

$$F = kx^3 - d\dot{x} \quad (2.1)$$

where *k* and *d* are stiffness and damping coefficients respectively, *x* is displacement and $\dot{x}$ is velocity (Pain and Challis, 2001).

The addition of wobbling masses to the structure of a simulation model increases the computational time due to more complex equations of motion and a greater number of parameters to be determined. Thus, these impact attenuating features should only be incorporated when necessary and consideration should be given to which rigid segments require the addition of a wobbling element.

Previous whole-body forward-dynamics simulation modelling studies have typically incorporated wobbling masses within the shank, thigh, and trunk with maximal displacements of 5 cm, 7.5 cm, and 10 cm permitted when determining viscoelastic parameters (Allen, 2010; Yeadon et al., 2010; Lewis, 2011; Felton, 2014). The source of a 10 cm limit for trunk wobbling mass displacement has been the study on viscera displacement during hopping by Minetti and Belli (1994) discussed in Section 2.4.1. As detailed in the previous section, this appears to be a vast overestimation. Indeed, the viscera only represents one portion of the trunk wobbling mass, with the remaining wobbling mass (including skeletal muscle and adipose tissue) likely displacing to a lesser degree than 10 cm, which is itself an increase of the 5 cm to 8 cm reported in the original study. Furthermore, it is unlikely that peak displacements of the various elements within trunk wobbling mass will occur synchronously, again reducing overall peak mass centre displacement.

Limits of 5 cm and 7.5 cm for shank and thigh wobbling mass displacements have been attributed to a study by Lafortune et al. (1992) in which external markers displaced 4.3 cm and 7.5 cm with respect to the tibia and femur respectively during loaded and unloaded knee flexion and extension. These displacements can be partially attributed to skin movement artefact, marker 'wobble', or experimental noise, and even the component that does relate to soft tissue movement is unlikely to relate closely to that following a single-leg impact of up to 13 Bodyweights such as during a modelled triple jump activity (Allen, 2010).

However, the 5 cm limit at the shank is relatively close to recent experimental results for shank soft tissue mass centre displacement during drop landings from 0.45 m (Furlong et al., 2016). Although maximum observed displacements from 0.30 m

were considerably less, and group average displacements were only 10 mm, 5 mm, and 20 mm in the anteroposterior, mediolateral, and superoinferior directions respectively, the maximum observed displacements of 33 mm, 16 mm, and 38 mm more closely resemble the value of 43 mm for marker movement reported by Lafortune et al. (1992) and used in subsequent simulation studies. As discussed in Section 2.4.1, though, the direction-specific maximum displacements of Furlong et al. (2016) did not necessarily coincide in time, trial, or subject, and so maximum absolute resultant displacement of the shank mass centre was likely less than the combined 53 mm. It is likely that any excessive compliance within existing simulation models, such as excessive wobbling mass peak displacements, serves to compensate for the lack of compliance elsewhere in the system such as at the pin joints between adjacent body segments.

Foot-Ground Compression

Ground contact models used in existing whole-body simulation models have been discussed in more detail in Section 2.3.4. However, they represent a valuable energy dissipating feature within the models. As with wobbling mass displacement (above), we have typically seen excessive compliance at the foot-ground interface. Whilst the studies outlined in Section 2.4.1 found maximum deformations of 11.5 mm and 12.7 mm at the shoe sole and human heel pad respectively (Kinoshita et al., 1993), simulation viscoelastic foot-ground interfaces have been allowed up to 56 mm of compliance, not only at the heel but also at the toe and MTP joint (Allen et al., 2012). Again, it remains likely that this excessive compliance compensates for the lack of compliance elsewhere between the site of impact and the first wobbling mass or indeed further up the body, such as ankle joint compression (Fragomen et al., 2014) or up to 13.4 mm of vertical compliance within the medial longitudinal foot arch (Nielsen et al., 2009).

When this additional compliance is missing, allowing additional displacement at the ground has been a necessity. Indeed, Allen et al. (2012) investigated the effects of varying foot-ground compliance limits on the ability of a whole-body forward-dynamics simulation model of triple jumping to match experimentally recorded performances and ground reaction forces. When foot spring compression was

limited to 20 mm, which is likely already excessive at sites other than the heel, the simulation model was only able to match experimental ground reaction forces to a 48% difference (Figure 2.9). Compression of 40 mm enabled a more acceptably matched ground reaction force, with a 16% difference, and the difference was reduced to 12.4% with the removal of all foot-ground compression constraints (Figure 2.10). This final condition saw compressions of between 43 mm and 56 mm obtained in the three phases of the action, and yet there were still large noticeable differences in the force-time histories. Whole-body mass centre position was within 4 mm of the experimental position at the times of these unrestricted maximum compressions, further supporting the argument that excessive foot-ground compression was replacing compression from elsewhere in the human body. Indeed, the authors concluded that the unrestricted model is appropriate for simulating kinematic performance but that it would need to incorporate compliance elsewhere in the link system to accurately calculate internal forces.

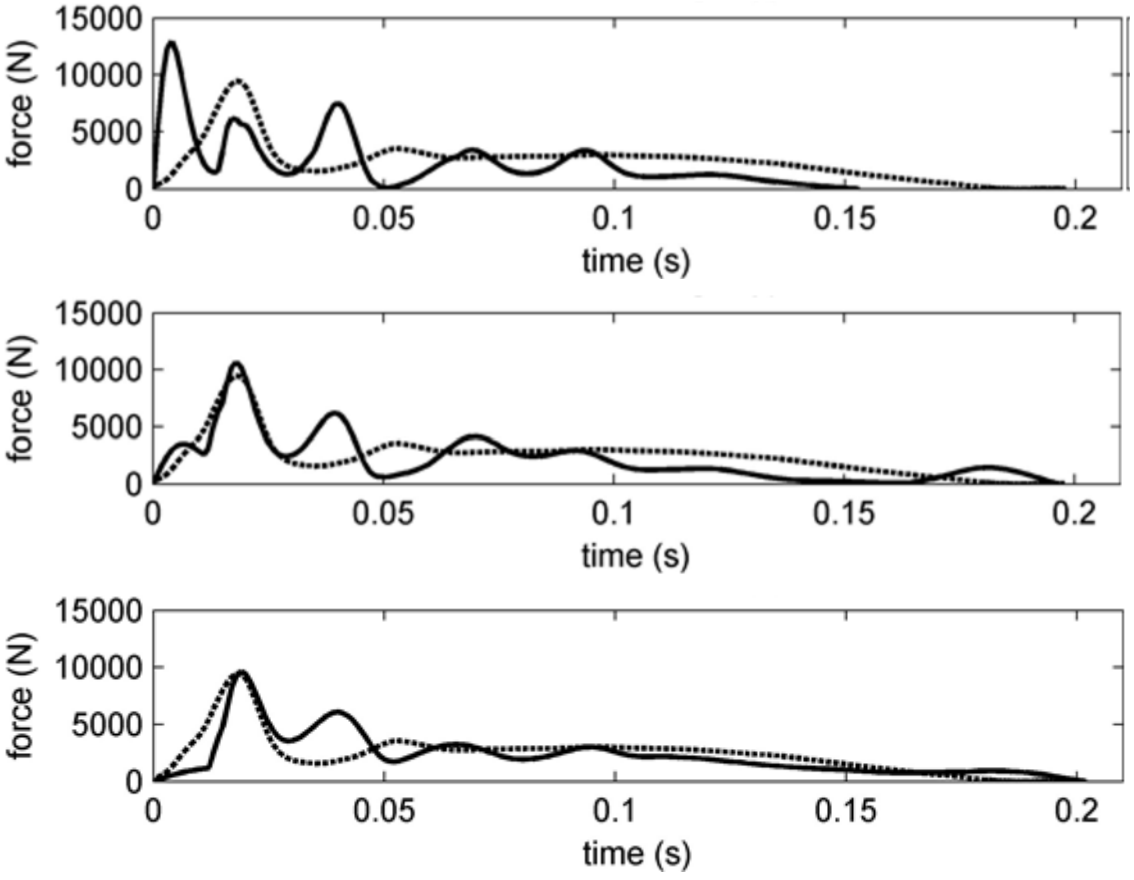

Figure 2.10 Differences between simulation (solid line) and experimentally recorded (broken line) vertical ground reaction forces during the jump phase of the triple jump.

Simulation foot-ground depression limited to 20 mm (top), 40 mm (middle), and unconstrained (bottom). Adapted from Allen et al. (2012).

Viscoelastic Joints

One such aspect in which future studies could incorporate compliance elsewhere in the link system is within joint structures. Previous forward-dynamics computer simulation models in the field of sports biomechanics have typically modelled the connection between adjacent rigid segments using frictionless pin joints. This relies on an assumption that the distal end of one body segment shares a common point with the proximal end of the connecting segment, a simplification of reality. This assumption neglects the influence of compliance within joint structures discussed in Section 2.4.1, and the subsequent effects on the kinetics and kinematics within the human musculoskeletal system. Thus, when modelling an activity such as drop jumping that is dependent upon an impact force, it may be appropriate to seek a more realistic representation of joint structures, potentially incorporating viscoelastic features within a joint to replicate the compression and force dissipation in vitro.

This assumption of a fixed and shared contact point is also questionable at the shoulder joint. Motion at the shoulder occurs at four different joints and the extent to which this is represented within simulation models has again depended upon the required complexity. Whilst a single degree of freedom pin joint was judged adequate to represent the shoulder during tumbling (Yeadon & King, 2002), Hiley and Yeadon (2003a) utilised a simple viscoelastic representation with the stiffness and damping coefficients obtained from a combination of experimental and theoretical data. This slightly more complex representation was deemed necessary to represent the translational movement of the shoulder joint during backward giant high bar circling. This was adequate in a whole-body model where the overall kinematics were of the most interest, whereas a more complex finite element model (van der Helm, 1994) has been necessary to address the contribution of individual muscles to shoulder joint movement.

2.5 SUMMARY OF LITERATURE

Any simulation model should remain as simplistic as possible whilst comprising sufficient complexity to answer the proposed research questions (Yeadon & King, 2008). Furthermore, the inclusion of subject-specific parameters such as joint torque profiles (King & Yeadon, 2002) within a simulation model is necessary to accurately evaluate a model against the performance of an individual. Lewis (2011) stated that the simulation of maximal effort human movement should include biarticular joint torque representations when initial whole-body momentum is not large and when multiple joint kinematics with a large biarticular muscle contribution are involved.

In high impact activities such as drop jumping and drop landing, much of the impact force is dissipated through internal body structures, preventing excessive forces from reaching the brain and other vital organs, or from causing acute or chronic musculoskeletal injuries. This is achieved through mechanisms including shoe compression; heel pad deformation; foot arch compliance; lower limb joint compression; soft tissue movement; spinal compression; and voluntary movement, although previous simulation models have been limited in their representation of these features. Indeed, Allen et al. (2012) showed a requirement for foot-ground compression and wobbling mass displacement far in excess of realistic limits to predict ground reaction forces with any acceptable level of accuracy. It seems that compliance elsewhere in the link system, such as through the introduction of viscoelastic joint structures, may be required to accurately model internal energy transmission or predict ground reaction forces alongside realistic compliance limits.

2.6 CHAPTER SUMMARY

In this chapter literature relating to the construction of a whole-body forward-dynamics simulation model of vertical jumping was described and critically evaluated. This was followed by a review of literature relating to impact attenuating mechanisms within the human body and a critique of existing attempts to represent these within whole-body simulation models.

CHAPTER 3

DROP LANDING AND DROP JUMP DATA COLLECTION

3.1 CHAPTER OVERVIEW

In this chapter, a description of the methodology used to collect kinematic and kinetic data of a subject performing drop landings and drop jumps is presented.

3.2 STATEMENT OF PURPOSE

The purpose of this thesis is to investigate the effect of incorporating joint compliance on the ability of a subject-specific computer simulation model to accurately predict ground reaction forces during dynamic jumping activities.

3.3 RESEARCH QUESTION ONE

What contribution does spinal and joint compression make to the attenuation of impact-related accelerations following landings?

3.4 INTRODUCTION

Since the purpose of this study, as detailed in Section 1.3 and 3.2, was to investigate the effect of incorporating joint compliance on the ability of a subject-specific computer simulation model to accurately predict ground reaction forces during dynamic jumping activities, the same single subject was used for all investigations within this thesis. The subject was a male national level 100 m sprinter (age: 23 years; height: 1.86 m; mass: 88.6 kg; personal best time: 10.50 s), with experience of using isovelocity dynamometers (see Chapter 6) and practicing drop jumps as part of training for his sport. The subject was free from any injuries that may affect his participation, had refrained from strenuous physical activity for 36 h

prior to the testing sessions, and completed a health screen questionnaire (Appendix 2) prior to taking part. The testing procedures were explained in accordance with Loughborough University ethical guidelines, and the subject completed an informed consent form (Appendix 3).

3.5 MEASUREMENT OF DROP LANDING AND DROP JUMPING

3.5.1 DATA COLLECTION ENVIRONMENT

The subject attended one laboratory testing session. Kinematics were recorded using an 18 camera (M^2 MCam) Vicon Motion Analysis System (OMG Plc, Oxford, UK) operating at 250 Hz to ensure concurrent frames with synchronous force platform and accelerometer data. The motion capture volume, of at least 2 m x 3 m x 4 m, was calibrated using a 240 mm calibration wand (14 mm retroreflective markers), with residual errors for all cameras of less than 0.2 mm. This meant that all residual errors were less than 0.1% of the camera lens to capture volume centre distance, as recommended by Vicon. An Ergocal (14 mm) static calibration frame was utilised to define the origin and global laboratory coordinate system. Medio-lateral, anterior-posterior, and vertical ground reaction forces were measured using an AMTI force platform (AMTI Inc., Watertown, MA; 600 x 400 mm, 1000 Hz). Acceleration data were recorded using lightweight Dytran triaxial cabled accelerometers (Dytran Instruments Inc., Chatsworth, CA; Figure 3.1), each weighing 10 grams and sampling at 1000 Hz, with a range of 100 g and a sensitivity of 50 $mV \bullet g^{-1}$, where g is acceleration due to gravity. All data were synchronised through Vicon software, with synchronisation checked by the dropping of a golf ball, covered in 3M reflective tape (Figure 3.2), on to the force platform, which was recorded both in Vicon and through the force platform. The position of the golf ball was tracked through time and the moment at which its position, as recorded in Vicon, contacted the ground was compared with the timing of the associated rise in ground reaction force to confirm synchronisation.

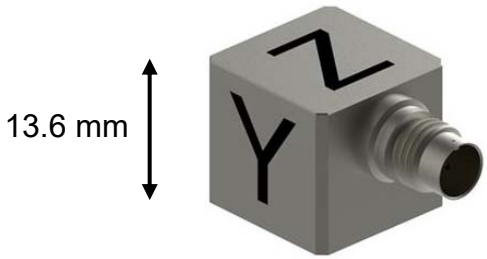

Figure 3.1. Lightweight Dytran triaxial accelerometer

Figure 3.2 Reflective ball used to test synchronisation.

3.5.2. RETROREFLECTIVE MARKERS

Fifty-seven 14 mm retroreflective markers were attached to the subject using a sports adhesive spray and double-sided tape (Figure 3.3). Forty-five markers were positioned over known bony landmarks or where appropriate on the sports shoes of the subject, in accordance with the marker set developed by Worthington (2010). The marker set was designed to be compatible with the joint centres of Yeadon's (1990) mathematical inertia model and the computer simulation model to be produced in the present thesis (Section 6.7). Typically pairs of markers were placed across a joint medio-laterally such that a line between both markers intersected the joint centre, which would most commonly be assumed to be halfway between the two markers. Markers were placed on the left and right anterior and posterior superior iliac spine to enable the hip joint centre algorithm of Davis et al. (1991) to be utilised. An additional 12 markers were placed on the non-dominant posterior shank (3: posteromedial; posterior; and posterolateral) and thigh (6: anteromedial; anterior; anterolateral; posteromedial; posterior; and posterolateral) as well as over the stomach (1: inferior abdominal area) and chest (2: medial and lateral) for further

analysis of soft tissue displacement. Retroreflective marker placement can be seen in full in Figure 3.3 and is detailed in Table 3.1.

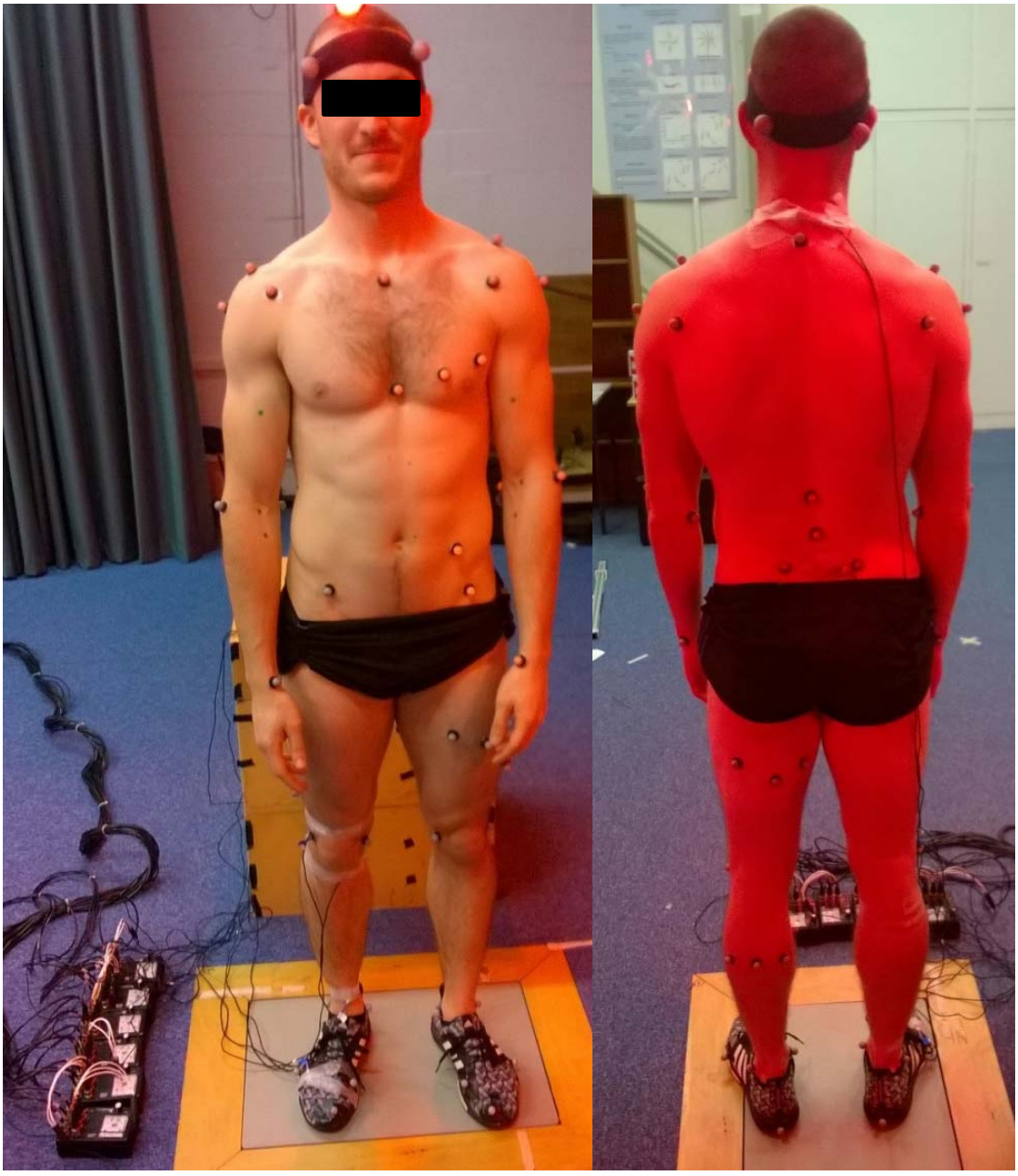

Figure 3.3 Positioning of reflective markers on the subject

Table 3.1. Retroreflective marker placements

joint / position	number of markers	marker position
toe	2	L/R on shoe over halux
MTP	4	L/R on shoe over 1st & 5th MTP joint
heel	2	L/R on shoe posterior to calcaneus
ankle	4	L/R; medial & lateral malleoli
calf	3	L; posteromedial; posterior; & posterolateral
knee	4	L/R; medial & lateral
thigh	6	L; anteromedial; anterior; anterolateral; posteromedial; posterior; & posterolateral
hip	4	L/R; anterior & posterior superior iliac spine
abdomen	1	L; inferior abdominal area
chest	3	xiphoid process & L pectoral (medial & lateral)
back	2	T10 & L1 vertebrae
neck	2	manubrium sterni & C7 vertebra
head	4	L/R; on headband; anterior & posterior
shoulder	8	L/R; anterior, posterior, lateral, & acromion process
elbow	4	L/R; medial & lateral
wrist	4	L/R; medial & lateral

3.5.3. ACCELEROMETERS

Lightweight Dytran triaxial accelerometers (1000 Hz) were positioned over the first metatarsophalangeal (MTP) joint, the distal and proximal anteromedial aspects of the tibia, the anterolateral distal femur (all on the dominant leg, established as the subject's preferred leg for kicking a ball), the L5 vertebra, and the C6 vertebra (Figure 3.4). The accelerometers were held in position by elastic tape tightened to the limit of subject comfort. Such tightening has been shown to minimise the negative influence of soft tissue movement on the accelerometer signal (Clarke et al., 1985; Valiant et al., 1987). Likewise, the use of lightweight accelerometers has been shown to have a similar effect (Ziegert & Lewis, 1979). All accelerometers

were positioned with the z-axis pointing vertically upwards in the anatomical position and were set to zero in the same orientation prior to attachment to the subject.

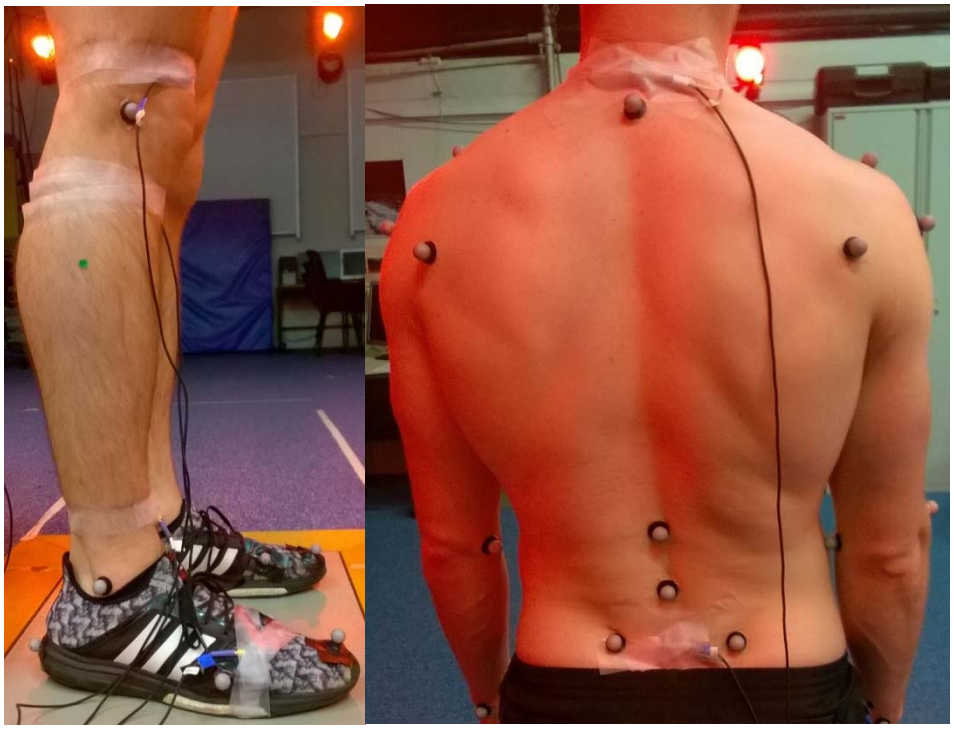

Figure 3.4 Positioning of accelerometers on the subject

3.6 PROTOCOL

A self-selected warm up was performed prior to the onset of data collection. The subject performed 2 successful double leg drop landings (Figure 3.5) and 2 successful double leg drop jumps for maximal height (Figure 3.6) from each of 0.30 m, 0.445 m, 0.595 m, and 0.74 m onto the force platform. Successful trials were those in which the subject landed with both feet wholly on the force platform, felt that he had performed a maximal effort (in the case of the drop jumps), and was judged to have stepped off the box horizontally rather than jumping upwards or stepping downwards. In the case of the drop landings, the subject was asked to hold a rigid body configuration after landing and try to minimise voluntary joint flexion. Use of the arms was permitted throughout each task, although the subject was asked to keep all bodily movements within the sagittal plane (i.e. arms moving forward and backward due to shoulder flexion/extension but not outward due to

shoulder abduction). Any trial with noticeable movement outside of the transverse plane was considered an unsuccessful trial and was repeated.

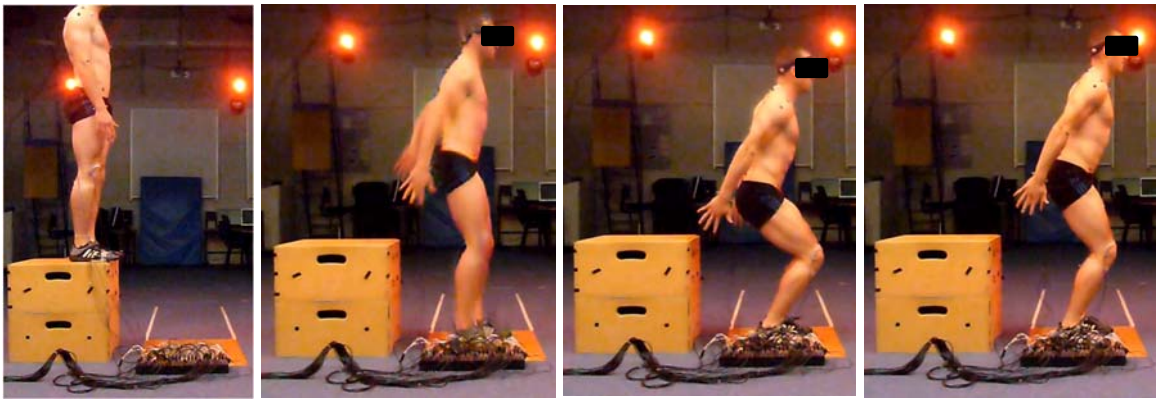

Figure 3.5 A drop landing trial performed from 0.595 m.

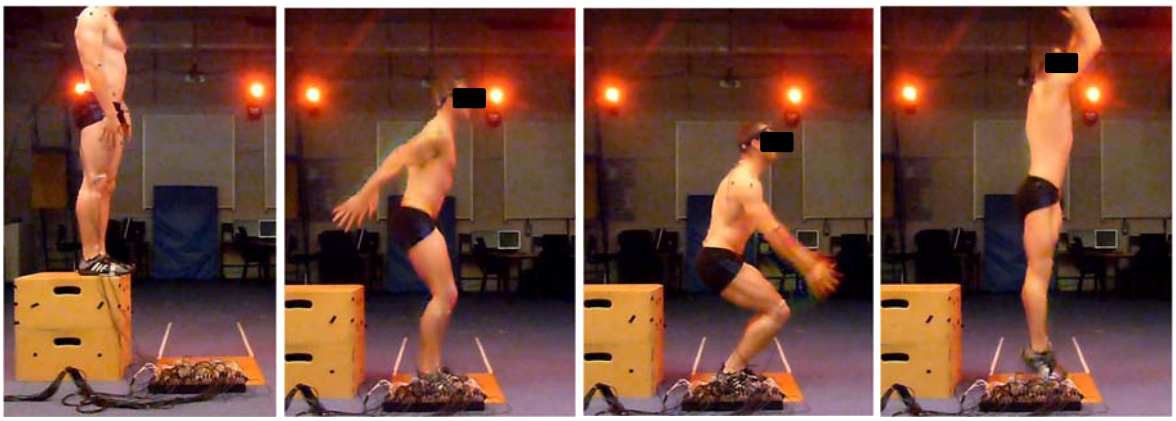

Figure 3.6 A drop jump trial performed from 0.595 m.

3.7 CHAPTER SUMMARY

This chapter has detailed the methodology utilised in the experimental data collection of drop landing and drop jumping performances. The use of motion capture, force platform, and accelerometers has been outlined. The next chapter will analyse the progressive transfer of accelerations through the body from the site of impact towards the head during these experimental trials.

CHAPTER 4

IMPACT SHOCK ATTENUATION DURING DROP LANDING AND DROP JUMPING

4.1 CHAPTER OVERVIEW

In this chapter, the reduction and analysis of acceleration signals recorded during the drop landing and drop jumping trials, as detailed in Chapter 3, will be presented. These data will then be used to quantify the progressive attenuation of the impact shock wave through the human body, and thus quantify the contribution of spinal and joint compression to the dissipation of energy during impact landings. Finally, conclusions will be drawn regarding the magnitude of the limitations associated with modelling the human body using pin joints during impacts.

4.2 INTRODUCTION

Existing literature relating to post-impact energy dissipation in humans was discussed in detail in Section 2.4 of the present thesis. Major contributors to this dissipation, which have been discussed individually in Section 2.4.1, include foot arch compliance, heel pad deformation, compliance within joint structures, spinal compression, and soft tissue movement, as well as voluntary joint actions.

Skin-mounted accelerometers have previously been utilised to gain an indication of energy dissipation throughout the human body (Hamill et al., 1995; Shorten & Winslow, 1992; Zhang et al., 2008). As the impact shock is attenuated, thus the measured accelerations would be expected to progressively decrease at sites further up the human body. Previous investigations offer no quantification of impact shock attenuation below the tibia, or any progressive attenuation throughout the body from tibia to head.

Any analysis of peaks in acceleration-time signals will include low frequency components due to voluntary muscular action, as well as high frequency

components due to electrical noise or resonance in the attachment of the accelerometers to the body of the subject. It is therefore important for future studies to utilise methods such the power spectral analysis in Shorten and Winslow (1992) to isolate the effects of passive shock wave attenuation in progressive stages up the body and therefore quantify the contribution of various mechanisms to energy dissipation. Conclusions can therefore be drawn regarding the magnitude of the limitations associated with modelling the human body using pin joints during impacts (Section 2.4.2).

Thus, the purpose of the present study was to quantify the progressive dissipation of post-impact kinetic energy and consequently shock wave accelerations by structures within the human body during impact landings, and to quantify the contribution of spinal and joint compression to this dissipation.

4.3 METHODS

4.3.1 DATA COLLECTION

One male 23 year old national level 100 m sprinter (height 1.86 m, mass 88.6 kg, personal best 10.50 s) performed 2 successful double leg drop landings (Figure 3.6) and 2 successful double leg drop jumps for maximal height (Figure 3.7) from each of 0.30, 0.445, 0.595, and 0.74 m onto a force platform. Lightweight Dytran triaxial accelerometers (1000 Hz) were positioned over the first metatarsophalangeal (MTP) joint, the distal and proximal anteromedial aspects of the tibia, the anterolateral distal femur (all on the dominant leg), the L5 vertebra, and the C6 vertebra (Figure 3.5). The accelerometers were held in position by elastic tape tightened to the limit of subject comfort. Full details of the subject, data collection environment, accelerometer and force platform set up, and testing protocol were presented in Chapter 3.

4.3.2 DATA ANALYSIS

Resultant accelerations were determined from axis-specific acceleration signals (Figure 4.1), before the power spectra of ground contact phase resultant

accelerations at each position on the body were determined for each trial by Fast Fourier Transformation of these time-domain resultant signals. The impact of interest in each trial was a one-off event (non- periodic), and of varying duration. For this reason, as in Shorten and Winslow (1992), several signal processing techniques were utilised that are specifically designed for discontinuous signals. Using the time of first ground contact as a trigger, a 0.1 s subsample of the subsequent resultant acceleration data were extracted for each trial. Time of first ground contact was identified from the synchronised force platform data (also operating at 1000 Hz) as the first time point at which the vertical ground reaction force rose above a threshold value of 10 N. This 0.1 s time period was sufficient to capture the initial large peak of the resultant acceleration after impact at each position on the body in its entirety before accelerations returned to much lower magnitudes (Figure 4.2).

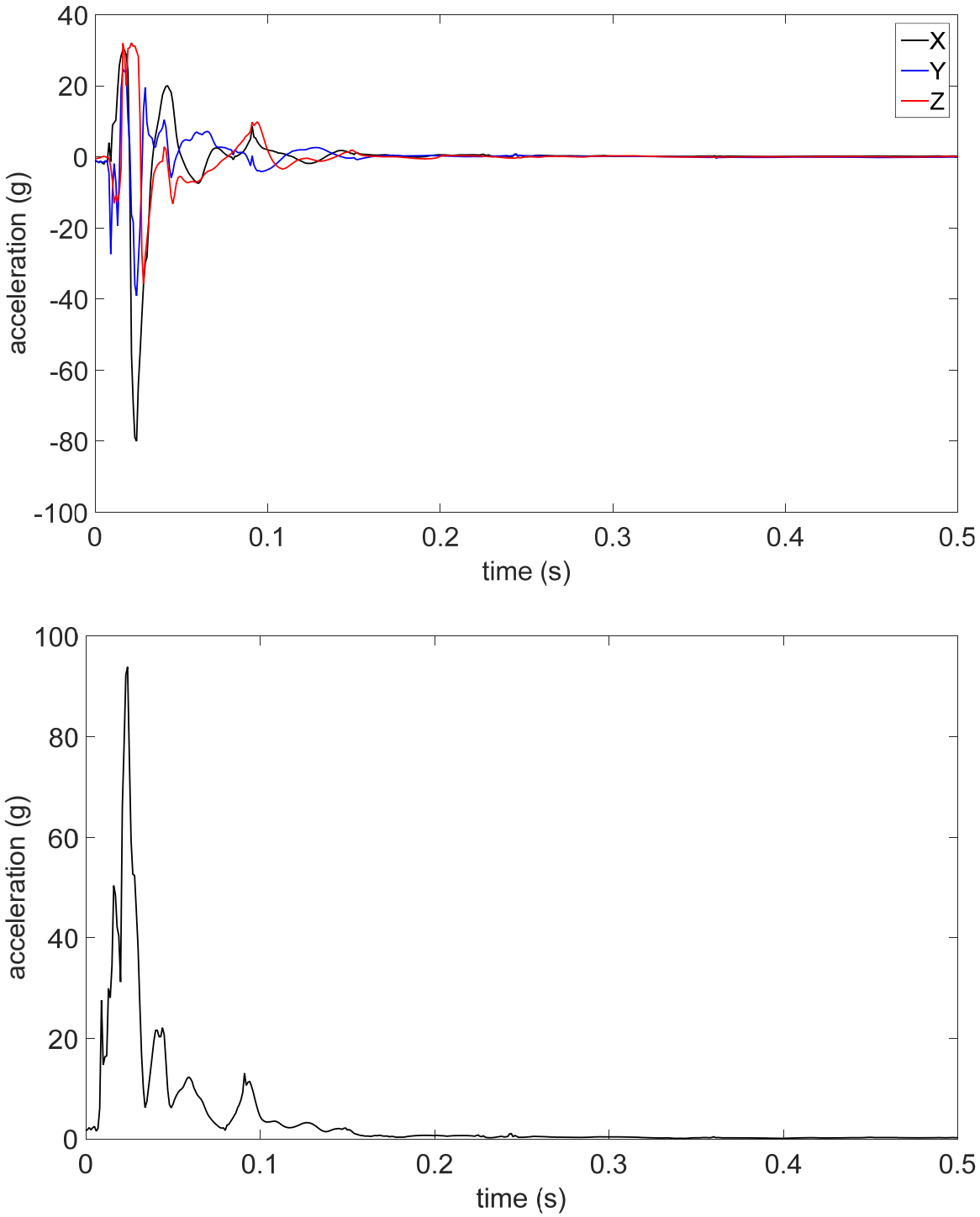

Figure 4.1. Individual axis components (top) and resultant acceleration (bottom) for the MTP joint following a drop landing from 0.75 m.

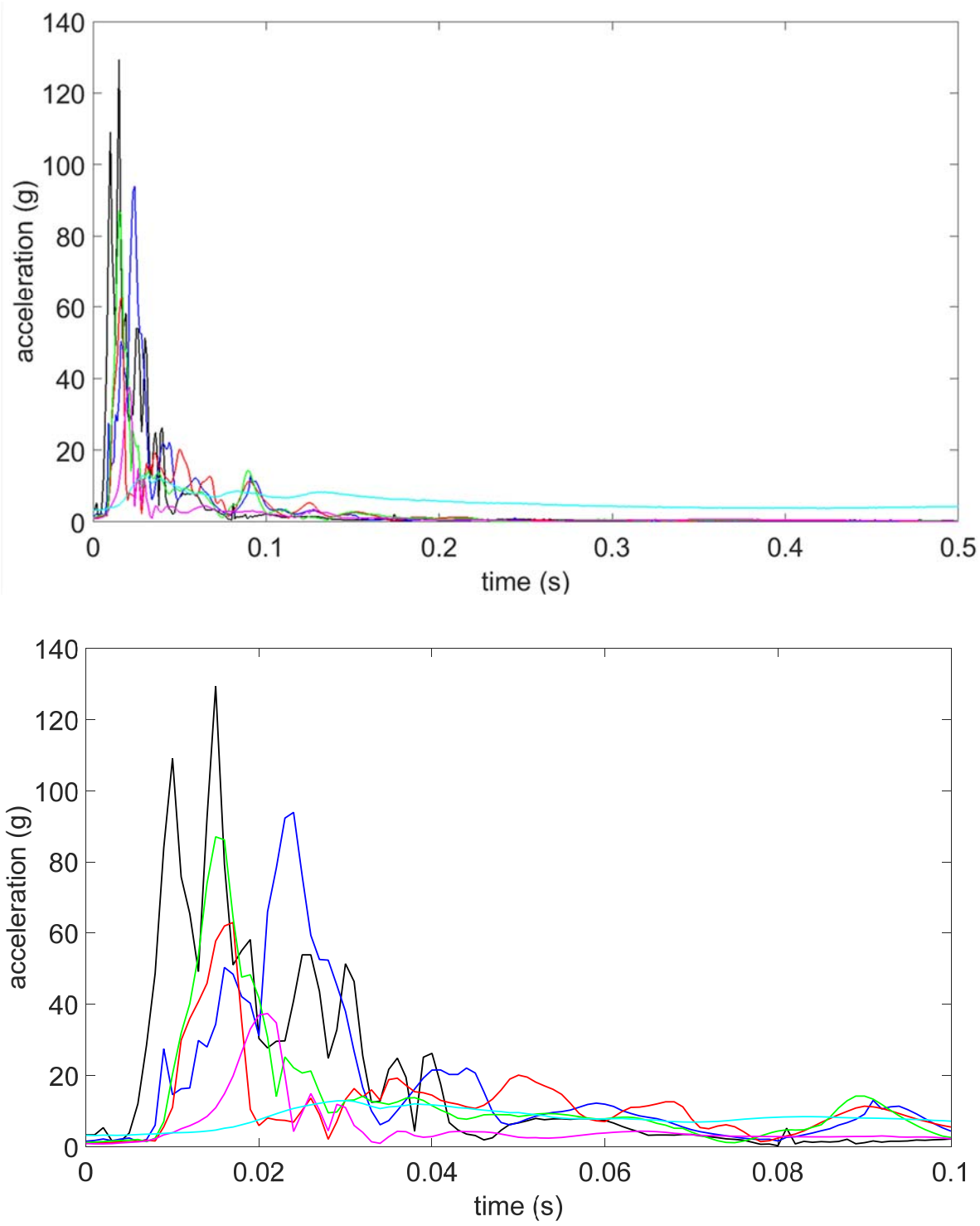

Figure 4.2. A 0.1 s subsample (bottom) taken from the resultant accelerations (top) during a drop landing from 0.75 m. Black: MTP; dark blue: distal tibia; red: proximal tibia; green: distal thigh; pink: L5; light blue: C6.

The average value of each signal during the subsample was subtracted throughout the subsample, and any linear trend was removed. This produced a sample for each resultant acceleration in the time domain with a mean of zero and equal start and end values (Figure 4.3). For a sampling frequency of 1000 Hz, a 0.1 s subsample would only enable the analysis of frequency components in 10 Hz intervals (sampling frequency / number of data points = 1000 / 100 = 10 Hz intervals). Therefore, each subsample was padded with values of zero to a total sample duration of 0.5 s. This ensured the presence of zero mean and no linear trend remained, whilst allowing frequency components to be analysed in 2 Hz intervals (sampling frequency / number of data points = 1000 / 500 = 2 Hz intervals).

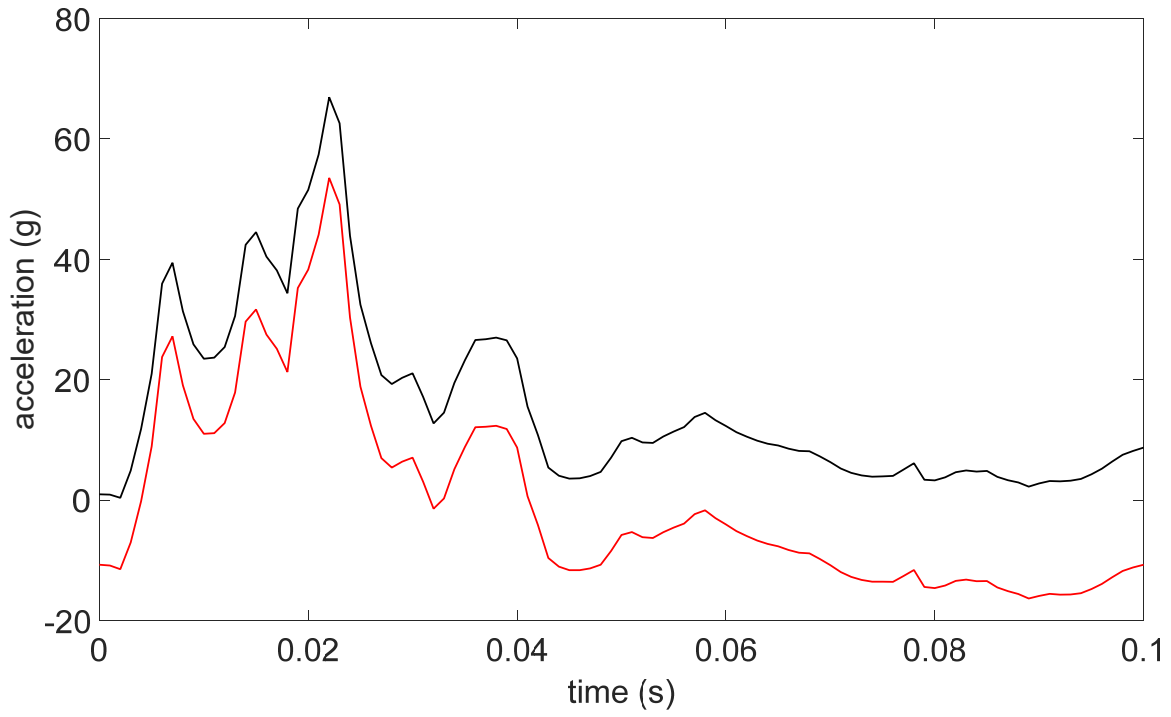

Figure 4.3. The mean and any linear trend removed (red) from distal tibia resultant acceleration (black) following a drop landing from 0.75 m.

The amplitude-frequency spectrum of each resultant acceleration subsample was then calculated, as in Shorten and Winslow (1992), using the Fast Fourier Transformation procedures of Newland (1984). Although it is possible to analyse frequency components up to the Nyquist frequency of half of the sampling frequency (in this case 500 Hz), for the purposes of this study only those frequency

components in the range of 2 to 100 Hz were considered. Previous research into impact acceleration attenuation following human foot-ground impacts (Shorten & Winslow, 1992; Hamill et al., 1995; Zhang et al., 2008) suggests this range is more than sufficient to identify the various components of the impact shock wave and its acceleration signal gain or attenuation.

The power, P_i, of each spectrum component is the square of its amplitude, A_i. Because the addition of a certain number of zeros, L, to the end of a fixed number, N, of adjusted acceleration values in the time-domain data reduces the calculated powers by a factor of N/(N+L), the inverse of this factor was applied to the calculated powers such that the true representative powers were given by:

$$P_i = \frac{{A_i}^2(N+L)}{N} \tag{4.1}$$

Due to the collection of two trials in each condition, there were two acceleration subsamples for each position on the body in each condition. These were ensemble averaged in the frequency domain, obtaining spectral estimates for each body position and trial type. However, as mentioned above, the interval between frequency components is dependent upon both the sampling frequency and the total number of data points in a sample. The amplitudes of the discrete power spectrum, in turn depend upon these intervals, as an alternative set of frequency component intervals would yield an alternative spectrum of frequency-amplitude results. Thus, the power spectral density, S_i, of each ensemble averaged signal frequency component was determined as the power, P_i, of that component divided by the frequency interval, Δf:

$$S_i = \frac{P_i}{\Delta f} \tag{4.2}$$

A spectrum of gain or attenuation data between two signals is known as a transfer function. This was calculated for each frequency component, in decibels, between different accelerometer positions on the body during the same trial condition, as 10 times the base-10 logarithm of the ratio between the first and second signal powers. For example, the transfer function, T_i, between the first MTP joint (position 1), and distal anteromedial aspect of the tibia (position 2) for each frequency component, i, was given by:

$$T_i = 10log_{10}\frac{S_{(2,i)}}{S_{(1,i)}} \quad (4.3)$$

4.3.3 STATISTICAL ANALYSIS

A two-way analysis of variance for repeated measures and a Tukey-Kramer pairwise comparison were utilised to detect significant differences between average peak resultant acceleration and time of peak resultant acceleration due to different positions on the body, and/or different trial conditions. Partial eta-squared (η^2) provided a measure of effect size. Pearson's product moment correlation coefficients assessed relationships between the determined parameters and the magnitude of peak resultant ground reaction forces. A P-value < 0.05 indicated statistical significance.

4.4 RESULTS

4.4.1 PEAK RESULTANT ACCELERATIONS

For peak resultant accelerations (Table 4.1), a significant main effect was observed in both drop landings and drop jumps, for accelerometer position (drop landings: $p < 0.001$; $\eta^2 = 0.99$, drop jumps: $p < 0.001$; $\eta^2 = 0.99$) but not for drop height (drop landings: $p = 0.16$; $\eta^2 = 0.69$, drop jumps: $p = 0.43$; $\eta^2 = 0.46$). Furthermore, no significant interaction effect between accelerometer position and drop height was observed (drop landings: $p = 0.25$; $\eta^2 = 0.61$, drop jumps: $p = 0.45$; $\eta^2 = 0.44$). However, large effect sizes were observed for all main and interaction effects. Peak resultant acceleration tended to increase with increasing drop height and decrease with increasing distance from the ground (Figure 4.4). These individual differences between drop heights were not significant for either trial condition ($0.26 < p < 1.00$), with all 95% confidence intervals for mean differences crossing zero. For drop landings, all differences between positions on the body were significant ($0.00 < p < 0.03$) other than peak resultant accelerations at the distal femur being not significantly lower than those at the distal tibia ($p = 0.49$), or greater than those at the proximal tibia ($p = 0.06$). For the drop jumps, peak resultant accelerations at

the distal tibia were non-significantly greater than those at the MTP ($p = 0.15$), those at the proximal tibia were not significantly lower than at the distal tibia ($p = 0.22$) or different to those at the distal femur ($p = 1.00$), and peak accelerations at the C6 vertebra level were non-significantly lower than at the L5 level ($p = 0.80$). All other differences were significant ($0.00 < p < 0.08$). On average, the peak resultant MTP acceleration was already reduced by 21 ± 9% at the distal tibia (23 ± 7% drop landings; 20 ± 11% drop jumps) and by 76 ± 11% (66 ± 6% drop landings; 86 ± 3% drop jumps) and 87 ± 3% (86 ± 3% drop landings; 89 ± 0% drop jumps) at the L5 and C6 vertebra levels respectively.

Table 4.1. Peak resultant accelerations (g).

	drop landings (m)				**drop jumps (m)**			
	0.30	**0.445**	**0.595**	**0.74**	**0.30**	**0.445**	**0.595**	**0.74**
MTP	94.1	120.0	118.5	113.8	102.0	110.0	114.0	111.0
distal tibia	72.4	89.7	102.0	80.4	75.0	95.5	88.7	92.0
proximal tibia	52.2	61.4	64.5	61.4	61.0	61.0	68.5	69.5
distal femur	65.3	81.4	89.0	74.5	60.5	61.0	62.5	78.1
L5	34.5	35.5	43.2	37.6	15.0	12.2	15.8	19.1
C6	17.5	14.5	16.1	13.6	11.5	11.8	13.0	12.1

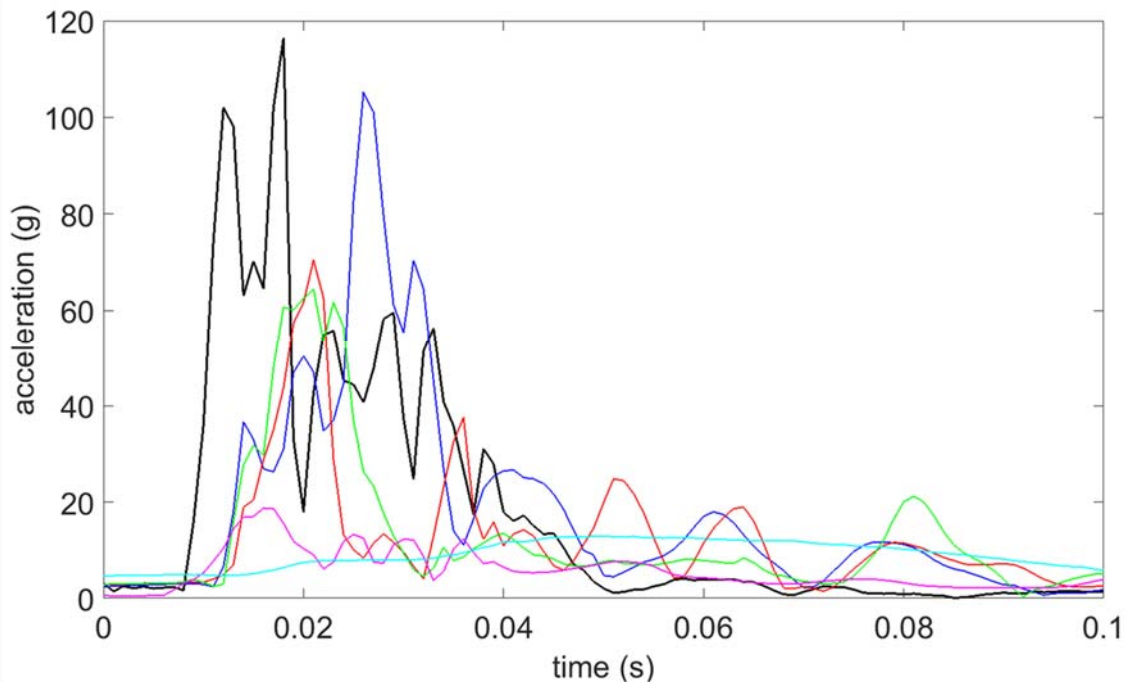

Figure 4.4. A typical time-domain acceleration signal from a 0.595 m drop jump. Black: MTP; dark blue: distal tibia; red: proximal tibia; green: distal thigh; pink: L5; light blue: C6.

Further significant main effects were observed between accelerometer position and timing of peak resultant acceleration relative to that of the MTP (Table 4.2) for both drop landings ($p < 0.001$; $\eta^2 = 0.94$) and drop jumps ($p < 0.001$; $\eta^2 = 0.96$), with all other peaks occurring after those at the MTP. Despite the significant main effect, there was no clear trend for the drop landings. The trend in drop jumps was for an increasingly delayed occurrence of peak accelerations with increased distance from the feet. However, this was only evident due to later peaks at the C6 level than at all other positions ($0.00 < p < 0.01$) as there were no differences between proximal tibia, distal femur, and/or L5 ($p = 1.00$ and 95% confidence intervals for mean differences all included zero) and no consistent trend for the distal tibia in relation to other positions (mean differences -0.029 to 0.006; $0.00 < p < 0.71$). No significant main effect was observed between this timing measure and drop height (drop landings: $p = 0.27$; $\eta^2 = 0.59$, drop jumps: $p = 0.45$; $\eta^2 = 0.45$). Indeed, no noticeable trend was present and all individual differences between heights were non-significant ($0.58 < p < 1.00$), with 95% confidence intervals for mean differences all including zero. Interaction effects between position and drop height were significant

for drop landings ($p = 0.02$; $\eta^2 = 0.70$) but not for drop jumps ($p = 0.83$; $\eta^2 = 0.30$). Again, all main and interaction effect sizes were large.

Table 4.2. Latency of peak resultant accelerations between MTP and more proximal sites (s).

	drop landings (m)				drop jumps (m)			
	0.30	**0.445**	**0.595**	**0.74**	**0.30**	**0.445**	**0.595**	**0.74**
distal tibia	0.029	0.028	0.046	0.023	0.043	0.023	0.023	0.033
prox. tibia*	0.023	0.020	0.040	0.016	0.037	0.017	0.018	0.027
distal femur	0.023	0.019	0.039	0.015	0.038	0.015	0.019	0.026
L5	0.027	0.024	0.020	0.029	0.043	0.016	0.013	0.025
C6	0.029	0.030	0.051	0.033	0.075	0.053	0.047	0.064

*prox. tibia: proximal tibia.

Peak vertical ground reaction forces averaged 10573 ± 1974 N (drop landings: 11454 ± 1439 N; drop jumps: 9692 ± 2122 N), with mean peak resultant ground reaction forces of 10673 ± 1982 N (drop landings: 11545 ± 1466 N; drop jumps: 9801 ± 2128 N). When both trial conditions were combined, peak resultant ground reaction force correlated significantly with peak resultant acceleration at the MTP, distal tibia, distal femur, and L5 ($0.00 < p < 0.04$; $0.46 < R < 0.82$) but not at the proximal tibia ($p = 0.19$; $R = 0.24$) or C6 ($p = 0.07$; $R = 0.38$). Time of peak acceleration relative to that at the MTP was not correlated to peak resultant ground reaction force at any body position ($0.07 < p < 0.34$; $-0.39 < R < -0.11$). When only the drop landing trials were considered (Figure 4.5), peak resultant ground reaction force was significantly correlated to peak acceleration at all sites below the C6 ($0.00 < p < 0.03$; $0.68 < R < 0.91$) but not at C6 level ($p = 0.45$; $R = -0.05$), and again no timings of peaks were correlated ($0.13 < p < 0.16$; $0.40 < R < 0.46$). Finally, for drop jumps, only peak resultant acceleration at the distal femur was related to peak resultant ground reaction force ($p = 0.02$; $R = 0.73$), with no other correlations for magnitude ($0.10 < p < 0.24$; $0.30 < R < 0.51$) or timings ($0.08 < p < 0.12$; $-0.55 < R < -0.48$) of peak accelerations.

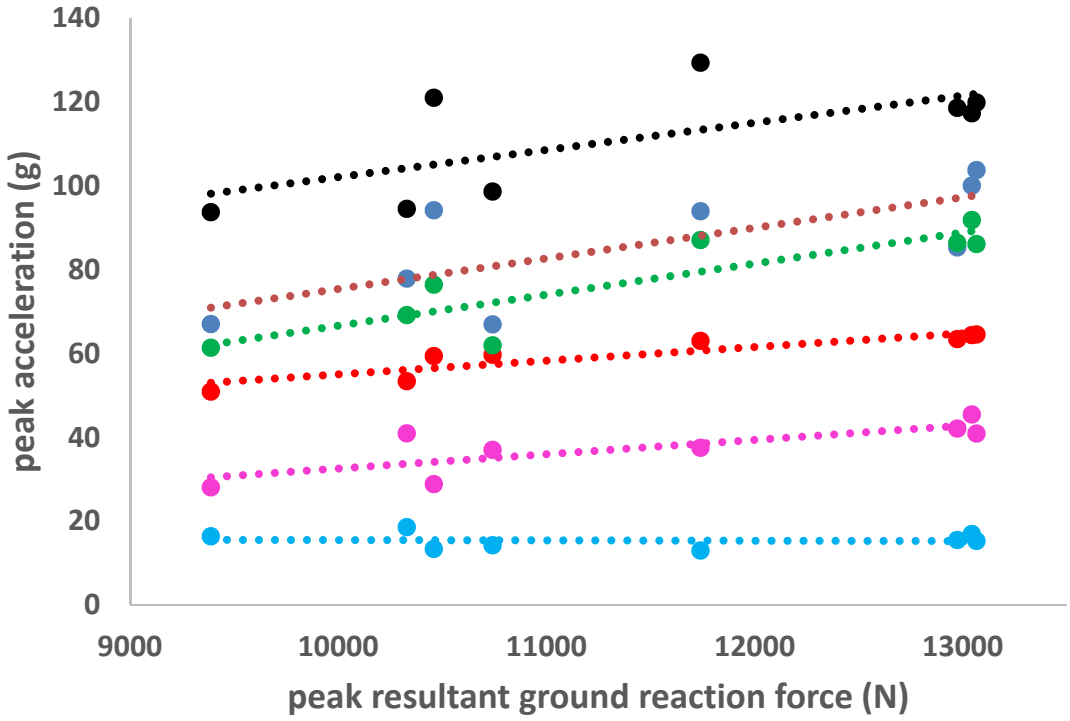

Figure 4.5. The relationship between peak resultant ground reaction force and peak acceleration at various positions on the body. Black: MTP; dark blue: distal tibia; red: proximal tibia; green: distal thigh; pink: L5; light blue: C6.

4.4.2 POWER SPECTRA AND TRANSFER FUNCTIONS

Power spectra contained two major components, corresponding to the active voluntary movement (2 – 14 Hz) and impact shock wave (16 – 26 Hz) related phases of the time-domain signals (Figure 4.6), determined from manual inspection of power spectra peaks for each acceleration signal. Transfer functions demonstrated progressive attenuation from the MTP towards the C6 vertebra within the 16 – 26 Hz frequency component in almost all conditions (Figures 4.7 - 4.11). Within the lower frequency component, associated with voluntary movement (2 – 14 Hz) there tended to be attenuation between adjacent positions on the body, except for between the proximal tibia and distal femur where there was typically a gain in power spectral density of the acceleration signal.

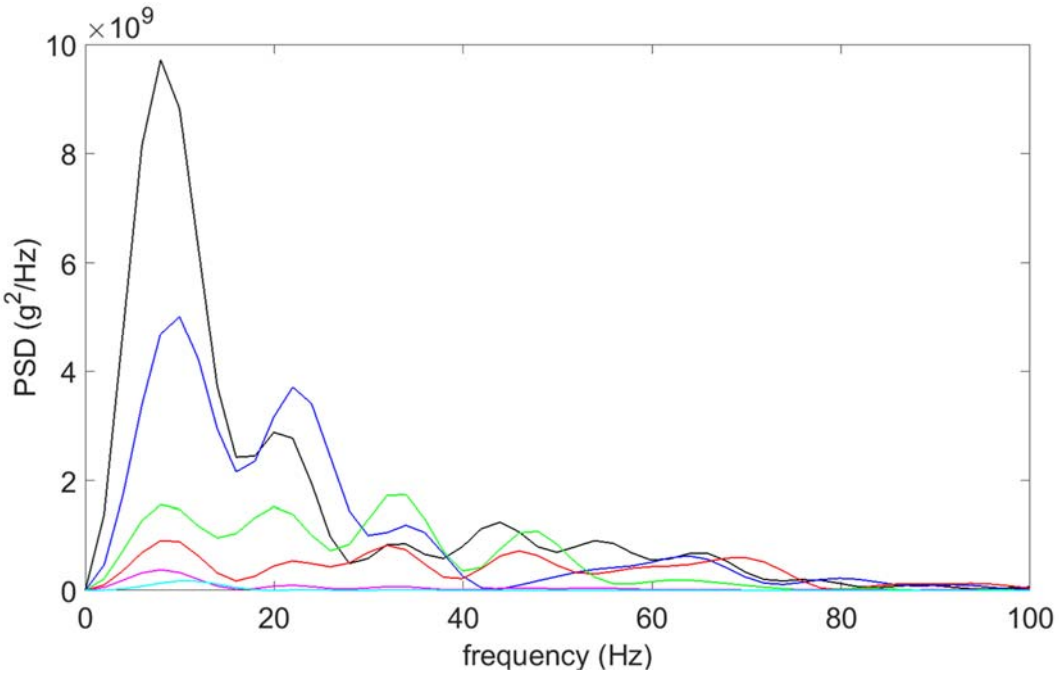

Figure 4.6. Adjusted power spectral densities for frequency components in 0.595 m drop jumps. Black: MTP; dark blue: distal shank; red: proximal shank; green: distal thigh; pink: L5; light blue: C6.

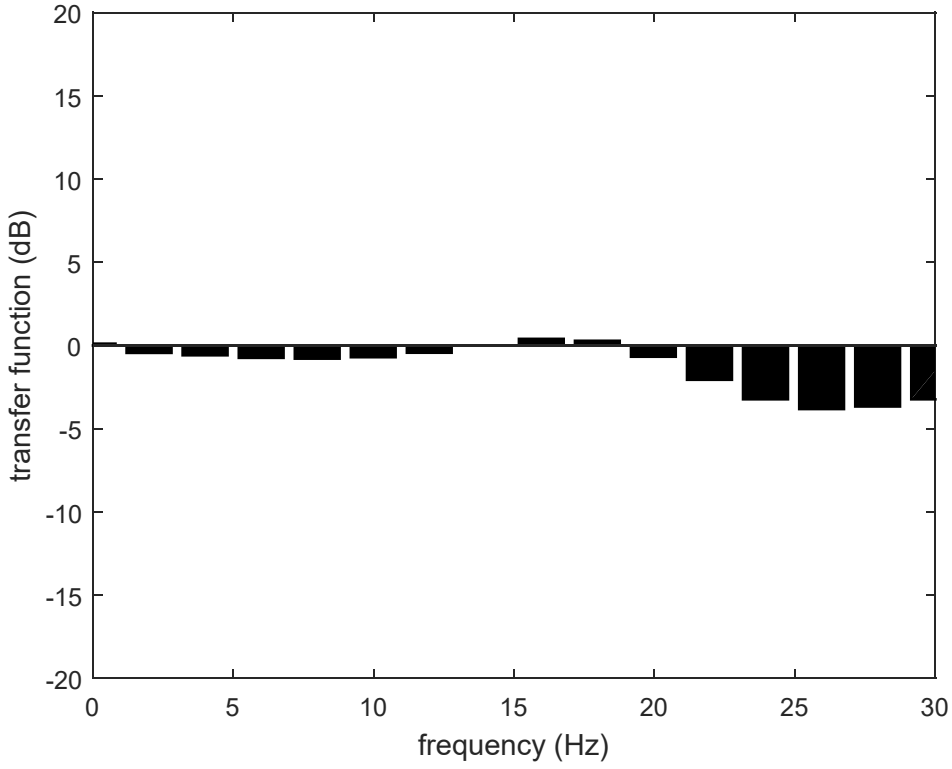

Figure 4.7. Transfer function between MTP and distal tibia accelerometer signals in 0.74 m drop jumps. Positive: signal gain; Negative; signal attenuation.

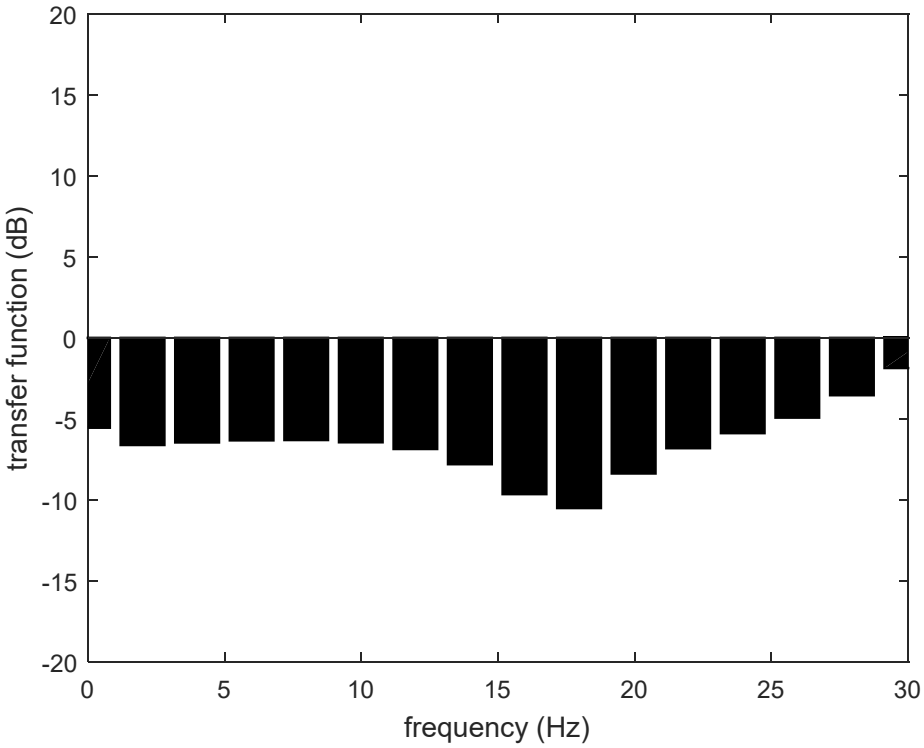

Figure 4.8. Transfer function between distal tibia and proximal tibia accelerometer signals in 0.74 m drop jumps. Positive: signal gain; Negative; signal attenuation.

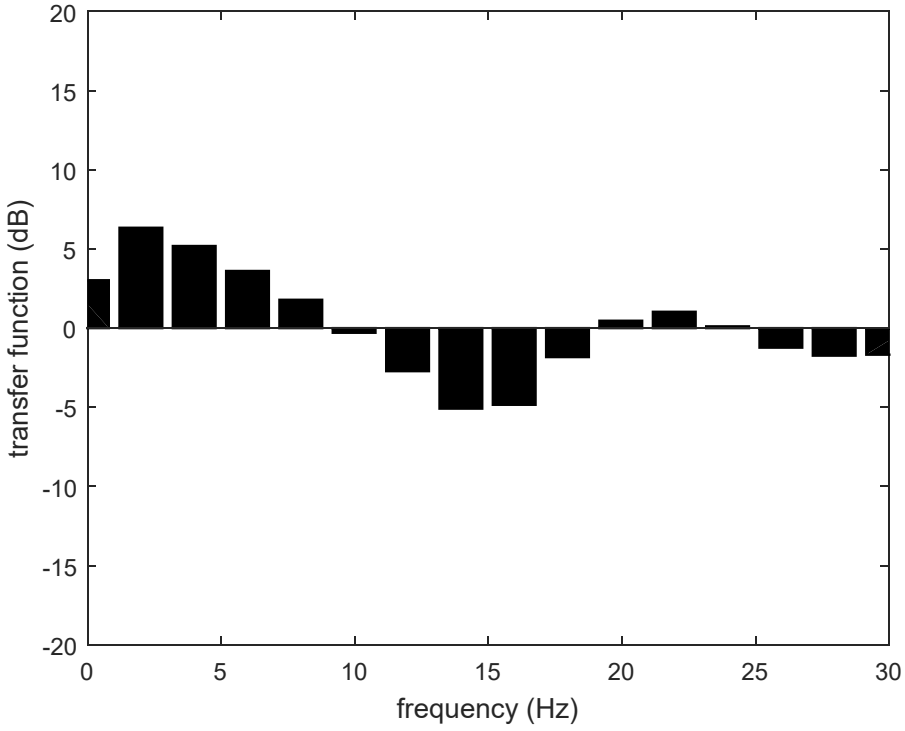

Figure 4.9. Transfer function between proximal tibia and distal femur accelerometer signals in 0.74 m drop jumps. Positive: signal gain; Negative; signal attenuation.

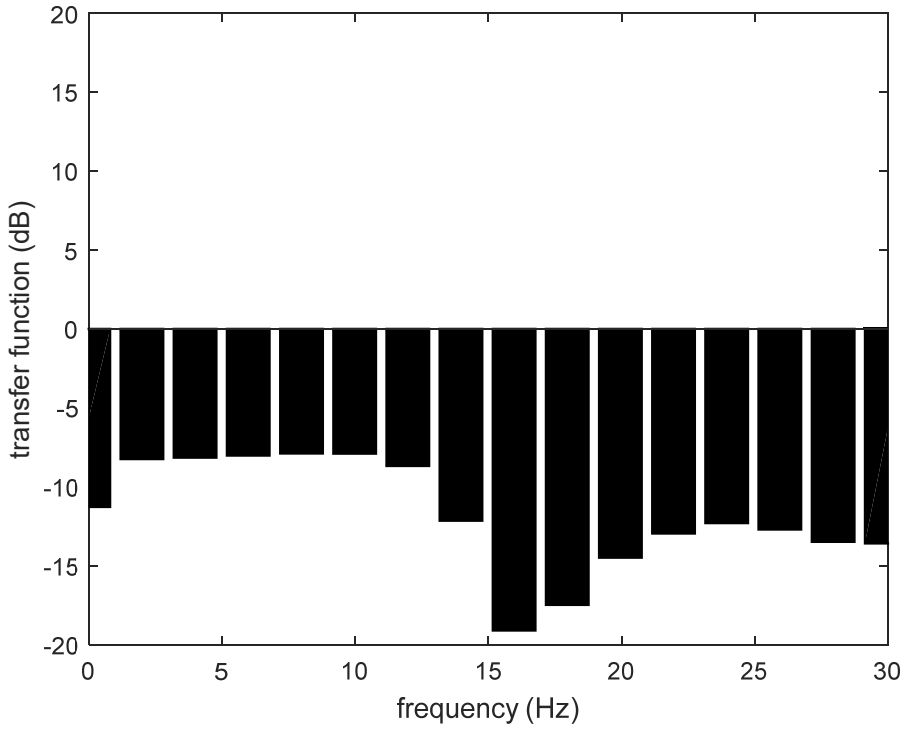

Figure 4.10. Transfer function between distal femur and L5 accelerometer signals in 0.74 m drop jumps. Positive: signal gain; Negative; signal attenuation.

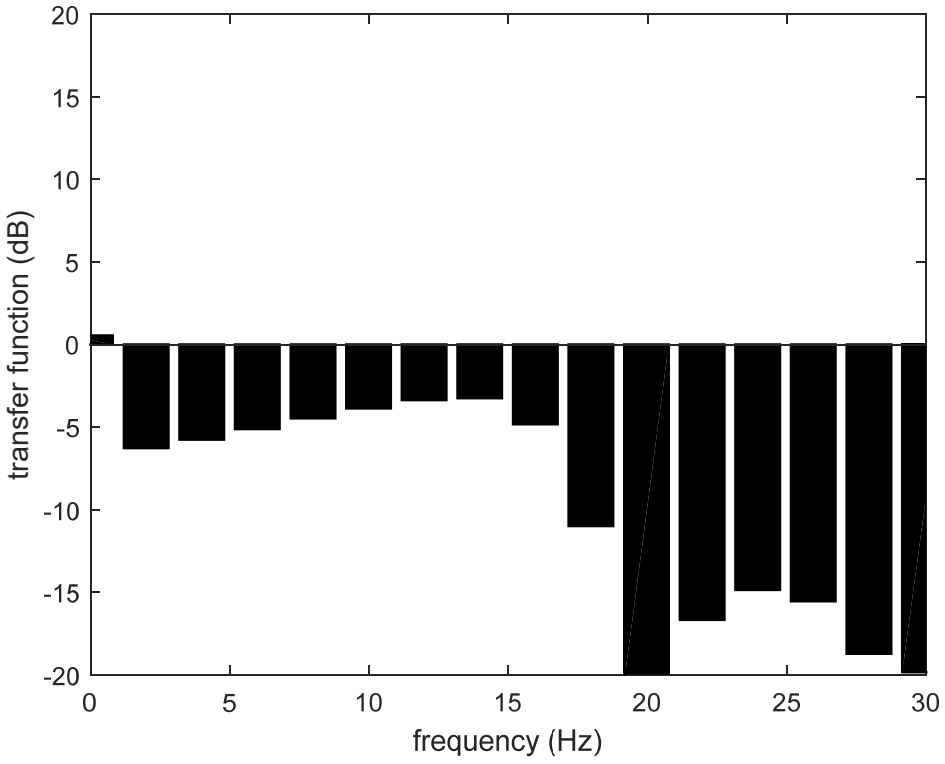

Figure 4.11. Transfer function between L5 and C6 accelerometer signals in 0.74 m drop jumps. Positive: signal gain; Negative; signal attenuation.

4.5 DISCUSSION

Peak accelerations tended to decrease progressively up the body. This ensured that the peak accelerations close to vital organs were less than 25% of those at the MTP joint, with even lower accelerations measured at the neck. Whilst the resultant accelerations included active joint motion, the impact component of the power spectra revealed attenuations even where there had been no reduction in peak acceleration. There was no overall trend for increasing time delays for occurrence of peak acceleration with height on the body, although it is possible that this may also have to do with the inclusion of a voluntary movement related component within the time-domain signal.

The amplifying effect of greater drop heights on peak accelerations was not significant, yet yielded large effect sizes. Thus, the lack of significance can be attributed to the presence of only one subject in the investigation and only two trials per condition. The fact that differences between positions on the body remained significant despite these limitations points towards the strength of those relationships and the magnitude of attenuation that the human body achieves as the shock wave is transmitted away from the site of impact. Indeed, the results showed that less than 25% of the peak acceleration observed at the MTP soon after impact reaches the lower back and hence major organs in the torso. The effects of the lower limbs, both voluntary and passive, therefore act to reduce the risk of serious injury to these organs. Furthermore, the accelerations towards the top of the spine were even lower. Thus, it can be said that the spine itself, as well as other features within the torso such as soft tissue displacement, protect the brain and vestibular organs from damage by further dissipating energy from an impact.

Indeed, peak acceleration occurred later at C6 level than at any other measured site on the body and was the only peak not correlated to peak resultant ground reaction force. Correlations, as shown in Figure 4.5, suggest that acceleration at all other positions, particularly during the more passive drop landings, will increase with each increase in magnitude of distal impact force experienced. However, the human body is capable of further dissipating the post-impact kinetic energy to ensure that greater impact forces do not lead to greater accelerations at the head. As seen in

Table 4.1, greater drop heights did not lead to increases in peak acceleration at C6 vertebra level in either trial type, despite increases further down the body. This agrees with the findings of Shorten and Winslow (1992), which showed that during treadmill running, impact attenuation between the tibia and the head increased with increases in running speeds. Likewise, Hamill et al. (1995) found unchanged peak head acceleration across running speeds. However, these findings disagree with Zhang et al. (2008) who found drop height to have no effect on impact attenuation between the tibia and the forehead during drop landings.

One possible explanation for the results of Zhang et al. (2008) is that they investigated the 21 to 50 Hz frequency component as being representative of the impact shock wave. The present study identified a range of 16 to 26 Hz, more akin to the 12 to 20 Hz identified by Shorten and Winslow (1992). Figure 4.12 illustrates the possible consequences of including higher frequency ranges within this component, particularly, in the figure's example, to the transfer function between the proximal tibia and distal femur. The slightly higher frequency range associated with impact forces in this study compared with that of Shorten and Winslow (1992) can perhaps be attributed to greater ground reaction forces, as well as a more vertically dominated force vector and a difference in action being performed.

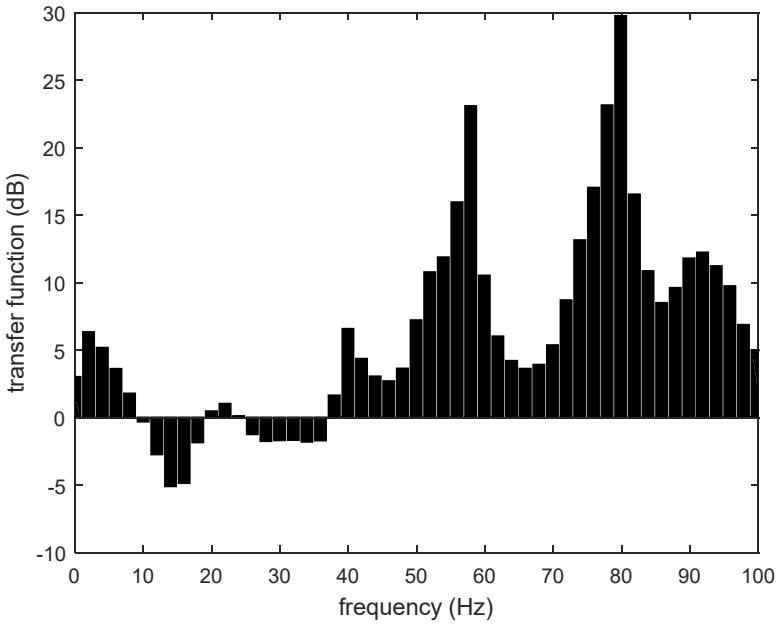

Figure 4.12. Transfer function between proximal tibia to distal femur accelerometer signals in 0.74 m drop jumps. Positive: signal gain; Negative; signal attenuation.

The presence of attenuation in the impact shock wave related range of frequency components, even between sites where there had been no reduction in peak acceleration, emphasises the importance of spectral analyses in human impact investigations. For example, in drop landings, peak accelerations at the distal femur were non-significantly greater than those at the proximal tibia. This difference was negligible on average in the drop jumps, with a p-value of 1.00. However, as displayed visually in Figure 4.12, this lack of overall reduction in acceleration across the knee joint can be attributed to signal gain outside of the frequency component of interest. The transfer function between the proximal tibia and distal femur included large signal gain throughout much of the voluntary movement related component (2 – 14 Hz) and also at high frequencies (> 26 Hz). This sometimes resulted in greater peak acceleration above the knee joint, despite signal attenuation in the range of frequencies associated with the impact shock wave (16 – 26 Hz). Indeed, the shank remains relatively stationary after landing, whilst voluntary flexion at the knee and hip allow a more gradual vertical deceleration of the subject's mass centre whilst still maintaining balance. This results in low frequency movement and acceleration in the thigh that is not present at the shank and so contributes to the acceleration signal gain at low frequencies.

It can therefore be said that the mechanical features of the knee joint contribute to attenuation of the impact shock wave, with lower acceleration within the relevant frequency range experienced directly above the joint compared with directly below. Unlike between accelerometer positions such as the distal and proximal shank, there is negligible soft tissue movement between the proximal tibia and distal femur. Thus, it is most likely that compliance and/or viscosity within the joint structure is responsible for the attenuation in shock wave acceleration. This argument is further supported by the work of Hoshino and Wallace (1987), who investigated the impact-absorbing properties of twenty cadaveric knees. Under the same applied impact loading, the peak force transmitted through the knee joint increased sequentially as meniscus, articular cartilage, and subchondral bone were damaged or removed (Figure 2.8). These results show that each of the above components within a knee joint has a dissipative property. These features explain the attenuation in impact shock wave acceleration observed across the knee joint in the present study.

Such compliance elsewhere within the human musculoskeletal system is likely to have a similar effect on the passive transmission of kinetic energy throughout the system. Although no accelerometer was positioned directly below the hip joint, it can be assumed that compliance within this joint, along with soft tissue displacement within the thigh, contributed partly to the attenuation between distal thigh and L5 accelerometer signals. Likewise, compliance within the ankle will have contributed to attenuation between the MTP and distal tibia. We know that for an unloaded leg, an average of 4.9 mm of distraction at the tibiotalar joint surfaces was required by Fragomen et al. (2014) to avoid surface contact with full weight-bearing. It isn't clear how closely this relates to magnitudes of compression during a drop landing for instance. However, other features such as medal longitudinal foot arch compliance will also contribute to acceleration attenuation from MTP joint to distal tibia, and any representation of compliance between these two points should incorporate each of these features.

Similarly, features within the trunk attenuated accelerations greatly. On average 11% of the reduction in peak acceleration compared with the MTP occurred between L5 and C6, with this value as high as 20% for the more passive drop landing conditions. Transfer functions highlighted greater magnitudes of attenuation within the impact-related frequency range from L5 to C6 (Figure 4.11) than between any other two adjacent accelerometer positions (Figures 4.7 - 4.10). Thus, the compliance within the trunk should not be ignored. Researchers should not assume that all of the attenuation occurs within the lower limbs or incorporate compliant representations at the lower extremities of the body only. It remains true that a certain proportion of the energy dissipation may be brought about through the effects of soft tissue displacement within the trunk, but in lean individuals such as the subject in the present study, this will be limited (see Section 2.4.2). Thus, compliance within the spine itself, namely the flattening of its curved shape, quantified at as high as 14.6 mm during drop landings (Bostock, 2009), is likely to contribute greatly. Further support for this argument can be found in Helliwell's (1989) comparison of subjects with and without ankylosing spondylitis, a condition involving fusion of the spine and thus minimal spinal compliance. The control group, but not the ankylosing spondylitis group, exhibited the ability to attenuate shock at frequencies above 15 Hz, similar to the 16 – 26 Hz range identified in the present study. Spinal compliance may also explain the fact that acceleration at the neck did

not increase in the present study with increases in ground reaction force, despite increases in peak acceleration at every other measured position below the base of the spine. Thus, it can be said that the final phase of energy dissipation prior to the shock wave reaching the head is spinal column compliance and as such this dissipative ability is of high importance.

The observed attenuation of impact accelerations across joint structures has implications for both experimental and theoretical investigations. The assumption that the distal end of one body segment shares a common point with the proximal end of the connecting segment neglects the influence of compliance within joint structures and the subsequent effects on the kinetics and kinematics within the human musculoskeletal system. Attenuation between sites above the MTP joint or between which there is little soft tissue highlights the fact that not all compliance within an accurate model of the human musculoskeletal system can be placed at the foot-ground interface or within wobbling masses (see Section 2.4.2). Likewise, the summed attenuating effects of these compliant features explain why previous simulation modelling investigations have been unable to successfully predict ground reaction forces in their absence and have required the arbitrary addition of extra compliance (Allen et al., 2012). Thus, it can be said that such effects of compliance within the spine and lower-limb joint structures should be considered when representing the connection between adjacent body segments in a theoretical investigation.

4.6 CHAPTER SUMMARY

This chapter demonstrated a progressive reduction in magnitude of accelerations in the human body with distance from the point of impact. Such effects of compliance within joint structures should be considered when representing the connection between adjacent body segments in models of human movement.

CHAPTER 5

CONSTRUCTION OF A COMPUTER SIMULATION MODEL OF DROP JUMPING

5.1 CHAPTER OVERVIEW

In this chapter, the development of a whole-body, forward-dynamics, torque-driven, computer simulation model of drop jumping using Autolev^{TM} is outlined, including justification and explanation of the structure, features, and function of the model. The determination of subject-specific input parameter values is also described.

5.2 INTRODUCTION

Previous chapters have outlined the rationale for the incorporation of compliance within representations of joint structures in the simulation modelling of high impact activities. Features including shoe compression, heel pad deformation, medial longitudinal foot arch compliance, compliance within lower limb joints, and spinal compliance have previously been overlooked in whole-body simulations. Existing simulation studies have attempted to compensate for insufficient compliance within articulating joints through the utilisation of excessive displacement of wobbling masses and/or excessive compression at the foot-ground interface (Section 2.4.2). However, this has resulted in an inability to accurately predict experimentally recorded ground reaction forces (Allen et al., 2012). Chapter 4 demonstrated a progressive attenuation of accelerations in the human body with distance from the point of impact. Acceleration attenuation was observed across joints in the frequency components associated with the impact shock wave, even where negligible soft tissue motion was present.

5.3 RESEARCH QUESTION TWO

The second research question within the present thesis (Section 1.4) asked whether it was necessary to represent the spinal column and ankle, knee, hip and/or shoulder joints in planar whole-body simulation models of drop jumping using representations of these structures which consider joint compression. Thus, it was essential to construct a model capable of being utilised to answering this question.

5.4 WHOLE-BODY SIMULATION MODEL OF DROP JUMPING

As stated in Section 2.2, simulation models should remain as simplistic as possible whilst comprising sufficient complexity to answer the proposed research questions (Yeadon & King, 2008). Furthermore, Alexander (1992) stated that the simpler the model, the easier it is to discover which of its features are essential to the observed effect. This is extremely important to the answering of research question two of the present thesis (Section 1.4) and so the simulation model was constructed in line with the intention that it should remain as simple as possible, whilst retaining adequate complexity to produce realistic whole-body kinetic and kinematic performances.

5.4.1 MODEL STRUCTURE

A rigid body model of drop jumping was developed using Autolev 3.4™ to generate equations of motion through Kane's method (Kane & Levinson, 1985). Through this method, the definition and calculation of partial velocities and angular velocities enables the kinetics and kinematics of the system to be described via the calculation of generalised active and inertial forces.

Since drop jumping is largely bilaterally symmetrical and occurs almost entirely in the sagittal plane, it was considered appropriate to develop a planar model and to combine the left and right limbs. The importance during drop jumping of rotation about and muscles spanning the key lower limb joints of the ankle, knee, and hip determined the requirement for inclusion of separate feet, shanks, thighs, and a trunk. To allow three distinct points of contact and interaction between the model

and the environment (ground), the feet were made up of separate rear foot and forefoot segments, and thus contact points at the toe, metatarsophalangeal joint, and heel (Figure 5.1). The inclusion of a separate forefoot segment ensured a dynamic centre of pressure between the toe and MTP during non-heel contact, rather than the centre of pressure in a one segment foot which would have been constrained to acting at the toe whilst the heel was not in contact with the ground. Additionally, a more accurate moment arm between the ankle joint and the point of force application facilitates more accurate joint torques and ground reaction forces. Thus, a one part foot would not have been appropriate for investigating the ability of a model to match experimental ground reaction forces. The rear foot was modelled as a triangular lamina between the ankle joint centre, MTP joint centre, and heel, with inertial properties as explained in more detail in Section 6.7.

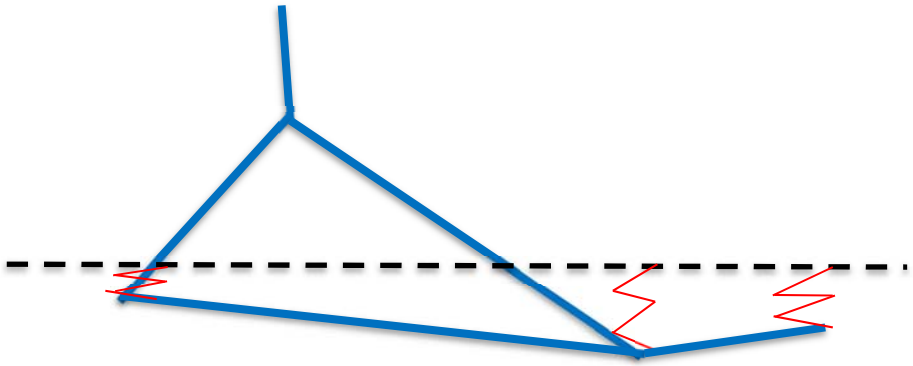

Figure 5.1. Representation of a two-part foot and the foot-ground interface

The contribution of the arms to changes in velocity and angular momentum during ground contact was facilitated through the addition of a two-part arm, with an upper arm connected to a forearm plus hand segment via an elbow joint. Previous planar whole-body simulation models of jumping performances (Allen, 2010; Lewis, 2011) have driven the elbow joint using angle-time histories from experimental performance data. However, it is felt that this constrains the technique and can cause limitations should the model be utilised to optimise technique in the future. Furthermore, the use of experimentally collected joint angle data can introduce errors due to any errors in the experimental data or any experimental movement

outside of the sagittal plane that cannot be replicated by the model. It was not considered necessary to separate the forearms and the hands as any motion about the wrist was likely to have only a negligible effect on performance and/or ground reaction force prediction. Likewise, a head and neck segment was included, at a fixed neck angle from the trunk (determined as 152.1° from the mean angle during experimental drop jumping trials) because the angle varied little (standard deviation from experimental drop jump trials = 4.2°) and was again likely to contribute little to the overall performance of the model. To model spinal compliance between adjacent segments (see Section 5.4.2), the trunk was separated into an upper and lower trunk at the level of the top of thorax (Section 6.7). Thus, the final model included nine rigid segments representing the forefoot, rear foot, shank, thigh, trunk, head plus neck, upper arm, and lower arm plus hand (Figure 5.2).

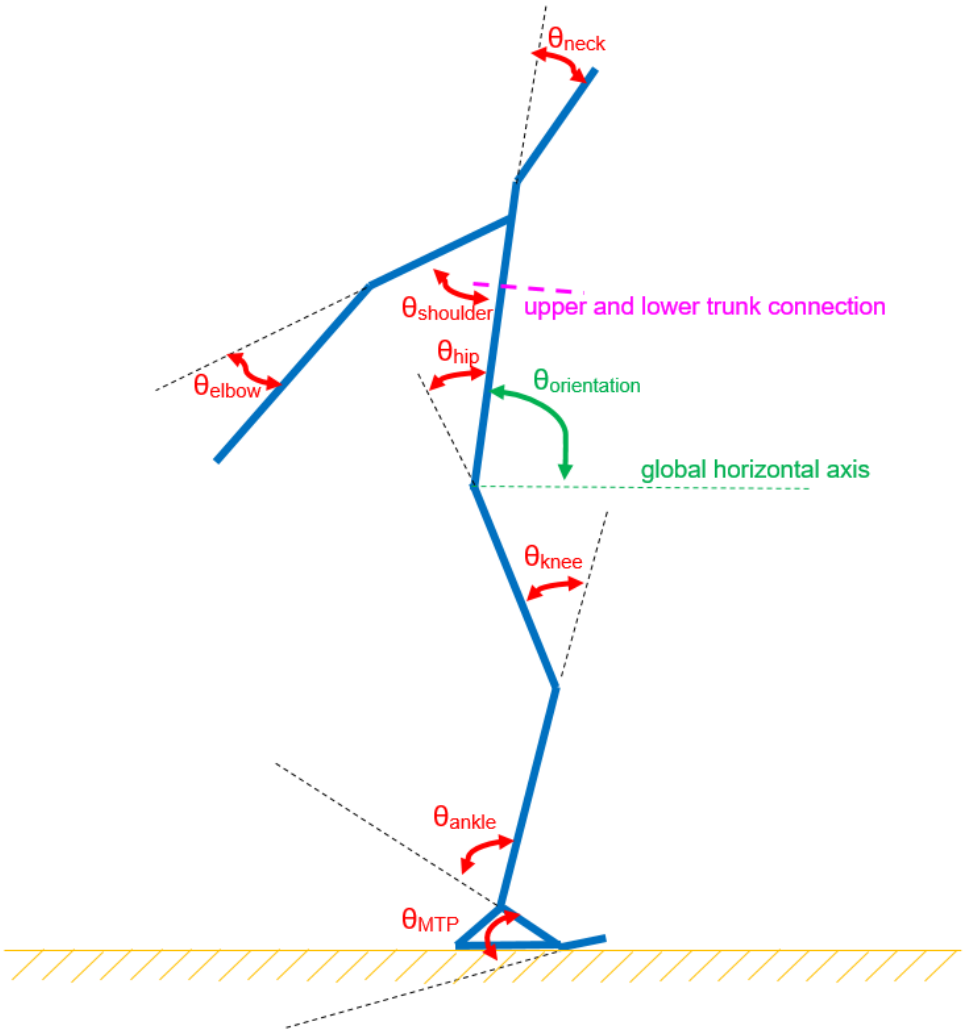

Figure 5.2. A planar, nine-segment rigid body model.

Each rigid model segment was defined as a set of coordinates defining a line between a specified origin and end-point (Table 5.1), or an origin and two end-points for the triangular rear foot (Figure 5.1).

Table 5.1. Segment defining lines in Autolev™

segment / axis	origin	end-point
global	(0,0)	
forefoot	distal end of toes	MTP joint centre
rear foot	MTP joint centre	ankle joint centre (and heel)
shank	ankle joint centre	knee joint centre
thigh	knee joint centre	hip joint centre
lower trunk	hip joint centre	nipple level
upper trunk	nipple level	neck joint centre
head and neck	neck joint centre	vertex
upper arm	shoulder joint centre	elbow joint centre
forearm and hand	elbow joint centre	distal end of fingers

Note: Neck joint centre is midway between manubrium sterni & C7 vertebra.

5.4.2 CONNECTIONS BETWEEN ADJACENT SEGMENTS

Other than the rear foot (a triangular lamina), each segment was modelled as a rod of specified mass, length, and moment of inertia about a transverse axis through its mass centre (see Section 6.7). The two rigid segments articulating at each of the MTP, neck, and elbow joints were connected by a frictionless pin joint, sharing a common point, as in previous whole-body simulation models of jumping activities (King, 1998; Wilson, 2003; Kong, 2005; Allen, 2010; Lewis, 2011).

At the ankle, knee, hip, shoulder, and mid-trunk, adjacent segments did not share a common point and were instead connected via a viscoelastic element with nonlinear stiffness. These viscoelastic springs were incorporated to represent the effects of compliance within joint structures present in vivo (Section 2.4.1). The spring at the

ankle joint, connecting the rear foot and shank, was included to represent the cumulative compliance within the medial longitudinal foot arch and the ankle joint itself. Viscoelastic elements at the knee and hip joints represented compliance within those structures in the human body. The spring at the connection between lower and upper rigid trunk segments was included to represent the flattening of the spine's curved shape following impact, with the shoulder spring modelling any passive depression of the shoulders following a landing impact. The force acting at either end of the springs at these joints was given by the same non-linear spring-damper equation traditionally used for forces at the attachment between rigid and wobbling segments (Pain & Challis, 2001):

$$R_i = (-k_{1,i}|r_i|^3 - k_{2,i}|\dot{r}_i|)\hat{r}_i \quad (5.1)$$

where R is a force vector; r is a vector defining the position of the point of attachment on the distal segment from that on the proximal segment; $\hat{r}$ is a unit vector in the direction of r; |r| is the magnitude of r; |ṙ| is the time derivative of |r|; k_1 and k_2 are the stiffness and damping coefficients respectively; and i represents the compliant joint. Each compliant joint has individual stiffness and damping parameters, determined during parameter determination and evaluation of the model (Section 7.5).

The viscoelastic spring connecting the lower trunk and upper trunk rigid segments was constrained to displace only in one plane, along the vector of the rigid lower trunk. Thus, the two rigid trunk segments could move towards or away from each other but not apart in a perpendicular direction, and the angle between them was constrained to be 0° (parallel with distal ends at greatest possible separation; Table 5.2).

It was further recognised that the flexion and extension of the shoulder in the sagittal plane, as modelled in the present model, is often accompanied by elevation and depression of the shoulder girdle in vivo. Thus, the position at which the shoulder joint spring attached on the rigid upper trunk varied according to the shoulder joint angle. For all data points during experimental drop jump trials, the shoulder joint centre (joint centres determined as in Section 7.3.1) was projected onto the closest point on the line from hip joint centre to neck joint centre. A cubic relationship (adjusted $R^2 = 0.96$; $p < 0.001$) was fitted for the distance from hip joint centre to

shoulder joint projection (x; m), against shoulder joint angle (θ; rad; Equation 5.2; Figure 5.3). The length of the lower trunk segment was subtracted from this relationship to give the equation used in the model to define the insertion position of the shoulder joint spring on the rigid upper trunk relative to the proximal end of that segment. Therefore, as the shoulder flexed forwards from being in line with the trunk or extended backwards from being in line with the trunk, the shoulder insertion was raised. The insertion lowered when the opposite movements were performed, moving the upper arm back towards the line of the trunk segments. The use of a cubic fit would prevent further extreme elevation of the shoulder should shoulder joint flexion in the model exceed that observed experimentally (Figure 5.3).

$$x = -0.01074\theta^3 + 0.04548\theta^2 + 0.00379\theta + 0.49112 \quad (5.2)$$

where *x* is distance from hip joint centre to shoulder joint projection onto the trunk, and θ is shoulder joint angle in radians.

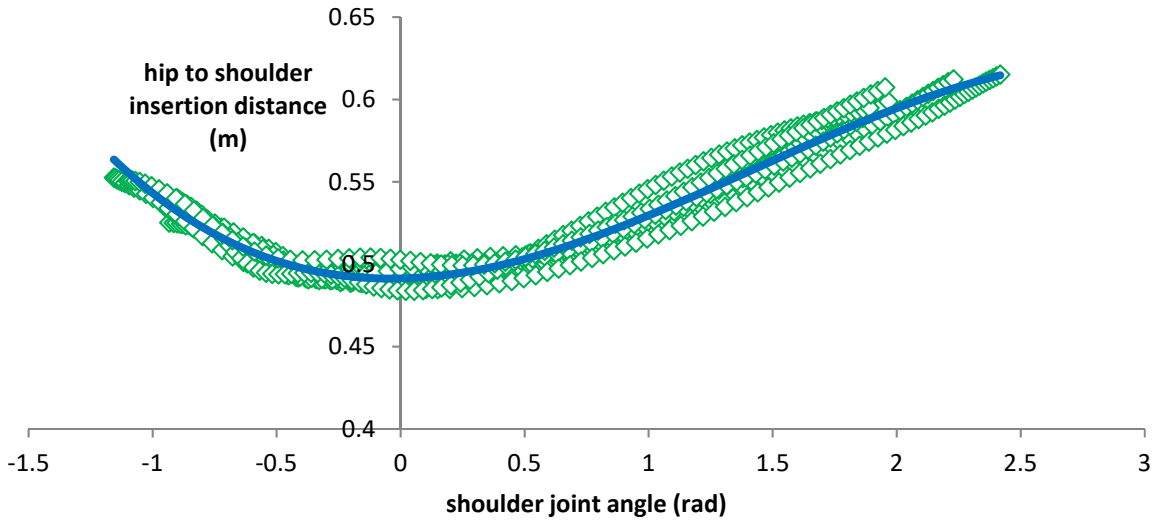

Figure 5.3. Cubic relationship for hip to shoulder insertion distance against shoulder angle (blue) for all experimental drop jump data points (green).

5.4.3 SIMULATION MODEL ANGLE DEFINITIONS

Angles between two adjacent rigid body segments were defined by planar rotations of one segment about the other, such that an angle of 0° defined two parallel segments whose distal ends were at their maximal separation. The joint angle was that by which it was required to rotate the child segment to align with the parent segment (Figure 5.2; Table 5.2). The orientation angle is that which describes the angle between global horizontal axis (parallel to the ground) and lower trunk segment longitudinal axis.

Table 5.2. Simulation model angle definitions

angle	parent segment	child segment
orientation	global horizontal axis	lower trunk
MTP	forefoot	rear foot
ankle	rear foot	shank
knee	shank	thigh
hip	thigh	lower trunk
mid-trunk	lower trunk	upper trunk
neck	upper trunk	head and neck
shoulder	upper trunk	upper arm
elbow	upper arm	forearm and hand

5.4.4 FOOT-GROUND INTERFACE

Vertical and horizontal ground reaction forces were each modelled as non-linear spring-dampers acting at the toe (distal end of forefoot segment), MTP joint, and heel (Figure 5.1). A vertical ground reaction force (R_{zi}; Equation 5.3) was applied at each of the three points (i) of force application according to their vertical displacement relative to the ground (z_i), and their vertical velocity ($\dot{z}_i$) in the global reference frame. Likewise, horizontal ground reaction forces ($R_{y,i}$; Equation 5.4) were applied at each point according to its horizontal position relative to at that

point's first moment of ground contact (y_i), and its horizontal velocity ($\dot{y}_i$), again in the global reference frame. Each ground reaction force was also determined by linear (k_{y1} horizontally; $k_{z1,i}$ vertically) and non-linear (k_{y2} horizontally; $k_{z2,i}$ vertically) stiffness parameters, as well as a damping (c_y horizontally; $c_{z,i}$ vertically) parameter.

$$R_{z,i} = -\left(k_{z1,i} z_i + k_{z2,i} {z_i}^2\right) - c_{z,i} \dot{z}_i |z_i| \tag{5.3}$$

$$R_{y,i} = \left[-\left(k_{y1} y_i + k_{y2} {y_i}^2\right) - c_y \dot{y}_i |y_i|\right] R_{z,i} \tag{5.4}$$

In both directions, the damping parameter was multiplied by the magnitude of the spring depression to prevent damping forces from acting at take off. Similarly, each horizontal ground reaction force was multiplied by the vertical ground reaction force at the same position and timing, to ensure that all forces decayed to zero prior to take off. The net vertical or horizontal ground reaction force was the sum of that at each of three contact points.

Horizontally, the same parameters are applied at all three contact points, whereas vertically, the parameters at the toe and MTP are common, but unique to those applied at the heel. The heel was given separate vertical parameters to model the additional compliance provided by the heel pad (Section 2.4.1) and thus enable greater depression. Negative displacement vertically represented compression of the foot-ground interface such that the foot point was positioned below the ground, whilst an anterior displacement was defined as positive horizontally. Ground reaction forces were constrained to zero when z_i was greater than or equal to zero, identifying that that part of the foot was not in contact with the ground.

5.4.5 WOBBLING MASSES

It was necessary to include wobbling masses within the model; due to their influence on the magnitude of forces in movements involving an impact (Pain & Challis, 2001). Thus, wobbling mass segments were added to the shank, thigh, and trunk (spanning lower and upper rigid trunk segments; Figure 5.4). Rigid and wobbling segments were connected at each end by a non-linear spring damper (Pain & Challis, 2001; Figure 5.5). The force applied by the viscoelastic spring connection was determined by Equation 5.1, the same equation as for the non-linear spring-dampers at

compliant joints (Section 5.4.2). Each of the three wobbling masses had independent stiffness and damping parameters, with these parameters consistent between the connections at proximal and distal ends of the same segment.

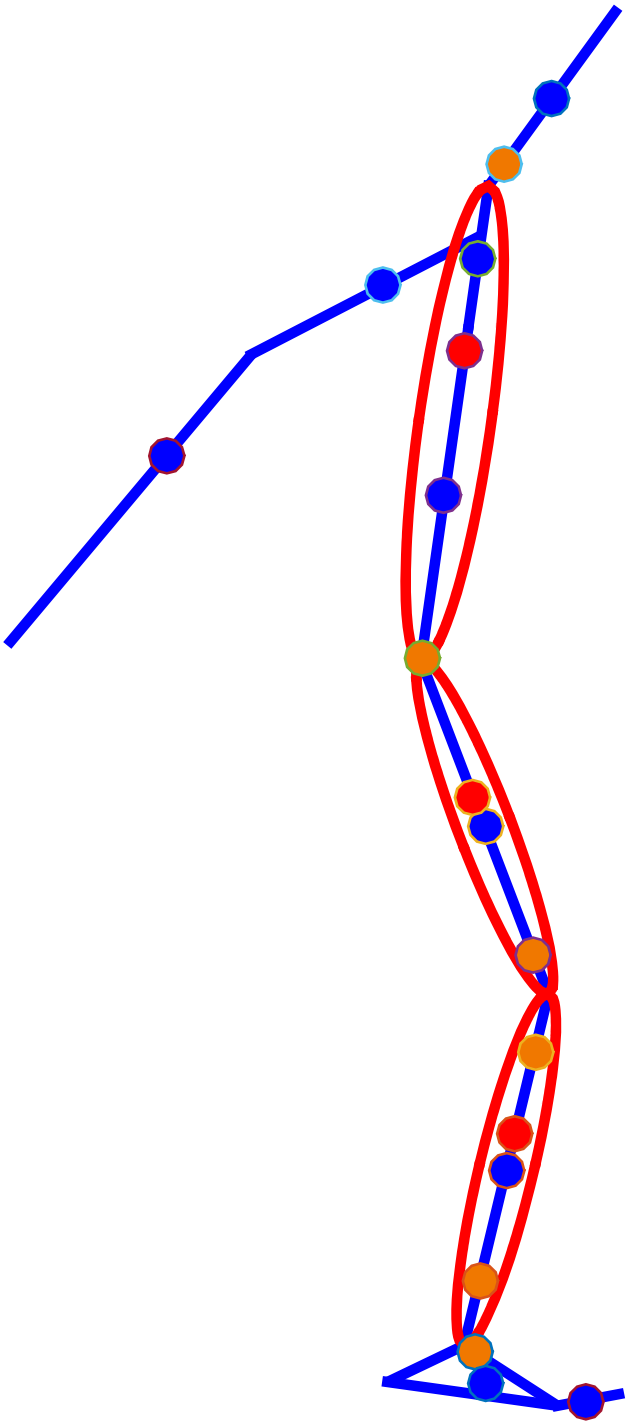

Figure 5.4. Model structure, showing rigid (blue) and wobbling (red) segments, with segmental mass centres (blue / red dots), and accelerometer positions (orange dots) displayed.

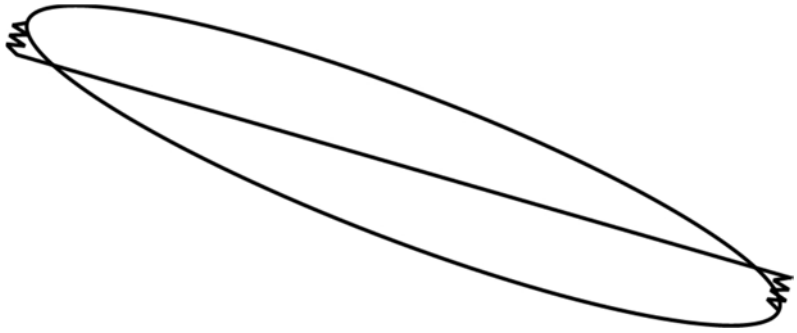

Figure 5.5. Non-linear spring-dampers connecting rigid and wobbling segments at each end (Allen, 2010).

Each of the rigid and wobbling elements required unique segmental inertia properties, despite Yeadon (1990) only giving properties for the whole-body segment. The combined properties of the two segmental components would therefore need to equal those determined for the entire segment in Section 6.7. A method based on the values for percentage of bone, muscle, and fat mass in individual body segments presented by Clarys and Marfell-Jones (1986) was used to divide the segmental mass into rigid and wobbling elements. Since the present subject's body fat percentage (9%; estimated from skinfold thickness; Durnin & Womersley, 1974) is much lower than the 32.4% average of the subjects in that study (Clarys et al., 1984), it was necessary to make some adjustments. The method of Allen (2010) was utilised, in which the results of two previous methods were averaged. The first converts the excess mass to muscle (Table 5.3), whilst the second converts it to both bone and muscle in a proportion that maintains the muscle-to-bone ratio of the segment (Table 5.4).

Previous subject-specific whole-body simulations (Allen, 2010; Felton, 2014) have used a literature body fat percentage of 34.6%, although this was the mean value reported by Clarys et al. (1994) for their thirteen female subjects. Segment fat percentage values have previously been taken, as will be the case in the present chapter, from Clarys and Marfell-Jones (1986). That study reported mean segmental fat percentage values for three male and three female embalmed cadavers, a subsample of those used in the earlier study by Clarys et al. (1994). It

is not clear which six of the 25 cadavers in the original sample were chosen and so it makes sense to use the mean body fat percentage of the six embalmed male and six embalmed female cadavers, as the subsample must have been taken from these and the male to female ratio is unaffected by this. A literature body fat percentage of 32.4% was therefore used.

Table 5.3. Method One – Converting excess mass to muscle

segment	shank	thigh	trunk
segment mass (kg)	5.27	12.54	35.29
literature segment fat mass (%)	28.78	42.63	32.65
Literature segment:total fat % ratio	0.89	1.32	1.01
assumed subject segment:total fat % ratio	0.89	1.32	1.01
subject segment fat mass (%)	7.99	11.84	9.07
fat to be redistributed (%)	20.79	30.79	23.58
literature segment bone mass (%)	21.69	9.03	13.06
assumed subject bone mass (%)	21.69	9.03	13.06
subject rigid mass (method 1; kg)	1.14	1.13	4.61
subject wobbling mass (method 1; kg)	4.13	11.40	30.68

Table 5.4. Method Two – Maintaining segmental muscle-to-bone ratio

segment	shank	thigh	trunk
segment mass (kg)	5.27	12.54	35.29
subject segment fat mass (Table 5.3; %)	7.99	11.84	9.07
subject segment fat-free mass (%)	92.01	88.16	90.93
literature bone mass (% of fat-free mass)	30.46	15.74	19.40
assumed subject bone mass (% of fat-free mass)	30.46	15.74	19.40
subject segment bone mass (% of segment mass)	28.03	13.88	17.64
subject rigid mass (method 2; kg)	1.48	1.74	6.22
subject wobbling mass (method 2; kg)	3.79	10.80	29.07

The mean of the two methods therefore estimated subject-specific rigid masses of 1.31, 1.44, and 5.42 kg and wobbling masses of 3.96, 11.10, and 29.88 kg for the shank, thigh, and trunk respectively. These masses were doubled for the shank and thigh to represent the combined left and right limbs within the simulation model. Segment lengths were equal to those determined for the entire body segment (Section 6.7).

The rigid elements of these three segments were modelled as cylinders of uniform density (Allen, 2010). As such, the centre of mass coincided with the midpoint of the segment, and the moment of inertia about the transverse axis could be calculated through knowledge of the equations governing moments of inertia and that the density of the cylinders were equal to the bone density of the respective segments (Clarys & Marfel-Jones, 1986; Dempster, 1955):

$$volume\ of\ cylinder = \pi \cdot radius^2 \cdot height \tag{5.5}$$

$$radius\ of\ cylinder = \sqrt{\frac{volume}{\pi \cdot height}} \tag{5.6}$$

$$volume = \frac{mass}{density} \tag{5.7}$$

Rigid segment masses are as specified above (1.31, 1.44, and 5.42 kg) and bone density is 1207.53, 1217.82 (both from Clarys and Marfell-Jones, 1986), and 1100 kgm^{-3} (Dempster, 1955) for the shank, thigh, and trunk respectively. Using the equation for the moment of inertia about the transverse axis of a cylinder of uniform density, the moment of inertia of the rigid elements could then be determined:

$$moment\ of\ inertia = \frac{length^2 \cdot mass}{12} + \frac{radius^2 \cdot mass}{4} \tag{5.8}$$

This gave segment moments of inertia about the transverse axis for the rigid shank, thigh, and trunk, of 0.0226, 0.0242, and 0.1660 $kg \bullet m^2$ respectively. Subsequently, these newly established rigid mass centre inertial parameters, in conjunction with the parallel axis theorem and taking moments about the proximal joint enabled equivalent values for the wobbling element to be determined. The parallel axis theorem dictates:

$$I_o = I_G + M \cdot d^2 \tag{5.9}$$

where I_O is the moment of inertia about a point O, I_G is the moment of inertia about the mass centre (G), M is the mass, and d is the distance between O and G.

The moment of inertia of the whole segment (s) is the sum of the moments of inertia of the wobbling (w) and rigid (r) elements:

$$I_{gs} + M_s {d_s}^2 = I_{gw} + M_w {d_w}^2 + I_{gr} + M_r {d_r}^2 \tag{5.10}$$

$$I_{gw} = I_{gs} + M_s {d_s}^2 - M_w {d_w}^2 - I_{gr} - M_r {d_r}^2 \tag{5.11}$$

Thus, the wobbling mass moments of inertia about the transverse axis were determined to be 0.0545, 0.1862, and 0.6287 kg•m^2 for the shank, thigh, and trunk respectively. Taking moments from the proximal joint, the centre of mass position of the wobbling element (*w*) can also be determined, from the mass (*M*) and distance from proximal end to centre of mass (*d*) of the whole segment (*s*) and rigid component (*r*):

$$M_s d_s g = M_r d_r g + M_w d_w g \tag{5.12}$$

$$d_w = \frac{M_s d_s - M_r d_r}{M_w} \tag{5.13}$$

This gave wobbling segment mass centre distances from the proximal joint of 0.1800, 0.1846, and 0.3928 m for the shank, thigh, and trunk, respectively. For the rigid trunk, the assumption of a rigid cylinder of uniform density was continued, enabling the division of the entire trunk rigid properties into separate properties for the lower and upper trunk. Thus, the rigid trunk mass was divided according to the ratio of the lengths, and the segmental mass centre remained half of the way along each segment. The rigid lower and upper trunk segment moments of inertia were then recalculated as above, using the mass and length of each segment, with the same radius as for the entire trunk previously. The trunk wobbling mass was connected to the proximal end of the lower rigid trunk and the distal end of the upper rigid trunk by non-linear spring dampers as described previously for the shank and thigh.

5.4.6 ACCELERATION OUTPUTS

A point was included on the rigid elements of the simulation model at each of the measured locations (marked in orange on Figure 5.4) for which the six accelerometers were attached to the subject during experimental trials (Section 3.4.3). Resultant acceleration-time histories were output from the simulation model at each of these points for later evaluation and comparison to the time-domain acceleration trends observed and reported on in Chapter 4.

5.4.7 TORQUE GENERATORS

Within the simulation model, subject-specific torque generators were incorporated at the MTP, ankle, knee, hip, shoulder, and elbow joints. Separate torque generators were employed for flexion and extension torques (dorsi and plantar flexion at the ankle). The MTP, shoulder, and elbow joints, as well as ankle dorsi flexion, utilised monoarticular torque generators, where the maximal strength was dependent on the joint angle and joint angular velocity at the joint about which the torque acts. The knee and hip, as well as ankle plantar flexion, utilised biarticular torque generators, incorporating the kinematics of both a primary and secondary joint into the calculation of maximal torque. For each torque generator, angle and angular velocity components were determined from simulation model joint angles in a manner intended to give a physiological representation of muscle length and velocity. In this manner, a positive velocity represented a concentric muscle action, whilst negative velocities represented eccentric muscle actions under lengthening. For example, the length and velocity of the ankle plantar flexor biarticular component was calculated using the posterior ankle and knee joint angles. As the ankle plantar flexes, and/or the knee flexes, the length of the biarticular gastrocnemius and plantaris muscle-tendon complexes shorten. The sum of the posterior ankle and knee joint angles would decrease, representing this shortening. The anterior and posterior angles used for each joint torque representation can be seen in Table 5.5. Chapter 6 describes the entire process of determining subject-specific maximal monoarticular and biarticular torque-angle-angular velocity relationships based upon experimental isovelocity dynamometer measures.

Table 5.5. Torque-generator angle definitions

angle	torque generators using this angle
superior MTP	MTP flexion
inferior MTP	MTP extension
anterior ankle	ankle dorsi flexion
posterior ankle	ankle plantar flexion (monoarticular & biarticular)
	knee flexion (biarticular)
anterior knee	knee extension (monoarticular & biarticular)
	hip flexion (biarticular)
posterior knee	ankle plantar flexion (biarticular)
	knee flexion (monoarticular & biarticular)
	hip extension (biarticular)
anterior hip	knee extension (biarticular)
	hip flexion (monoarticular & biarticular)
posterior hip	knee flexion (biarticular)
	hip extension (monoarticular & biarticular)
anterior shoulder	shoulder flexion
posterior shoulder	shoulder extension
anterior elbow	elbow flexion
posterior elbow	elbow extension

Whole-body forward-dynamics simulation models since 2003 have typically (Wilson, 2003; Kong, 2004; Allen, 2010; Lewis, 2011; Felton, 2014) used a seven-parameter tetanic torque-velocity relationship with four parameters governing a Hill-type hyperbola (Hill, 1938) over concentric velocities, and a rectangular hyperbola over eccentric velocities (Figure 5.6; Yeadon et al., 2006). Concentric and eccentric velocities intersect at isometric conditions (zero velocity), with a gradient of 4.3 (Huxley, 1957).

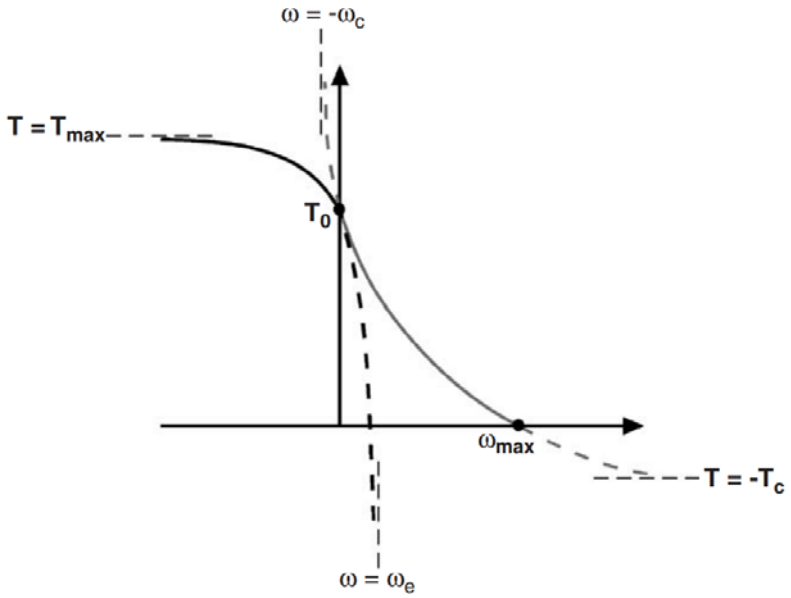

Figure 5.6. The four-parameter maximum torque function comprising branches of two rectangular hyperbolas with asymptotes $T = -T_c$ and $\omega = -\omega_c$, and $T = T_{max}$ and $\omega = \omega_e$. Yeadon et al., 2006.

Differential activation, however, has been represented by two alternative functions. Both are of a sinusoidal form, although Yeadon et al.'s (2006) original function required a computationally slow calculation of the roots of the equation once implemented within forward-dynamics models. A subsequent exponential function (Figure 5.7; Jackson, 2010; Forrester et al., 2011) still used three parameters as with Yeadon et al.'s (2006) function but was computationally faster when implemented within a model. Lewis (2011) optimised both functions for his biarticular torque fits, and the resulting general shapes were almost identical. Therefore, the computationally faster exponential function was used in that (Lewis, 2011), and this thesis (Section 6.5.1).

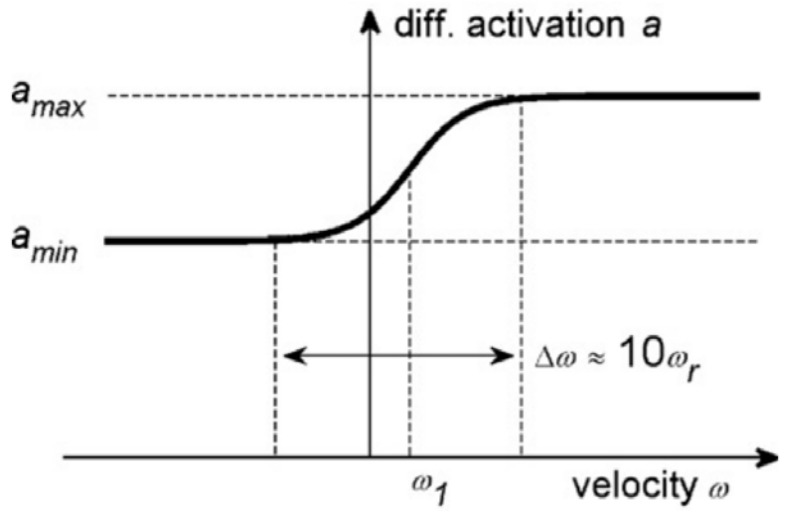

Figure 5.7. Differential activation-angular velocity sigmoid ramp up function. The three parameters are: the low plateau activation level (a_{min}); ω_r which gives the angular velocity range over which the ramp occurs (~10 ω_r) and the midpoint angular velocity of the ramp (ω_1). Forrester et al., 2011.

As with differential activation, the torque-angle relationship has also been represented by two alternative functions. Lewis (2011), in his development of biarticular torque parameters, investigated the differences between the quadratic function of King et al. (2006), and the bell-shaped curve of Forrester et al. (2011). For ankle joint isometric torques, the quadratic function provided a closer representation of experimentally measured maximal dynamometer torques. Thus, the quadratic function of King et al. (2006) was used in Lewis (2011) as well as in the present study (Section 6.5.1). As in Lewis (2011), Forrester et al.'s (2011) method of initially obtaining torque-angle parameters using only isometric data was utilised to gain an initial estimate for these three parameters, before the bounds were narrowed on these parameters when all dynamic torque measurements were subsequently fitted.

The joint torque (T) generated for any given monoarticular joint angle, θ, and angular velocity, ω, or combined biarticular component angle and angular velocity (see Section 6.5.2), was determined by the tetanic torque, $T_{(4)}$. This was itself determined from four free parameters (Figure 5.6), and then multiplied by proportion of maximal activation possible at that velocity (a), and the proportion of maximum activation possible at that component angle (T_θ):

$$T = T_{(4)} T_\theta a \tag{5.14}$$

T_θ was represented by a quadratic torque-angle function, as described above. For concentric velocities (Figure 5.6; nomenclature is in Table 5.6):

$$T_{(4)} = \frac{c}{(\omega_c + \omega)} - T_c \tag{5.15}$$

where:

$$T_c = \frac{T_0 \omega_c}{\omega_{max}} \tag{5.16}$$

and

$$c = T_c(\omega_{max} + \omega_c)\ . \tag{5.17}$$

For eccentric velocities (Figure 5.6):

$$T_{(4)} = \frac{E}{(\omega_e - \omega)} - T_{max} \tag{5.18}$$

where:

$$\omega_e = \frac{(T_{max} - T_0)\omega_{max}\omega_c}{T_0 k(\omega_{max} + \omega_c)}\ , \tag{5.19}$$

$$E = -(T_{max} - T_0)\omega_e, \tag{5.20}$$

and

$$T_{max} = 1.4T_0. \tag{5.21}$$

For both concentric, and eccentric joint angular velocities, the proportion of maximal activation possible at that velocity, a, was given by a sinusoidal velocity-activation function (Figure 5.7):

$$a = a_{min} + \frac{1 - a_{min}}{1 + e^{-\frac{\omega - \omega_1}{m}}} \tag{5.22}$$

Finally, King et al.'s (2006) quadratic torque-angle function provided the proportion of maximum activation possible at that component angle (T_θ):

$$T_\theta = 1 - k_2(\theta - \theta_{opt})^2 \quad (5.23)$$

Table 5.6. Torque parameter nomenclature

parameter	description
T_{max} (Nm)	maximum eccentric torque
T_0 (Nm)	maximum isometric torque
ω_{max} (rad·s^{-1})	maximum concentric velocity
ω_c (rad·s^{-1})	vertical asymptote of concentric torque hyperbola
k_2	width of torque-angle curve
θ_{opt}	optimum angle of component
a_{min}	minimum activation
m	parameter governing rate of activation
ω_1 (rad·s^{-1})	point of inflexion in differential activation function

For the biarticular joint torque generators, the same functions as above were used for both the monoarticular and biarticular components, which were then summed using the ratio of moment arms at the primary and secondary joints (Section 6.5.2). To maintain simplicity, a single fixed moment arm ratio was used for each biarticular torque generator, as in Lewis (2011). Out et al. (1996) demonstrated that this assumption was sufficient to provide realistic joint torque estimates, despite the presence of more complex joint angle-moment arm relationships in vivo (Spoor et al., 1990; Visser et al., 1990).

5.4.8 MUSCLE-TENDON INTERACTIONS

Within each torque generator component, the muscle-tendon interactions were represented through the inclusion of both a contractile component, CC, representing the muscle, and a series elastic component, SEC, representing the tendon and aponeurosis. King (1998) showed that during periods of constant joint velocity on an isovelocity dynamometer, the contractile component angular velocity was

approximately equal to the joint angular velocity. It was therefore assumed in the present study that the contractile component velocity was equal to the joint angular velocity. It was necessary to recalculate the contractile component angle (see simulation model work flow in Section 7.4) and so it was assumed that: a) the joint torque, T_j, was equal to the series elastic component torque, T_{SEC}; b) the contractile component torque, T_{CC}, was equal to the series elastic component torque; and c) the series elastic component acted as a torsional spring, and as a function of series elastic component angle, θ_{sec}. It was therefore possible to recalculate the contractile component angle as follows, given the joint angle, θ_j, joint torque, and an estimate of the series elastic component stiffness, K:

$$T_{SEC} = T_j \tag{5.24}$$

$$T_{CC} = T_{SEC} \tag{5.25}$$

$$T_{SEC} = K\theta_{SEC} \tag{5.26}$$

Thus:

$$\theta_{CC} = \theta_j - \theta_{SEC} \tag{5.27}$$

Using the recalculated contractile component angle in the quadratic torque-angle function would cause the joint torque-angle relationship to be skewed by the series elastic component angle. To avoid this, as in Lewis (2011), joint torques were calculated using the joint angles calculated by the simulation model. Making joint torque a function of joint angle, and contractile component velocity allows any skewness to be present within the contractile component angle instead. However, this does not mean that the influence of the series elastic component is neglected. On the contrary, the series elastic component still interacts with the contractile component within the joint torque subroutine of the simulation model as outlined in the simulation model workflow diagram (Section 7.4). Using the joint angle to determine joint torque in this way ensures that calculated joint torques more closely resemble those measured on the dynamometer (Chapter 6) at close to maximal activation levels such as those expected during a maximal effort drop jump.

As in previous whole-body forward-dynamics simulations utilising subject-specific torque generators, series elastic component stiffness, or tendon stiffness, was

estimated using values for tendon length reported in the literature alongside the assumption of a 5% tendon stretch during maximal isometric contractions (Muramatsu et al., 2001; Finni & Komi, 2002). Joint torque under maximal isometric conditions was calculated using the subject-specific maximal isometric torque parameter, T_0, and the differential activation at zero velocity, both calculated from the subject-specific joint torque parameters as described above and determined in Section 6.6.

The length of the series elastic component, l_{SEC}, was calculated as follows (Figure 5.6):

$$l_{SEC} = l_t + l_b - l_f cos\alpha \tag{5.28}$$

where l_t is the tendon length, l_b is the muscle belly length, l_f is the muscle fibre length, and α is the pennation angle of the muscle. This series elastic component was then scaled to the subject in the present study using the heights (h) of that subject (subj) and those in the literature (lit) from which the series elastic length was calculated:

$$l_{sec,subj} = l_{sec,lit} \frac{h_{subj}}{h_{lit}} \tag{5.29}$$

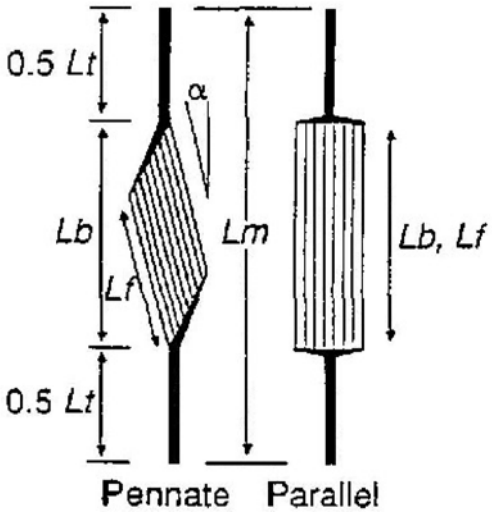

Figure 5.8. Muscles with pennate and parallel muscle fibres. Adapted from Pierrynowski (1995)

To scale the moment arms from the literature to the present subject, the bodies of the present subject and those in the literature were considered as proportional to a cylinder, such that:

$$mass \propto radius^2 \cdot height \tag{5.30}$$

$$radius \propto \sqrt{\frac{mass}{height}} \tag{5.31}$$

As such, the moment arms (d) were scaled according to the ratio of the theoretical radii (r):

$$d_{subj} = d_{lit} \frac{r_{subj}}{r_{lit}} \tag{5.32}$$

The contribution of each muscle (T_i) within the monoarticular or biarticular joint torque generator to maximum isometric torque was determined as:

$$T_i = T_0 \frac{PCSA_i d_i}{\sum_j^n PCSA_j d_j} \tag{5.33}$$

where n is the number of muscles, PCSA is the physiological cross-sectional area of the muscle, and *d* is the moment arm of the muscle. For joints with biarticular joint torque generators, the contribution of monoarticular or biarticular muscle was calculated relative to the maximal isometric torque for just the relevant (monoarticular or biarticular) component of the torque generator. Separate series elastic component stiffness values were then determined for the monoarticular and biarticular components (see Tables 5.7 - 5.10) As discussed above, the change in length of the series elastic component under maximal isometric contraction was assumed to be 5% of its total length (Finni & Komi, 2002). The change in series elastic component angle associated with this change was the change in length divided by the moment arm, and the stiffness of an individual's muscle's series elastic component (k_i) was calculated by dividing its contribution to maximal isometric torque ($T_{0,i}$) by the associated angle change ($\Delta\theta_{SEC,i}$):

$$k_i = \frac{T_{0,i}}{\Delta\theta_{SEC,i}} \tag{5.34}$$

The total stiffness of the series elastic component at a joint was the sum of the individual stiffness values for each of the muscles spanning the joint (Tables 5.7 -

5.10). Because none of the studies previously used to obtain literature values tendon lengths, moment arms, pennation angles, and physiological cross-sectional areas referred to the muscles spanning the elbow or the MTP, it was necessary to estimate total series elastic stiffness at these joints by scaling from an adjacent joint. As such, the MTP series elastic component stiffnesses were scaled from those at the ankle (MTP flexion from ankle dorsi flexion, and MTP extension from ankle plantar flexion) according to the relative magnitudes of the maximal isometric torque parameter, as this was the only subject-specific torque parameter used in the calculation of series elastic component stiffness. Likewise, the elbow was scaled from the shoulder accordingly.

Table 5.7. Ankle joint series elastic component stiffness and related parameters

action / muscle	α (°)	l_b (mm)	l_f (mm)	l_t (mm)	l_m (mm)	l_{SEC} (mm)	scaled L_{SEC} (mm)	scaled d (mm)	PCSA (mm^2)	stiffness ($Nm \cdot rad^{-1}$)	net stiffness ($Nm \cdot rad^{-1}$)	source
dorsi flexion												
tibialis anterior	9	117	99	217	334	236	247	42	2040	107	**208.5**	Rugg et al. (1990)
extensor digitorum longus	11	124	101	344	468	369	386	47	1050	40		Spoor et al. (1990)
peroneus tertius	12	85	75	112	197	124	129	39	342	32		Spoor et al. (1990)
extensor halluces longus	7	111	92	248	359	268	280	55	485	29		Spoor et al. (1990)
monoarticular plantar flexion												
soleus	26	129	49	227	356	312	327	56	11868	414	**497.9**	Rugg et al. (1990)
flexor halluces longus	17	211	55	261	472	419	439	34	1408	22		Klein et al. (1996)
flexor digitorum longus	11	140	48	311	451	404	423	26	991	12		Spoor et al. (1990)
tibialis posterior	17	162	43	252	414	373	390	10	3622	19		Klein et al. (1996)
peroneus longus	10	159	60	304	463	404	423	16	2144	17		Klein et al. (1996)
peroneus brevis	8	109	64	156	265	202	212	12	1154	13		Klein et al. (1996)
biarticular plantar flexion												
gastrocnemius (lateral)	11	225	88	226	451	365	382	56	1990	133	**408.0**	Rugg et al. (1990)
gastrocnemius (medial)	14	248	68	207	455	389	407	56	4177	262		Rugg et al. (1990)
plantaris	4	90	73	359	449	376	394	56	209	14		Rugg et al. (1990)

Table 5.8. Knee joint series elastic component stiffness and related parameters

action / muscle	α (°)	l_b (mm)	l_f (mm)	l_t (mm)	l_m (mm)	l_{SEC} (mm)	scaled L_{SEC} (mm)	scaled d (mm)	PCSA (mm^2)	stiffness ($Nm•rad^{-1}$)	net stiffness ($Nm•rad^{-1}$)	source
monoarticular knee flexion												
biceps femoris (short head)	15	152	146	96	248	107	112	37	1024	1425	**1425.4**	Duda et al. (1996)
biarticular knee flexion												
biceps femoris (long head)	7	274	101	158	432	332	347	39	2881	140	**396.3**	Duda et al. (1996)
semitendinosus	4	288	175	196	484	309	324	44	938	55		Duda et al. (1996)
semimembranosus	15	304	79	116	421	344	360	33	3988	158		Duda et al. (1996)
gracillis	2	322	310	148	470	160	168	20	340	18		Duda et al. (1996)
sartorius	0	430	430	108	538	108	113	18	365	25		Duda et al. (1996)
monoarticular knee extension												
vastus lateralis	11	273	110	138	411	303	317	40	6880	540	**1365.4**	Duda et al. (1996)
vastus intermedius	6	320	106	87	407	302	315	42	5368	445		Duda et al. (1996)
vastus medialis	10	360	112	49	409	299	313	41	4674	381		Duda et al. (1996)
biarticular knee extension												
rectus femoris	10	302	88	186	488	401	420	44	3357	370	**369.5**	Duda et al. (1996)

Table 5.9. Hip joint series elastic component stiffness and related parameters

action / muscle	α (°)	l_b (mm)	l_f (mm)	l_t (mm)	l_m (mm)	l_{SEC} (mm)	scaled L_{SEC} (mm)	scaled d (mm)	PCSA (mm^2)	stiffness ($Nm•rad^{-1}$)	net stiffness ($Nm•rad^{-1}$)	source
monoarticular hip flexion												
tensor fasciae latae	2	313	139	204	517	378	396	41	516	65	**515.1**	Duda et al. (1996)
sartorius	0	430	430	108	538	108	113	59	365	232		Duda et al. (1996)
psoas major	5	238	190	54	292	103	108	14	1383	218		Duda et al. (1996)
monoarticular hip extension												
gluteus maximus superficial	0	171	171	409	580	409	429	50	2185	193	**630.1**	Duda et al. (1996)
adductor magnus posterior	3	242	194	81	323	129	136	47	1674	438		Duda et al. (1996)

Table 5.10. Shoulder joint series elastic component stiffness and related parameters

action / muscle	α* (°)	l_b* (mm)	l_f* (mm)	l_t* (mm)	l_m* (mm)	l_{SEC}* (mm)	scaled L_{SEC} (mm)	scaled d (mm)	PCSA* (mm^2)	stiffness ($Nm•rad^{-1}$)	net stiffness ($Nm•rad^{-1}$)	moment arm source
shoulder flexion												
biceps brachii (long head)	0	163	146	183	345	200	226	25	7	18	**1225.9**	Basset et al. (1990)
deltoid anterior	22	126	99	26	152	61	68	43	223	361		Basset et al. (1990)
coracobrachialis	27	132	78	17	149	79	90	37	37	72		Basset et al. (1990)
pectoralis major (sternal)	25	171	143	47	218	88	99	63	340	378		Basset et al. (1990)
pectoralis major (clavicular)	17	154	137	23	177	46	51	63	373	397		Basset et al. (1990)
shoulder extension												
triceps brachii (long head)	12	208	137	200	408	274	310	50	46	135	**1846.8**	Basset et al. (1990)
deltoid posterior	18	153	120	40	193	79	90	54	235	655		Basset et al. (1990)
lattisimus dorsi (superior)	25	227	184	83	310	144	162	120	270	364		Basset et al. (1990)
lattisimus dorsi (middle)	19	283	185	97	380	205	231	120	243	312		Basset et al. (1990)
lattisimus dorsi (inferior)	21	316	244	80	396	169	191	120	294	382		Basset et al. (1990)

* source: Langenderfer et al. (2004)

5.4.9 PASSIVE TORQUE GENERATORS

As detailed in Section 6.3, the measured voluntary torques from the dynamometer did not include passive torque components. These were adjusted for using a calibration trial in which the subject remained relaxed throughout the range of motion. As such the torque generators in the simulation model do not represent passive joint torques due to structures such as tendons and ligaments within the limbs (Pavol & Grabiner, 2000). It was therefore necessary to include an additional passive torque generator within the lower limb joints of the MTP, ankle, knee, and hip. These passive torques acted to prevent joint kinematics from exceeding anatomical limits. Passive torque generators were not included at the shoulder or elbow for the benefit of simplicity.

At the ankle (A), knee (K), and hip (H), passive torques were determined by a mathematical model of a generic subject, from ten males in the study of Riener and Edrich (1999) of comparable age, mass, and height to the present subject. Biarticular muscles were accounted for within these mathematical models by the inclusion of adjacent joint angles where relevant. Thus, each passive torque was determined from the modelled joint angle (θ) at the primary and any relevant secondary joints:

$$passive\ ankle\ torque = e^{(2.1016-0.0843\theta_A-0.0176\theta_K)} - e^{(-7.9763+0.01949\theta_A+0.0008\theta_K)} - 1.792 \quad (5.35)$$

$$passive\ knee\ torque = e^{(1.8-0.046\theta_A-0.0352\theta_K+0.0217\theta_H)} - e^{(-3.971-0.0004\theta_A+0.0495\theta_K-0.0128\theta_H)} - 4.820 + e^{2.22(-0.15\theta_K)} \quad (5.36)$$

$$passive\ hip\ torque = e^{(1.4655-0.0034\theta_K-0.0750\theta_H)} - e^{(-1.3404-0.0226\theta_K+0.0305\theta_H)} + 8.072 \quad (5.37)$$

Passive torque at the MTP joint was represented, as in Allen (2010) by the following function:

$$passive\ MTP\ torque = 0.000025e^{(11.5(\theta_{MTP}-\pi))} \quad (5.38)$$

5.4.10 TORQUE GENERATOR ACTIVATION TIMINGS

The activation level, a, of each subject-specific torque generator was governed by a quintic activation function against time (Yeadon & Hiley, 2000), which could vary between zero (completely inactive) and one (fully active). The quintic function had zero velocity and acceleration at the endpoints:

$$a = t^3\left[6\left(\frac{t-t_0}{t_1-t_0}\right)^2 - 15\left(\frac{t-t_0}{t_1-t_0}\right) + 10\right] \quad (5.39)$$

where t is the time, t_0 is the initial time at which activation is zero, and t_1 is the final time at which activation equals one.

The activation level of each torque generator could ramp up to twice during the duration of the simulation, involving two quintic functions. This enabled the activation profile to 'ramp up-ramp up', 'ramp up-ramp down', 'ramp down-ramp up', or 'ramp down-ramp down' or indeed to remain constant or to simply ramp up or down once. For example, Figure 5.7 shows an example of a 'ramp up-ramp down' activation profile. The activation level of the torque-generator is given by the bold line. The activation level is initially set at a level of a_0. The first quintic function ramps for a time period of tr_1, beginning at time ts_1. The activation level remains at a_0 until the first quintic function exceeds this level, at which point the activation level follows the quintic function until reaching an activation level of a_1. Activation remains at a_1 until a time governed by a second quintic function of start time ts_2 and duration tr_2, which acts in a similar manner to the first. The activation level follows this second function from the time it reaches the current level of activation, a_1, until the time it reaches the final activation level a_2. Activation level will remain at a_2 for the remainder of the simulation. Ramp times, tr_1 and tr_2 represent the time taken to ramp between activation levels of zero and one, or vice versa. Bounds placed on the activation parameters during parameter determination and evaluation of the

model to ensure realistic torque generator control are explained in Section 7.5.2. The final generated joint torque was calculated by the multiplication of the activation level at any given point in time, and the subject-specific maximal torque determined from the relevant nine-parameter monoarticular or nineteen-parameter biarticular torque profile (Section 5.4.7.; Section 6.5.1; and Section 6.5.2).

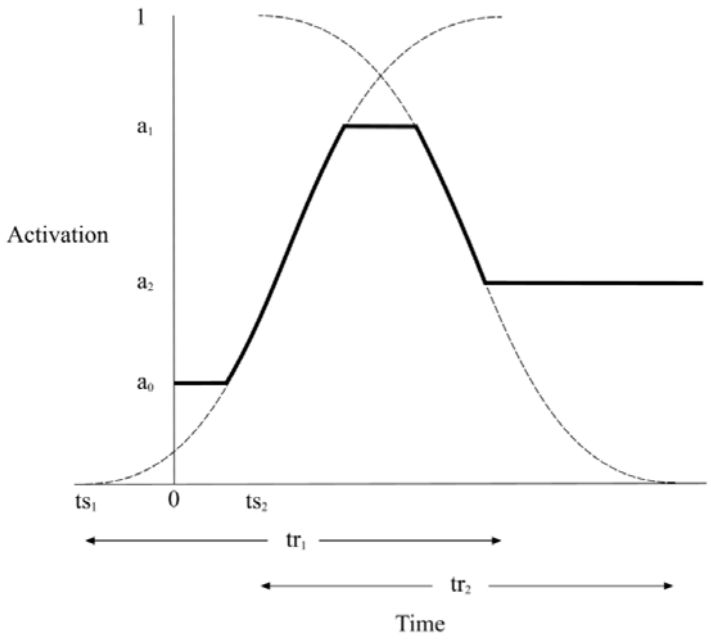

Figure 5.9. A 'ramp up-ramp down' torque generator activation profile against time. Adapted from Allen (2010).

5.4.11 EQUATIONS OF MOTION

As mentioned previously, the computer simulation was constructed using Autolev™ Professional Version 3.4 (Appendix 4; Kane & Levinson, 1996), which utilises Kane's method to formulate the equations of motion for multibody simulations. As seen in Appendix 4, the simulation model is constructed using generalised coordinates, generalised velocities, inertia parameters, and all the internal and external forces and torques acting on the system. The generalised coordinates are used to define the position and orientation of each segment of the model with respect to the global origin and to previously defined segments. Generalised velocities are linear combinations of the generalised coordinates' time derivatives

(Kane & Levinson, 1985). Known force and torque equations are specified, along with the subject-specific segmental inertia parameters determined in Section 5.4.5 and Section 6.7. Autolev™ develops expressions for generalised active and inertial forces, and the simulation is advanced over the specified time step through a Kutta-Merson integration method. Code to run the simulation is output from Autolev™ in the FORTRAN programming language. Also generated are an input file containing all of the input parameters for the model, and a list of output files and their contents to be produced for each simulation. The FORTRAN code can then be manually edited and added to with the addition of subroutines to define features such as the subject-specific torque generators (Section 5.4.7), passive torque generators (Section 5.4.9), or activation profiles (Section 5.4.10).

5.4.12 MECHANICAL CHECKS

To confirm that the constructed simulation model obeyed the fundamental laws of physics, several checks were carried out. Each check successfully confirmed that the model was working correctly. Firstly, all damping within the system was set to zero, and the joint torque generator activation levels were also set to zero, to confirm that total energy within the system was conserved. Secondly, the ground reaction forces were set to zero, confirming that whole-body angular momentum was conserved during flight and that whole-body centre of mass acceleration was equal to acceleration due to gravity.

5.5 CHAPTER SUMMARY

In this chapter, the structure of the computer simulation model of drop jumping was described, including individual features of the model such as the subject-specific torque generators. Chapter six describes the process of collecting experimental torque data and determining the subject-specific maximal torque profiles for the model, whilst chapter seven will detail the parameter determination and evaluation of the model.

CHAPTER 6

DETERMINING SUBJECT-SPECIFIC PARAMETERS

6.1 CHAPTER OVERVIEW

This chapter presents the methodologies utilised to determine subject-specific joint torque parameters to be used as inputs to the computer simulation model. The data collection procedures on an isovelocity dynamometer are detailed, before the analysis of this data is explained and presented. The measurement procedure and calculations utilised to derive a subject-specific inertia model are also outlined.

6.2 INTRODUCTION

In any torque-driven whole-body simulation model of maximal effort human activity it is important to determine joint torque parameters specific to the subject being modelled to ensure that the torques generated by the model remain within physiologically realistic and achievable limits. Maximal joint torques can be measured on an isovelocity dynamometer (e.g. Cybex or Isocom) with a powered crank able to rotate throughout a pre-defined range of angles whilst varying the resistance to maintain a pre-defined angular velocity. The subject exerts maximal torques on the crank, either concentrically or eccentrically, with this torque being measured by a strain gauge within in the crank.

Several limitations inherent within this methodology have been highlighted previously. For example, the angular velocity of the crank is not always at the constant pre-defined value. Indeed, the crank angular velocity has been seen to oscillate slightly, as well as ‘overshooting’ temporarily when accelerating up to speed at the start of the range of motion or decelerating shortly before the end of the range of motion (Osternig et al., 1982). Furthermore, as the desired angular velocity increases, the angle range during which constant velocity is achieved decreases (Chow et al., 1997). This is due to increased acceleration and deceleration demands and so greater angular displacement during these periods.

Further errors are introduced when gravitational and inertial effects are not considered (Chow et al., 1997), although this is a rarity in modern machines. Finally, different exercises have produced mixed results for within-day, inter-day, and inter-machine reliability (Madsen, 1996). However, many of these limitations can be accounted for in the collection and analysis of the data. As Chow (2001) stated, recognising the limitations of such isovelocity dynamometers does not detract from the valuable contribution that they make to the understanding of muscular function.

6.3 JOINT TORQUE MEASUREMENT PROTOCOL

Maximal effort flexion and extension (dorsi and plantarflexion at the ankle) torques were recorded on a Con-Trex MJ isovelocity dynamometer (CMV AG, Switzerland). The subject was firmly strapped in to the dynamometer chair to restrict movement other than at the joint of interest, which would negatively affect the alignment between the joint and crank axes of rotation. The crank axis was visually aligned with the functional joint centre under load.

One set of maximal joint torque measurements was performed for ankle dorsiflexion and for flexion and extension at the hip, shoulder, and elbow (Figure 6.1). The ankle plantarflexion, and knee flexion and extension measurements were repeated at three different secondary joint angles to account for the effects of biarticular muscles (Figure 6.2). These muscles span two joints and so their force-length characteristics are determined by both the primary and secondary joint angle, which must be accounted for in the strength capabilities of the simulation model (see Section 5.4.7). The biarticular parameters at the hip were calculated with knowledge of the previously determined parameters at the knee.

Figure 6.1. Isovelocity dynamometer configuration for ankle dorsiflexion (top left); hip flexion and extension (top right); shoulder flexion and extension (bottom left); and elbow flexion and extension (bottom right).

Figure 6.2. Isovelocity dynamometer configuration at three secondary joint angles each for ankle plantarflexion (top); and knee flexion and extension (bottom).

The ankle was tested with the dynamometer bed laid flat at 0°. The knee angle during dorsiflexion testing, measured using a manual goniometer, was 149.5°, whilst plantarflexion was tested at secondary knee joint angles of 164°, 124°, and 93.3°. The knee angle was modified by an attachment used to raise and lower the thigh of the subject whilst laying on the dynamometer bed (Figure 6.2). Knee flexion and extension were tested at hip angles, again measured with a manual goniometer, of 105°, 125°, and 145°. These hip angles were achieved through dynamometer back rest angles of 88°, 57°, and 49° respectively. Hip flexion and extension trials were performed with the participant's knee joint angle constrained by a solid foam wedge strapped firmly behind the knee limiting any movement (Figure 6.1). Thus, the mean posterior knee joint angle was 76° during hip flexion trials, and 104° during hip extension trials.

For each set of measurements, the participant warmed up through a series of isometric contractions of progressively increasing intensity. Maximal isometric joint torque measurements were then collected at 512 Hz for up to five seconds, at seven joint angles spaced throughout the subject's range of motion (at 5, 20, 40, 50, 60, 80, and 95% of the range of motion), with trials performed in a randomly selected order. The subject was encouraged to begin each trial in a relaxed state before increasing the effort to reach maximum voluntary contraction. During each trial, whilst active load was being applied, a mechanical goniometer was used to measure the joint angle, so that any offset between crank and joint angles could be later accounted for when calculating joint torque parameters. Rest periods of 60 s between trials and 10 minutes between sets of measurements whilst changing dynamometer set up were given. For ankle dorsiflexion and knee extension, the first isometric trial of the set of measurements was repeated at the end of the set, to assess whether the later trials were likely to be subject to fatigue. Isovelocity joint torque measurements were then also taken at 512 Hz during a concentric-eccentric protocol with trials in $50°\cdot s^{-1}$ increments from $50°\cdot s^{-1}$ to $300°\cdot s^{-1}$ (ankle and elbow), $350°\cdot s^{-1}$ (shoulder) or $400°\cdot s^{-1}$ (knee and hip) depending on the joint. The regular increments were utilised since adoption of a randomised order of velocities could have resulted in submaximal torques at high angular velocities (Yeadon et al., 2006). Three repetitions of the concentric-eccentric protocol were performed in each isovelocity trial, with only one trial performed at each velocity unless it was

believed by the subject or the researcher to be submaximal, in which case the trial was repeated.

The passive torque component of the measured joint torque was calculated and removed through the utilisation of a calibration trial for each dynamometer set up position, in which the participant remained relaxed and produced no voluntary torque as the crank arm rotated through the full range of motion. This methodology calculates the gravitational torque caused by the weight of the crank and limb, as well as the passive torque due to tendons and ligaments within the limbs (Pavol & Grabiner, 2000). Thus, the resultant torque output from the dynamometer software was that due to the contractile component, exerted actively by the participant during the trial.

6.4 DATA REDUCTION

Crank angle and raw torque data collected by the dynamometer were filtered using a zero lag, low pass, fourth order Butterworth filter, with a cut off frequency of 12 Hz identified through residual analysis (Winter, 1990). It was also necessary to correct the recorded crank angle for joint angle-crank angle offsets. These angles differ due to the way in which the subject's limb is attached to the crank arm. During every isometric trial, a manual goniometer was used to measure the primary joint angle being tested. Subsequently, for each dynamometer set-up condition, a line was fitted to joint angle against the recorded crank angle. Thus, the equation of this line could be used to convert crank angle to joint angle at every time point in all isometric and isovelocity dynamometer recordings. Joint angular velocity was determined from the derivative of the joint angle time history.

For isovelocity measures, joint torques during periods of acceleration or deceleration were removed by selecting only data points at which the velocity was greater than 95% of the desired velocity. Velocity overshoot was removed using Schwartz et al's (2010) method in which the change in velocity is normalised to the instantaneous velocity. Of the three repetitions performed in each trial, only data from the repetition with the greatest peak torque was taken forward for use in

determining the joint torque parameters. Likewise, for isometric measures, only the peak joint torque during each trial was used.

6.5 PARAMETER DETERMINATION

The resulting data set consisted of seven maximal voluntary isometric torques at different joint angles, and a range of isovelocity torques at differing joint angular velocities and throughout a range of joint angles, for each testing configuration (once or three times per joint action, depending on the modelling of biarticular muscles, and hence the number of parameters to be determined). This data was then used to determine a nine-parameter function for monoarticular joint torque generators, and a nineteen-parameter function for biarticular joint torque generators.

6.5.1 NINE-PARAMETER MONOARTICULAR TORQUE FUNCTIONS

For monoarticular joint torque generators and monoarticular components within biarticular joint torque generators, a nine-parameter, single-joint function expressed the maximal voluntary joint torque as a function of joint angle and joint angular velocity. The function comprises a two-parameter quadratic torque – angle relationship multiplied by a seven-parameter torque – angular velocity relationship (King et al., 2006). The torque-angular velocity relationship used was the same as that used by Lewis (2011) in monoarticular and biarticular torque profiles and was based upon that of Jackson (2010) and Forrester et al. (2011) for a tetanic Hill type curve (Hill, 1938) multiplied by a differential activation function (see Section 5.4.7). The differential activation function modelled maximum voluntary activation, a, from joint velocity, ω, minimum muscle activation, a_{min}, activation rate, m, and point of inflexion, ω_1:

$$a = a_{min} + \frac{1-a_{min}}{1+e^{-\frac{\omega-\omega_1}{m}}} \quad (6.1)$$

To determine the nine joint torque parameters, an unbiased weighted root mean square difference between the joint torque calculated from the parameters, and that

measured during the isometric and isovelocity dynamometer trials was calculated, as below (Lewis, 2011):

$$RMSD = \sqrt{\frac{n+m}{N+m-f}}\left(\sqrt{\frac{w_1 \sum_{i=1}^{n} \omega_i {x_i}^2 + w_2 \sum_{j=1}^{m} \omega_j {y_j}^2}{n w_1 \sum_{i=1}^{n} \omega_i + m w_2 \sum_{j=1}^{m} \omega_j}}\right) \quad (6.2)$$

For data points (i) where the measured torque exceeded the function calculated value: w_1 = 100; n = the number of data points; x_i = the difference between measured and calculated torques; ω_i = angular velocity.

For data points (j) where the measured torque was less than the function calculated value: w_2 = 1, m = the number of data points; y_j = the difference between measured and calculated torques; ω_j = angular velocity.

For all data points: f = number of function parameters (9 or 19).

The use of such a weighted root mean square difference produces a function that represents maximum voluntary torque rather than an average experimentally produced torque. This is achieved by the weighted component encouraging the function to give better agreement with larger torque measurements. Such a method has previously been used successfully in representations of maximal voluntary knee torques (Forrester et al., 2011) and in monoarticular and biarticular representations at several joints to be used in subject-specific computer simulation (Lewis, 2011). Lewis' (2011) chosen weightings of 100 and 1 were used in the present study, which were originally chosen from torque functions fitted to pseudo data sets including random noise representative of torque measurement errors. It is considered that experimentally collected torque data is more likely to be submaximal than supramaximal.

The above function (Equation 6.2) was minimised using a Simulated Annealing Algorithm (Corana et al., 1987; see Section 7.5 for more information on simulated annealing algorithms). All parameters were given upper and lower bounds, which were based wherever possible on physiologically realistic values available in the literature (see Tables 6.1 – 6.12). The same bounds were used as in Lewis (2011), except for the upper bound on maximum velocity of each joint action, which was

scaled from the subject of Lewis through the multiplication by a factor of 1.5 as an absolute upper bound given the ability of the 100 m sprinter used in the present study to generate high joint velocities. Bounds at the elbow (Table 6.11 – 6.12) were determined based on bounds previously used at other joints (Lewis, 2011).

Finally, the surface of the determined torque fit was raised in an attempt to replicate true maximal torque values, as in Allen (2010). It was decided not to originally calculate fits with 100% of experimental values less than or equal to calculated values, as this made it difficult for the optimisation algorithm to accurately match the shape of the experimental data. However, it remained true that the subject had indeed achieved each of the measured torque values. The average difference between measured and calculated torques for all data points where the former exceeded the latter was calculated, with isometric and isovelocity data points weighted such that each accounted for 50% of the calculated mean. Maximum eccentric and isometric torque parameters were subsequently increased by these mean values, with all other parameters unchanged from the optimised values. This had the effect of raising the previously determined torque fit by the calculated torque offset whilst maintaining the shape of the surface fit.

6.5.2 NINETEEN-PARAMETER BIARTICULAR TORQUE FUNCTIONS

For biarticular joint torque generators, a nineteen-parameter, two-joint function incorporated both monoarticular and biarticular components and thus expressed the maximal voluntary primary joint torque as a function of primary joint angle, secondary joint angle, and the two corresponding angular velocities (Lewis, 2011). This nineteen-parameter function consisted of the sum of a nine-parameter monoarticular function (King et al., 2006), exactly as in Section 6.5.1, and a ten parameter biarticular function. The ten-parameter function was based upon the nine-parameter function described in Section 6.5.1, with the addition of one parameter, R, representing the ratio of moment arms at the primary (d_P) and secondary (d_S) joint ($R = d_S / d_P$). Thus, the secondary joint angle could be added to that of the primary joint in a meaningful way so that the combined angle represented the ‘length’ of the biarticular component, θ_B, where $\theta_B = \theta_P + R\theta_S$.

Likewise, the two component angular velocities were combined to give a biarticular component angular velocity, ω_B of $\omega_B = \omega_P + R\omega_S$. A subsequent nine-parameter biarticular function of θ_B and ω_B was determined in the same way as for monoarticular components (Section 6.5.1). Bounds for the relative contributions of monoarticular and biarticular components to total joint torque were those used in Lewis (2011), taken from the literature. Parameter bounds, optimisation, and adjustment were performed exactly as detailed in Section 6.5.1.

6.5.3 THE HIP JOINT

At the hip, the parameters for the biarticular components were taken from the previously determined parameters at the knee. That is, the biarticular knee extensors were utilised for hip flexion, and the biarticular knee flexors were utilised for hip extension. The maximal torque generated by the biarticular component was calculated from these parameters, as well as the ratio of moment arms determined at the knee. Monoarticular hip parameters were allowed to vary during the optimisation process as detailed in Section 6.5.1.

6.5.4 THE METATARSOPHALANGEAL JOINT

Since the metatarsophalangeal joint of the foot was to be driven by subject-specific joint torque generators in the computer simulation model (see Section 7.3.7) but no dynamometer data had been collected at this joint, the torque parameters were estimated using the method of Allen (2010). Allen presented a situation of maximal MTP and ankle torque generation in which taking moments about the point of force application, the toes, revealed a moment arm at the MTP that was roughly one third of that for the ankle. Thus, the MTP joint was considered to have the same torque-angular velocity parameters as the ankle joint but with one third of the maximum isometric torque. For the purposes of the present study, in which the ankle joint plantar flexor torque consisted of monoarticular and biarticular components, their maximal torques were summed prior to scaling, but the MTP joint extensors were given the torque-angular velocity properties of the monoarticular ankle plantar flexors. The torque-angle relationship from the ankle was not included in order to

avoid projecting the same optimum angle onto the MTP joint; therefore, a seven-parameter function was used for each of the MTP flexors and extensors.

6.6 RESULTS

6.6.1 ANKLE DORSIFLEXION

The calculated nine-parameter function (Table 6.1) resulted in a weighted root mean square difference between measured and calculated torques of 3 Nm (3% of maximum torque) with 10% of measured data points originally greater than corresponding calculated ones prior to adjustment (Figure 6.3). These results are comparable to those of Lewis (2011; 3 Nm; 4% maximum torque) and Felton (2014; 2 Nm; 3% maximum torque). A repeat measurement of the first isometric trial at the end of the data collection procedure showed a 0% difference in peak torque, and hence no signs of ankle dorsiflexion fatigue within the subject.

Table 6.1. Ankle dorsiflexion subject-specific torque generator parameters.

parameter	description	value	bounds {lower (LB); upper (UB)}
T_{max} (Nm)	maximum eccentric torque, equal to $1.4T_0$ (Dudley et al., 1990; Webber & Kriellers, 1997)	99.17	constrained by T_0
T_0 (Nm)	maximum isometric torque	71.36	± 20% peak measured isometric torque
ω_{max} (rad·s^{-1})	maximum concentric velocity	13.34	6.4; 13.4
ω_c (rad·s^{-1})	vertical asymptote ($\omega = -\omega_c$) of Hill hyperbola describing concentric torques	4.65	0.15 ω_{max}; 0.5 ω_{max} (LB: Umberger et al., 2006; UB: Scovil & Ronsky, 2006)
k_2	width of torque-angle curve	1.95	0.5; 4.0
θ_{opt}	optimum angle of component	2.40	1.7; 3.5 (UB permitted outside joint range where curve may be ascending only)
a_{min}	minimum activation (where maximum activation, $a_{max} = 1.0$)	0.79	0.2; 1.0
m	parameter governing rate of activation	0.67	0.0; 1.0 (based on activation increasing over a range of 240 °s^{-1}; Amiridis et al., 1996)
ω_1 rad·s^{-1})	point of inflexion in differential activation function	0.60	-0.5; 3.0 (as above)

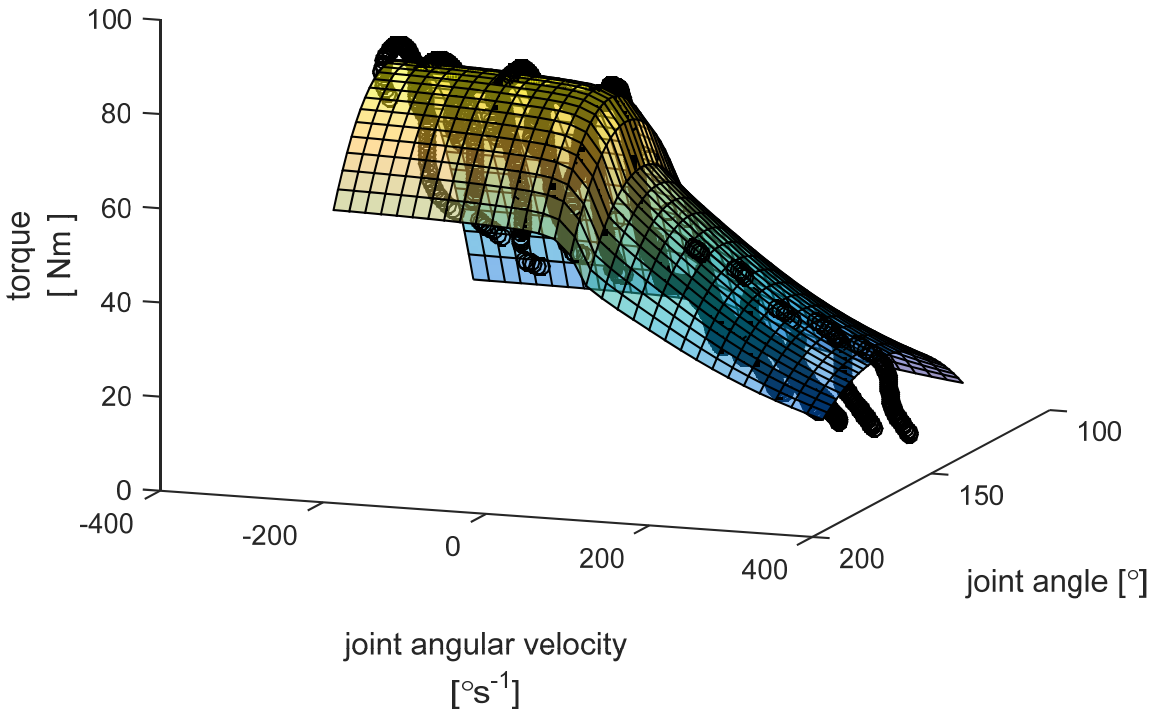

Figure 6.3. Nine-parameter, subject-specific, ankle dorsiflexion torque function, fitting experimental torques (black dots).

6.6.2 MTP FLEXION

As detailed in Section 6.5.4, the MTP flexion parameters were scaled from those for ankle dorsiflexion. The seven parameters describing maximum voluntary torque for this joint action are presented in Table 6.2.

Table 6.2. MTP flexion subject-specific torque generator parameters.

parameter	description	value
T_{max} (Nm)	maximum eccentric torque, equal to $1.4T_0$ (Dudley et al., 1990; Webber & Kriellers, 1997)	33.06
T_0 (Nm)	maximum isometric torque	23.79
ω_{max} (rad·s^{-1})	maximum concentric velocity	13.34
ω_c (rad·s^{-1})	vertical asymptote ($\omega = -\omega_c$) of Hill hyperbola describing concentric torques	4.65
a_{min}	minimum activation (where maximum activation, $a_{max} = 1.0$)	0.79
m	parameter governing rate of activation	0.67
ω_1 (rad·s^{-1})	point of inflexion in differential activation function	0.60

6.6.3 ANKLE PLANTARFLEXION

The calculated nineteen-parameter function (Table 6.3) resulted in a weighted root mean square difference between measured and calculated torques of 11 Nm (4% of monoarticular maximum torque; 2% of combined maximum torque) with 8% of measured data points originally greater than corresponding calculated ones prior to adjustment (Figure 6.4). These results are comparable to those of Lewis (2011; 12 Nm; 19% measured > calculated; 6% maximum monoarticular torque) and Felton (2014; 10 Nm; 4% maximum torque).

Table 6.3. Ankle plantar flexion subject-specific torque generator parameters.

parameter	monoarticular	biarticular	bounds {lower (LB); upper (UB)}
T_{max} (Nm)	298.28	199.08	constrained by T_0
T_0 (Nm)	216.02	145.16	± 60% peak measured isometric torque
ω_{max} (rad·s^{-1})	25.32	25.44	14.6; 26.4
ω_c (rad·s^{-1})	4.58	12.15	0.15 ω_{max}; 0.5 ω_{max} (LB: Umberger et al., 2006; UB: Scovil & Ronsky, 2006)
k_2	0.36	0.99	0.2; 2.0
θ_{opt}	1.18	1.80	1.1; 2.3 (UB permitted outside joint range where curve may be ascending only)
a_{min}	0.97	0.80	0.2; 1.0
m	0.11	0.49	0.0; 1.0 (based on activation increasing over a range of 240 °s^{-1}; Amiridis et al., 1996)
ω_1 (rad·s^{-1})	1.56	1.56	-0.5; 3.0 (as above)
R		0.15	0.15; 0.7 (LB: Refshauge et al., 1995; UB: ~150% estimated from Grieve et al., 1978)

Nomenclature: see Table 6.1; R = moment arm ratio (secondary joint: primary joint).

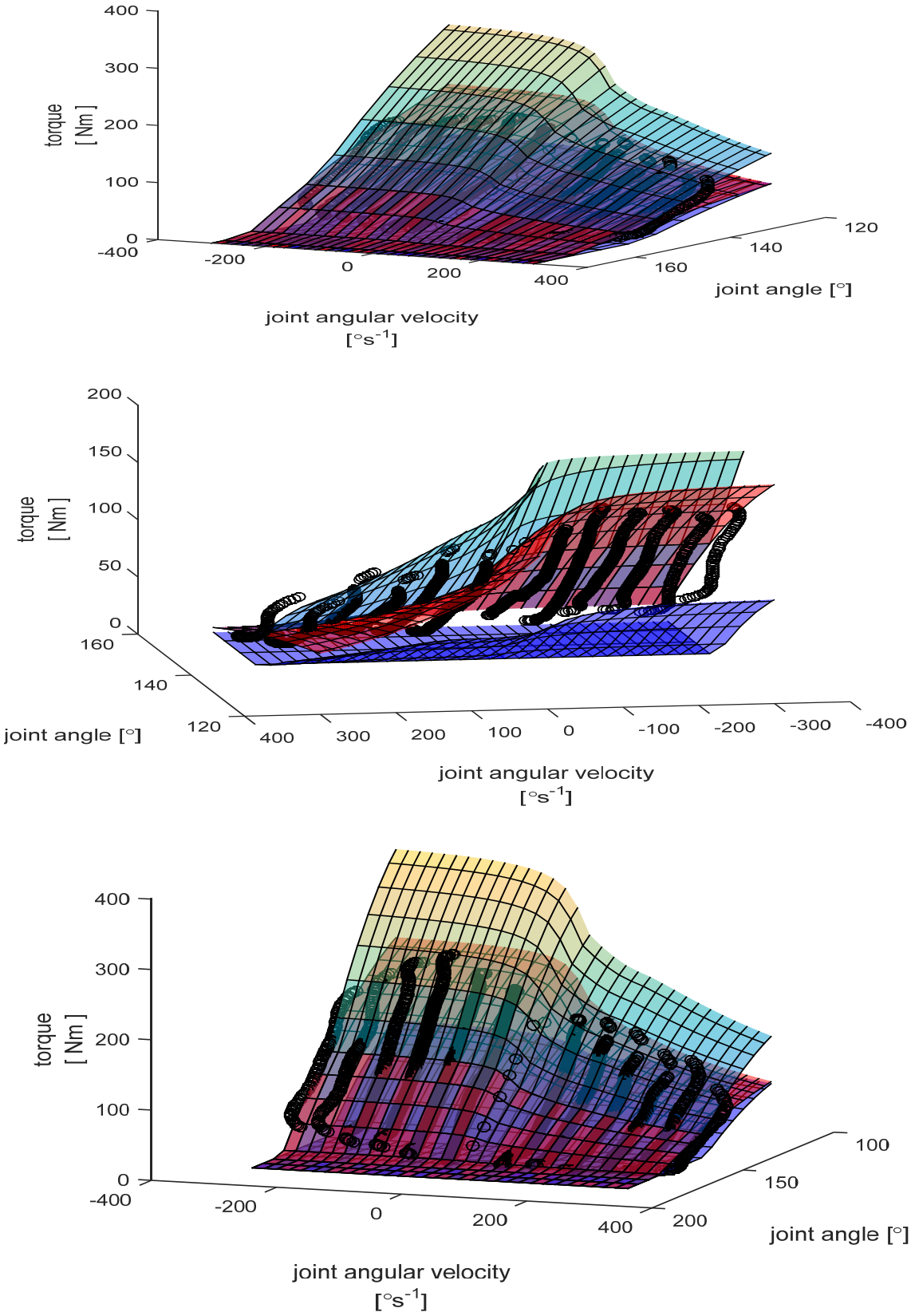

Figure 6.4. Nineteen-parameter, subject-specific, biarticular, ankle plantarflexion torque function, fitting experimental torques (black dots) at a secondary knee joint angle of 93° (top), 124° (middle), and 164° (bottom). Three surfaces showing monoarticular torque component; biarticular torque component, and total torque.

6.6.4 MTP EXTENSION

As detailed in Section 6.5.4, the MTP extension parameters were scaled from those for ankle plantar flexion. The seven parameters describing maximum voluntary torque for this joint action are presented in Table 6.4.

Table 6.4. MTP extension subject-specific torque generator parameters.

parameter	description	value
T_{max} (Nm)	maximum eccentric torque, equal to $1.4T_0$ (Dudley et al., 1990; Webber & Kriellers, 1997)	165.79
T_0 (Nm)	maximum isometric torque	120.39
ω_{max} (rad·s^{-1})	maximum concentric velocity	25.32
ω_c (rad·s^{-1})	vertical asymptote ($\omega = -\omega_c$) of Hill hyperbola describing concentric torques	5.58
a_{min}	minimum activation (where maximum activation, $a_{max} = 1.0$)	0.97
m	parameter governing rate of activation	0.11
ω_1 (rad·s^{-1})	point of inflexion in differential activation function	1.56

6.6.5 KNEE FLEXION

The calculated nineteen-parameter function (Table 6.5) resulted in a weighted root mean square difference between measured and calculated torques of 32 Nm (11% of monoarticular maximum torque; 6% of combined maximum torque) with 16% of measured data points originally greater than corresponding calculated ones prior to adjustment (Figure 6.5). These results are comparable to those of Lewis (2011; 14 Nm; 12% measured > calculated; 9% maximum monoarticular torque) and Felton (2014; 9 Nm; 5% maximum torque).

Table 6.5. Knee flexion subject-specific torque generator parameters.

parameter	monoarticular	biarticular	bounds {lower (LB); upper (UB)}
T_{max} (Nm)	298.48	254.38	constrained by T_0
T_0 (Nm)	215.74	184.24	± 20% peak measured isometric torque
ω_{max} (rad·s^{-1})	29.11	15.14	14.7; 29.1
ω_c (rad·s^{-1})	14.56	2.28	0.15 ω_{max}; 0.5 ω_{max} (LB: Umberger et al., 2006; UB: Scovil & Ronsky, 2006)
k_2	0.83	1.42	0.2; 2.0
θ_{opt}	2.57	5.36	monoarticular: 2.3; 3.6, biarticular: 5.0; 21.0 (UB permitted outside joint range where curve may be ascending only)
a_{min}	0.67	0.99	0.2; 1.0
m	1.00	0.87	0.0; 1.0 (based on activation increasing over a range of 240 °s^{-1}; Amiridis et al., 1996)
ω_1 (rad·s^{-1})	1.40	1.05	-0.5; 3.0 (as above)
R		0.68	0.5; 3.0 (based on the range of values for male specimens in Duda et al. (1996))

Nomenclature: see Table 6.1; R = moment arm ratio (secondary joint: primary joint).

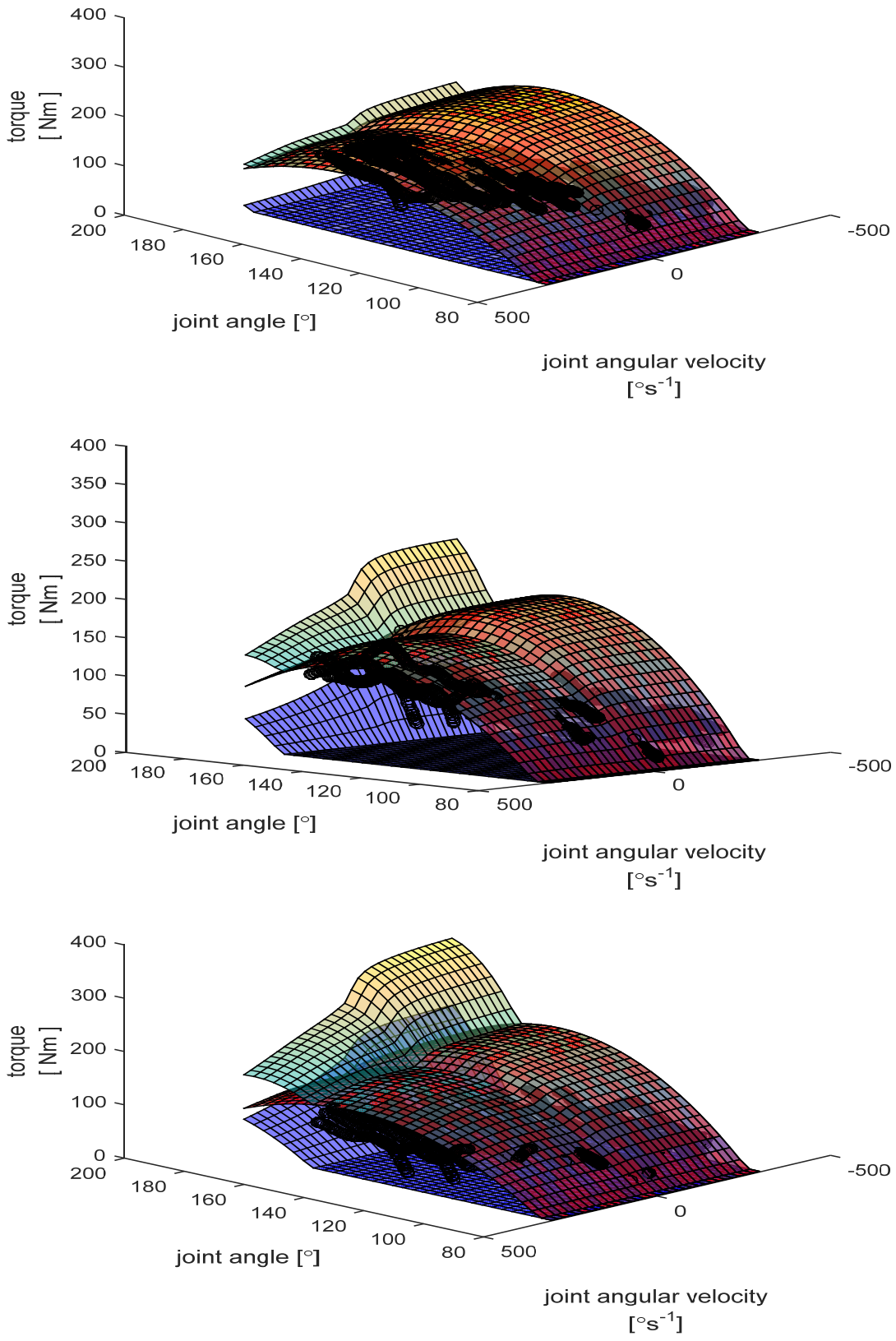

Figure 6.5. Nineteen-parameter, subject-specific, biarticular, knee flexion torque function, fitting experimental torques (black dots) at a secondary hip joint angle of 105° (top), 125° (middle), and 145° (bottom). Three surfaces showing monoarticular torque component; biarticular torque component, and total torque.

6.6.6 KNEE EXTENSION

The calculated nineteen-parameter function (Table 6.6) resulted in a weighted root mean square difference between measured and calculated torques of 31 Nm (4% of monoarticular maximum torque; 3% of combined maximum torque) with 20% of measured data points originally greater than corresponding calculated ones prior to adjustment (Figure 6.6). These results are comparable to those of Lewis (2011; 26 Nm; 22% measured > calculated; 9% maximum monoarticular torque) and Felton (2014; 46 Nm; 10% maximum torque). A repeat measurement of the first isometric trial at the end of the data collection procedure showed an 8% difference in peak torque, and hence no major fatigue within the subject, although this slight fatigue could still account for some submaximal data.

Table 6.6. Knee extension subject-specific torque generator parameters.

parameter	monoarticular	biarticular	bounds {lower (LB); upper (UB)}
T_{max} (Nm)	732.97	243.40	constrained by T_0
T_0 (Nm)	526.06	176.37	± 20% peak measured isometric torque
ω_{max} (rad·s^{-1})	35.11	24.78	17.7; 35.1
ω_c (rad·s^{-1})	17.55	6.42	0.15 ω_{max}; 0.5 ω_{max} (LB: Umberger et al., 2006; UB: Scovil & Ronsky, 2006)
k_2	0.45	1.93	0.2; 2.0
θ_{opt}	1.71	1.92	monoarticular: 0.8; 3.2, biarticular: 0.9; 7.0 (UB permitted outside joint range where curve may be ascending only)
a_{min}	0.23	1.00	0.2; 1.0
m	0.73	0.72	0.0; 1.0 (based on activation increasing over a range of 240 °s^{-1}; Amiridis et al., 1996)
ω_1 (rad·s^{-1})	1.16	1.33	-3.0; 1.57 (as above)
R		0.51	0.4; 1.4 (based on the range of values for male specimens in Duda et al. (1996))

Nomenclature: see Table 6.1; R = moment arm ratio (secondary joint: primary joint).

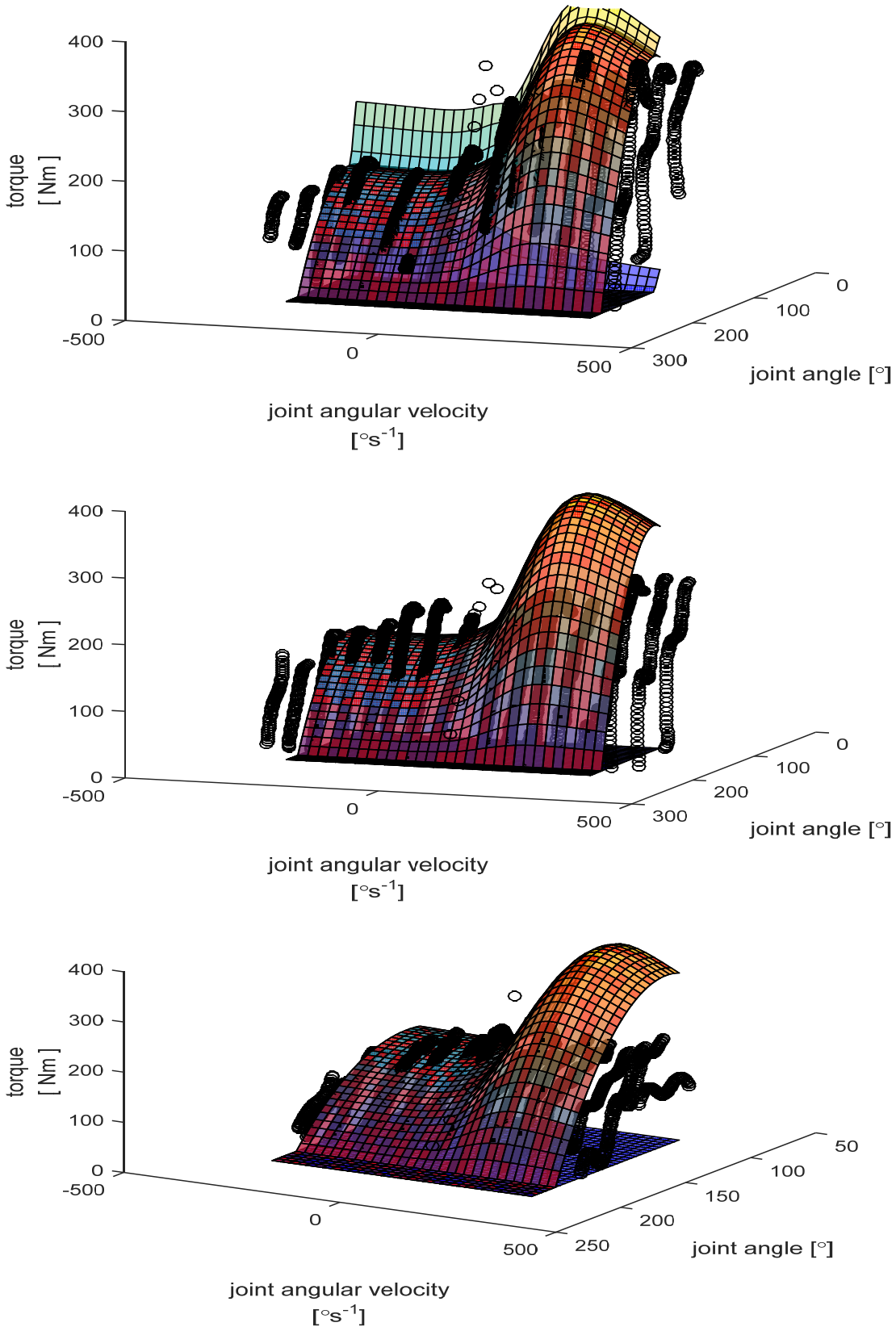

Figure 6.6. Nineteen-parameter, subject-specific, biarticular, knee extension torque function, fitting experimental torques (black dots) at a secondary hip joint angle of 105° (top), 125° (middle), and 145° (bottom). Three surfaces showing monoarticular torque component; biarticular torque component, and total torque.

6.6.7 HIP FLEXION

The calculated nineteen-parameter function (monoarticular parameters in Table 6.7; biarticular parameters are the same as for knee extension in Table 6.6) resulted in a weighted root mean square difference between measured and calculated torques of 39 Nm (20% of monoarticular maximum torque; 12% of combined maximum torque) with 16% of measured data points originally greater than corresponding calculated ones prior to adjustment (Figure 6.7). These differences are greater than those of Lewis (2011; 8 Nm; 5% maximum torque) and Felton (2014; 15 Nm; 7% maximum torque).

Table 6.7. Hip flexion subject-specific torque generator parameters.

parameter	description	value	bounds {lower (LB); upper (UB)}
T_{max} (Nm)	maximum eccentric torque, equal to $1.4T_0$ (Dudley et al., 1990; Webber & Kriellers, 1997)	188.68	constrained by T_0
T_0 (Nm)	maximum isometric torque	137.76	± 20% peak measured isometric torque
ω_{max} (rad·s^{-1})	maximum concentric velocity	15.00	7.5; 15.0
ω_c (rad·s^{-1})	vertical asymptote ($\omega = -\omega_c$) of Hill hyperbola describing concentric torques	7.50	0.15 ω_{max}; 0.5 ω_{max} (LB: Umberger et al., 2006; UB: Scovil & Ronsky, 2006)
k_2	width of torque-angle curve	0.20	0.2; 2.0
θ_{opt}	optimum angle of component	2.27	1.0; 4.0 (UB permitted outside joint range where curve may be ascending only)
a_{min}	minimum activation (where maximum activation, $a_{max} = 1.0$)	0.92	0.2; 1.0
m	parameter governing rate of activation	0.49	0.0; 1.0 (based on activation increasing over a range of 240 °s^{-1}; Amiridis et al., 1996)
ω_1 (rad·s^{-1})	point of inflexion in differential activation function	1.57	-3.0; 1.57 (as above)

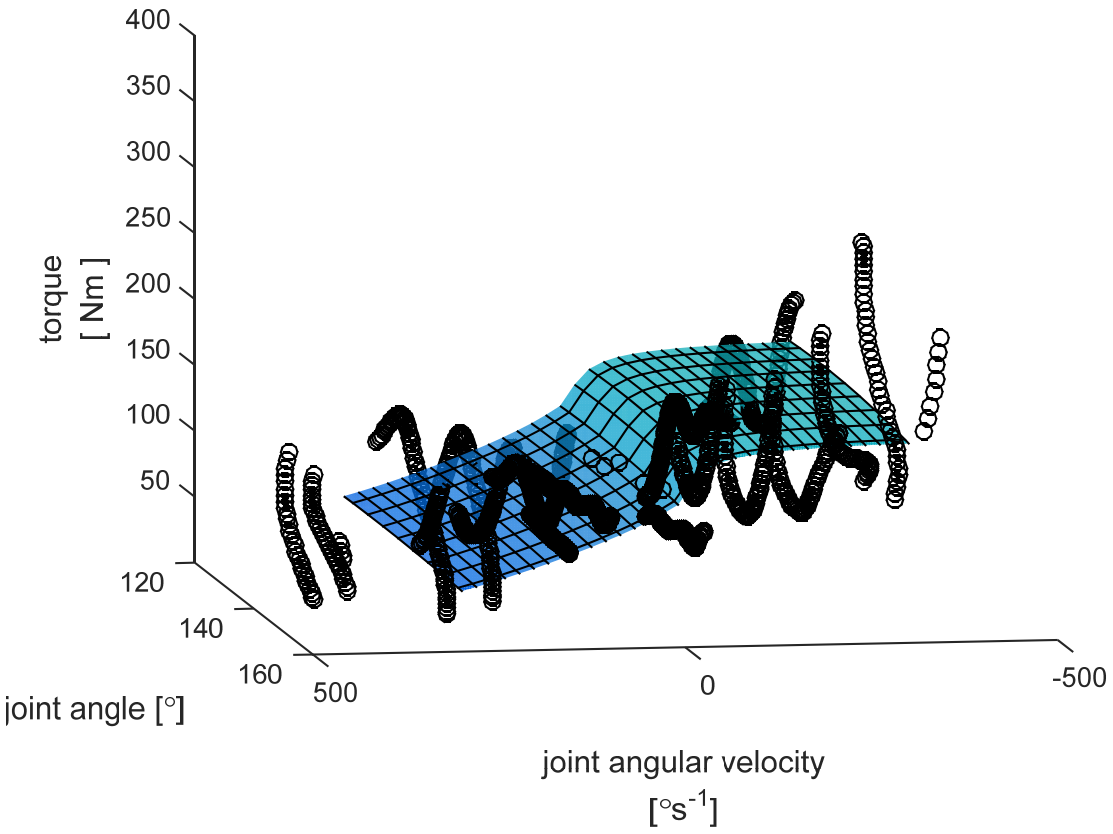

Figure 6.7. Nineteen-parameter, subject-specific, biarticular hip flexion torque function, fitting experimental torques (black dots).

6.6.8 HIP EXTENSION

The calculated nineteen-parameter function (monoarticular parameters in Table 6.8; biarticular parameters are the same as for knee flexion in Table 6.5) resulted in a weighted root mean square difference between measured and calculated torques of 13 Nm (6% of monoarticular maximum torque; 3% of combined maximum torque) with 15% of measured data points originally greater than corresponding calculated ones prior to adjustment (Figure 6.8). These results are comparable to those of Lewis (2011; 10 Nm; 7% monoarticular maximum torque) and Felton (2014; 50 Nm; 8% maximum torque).

Table 6.8. Hip extension subject-specific torque generator parameters.

parameter	description	value	bounds {lower (LB); upper (UB)}
T_{max} (Nm)	maximum eccentric torque, equal to $1.4T_0$ (Dudley et al., 1990; Webber & Kriellers, 1997)	204.29	constrained by T_0
T_0 (Nm)	maximum isometric torque	145.92	± 20% peak measured isometric torque
ω_{max} ($rad \cdot s^{-1}$)	maximum concentric velocity	13.06	11.6; 23.1
ω_c ($rad \cdot s^{-1}$)	vertical asymptote ($\omega = -\omega_c$) of Hill hyperbola describing concentric torques	2.00	0.15 ω_{max}; 0.5 ω_{max} (LB: Umberger et al., 2006; UB: Scovil & Ronsky, 2006)
k_2	width of torque-angle curve	0.20	0.2; 2.0
θ_{opt}	optimum angle of component	2.70	0.9; 3.6 (UB permitted outside joint range where curve may be ascending only)
a_{min}	minimum activation (where maximum activation, $a_{max} = 1.0$)	0.60	0.2; 1.0
m	parameter governing rate of activation	0.51	0.0; 1.0 (based on activation increasing over a range of 240 $°s^{-1}$; Amiridis et al., 1996)
ω_1 ($rad \cdot s^{-1}$)	point of inflexion in differential activation function	1.57	-3.0; 1.57 (as above)

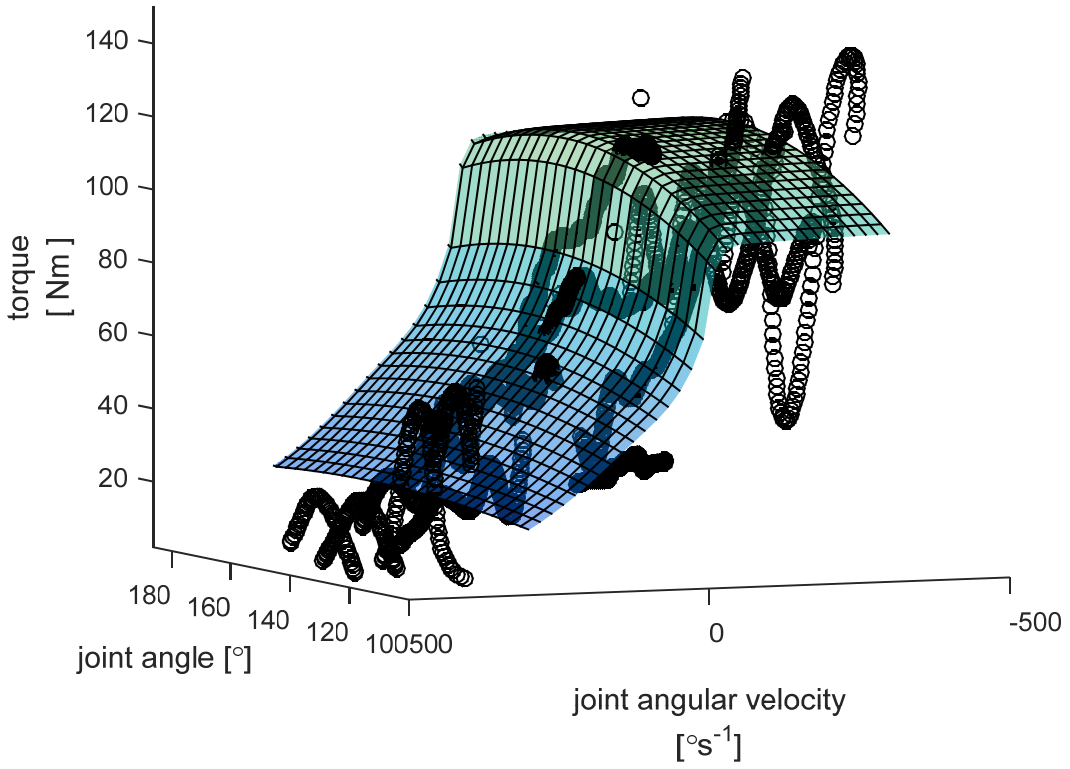

Figure 6.8. Nineteen-parameter, subject-specific, biarticular hip extension torque function, fitting experimental torques (black dots).

6.6.9 SHOULDER FLEXION

The calculated nine-parameter function (Table 6.9) resulted in a weighted root mean square difference between measured and calculated torques of 9 Nm (7% of maximum torque) with 6% of measured data points originally greater than corresponding calculated ones prior to adjustment (Figure 6.9). These results are comparable to those of Lewis (2011; 7 Nm; 9% maximum torque) and Felton (2014; 7 Nm; 6% maximum torque).

Table 6.9. Shoulder flexion subject-specific torque generator parameters.

parameter	description	value	bounds {lower (LB); upper (UB)}
T_{max} (Nm)	maximum eccentric torque, equal to $1.4T_0$ (Dudley et al., 1990; Webber & Kriellers, 1997)	126.39	constrained by T_0
T_0 (Nm)	maximum isometric torque	91.27	± 20% peak measured isometric torque
ω_{max} ($rad \cdot s^{-1}$)	maximum concentric velocity	20.16	12.5; 24.8
ω_c ($rad \cdot s^{-1}$)	vertical asymptote ($\omega = -\omega_c$) of Hill hyperbola describing concentric torques	8.34	0.15 ω_{max}; 0.5 ω_{max} (LB: Umberger et al., 2006; UB: Scovil & Ronsky, 2006)
k_2	width of torque-angle curve	0.01	0.0; 2.0
θ_{opt}	optimum angle of component	1.90	-1.0; 3.3 (UB permitted outside joint range where curve may be ascending only)
a_{min}	minimum activation (where maximum activation, $a_{max} = 1.0$)	0.87	0.2; 1.0
m	parameter governing rate of activation	0.24	0.0; 1.0 (based on activation increasing over a range of 240 $°s^{-1}$; Amiridis et al., 1996)
ω_1 ($rad \cdot s^{-1}$)	point of inflexion in differential activation function	2.95	-0.5; 3.0 (as above)

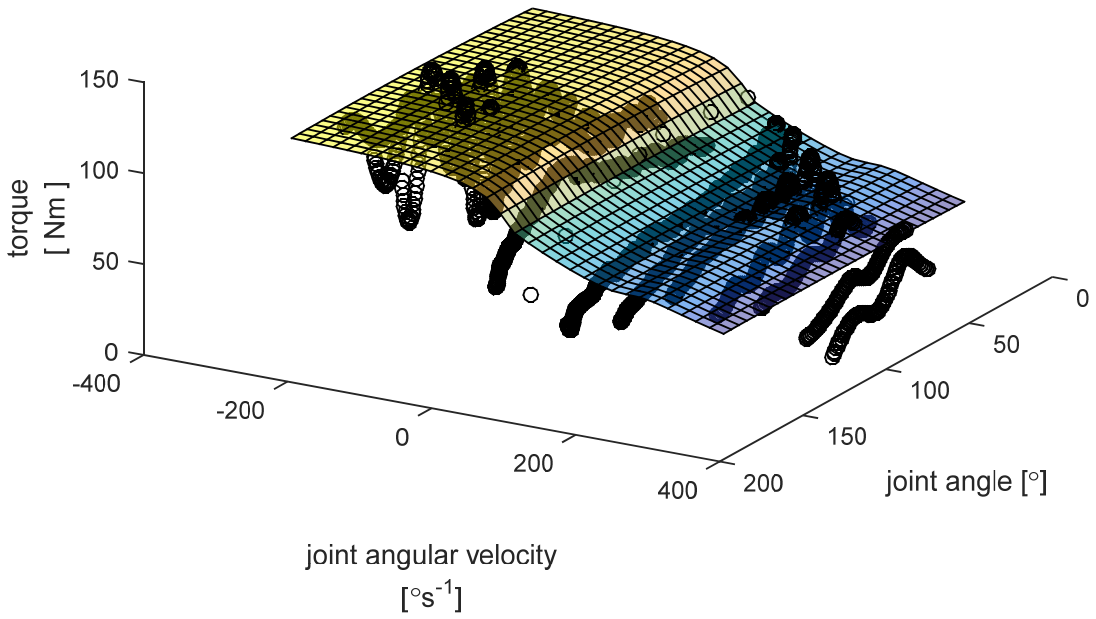

Figure 6.9. Nine-parameter, subject-specific, shoulder flexion torque function, fitting experimental torques (black dots).

6.6.10 SHOULDER EXTENSION

The calculated nine-parameter function (Table 6.10) resulted in a weighted root mean square difference between measured and calculated torques of 11 Nm (4% of maximum torque) with 10% of measured data points originally greater than corresponding calculated ones prior to adjustment (Figure 6.10). These results are comparable to those of Lewis (2011; 10 Nm; 9% maximum torque) and Felton (2014; 17 Nm; 13% maximum torque).

Table 6.10. Shoulder extension subject-specific torque generator parameters.

parameter	description	value	bounds {lower (LB); upper (UB)}
T_{max} (Nm)	maximum eccentric torque, equal to $1.4T_0$ (Dudley et al., 1990; Webber & Kriellers, 1997)	250.62	constrained by T_0
T_0 (Nm)	maximum isometric torque	181.36	± 20% peak measured isometric torque
ω_{max} ($rad \cdot s^{-1}$)	maximum concentric velocity	18.26	11.4; 22.7
ω_c ($rad \cdot s^{-1}$)	vertical asymptote ($\omega = -\omega_c$) of Hill hyperbola describing concentric torques	8.98	0.15 ω_{max}; 0.5 ω_{max} (LB: Umberger et al., 2006; UB: Scovil & Ronsky, 2006)
k_2	width of torque-angle curve	0.13	0.2; 2.0
θ_{opt}	optimum angle of component	2.20	1.0; 2.9 (UB permitted outside joint range where curve may be ascending only)
a_{min}	minimum activation (where maximum activation, $a_{max} = 1.0$)	0.67	0.2; 1.0
m	parameter governing rate of activation	0.81	0.0; 1.0 (based on activation increasing over a range of 240 $°s^{-1}$; Amiridis et al., 1996)
ω_1 ($rad \cdot s^{-1}$)	point of inflexion in differential activation function	0.52	-0.5; 3.0 (as above)

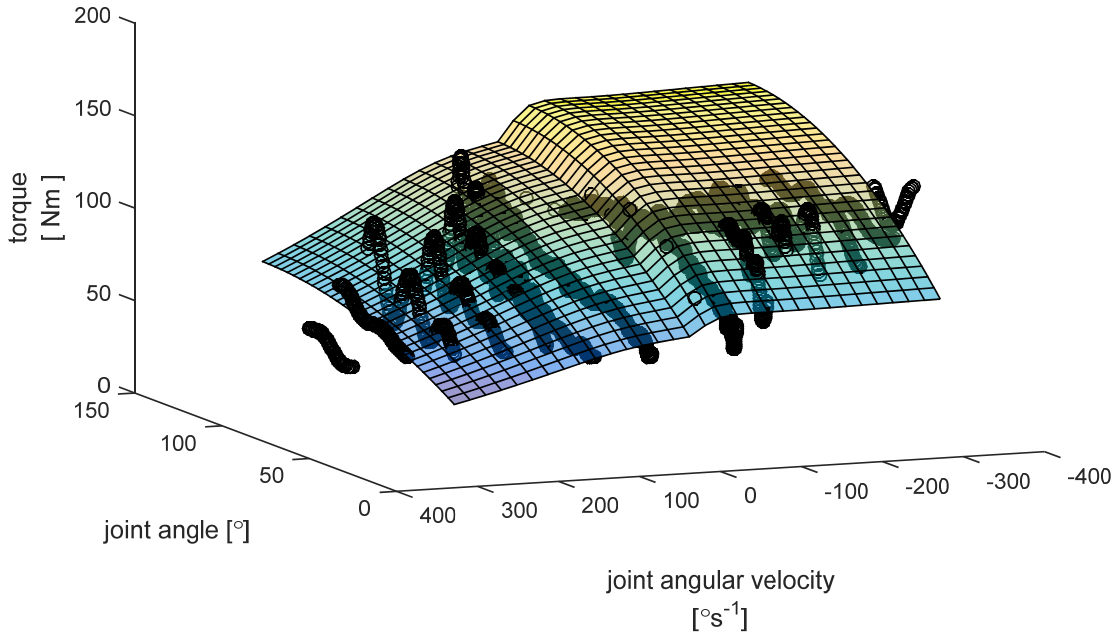

Figure 6.10. Nine-parameter, subject-specific, shoulder extension torque function, fitting experimental torques (black dots).

6.6.11 ELBOW FLEXION

The calculated nine-parameter function (Table 6.11) resulted in a weighted root mean square difference between measured and calculated torques of 3 Nm (3% of maximum torque) with 11% of measured data points originally greater than corresponding calculated ones prior to adjustment (Figure 6.11). Previous whole-body simulation models have not used subject-specific torque profiles at the elbow joint and so are not available for comparison.

Table 6.11. Elbow flexion subject-specific torque generator parameters.

parameter	description	value	bounds {lower (LB); upper (UB)}
T_{max} (Nm)	maximum eccentric torque, equal to $1.4T_0$ (Dudley et al., 1990; Webber & Kriellers, 1997)	92.47	constrained by T_0
T_0 (Nm)	maximum isometric torque	66.56	± 40% peak measured isometric torque
ω_{max} ($rad \cdot s^{-1}$)	maximum concentric velocity	49.40	6.3; 49.5
ω_c ($rad \cdot s^{-1}$)	vertical asymptote ($\omega = -\omega_c$) of Hill hyperbola describing concentric torques	9.22	0.15 ω_{max}; 0.5 ω_{max} (LB: Umberger et al., 2006; UB: Scovil & Ronsky, 2006)
k_2	width of torque-angle curve	0.29	0.2; 2.0
θ_{opt}	optimum angle of component	2.22	1.5; 6.3 (UB permitted outside joint range where curve may be ascending only)
a_{min}	minimum activation (where maximum activation, $a_{max} = 1.0$)	0.87	0.2; 1.0
m	parameter governing rate of activation	0.17	0.0; 1.0 (based on activation increasing over a range of 240 $°s^{-1}$; Amiridis et al., 1996)
ω_1 ($rad \cdot s^{-1}$)	point of inflexion in differential activation function	-0.33	-0.5; 3.0 (as above)

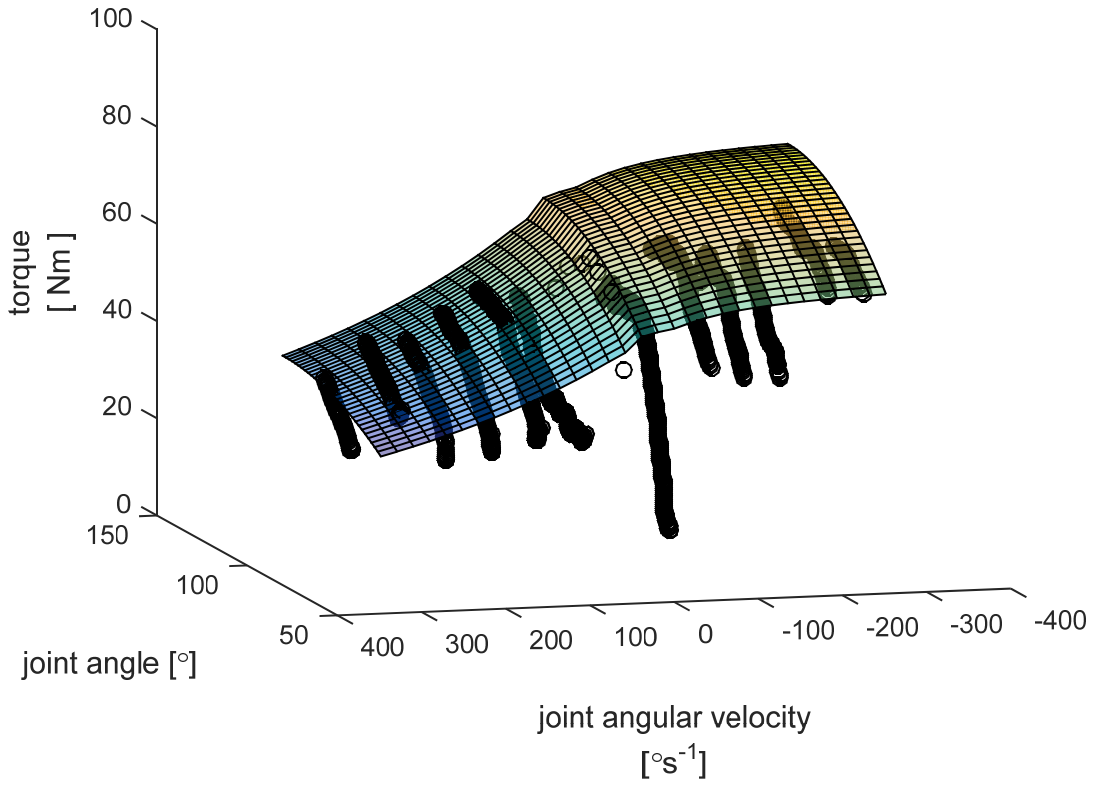

Figure 6.11. Nine-parameter, subject-specific, elbow flexion torque function, fitting experimental torques (black dots).

6.6.12 ELBOW EXTENSION

The calculated nine-parameter function (Table 6.12) resulted in a weighted root mean square difference between measured and calculated torques of 1 Nm (2% of maximum torque) with 18% of measured data points originally greater than corresponding calculated ones prior to adjustment (Figure 6.12). Previous whole-body simulation models have not used subject-specific torque profiles at the elbow joint and so are not available for comparison.

Table 6.12. Elbow extension subject-specific torque generator parameters.

parameter	description	value	bounds {lower (LB); upper (UB)}
T_{max} (Nm)	maximum eccentric torque, equal to $1.4T_0$ (Dudley et al., 1990; Webber & Kriellers, 1997)	74.18	constrained by T_0
T_0 (Nm)	maximum isometric torque	53.07	± 40% peak measured isometric torque
ω_{max} (rad·s^{-1})	maximum concentric velocity	44.81	5.7; 45.3
ω_c (rad·s^{-1})	vertical asymptote ($\omega = -\omega_c$) of Hill hyperbola describing concentric torques	14.03	0.15 ω_{max}; 0.5 ω_{max} (LB: Umberger et al., 2006; UB: Scovil & Ronsky, 2006)
k_2	width of torque-angle curve	0/52	0.2; 2.0
θ_{opt}	optimum angle of component	1.54	0.6; 6.3 (UB permitted outside joint range where curve may be ascending only)
a_{min}	minimum activation (where maximum activation, a_{max} = 1.0)	0.88	0.2; 1.0
m	parameter governing rate of activation	0.37	0.0; 1.0 (based on activation increasing over a range of 240 °s^{-1}; Amiridis et al., 1996)
ω_1 (rad·s^{-1})	point of inflexion in differential activation function	2.15	-0.5; 3.0 (as above)

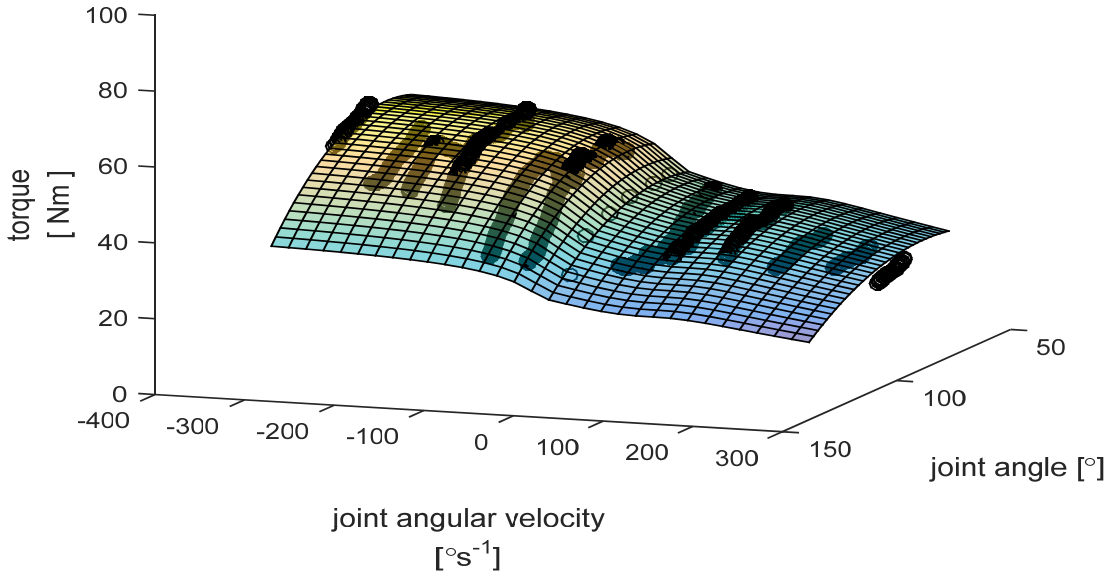

Figure 6.12. Nine-parameter, subject-specific, elbow extension torque function, fitting experimental torques (black dots).

6.7 SUBJECT-SPECIFIC INERTIA MODEL

Yeadon's (1990) mathematical inertia model was used throughout this thesis, both in the reduction and analysis of experimental kinematic performance data (Section 7.3.1), and as input to the subject-specific computer simulation model (Section 7.4). A series of 95 independent anthropometric measurements were taken, consisting of 34 lengths, 3 depths, 17 widths, and 41 perimeters at prescribed locations on all four limbs, as well as the head and torso. These measurements were used to model the human body as a series of three-dimensional geometric shapes, including 'stadium' solids for the torso segments using perimeter and width measurements (Figure 6.13). The model was used to calculate segmental mass; mass centre location; and moment of inertia about each of three primary axes, for each of the following 15 body segments:

- 2 x forefoot, from metatarsophalangeal (MTP) joint centre to distal end of toes;
- 2 x rear foot, from MTP joint centre to ankle joint centre;
- 2 x shank, from ankle joint centre to knee joint centre;
- 2 x thigh, from knee joint centre to hip joint centre;
- Lower trunk, from hip joint centres to top of thorax;
- Upper trunk; from top of thorax to base of neck;
- Head plus neck, from base of neck to vertex;
- 2 x upper arm, from shoulder joint centre to elbow joint centre;
- 2 x forearm plus hand, from elbow joint centre to distal end of fingers.

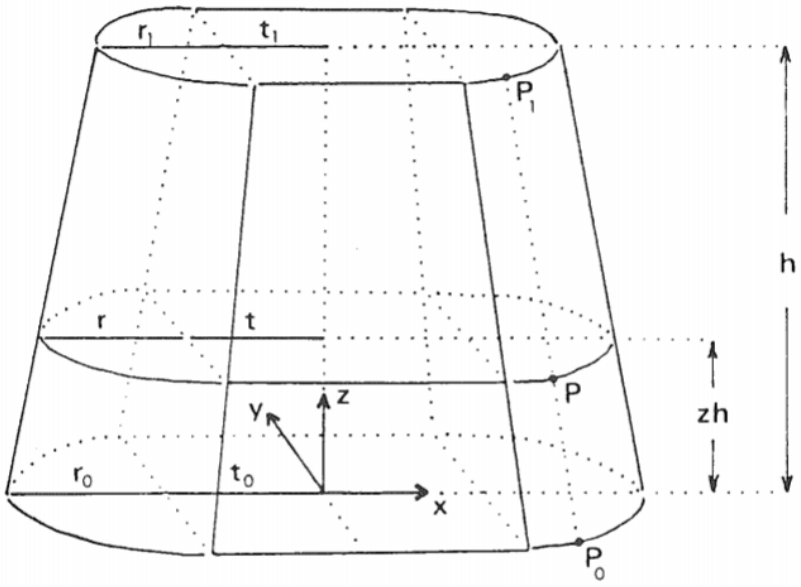

Figure 6.13. A stadium solid (Yeadon, 1990)

Segmental density values were taken from Chandler et al. (1975), providing a maximum error in total body mass calculation using Yeadon's (1990) original uncorrected methodology of 2.3%. In the present thesis segmental density values were adjusted to ensure the correct total body mass. Prior to this correction, the estimated body mass from the model had been 80.1 kg, giving an error of 9.5% when compared with the subject's measured mass of 88.6 kg. The present subject's muscular physique perhaps resulted in segmental density values that were underestimated by Chandler et al's (1975) literature values.

For application to the simulation model, inertia parameters for left and right limbs were averaged, with the masses summed. In addition, the inertial properties of the two-part feet were adjusted to include the effects of the shoes. To allow contact points in the simulation model at both the MTP joint and the heel (described in more detail in Section 5.4.4), as well as providing a more realistic representation of rear foot mass centre location that does not sit precisely on the line between MTP and ankle, the rear foot was modelled as a triangular segment with corners at the MTP joint centre, ankle joint centre, and heel. Segmental lengths were adjusted based on the same anthropometric measurements taken with the shoes on. Maintaining Yeadon's (1990) assumption of uniform density across the foot, the additional mass of the shoe was therefore assumed to be distributed between rear foot and forefoot

in the same proportions as the unshod foot model and added to each segmental mass accordingly. Segmental densities were first increased via the addition of the extra shoe mass into the same unshod volume. This led to the calculation of a new, greater segmental moment of inertia. The additional estimated moment of inertia due to the shoe alone was then increased in proportion to the increase in two-dimensional area (only the moment of inertia about the transverse axis was to be used in the simulation model and the experimental data analysis) of the segment in shod compared with unshod conditions. Mass centre locations for shoe and foot separately were assumed to be the same proportion of the distance along the segment, leading to a weighted mean of shoe and foot masses and mass centre locations to provide a combined mass centre location. Finally, the rear foot centre of mass was assumed to lie an equal proportion of the distance along the MTP to ankle and MTP to heel lines, being positioned half way between both positions. Table 6.13 provides the final segmental inertia parameters, including the added shoes, combined for left and right limbs where appropriate.

Table 6.13. Subject-specific segmental inertia parameters, combined for left and right limbs where appropriate.

body segment	length (m)	mass (kg)	mass centre location relative to proximal joint (m)	MOI about transverse axis through mass centre ($kg \cdot m^2$)
forefoot	0.085	0.477	0.035	0.0003
rear foot	0.139	2.293	0.063	0.0059
shank	0.453	10.542	0.192	0.1584
thigh	0.447	25.073	0.189	0.4245
lower trunk	0.418	24.433	0.323	0.5218
upper trunk	0.182	10.860	0.085	0.0701
head plus neck	0.269	5.611	0.136	0.0344
upper arm	0.323	6.323	0.138	0.0588
forearm plus hand	0.469	3.710	0.168	0.0568

6.8 CHAPTER SUMMARY

This chapter detailed the collection of maximal voluntary isometric and isovelocity joint torque data on a dynamometer. The determination of subject-specific joint torque parameters for each joint action were explained and presented. Monoarticular and biarticular torque functions were obtained, fitting experimentally collected torques in most cases similarly to or more closely than previously reported torque fits in the literature. Finally, subject-specific segmental inertia parameters were determined.

CHAPTER 7

PARAMETER DETERMINATION AND MODEL EVALUATION

7.1 CHAPTER OVERVIEW

In this chapter, the process of determining viscoelastic parameters for a simulation model of drop jumping containing compliant joints is outlined. This model, and an equivalent model representative of pin joints in place of compliant joints, are evaluated against experimental drop jump performance data. All stages of this process are explained, prior to the presentation of the evaluation results.

7.2 INTRODUCTION

Before any simulation model can be used to answer research questions and draw accurate conclusions, it is necessary to evaluate the model. Evaluation against experimental performance data can ensure that the model is a sufficiently accurate representation of the activity and the mechanical system being modelled. This process also enables the quantification of errors within the model and can highlight the effects of any inherent assumptions. It is important that such knowledge can subsequently be considered when critically analysing the simulation model results prior to their use to inform future research and scientific knowledge.

Likewise, it is also important to determine accurate parameters for use within the simulation model. The kinetic and kinematic performance of the simulation model, and any inferences drawn from them, are dependent upon the accuracy of parameters such as the viscoelastic stiffness and damping parameters at the foot-ground interface, wobbling masses, and compliant joints within the model. As such, parameter determination and evaluation of the model are highly important stages of the simulation modelling process, and both rely on the use of accurate experimental data.

7.3 EXPERIMENTAL DROP JUMP PERFORMANCE DATA

The kinetic and kinematic data collected during drop jumps from four different heights, as explained in Section 3.4 and Section 3.5, were processed in the same way for every trial, as explained below.

7.3.1 KINEMATIC DATA

Joint centre coordinates

Retroreflective marker data (Section 3.4.2) were manually labelled and processed within Vicon Nexus 1.7 Software. Very few gaps, where a marker had failed to track, were present in the labelled marker trajectory during the period of ground contact (identified between touchdown and take off as explained later). The maximum gap length during ground contact was seven frames (0.028 s). Any gap lasting for three frames or less was filled using the 'spline fill' function within Vicon Nexus. Within this function, a spline is fitted to the marker trajectory on either side of the gap and interpolated to estimate the missing marker displacement values. Each filled marker trajectory was visually inspected to ensure only realistic trajectories were carried forward to further analysis. Gaps of four to seven frames duration were filled using Vicon Nexus' 'pattern fill' function. This function uses the shape of another marker's gap-free trajectory to fill the gap. In all cases, the selected gap-free marker utilised was either on the opposite side of the same joint (e.g. using left lateral knee markers to fill left medial knee marker gaps) or attached to the same segment (e.g. using manubrium sterni markers to fill xiphoid process marker gaps). Again, all filled trajectories were inspected visually. The number and duration of filled marker trajectories was considered when selecting trials for further analysis and for use in evaluation of the simulation model (Section 7.5). Markers placed on soft tissue (calf, thigh, abdominal area, and chest) for the purposes of soft tissue displacement analysis were not gap filled, in order to not distort the true maximal displacement of each marker relative to the underlying bone.

All further processing of experimental data, unless otherwise stated, was performed in MATLAB (Version 8.0, The MathWorks Inc., Natick, MA, 2012). The instant of touchdown and take off were identified from force platform data as the first time point at which the vertical ground reaction force exceeded a threshold of 10 N, and the first subsequent time point at which it dropped below that same threshold, respectively.

Although all marker trajectories were relatively smooth, it was necessary to filter the data to remove any noise from the marker data, limit any skin movement artefact that may be present, and obtain the best possible estimate of true joint centre location throughout the trials. This was especially the case when any noise would be magnified during differentiation to obtain velocities and accelerations. Because any noise or skin movement artefact was present in the recorded marker locations, filtering these raw data was thought to be more representative of reality than would be filtering joint angles at a later point in the data reduction procedure. Likewise, differing magnitudes and relative proportions of noise and skin movement artefact would be present at each marker location on the body. It was therefore important to determine the appropriate cut-off frequency to be used when filtering displacement data for each marker.

Several alternative methods for determining filtering cut-off frequency were used, before the results of each of these methods were considered when choosing a final cut-off frequency for each marker. As with gap filling, markers placed on soft tissue (calf, thigh, abdominal area, and chest) for the purposes of soft tissue displacement analysis were not filtered, to not distort the true maximal displacement of each marker. Of the remaining markers, a representative sample of 14 markers (anterior-posterior and vertical displacements) were analysed across a further sample of two trials: a drop jump from the lowest height of 0.30 m; and a drop jump from the greatest height of 0.74 m.

Each marker trajectory was analysed, between touchdown and take off, using the residual analysis method of Winter (1990). Determining a cut-off frequency is necessarily a compromise between the amount of signal distortion and the amount of noise permitted. The method of Winter (1990) assumes both errors should be equal (Figure 7.1). An example plot of the residuals for right toe anterior-posterior marker displacement is displayed in Figure 7.2.

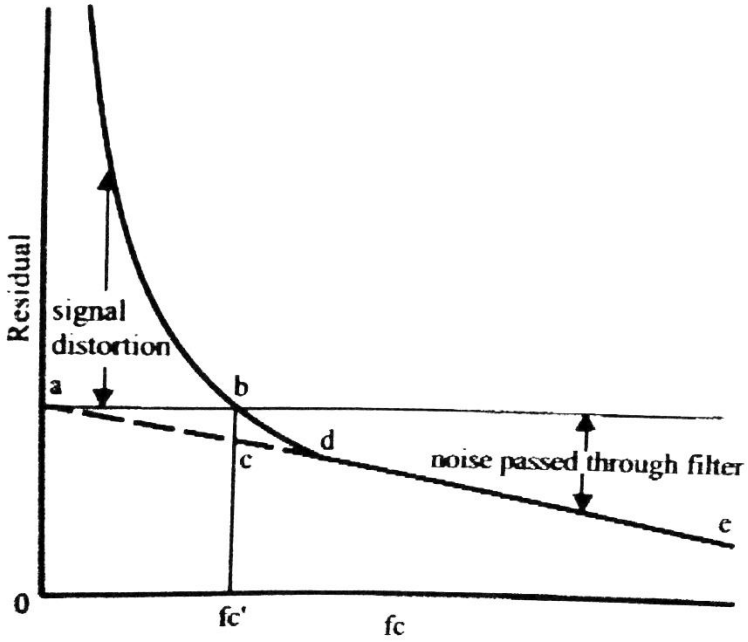

Figure 7.1. Residual analysis method to determine appropriate filtering cut-off frequency (fc') with equal signal distortion and permitted noise. Adapted from Winter (1990).

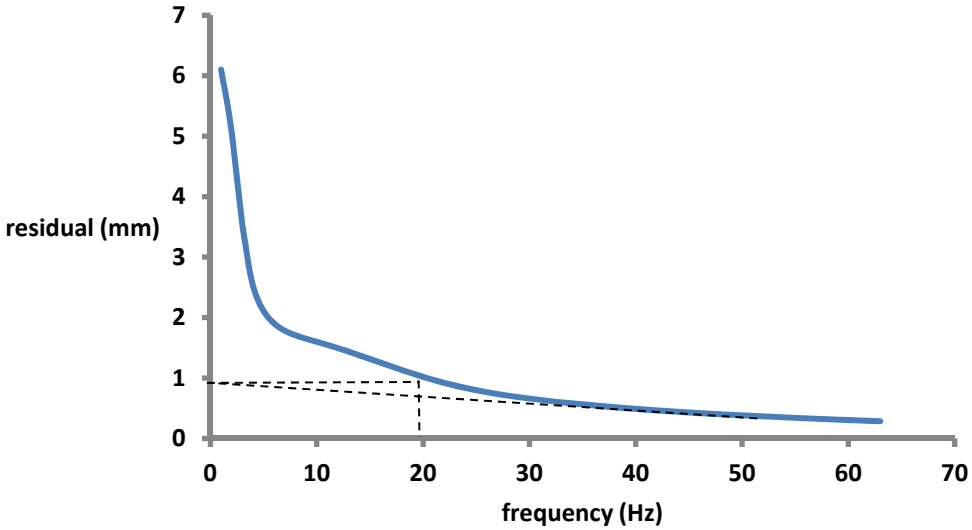

Figure 7.2. Residual analysis plot of right toe anterior-posterior marker displacement for a drop jump from 0.74 m

Secondly, a power spectral density analysis was performed on the marker displacement data, with the mean and any general trend removed, and calculated using the same method as for the accelerometer data in Section 4.3.2 (Figure 7.3). Considering the cumulative power spectral density, potential cut-off frequencies were considered as the frequencies below which 95% or 99% of the power occurred (Figure 7.4; Antonsson & Mann, 1985). Power spectral density plots were also inspected visually. Pre- and post-filtering marker displacement curves were then visually inspected (Figure 7.5) for each of the potential cut-off frequencies determined from residual analysis and cumulative power spectral densities, prior to the final cut-off frequencies being selected (Table 7.1). Where uncertainty existed, the higher of the potential cut-off frequencies was selected to minimise signal distortion.

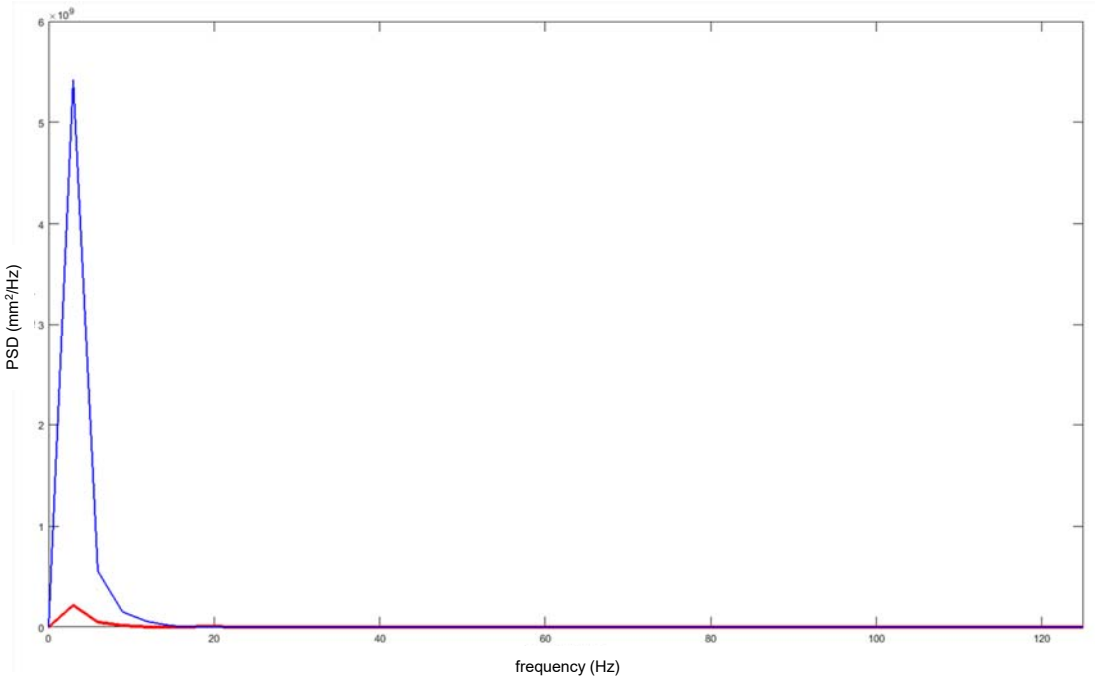

Figure 7.3. Power spectral density of anterior-posterior (red) and vertical (blue) right anterior superior iliac spine marker displacement for a drop jump from 0.74 m.

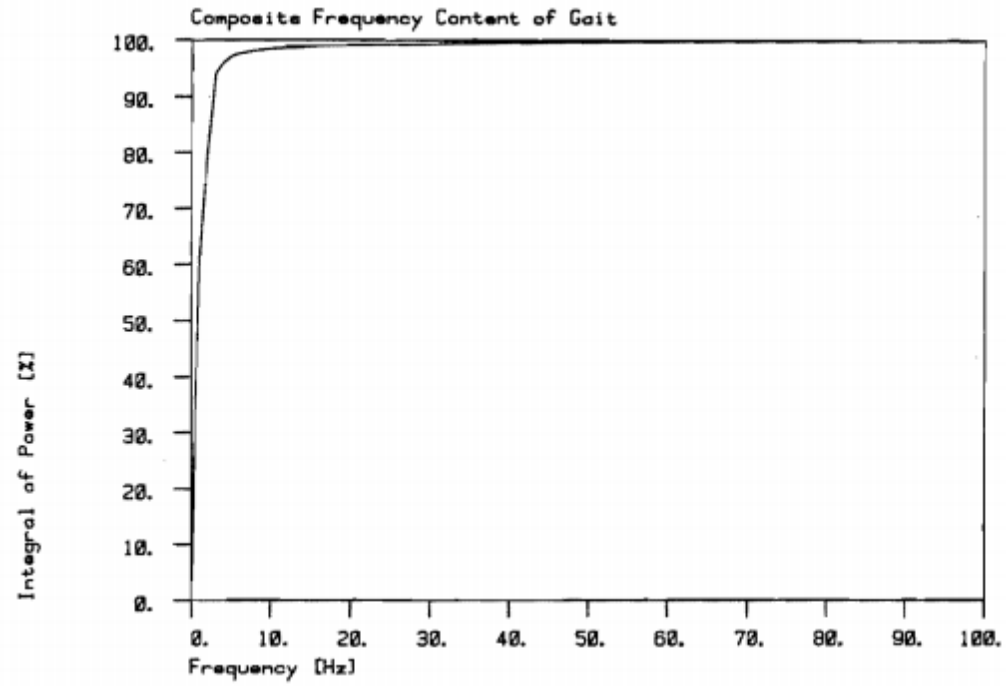

Figure 7.4. Cumulative power spectral density to determine cut-off frequency for filtering (Antonsson & Mann, 1985).

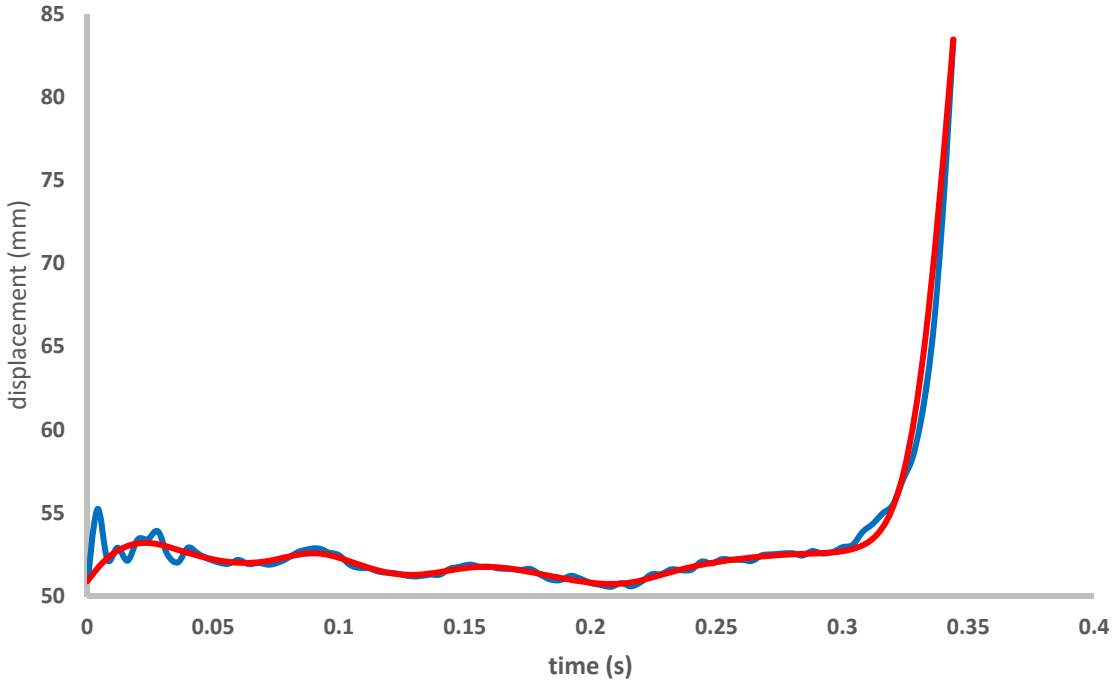

Figure 7.5. Comparison of raw data (blue) and filtered data (filtered at 26 Hz; red) of left fifth metatarsophalangeal joint vertical displacement data for a drop jump from 0.30 m.

Table 7.1. Cut-off frequencies determined for filtering of marker data.

marker	cut-off frequency (Hz)		markers locations cut-off frequency applied to
	anterior-posterior	vertical	
right toe	20	23	toes
right 1st MTP	18	21	1st MTPs
right 5th MTP	15	26	5th MTPs
right calcaneus	20	20	heels
right medial malleolus of ankle	18	23	all ankle markers
right lateral knee	15	18	all knee markers
right anterior superior iliac spine	24	12	ASISs
left posterior superior iliac spine	18	12	PSISs and back
left anterior head	15	12	all head, chest, and neck
left acromion	16	12	acromions
left posterior shoulder	15	9	posterior shoulders
right anterior shoulder	21	12	anterior and lateral shoulders
left medial elbow	14	9	all elbow markers
right lateral wrist	10	12	all wrist markers

All marker displacement data were then filtered between touchdown and take off using a fourth order double-pass Butterworth filter with the selected cut-off frequencies. Pre-touchdown marker displacement data were filtered separately at the same cut-off frequencies to avoid filtering across the landing impact and smoothing the deceleration upon landing, especially at positions such as the feet that decelerate rapidly. Raw and filtered marker trajectories were visually inspected for a final time (Figure 7.5) to ensure realistic trajectories remained. For example, the filtered left fifth metatarsophalangeal joint vertical displacement in Figure 7.5 retains the overall trend of the raw data but without the initial marker wobble upon impact between the foot and the ground.

Joint centres were calculated from filtered marker coordinates. In most cases, joint centres were calculated from the pair of markers placed across the joint (Table 3.2), with the joint centre defined as the midpoint of the marker locations at each time point (Ranson et al., 2009). However, there were some exceptions: toe and heel coordinates were defined from a single marker; hip joint centres were calculated from the four markers placed over the left and right anterior and posterior superior

iliac spine using the algorithm of Davis et al. (1991) - their algorithm was based on the radiographic examination of 25 hip studies and defined hip joint centres relative to a local pelvis coordinate system; the neck joint centre was defined using the methodology of Roosen (2007) as one eighth of the way from the C7 vertebrae marker to the manubrium sterni marker; the centre of the head was defined as the average position of the four head markers; and the shoulder joint centre was defined as the point at which the lateral shoulder marker intersected the line from anterior to posterior shoulder markers.

Joint angle-time histories

To determine two-dimensional joint angles both for initial input into the simulation model and for evaluation of subsequent model performance, there were two options. The first was projection of the angle onto the sagittal plane; and the second was rotation of the segment's coordinate system to obtain an angle in the sagittal plane. Allen (2010) trialled both methods and found that the projection angle allowed a better match between simulation and experimental performance data, therefore this method was used in this study.

Each joint centre, calculated as above, was projected onto the sagittal plane by using only the anterior-posterior and vertical coordinates from the filtered Vicon three-dimensional motion capture marker data (Figure 7.6). As with the number and duration of untracked marker gaps, the magnitude of marker displacement in the medio-lateral plane, an indicator of out of plane movement, would be used when selecting the trials to be used in evaluation of the simulation model. Angles were calculated to most closely reflect the angles used within the simulation model for future comparison. As such, the hip angle was that between the knee joint centre, hip joint centre, and neck joint centre, reflecting the use of a rigid trunk in simulation model hip angle calculation. The shoulder joint angle was similarly that between the hip joint centre, the shoulder joint centre, and the elbow joint centre. The neck angle was between hip joint centre, neck joint centre, and the centre of the head. All other joint angles were determined between adjacent segments of the body, just as in the simulation model. Left and right limb joint angles were averaged to provide

representative unilateral joint angles for use in the simulation model featuring combined left and right limbs (Section 5.4.1).

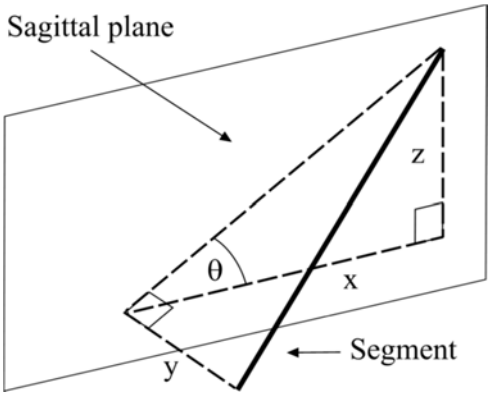

Figure 7.6. The projection of a segment between two joint centres onto the sagittal plane (Allen, 2010).

Because the recording rate of the force platform (1000 Hz) exceeded that of Vicon (250 Hz), it was possible for the first Vicon frame during ground contact to occur one to three force platform frames after touchdown. Joint kinematics at this time will have been affected by the foot-ground impact. Therefore, in trials where this was the case, joint angles at the last Vicon frame before impact were used as representative of those immediately prior to touch down.

For the simulation model and the optimisation score function subroutine (Section 7.5.3) to read in joint angles at time periods other than the exact time at which Vicon frames were recorded, it was necessary to spline the joint angle time histories between this first frame and the time of take off. Quintic splines (Wood & Jennings, 1979) were fitted to each joint angle time history using FORTRAN code, with six coefficients calculated for each time step. This provided the possibility for the simulation model to read in and use the spline coefficients to interpolate joint angles between time-steps. Joint angular velocities and angular accelerations could also be determined from the coefficients at any point in time. It was decided not to use the splines to smooth the angle data because the raw marker displacement data had already been filtered and smoothing at that initial stage of processing was felt to provide a more realistic representation of the noise within the system. The splines

fitted were therefore simply interpolating splines and did not alter joint angles at the times of the Vicon frame recordings.

Whole-body centre of mass trajectory

Whole-body centre of mass position was determined at each Vicon time frame using the subject-specific segmental inertia parameters obtained using Yeadon's (1990) inertia model (Section 6.7). To ensure the most representative comparison between experimental performance data and simulation model, the same segment definitions and centre of mass locations were used as in the simulation model. Thus, the entire trunk was treated as one rigid segment, the hand was included in a forearm plus hand segment along the line of the forearm, and each segmental mass centre was positioned along the line from proximal to distal end of the segment, except for the rear foot where the mass centre was positioned as defined in Section 6.7. Although there are limitations associated with the assumption of segmental mass centres lying exactly on the line between segment end points (Kingma et al., 1995), this is the simplest representation and provides sufficient accuracy. Furthermore, this is the representation employed within the simulation model and so allows for a like-for-like comparison of mass centre trajectories and velocities. With lean subjects such as the one in the present study, any anterior shift of the trunk mass centre caused by adipose tissue for example (Kingma et al., 1995) is likely to be minimal.

Whole-body mass centre displacement in the anterior-posterior and vertical directions were splined with quintic interpolating splines (Wood & Jennings, 1979) in the same way as described for joint angles above. The splines were used to obtain instantaneous whole-body mass centre velocity at take off. Along with the use of constant acceleration equations, this in turn determined the jump height (calculated as peak height of mass centre relative to mass centre height during a standing static trial). To minimise negative consequences of any errors in marker data at the instant of touchdown, mass centre velocities at this time point, for use as simulation model initial conditions (Section 7.4), were determined using constant acceleration equations between the point of greatest pre-touchdown mass centre height (given a vertical velocity of zero) and touchdown. It was accepted that small errors may still be present within these initial whole-body mass centre velocities,

and so they were allowed to vary by ± 0.1 ms^{-1} during the optimisation process to determine viscoelastic parameters and evaluate the model (Section 7.5.2).

7.3.2. GROUND REACTION FORCES

It is commonly considered that force platform data should be filtered in the same way and with the same cut-off frequency as kinematic data (Kristianslund et al., 2012). However, this is largely for the purposes of determining experimental joint moments (Kristianslund et al., 2012; 2013; van den Bogert & de Koning, 1996). Furthermore, when anterior-posterior and vertical ground reaction ground reaction forces were filtered at the greatest of the cut-off frequencies used for kinematics (26 Hz; Table 7.1) and thus the frequency that would retain the greatest proportion of the true signal, the peak ground reaction forces due to the landing impact were severely reduced (Figure 7.7). Therefore, the raw force platform data were used for the purposes of evaluating the simulation model. As with the joint angles and whole-body mass centre position, quintic interpolating splines (Wood & Jennings, 1979) were fitted to the anterior-posterior and vertical ground reaction forces, and anterior-posterior centre of pressure between touchdown and take off.

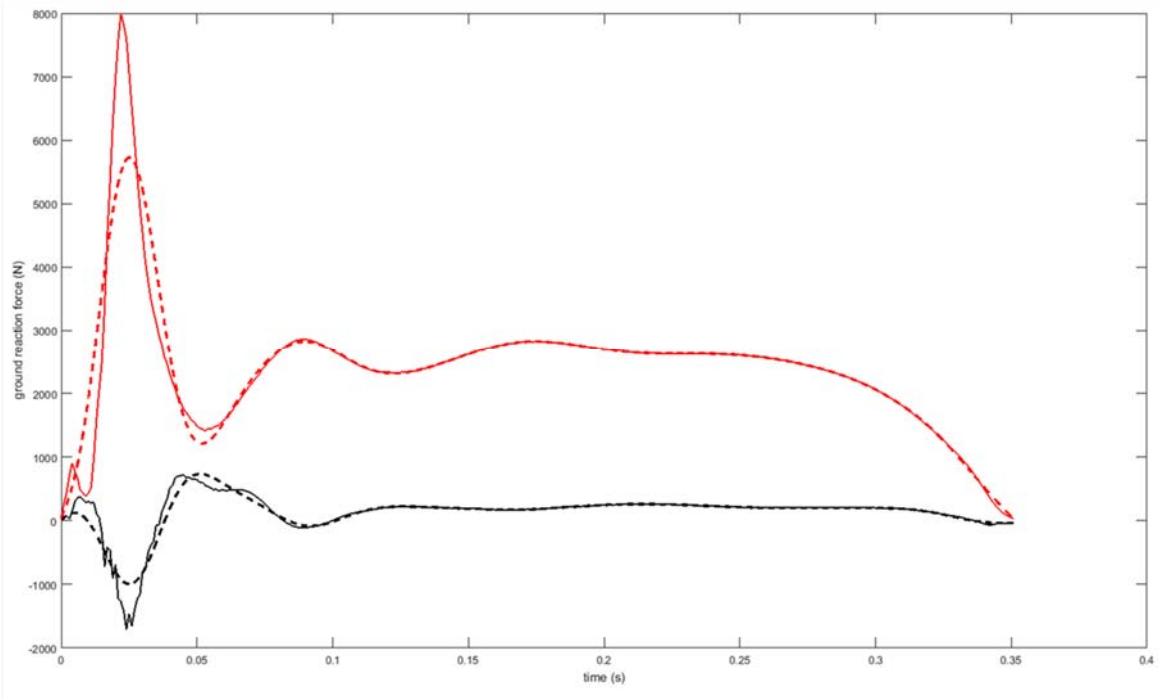

Figure 7.7. Raw (solid line) and filtered (dashed line) anterior-posterior (black) and vertical (red) ground reaction forces for a drop jump from 0.595 m.

7.4. INITIAL CONDITIONS AND WORK FLOW

Each simulation begins with a set of initial conditions, mostly determined from experimental data. These represent the angles and angular velocities of each joint, the position of the toe, the whole-body centre of mass velocity, the whole-body orientation and angular velocity, the torque generator activation levels, and the initial displacements of each viscoelastic element within the model. Joint and orientation angles and angular velocities, as well as mass centre velocities, were taken from the first time point (representative of touchdown conditions) in the splined experimental data. The anterior-posterior position of the toe was set to a coordinate of zero, whilst the vertical coordinate was set such that the MTP joint (the first point of contact experimentally) had an initial height of zero (i.e. at the level of the ground) at touchdown. Each spring-damper within the simulation model was given initial conditions of zero displacement and velocity. Finally, the initial activation of the torque generators was varied within the optimisation routine (Section 7.5.1) but was constrained to be less than or equal to 0.5 (50% of maximum activation) at touchdown (Section 7.5.2).

The following diagram (Figure 7.8 to Figure 7.12) illustrates the work flow of the forward-dynamics whole-body computer simulation model of drop jumping and shows the interaction between the series elastic component (SEC) and the contractile component within each joint torque generator. The simulations were advanced using a fourth-order Runge-Kutta algorithm with adaptive step size (Figure 7.9 and Figure 7.12) at main time steps of 0.001 s.

Each simulation was terminated at the point of take off (Figure 7.9 and Figure 7.12), which was determined as the first time point after 0.2 s at which all three points of contact on the foot were at a vertical height of greater than zero (i.e. above the ground). To encourage the optimisation procedure to converge on a realistic solution, simulations in which the foot temporarily left the ground prior to 0.2 s were not terminated but instead were penalised according to the duration of time for which there was no ground reaction force being applied (Section 7.5.4).

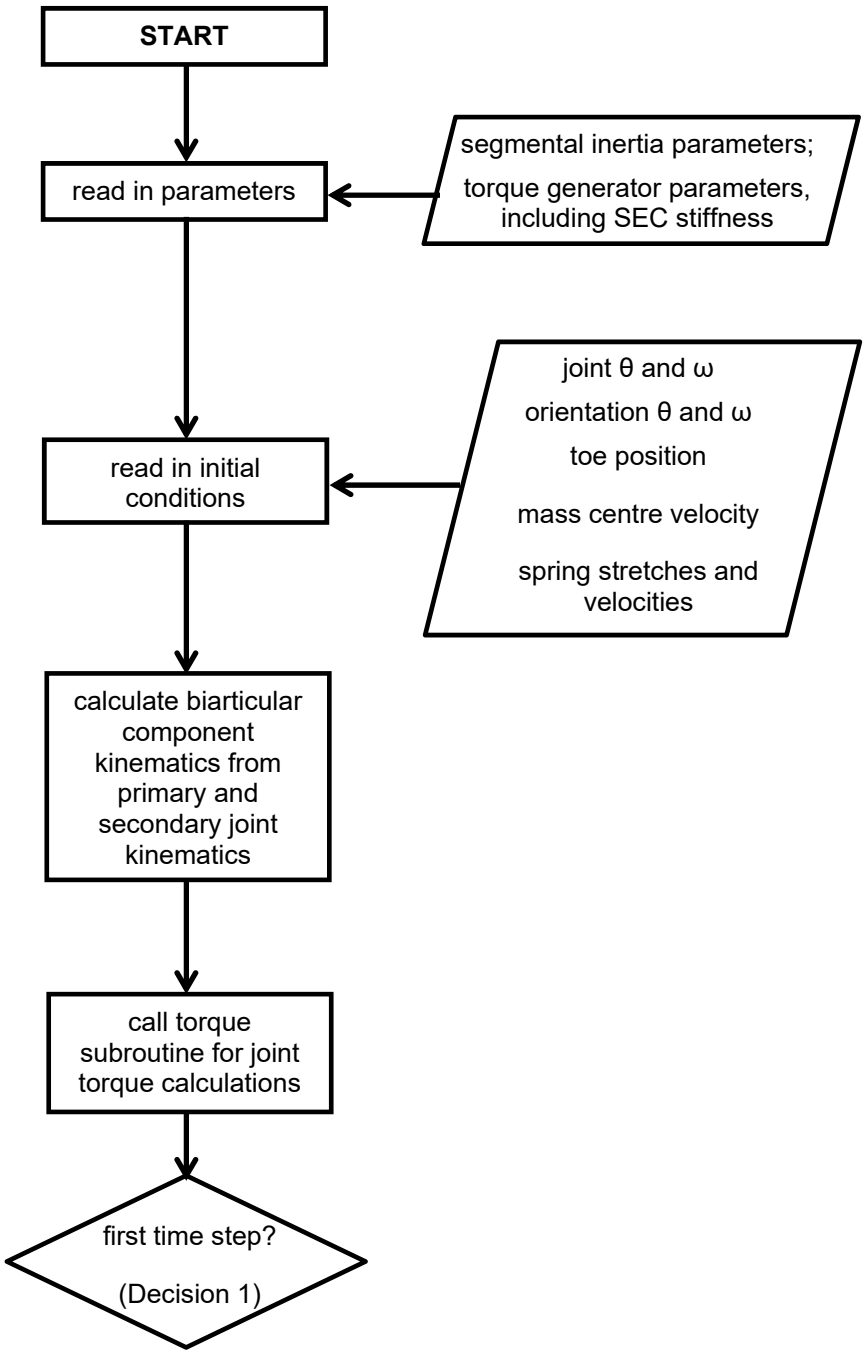

Figure 7.8. Simulation model work flow diagram; part 1.

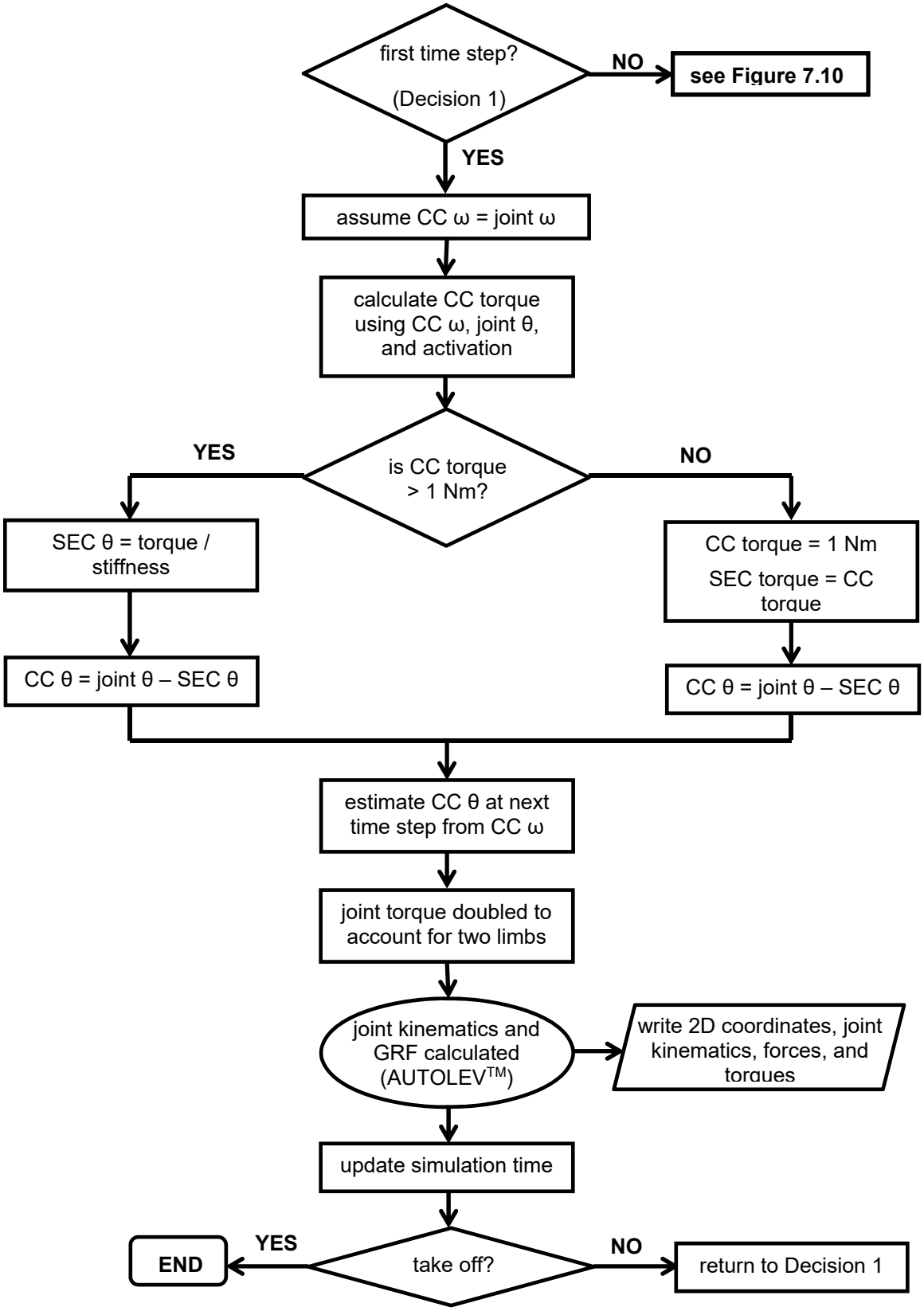

Figure 7.9. Simulation model work flow diagram; part 2.

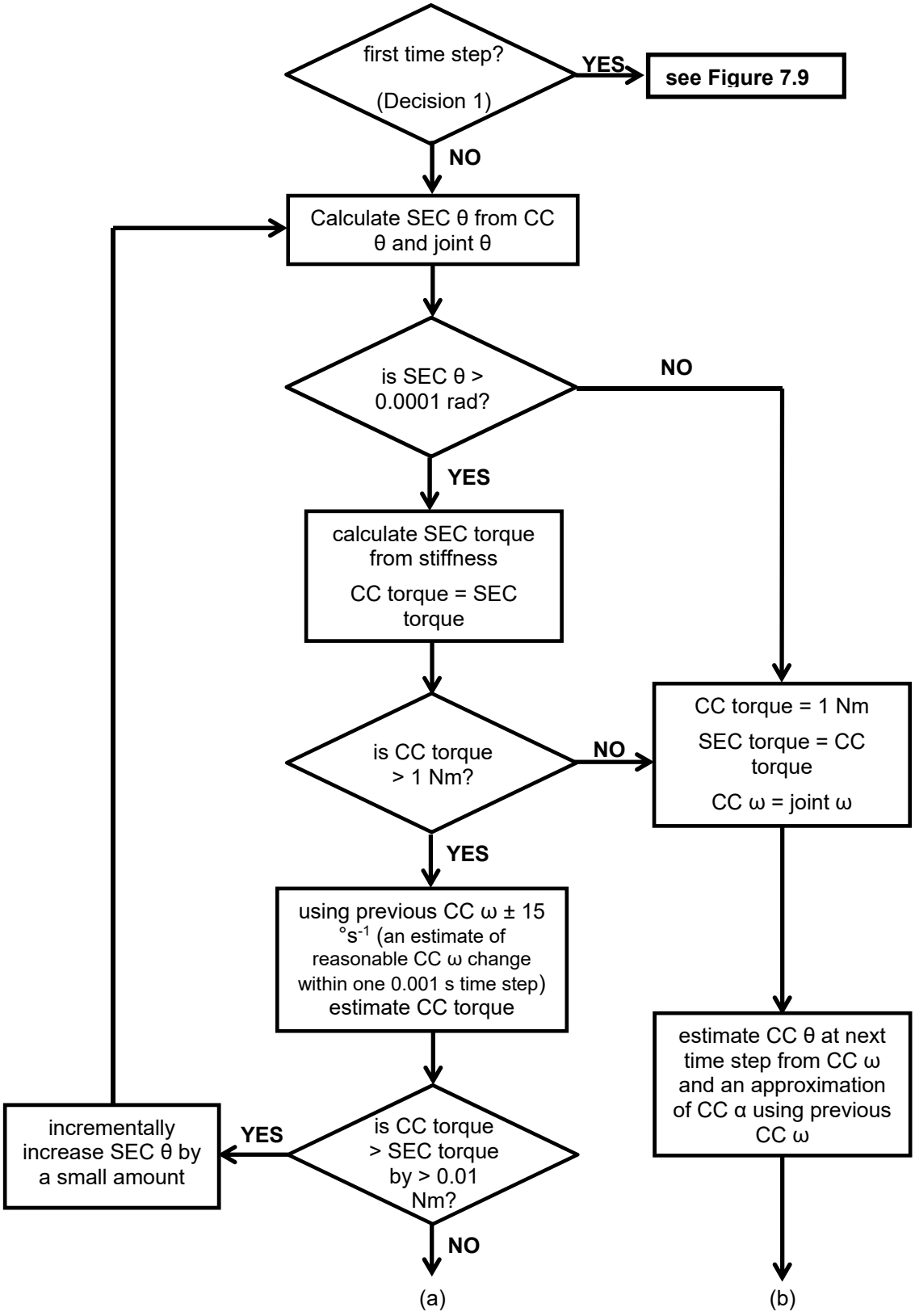

Figure 7.10. Simulation model work flow diagram; part 3.

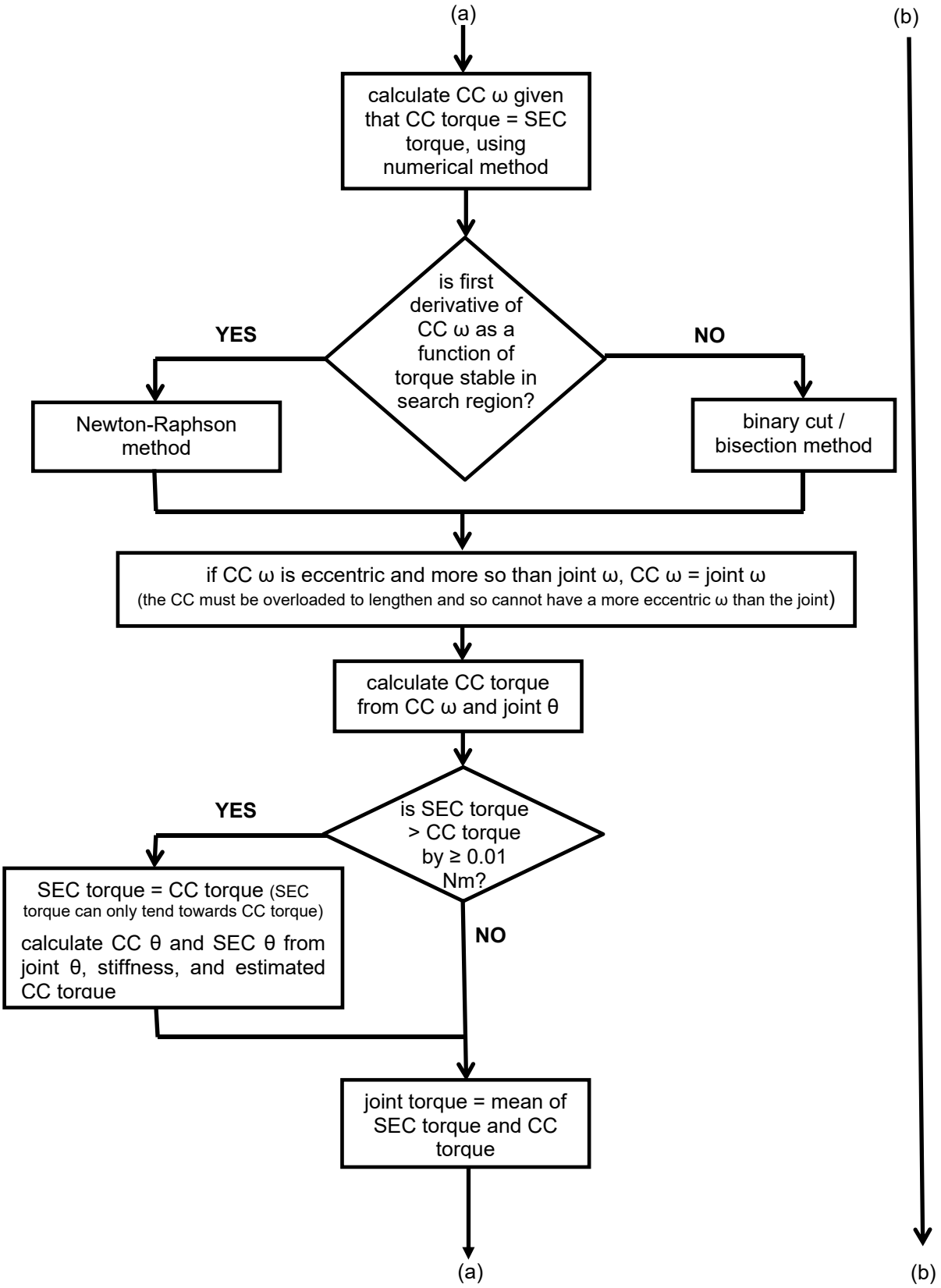

Figure 7.11. Simulation model work flow diagram; part 4.

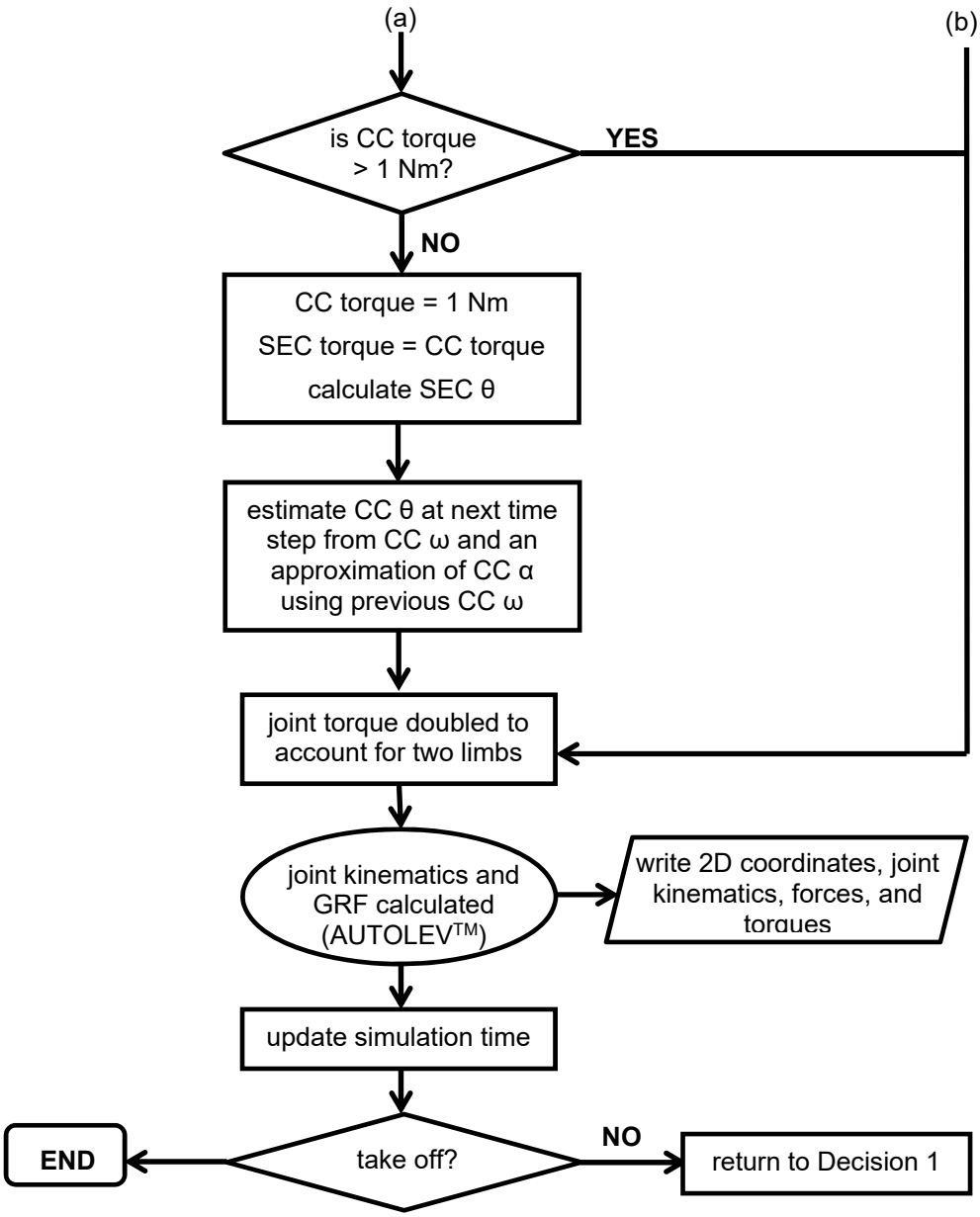

Figure 7.12. Simulation model work flow diagram; part 5

7.5 OPTIMISATION ALGORITHM

To determine model parameters, and to evaluate the simulation model, a matching simulation of a representative drop jumping trial from 0.595 m (the third highest of the four heights recorded experimentally; Section 3.5) was obtained. This trial was selected for a number of reasons: it was felt that parameters determined for a trial from this height would potentially be applicable for future application to the other recorded heights; the trial selected was a maximal performance (jump height = 0.699 m); it had minimal marker loss; and there was minimal out of plane movement (Section 7.3.1).

Four different algorithms were evaluated by van Soest and Casius (2003) on their performance when solving 'hard' optimisation problems. Such an optimisation problem was defined as meeting the following criteria:

- a non-smooth, or even discontinuous, objective function which typically has many local optima;
- an objective function that is available only in implicit form, thus necessitating time consuming simulations to be performed for every function evaluation; and
- an optimisation parameter space that cannot be kept very low even for relatively simple models.

The present simulation model (Section 5) and score function (Section 7.5.3) meet each of these criteria, and so the findings of van Soest and Casius (2003) are of direct relevance. They evaluated four algorithms, namely Downhill Simplex Algorithm, Sequential Quadratic Programming, Genetic Algorithm, and Simulated Annealing Algorithm, for five separate problems. These problems included two musculoskeletal performance optimisation problems of direct relevance to the present study. All algorithms succeeded in converging to a reasonable optimum in a six-parameter vertical jumping problem, although Downhill Simplex Algorithm and Sequential Quadratic Programming struggled with a slightly more complex 16 parameter sprint cycling problem. Genetic and Simulated Annealing Algorithms had no such problem, leading the authors to suggest that both can find global optima in hard optimisation problems.

Simulated annealing algorithms (Kirkpatrick et al., 1983) were developed for combinatorial optimisation problems but have since been extended to solve continuous global optimisation problems (Locatelli, 2000). The algorithms are based upon an analogy with the cooling of a liquid metal. The molecules of a liquid metal move freely at high temperatures but if the temperature is slowly decreased then the thermal mobility of the liquid reduces, and the molecules form a pure crystal, corresponding to the state of minimum energy, or in the case of the algorithm the lowest cost function and therefore the global optimum solution in the algorithm. If the temperature decreases too quickly then the liquid metal forms a polycrystalline or amorphous state with a high energy instead of a pure crystal. This represents a local optimum within the optimisation search space. Based on this physical model, simulated annealing algorithms randomly generate a candidate point at each iteration and decide whether to move the candidate point or to stay at the current point for the next iteration, with this process occurring through a random mechanism and controlled by a 'temperature' parameter (Locatelli, 2000).

Genetic algorithms (Holland, 1975), on the other hand, are based upon the Darwinian principle of 'survival of the fittest' and natural evolution (Yang et al., 1998). An initial population of a pre-defined size is created through the random selection of parameters from within the parameter space (between pre-defined lower and upper bounds for each parameter; Section 7.5.2). Each individual set of parameters represent the chromosomes of one individual. Each individual (one set of chromosomes/parameters and so one simulation) is then assigned a fitness value through an objective function (Section 7.5.3). Fit individuals (those simulations with the greatest fitness values) are selected to pass on their chromosomes to the next generation, while less fit individuals die off. This process of generating the next generation of individuals occurs through three possible operations of selection of the chromosomes, crossover of the chromosomes, or indeed mutation of the chromosomes. The process is repeated for a pre-defined number of generations, or until a global optimum is found.

Simulated annealing has been shown to be capable of providing very high reliability when minimising multimodal functions, albeit at a high computational cost and one which increases linearly with the number of problem dimensions (Corana et al., 1987). One advantage of Genetic Algorithm over Simulated Annealing Algorithm,

however, is the ease with which it can be parallelised, enabling a substantial reduction in computer processing time and thus speeding the optimisation process considerably. For this reason, the matched simulation in the present study was obtained using a parallelised genetic algorithm (Carroll, 2001; van Soest & Casius, 2003). The parallelised optimisation ran on 6 computer nodes of 12 processors each (a total of 72 processors simultaneously, reducing real world optimisation time) for ten thousand generations, each with a population size of 360 individuals.

7.5.1 PARAMETERS VARIED

A total of 133 parameters were varied within the Genetic Algorithm optimisation. These consisted of nine ground contact viscoelastic parameters, six wobbling mass viscoelastic parameters, ten compliant joint viscoelastic parameters, three touchdown velocity parameters, and 105 joint torque activation parameters.

Ground contact viscoelastic parameters

The nine ground contact viscoelastic parameters (Section 5.4.4) varied were:

- Toe and MTP vertical linear stiffness ($k_{z1,i}$ in Equation 5.3);
- Toe and MTP vertical non-linear stiffness ($k_{z2,i}$ in Equation 5.3);
- Toe and MTP vertical damping ($c_{z,i}$ in Equation 5.3);
- Heel vertical linear stiffness ($k_{z1,i}$ in Equation 5.3);
- Heel vertical non-linear stiffness ($k_{z2,i}$ in Equation 5.3);
- Heel vertical damping ($c_{z,i}$ in Equation 5.3);
- Toe, MTP, and heel horizontal linear stiffness (k_{y1} in Equation 5.4);
- Toe, MTP, and heel horizontal non-linear stiffness (k_{y2} in Equation 5.4);
- Toe, MTP, and heel horizontal damping (c_y in Equation 5.4).

Wobbling mass viscoelastic parameters

The six wobbling mass viscoelastic parameters (Section 5.4.5; Equation 5.1) varied were:

- Shank non-linear stiffness ($k_{1,i}$);
- Shank damping ($k_{2,i}$);
- Thigh non-linear stiffness ($k_{1,i}$);
- Thigh damping ($k_{2,i}$);
- Trunk non-linear stiffness ($k_{1,}$);
- Trunk damping ($k_{2,i}$).

Compliant joint viscoelastic parameters

The ten compliant viscoelastic parameters (Section 5.4.2; Equation 5.1) varied were:

- Ankle non-linear stiffness ($k_{1,i}$);
- Ankle damping ($k_{2,i}$);
- Knee non-linear stiffness ($k_{1,i}$);
- Knee damping ($k_{2,i}$);
- Hip non-linear stiffness ($k_{1,i}$);
- Hip damping ($k_{2,i}$);
- Mid-trunk non-linear stiffness ($k_{1,i}$);
- Mid-trunk damping ($k_{2,i}$);
- Shoulder non-linear stiffness ($k_{1,i}$);
- Shoulder damping ($k_{2,i}$).

Touchdown velocity parameters

The three touchdown (initial condition) velocities (Section 7.4) varied were:

- Vertical whole-body centre of mass velocity;
- Horizontal whole-body centre of mass velocity;
- Orientation angular velocity.

Joint torque activation parameters

The 105 joint torque activation parameters (Section 5.4.10) varied by the genetic algorithm consisted of seven parameters independently for each of the following fifteen joint torque generators (Section 5.4.7):

- MTP flexion;
- MTP extension;
- ankle dorsiflexion;
- monoarticular ankle plantar flexion;
- biarticular ankle plantar flexion;
- monoarticular knee flexion;
- biarticular knee flexion / hip extension;
- monoarticular knee extension;
- biarticular knee extension / hip flexion;
- monoarticular hip flexion;
- monoarticular hip extension;
- shoulder flexion;
- shoulder extension;
- elbow flexion;
- elbow extension.

For each of the above joint torque generators, the following seven activation parameters (Section 5.4.10) were varied:

- initial activation level, a_0;
- primary ramp start time, ts_1;
- primary ramp duration, tr_1;
- primary ramp final activation level, a_1;
- activation plateau duration, tp;
- secondary ramp duration, tr_2;
- secondary ramp final activation level, a_2.

The secondary ramp start time, ts_2, utilised in the activation timing explanation of Section 5.4.10 was calculated as the sum of ts_1, tr_1, and tp. This ensured that parameters for both the primary and secondary activation ramp could be varied

independently within the genetic algorithm without resulting in times for ts_2 that were before the primary ramp had concluded.

7.5.2 PARAMETER BOUNDS

Lower and upper bounds were specified for each of the 133 varied parameters. Wherever possible these were based upon either experimental data on the present subject or values from the literature.

Ground contact viscoelastic parameters

Bounds were placed around the foot-ground interface viscoelastic parameters based upon knowledge of similar parameters used in previous whole-body forward-dynamics simulation models, as well as the magnitudes of experimental ground reaction forces and horizontal foot displacement in the present study and realistic levels of foot-ground compression (Section 2.4.1 and Section 7.5.4). The bounds were deliberately wide (Table 7.2) to enable the optimisation algorithm to find the combination of parameters that provided the best match between experimental and simulation performances and ground reaction forces.

Table 7.2. Ground contact viscoelastic parameter bounds

parameter	units	lower bound	upper bound
toe and MTP vertical linear stiffness	$N\ m^{-1}$	30	5×10^5
toe and MTP vertical non-linear stiffness	$N\ m^{-2}$	1000	5×10^6
toe and MTP vertical damping	$N\ s\ m^{-1}$	1000	7×10^6
heel vertical linear stiffness	$N\ m^{-1}$	30	5×10^5
heel vertical non-linear stiffness	$N\ m^{-2}$	1000	5×10^6
heel vertical damping	$N\ s\ m^{-1}$	1000	7×10^6
foot-ground horizontal linear stiffness	$N\ m^{-1}$	0.01	150
foot-ground horizontal non-linear stiffness	$N\ m^{-2}$	400	1500
foot-ground horizontal damping	$N\ s\ m^{-1}$	100	5×10^5

Wobbling mass viscoelastic parameters

As with the viscoelastic parameters at the foot-ground interface above, and for the same reasons, wide bounds (Table 7.3) were placed around the wobbling mass viscoelastic parameters based upon knowledge of similar parameters used in previous whole-body forward-dynamics simulation models, as well as the magnitudes of experimental soft tissue displacement relative to the underlying bone in the present study (Section 7.5.4) and realistic levels of wobbling mass displacement (Section 2.4.1 and Section 7.5.4).

Table 7.3. Wobbling mass viscoelastic parameter bounds

parameter	units	lower bound	upper bound
shank non-linear stiffness	N m^{-3}	9 x 10^6	2.5 x 10^7
shank damping	N s m^{-1}	1500	4500
thigh non-linear stiffness	N m^{-3}	100	1x10^6
thigh damping	N s m^{-1}	1000	7500
trunk non-linear stiffness	N m^{-3}	5 x 10^5	2 x 10^6
trunk damping	N s m^{-1}	1500	6000

Compliant joint viscoelastic parameters

As previous whole-body simulation studies have not included spring-dampers within their representations of joint structures, the bounds around the viscoelastic parameters at these spring-dampers in the genetic algorithm optimisation of the present study (Table 7.4) were determined loosely based upon knowledge of experimentally recorded ground reaction forces and realistic joint compression limits (Section 2.4.1 and Section 7.5.4), as well as a trial and error process in initial pilot simulations.

Table 7.4. Compliant joint viscoelastic parameter bounds

parameter	units	lower bound	upper bound
ankle non-linear stiffness	N m^{-3}	2 x 10^8	1 x 10^9
ankle damping	N s m^{-1}	4000	2 x 10^4
knee non-linear stiffness	N m^{-3}	1.3 x 10^{10}	3 x 10^{10}
knee damping	N s m^{-1}	2000	1 x 10^4
hip non-linear stiffness	N m^{-3}	1 x 10^9	1.3 x 10^{10}
hip damping	N s m^{-1}	1000	1.2 x 10^4
mid-trunk non-linear stiffness	N m^{-3}	1 x 10^7	7 x 10^7
mid-trunk damping	N s m^{-1}	1500	5000
shoulder non-linear stiffness	N m^{-3}	5 x 10^8	3 x 10^9
shoulder damping	N s m^{-1}	2500	7500

Touchdown velocity parameters

To compensate for errors in the tracking of retroreflective markers, the calculation of subject-specific segmental inertia parameters, and hence the calculation of whole-body centre of mass positions and/or orientation and their respective velocities, small variations were allowed in the whole-body kinematics at touchdown from those previously determined (Section 7.3.1; Yeadon & King, 2002; Wilson et al., 2006). Whole-body centre of mass vertical and horizontal velocities at touchdown could vary by ± 0.1 ms^{-1} and the orientation angular velocity by ± 0.1 $rad \cdot s^{-1}$.

Joint torque activation parameters

Initial activation levels at touchdown were constrained to be no more than 0.5, and the first ramp in activation level could begin up to 50 ms prior to touchdown, providing activation did not exceed the 0.5 touchdown threshold. Ramp time durations were constrained to be no less than 70 ms (Freund & Büdingen, 1978; Bobbert and van Zandwijk, 1999). All other activation levels could vary between zero and one.

7.5.3 SCORE FUNCTION

For each simulation, a score was determined via an objective function comprising five components, adapted from Wilson et al. (2006), each calculated from the difference between simulation and experimental performance for the selected drop jump from 0.595 m (Section 7.5):

- S_{ori} = score for difference in orientation angle;
- S_{ang} = score for differences in joint configuration angles;
- S_{grf} = score for differences in ground reaction forces;
- S_{tgc} = score for difference in time duration of ground contact;
- S_{jh} = score for difference in jump height.

S_{ori} was calculated as the overall RMS difference in trunk orientation angle in degrees (1° = a score of 1%). Similarly, S_{jh} was the difference in cm (1 cm = a score of 1%) between experimental and simulation jump height (simulation jump height determined from whole-body mass centre height and vertical velocity at take off using constant acceleration). For S_{tgc}, 10 ms was given a difference score of 1%. The calculation of S_{ang} and S_{grf} were more complex and multifactorial.

An RMS difference between joint angle in degrees was determined at each of the MTP (RMS_{mtp}), ankle (RMS_{ank}), knee (RMS_{kne}), hip (RMS_{hip}), shoulder (RMS_{sho}), and elbow (RMS_{elb}) joints. S_{ang} was hence determined by taking the overall RMS of these individual angle component differences (1° = a score of 1%):

$$S_{ang} = \sqrt{\frac{RMS_{mtp}{}^2 + RMS_{ank}{}^2 + RMS_{kne}{}^2 + RMS_{hip}{}^2 + RMS_{sho}{}^2 + RMS_{elb}{}^2}{6}} \quad (7.1)$$

Combining the individual component angle differences utilising an RMS in this way reduces the chance of any one component being neglected during the optimisation process and increases the chances of a similar level of match being found at each joint.

Likewise, the S_{grf} was comprised of two constituent parts, one for the anterior-posterior horizontal ground reaction force ($S_{grf,y}$) and one for the vertical ground reaction force ($S_{grf,z}$). The vertical component was itself determined by the following function:

$$S_{grf,z,peak} = \sqrt{\frac{S_{tpeak}{}^2 + S_{Fpeak}{}^2}{2}}, \quad (7.2)$$

where S_{tpeak} is the difference in timing of peak ground reaction force. Each 10 ms difference was given a score of 1%, weighting such a difference equivalently to a 1° error in angle measures. S_{Fpeak} is the absolute difference in peak vertical ground reaction force, as a percentage of peak vertical ground reaction force. This combined peak force-related score was then combined with the overall RMS difference in vertical ground reaction force, again as a percentage of peak vertical ground reaction force ($S_{grf,z,RMS}$):

$$S_{grf,z} = \sqrt{\frac{S_{grf,z,peak}{}^2 + S_{grf,z,RMS}{}^2}{2}} \quad (7.3)$$

The horizontal component ($S_{grf,y}$) was simply an RMS difference between simulation and performance anterior-posterior ground reaction force, expressed as a percentage of peak vertical ground reaction force. Expressing both vertical and horizontal differences as a percentage of peak vertical force ensures that the same absolute difference (in N) receives the same score (in %) for both directions and prevents an optimisation procedure that favours a closer horizontal ground reaction force match due to the lower peak force in that direction. Finally, the horizontal and vertical ground reaction force score components were combined, again using an RMS to decrease chances of either being neglected during the optimisation process:

$$S_{grf} = \sqrt{\frac{{S_{grf,y}}^2 + {S_{grf,z}}^2}{2}} \tag{7.4}$$

The overall score for each simulation was calculated as the overall RMS of each of the five components listed at the beginning of this section (Equation 7.5). Components were thus weighted equally, with one degree of difference in angular measures or one centimetre of difference in linear measures considered comparable to a one percent difference in the other measures (Wilson et al., 2006).

$$score = \sqrt{\frac{{S_{ori}}^2 + {S_{ang}}^2 + {S_{grf}}^2 + {S_{tgc}}^2 + {S_{jh}}^2}{5}} \tag{7.5}$$

7.5.4 PENALTY FUNCTIONS

Penalties were implemented in the score function to limit spring-damper displacements within the model to realistic levels, as well as penalising simulations in which any joint exceeded its anatomical range of motion, or in which the foot temporarily left the ground prior to the take off conditions being met (Section 7.4). The score for an individual simulation was increased in proportion to the magnitude in which certain thresholds were exceeded for each of these conditions, as outlined below.

Premature take off penalty

As stated in Section 7.4, each simulation was terminated at the first time point after 0.2 s at which all three points of contact on the foot were at a vertical height of greater than zero. For every 0.001 s prior to 0.2 s that the vertical ground reaction force was equal to zero (i.e. all three contact points of the foot were above the ground) prior to the initiation of the take-off criteria (at 0.2 s) a value of 1.0 was added to the score for that simulation. Premature take off was already penalised through the score component attributed to time of ground contact, while this additional penalty discriminated against simulations in which the feet temporarily left the ground early in the simulation.

Joint range of motion penalty

A penalty value of 1.0 was added to the objective score function for each degree by which any of the joints in the model exceeded the pre-determined anatomical range of motion displayed in Table 7.5.

Table 7.5. Joint range of motion limits

joint	lower angle limit (°)	upper angle limit (°)
MTP	80	170
ankle	70	170
knee	45	180
hip	45	200
shoulder	-60	150
elbow	20	180

Horizontal foot-ground displacement penalty

During experimental drop jumping trials (Section 3.5), the maximum observed horizontal displacement of toe, MTP joint centre, or heel whilst that point was in

contact with the ground was 2.28 cm. As discussed in the literature review of Section 2.4.1, Dai et al. (2006) utilised a 3D finite element model to demonstrate that foot slippage displacement inside a shoe of 2.0 mm was possible during sockless shod walking, with 3.7 mm of displacement inside the shoe possible when socks were worn, regardless of the sock-skin frictional properties. The subject in the present study was sockless, however the magnitudes of impact ground reaction forces experienced were much greater than those during walking. The maximum observed foot displacement inside a shoe of 0.37 cm was therefore added to the 2.28 cm of horizontal shoe displacement in the present study to define a limit of 2.65 cm. For every millimetre of horizontal foot displacement further than 2.65 cm during ground contact, a penalty value of 0.1 was added to the objective score function for that simulation.

Vertical foot-ground deformation penalty

Vertically, the spring-damper at the MTP joint and the toe were considered representative of foot-shoe-ground interactions, whilst that at the heel also incorporated the additional compliance due to heel pad deformation. Kinoshita et al. (1993; discussed in Section 2.4.1) reported 9.3 mm and 11.5 mm sports shoe sole deformations under free-fall impact testing at the centre of the heel portion for five cycles from 30 mm and 50 mm drop height conditions respectively. In the present study, the greater deformation of 11.5 mm was taken as an upper limit for shoe-ground deformation and so for every mm of further vertical foot-ground deformation beyond this limit at the MTP and toe, a penalty value of 0.1 was added to the objective score function for that simulation. Penalties were applied independently for each foot contact point.

Of the numerous heel pad deformation studies discussed in Section 2.4.1, the greatest observed deformation in a single subject was 12.7 mm, again in the study of Kinoshita et al. (1993). Values of around this magnitude appear to represent a physiological maximum, with no further increase in deformation with increases in ground reaction force. As such, the 12.7 mm for the heel pad was added to the 11.5 mm for the shoe-ground interaction to create a penalty threshold of 24.2 mm

for vertical heel-ground compression in the simulation model. For every mm of compression beyond this limit, a penalty of 0.1 was added to the score.

Wobbling mass displacement penalty

Recent work (see Section 2.4.1) has quantified shank soft tissue mass centre displacement during drop landings from 0.30 m and 0.45 m using fifty-six 6.4 mm markers positioned around the shank (Furlong et al., 2016). However, equivalent data were not available for the thigh and trunk. Because the present subject was a lean individual, maximum observed displacements were unlikely to be representative of this subject and so absolute limits of shank soft tissue displacement were determined to be the mean of the average and maximum observed values of Furlong et al. (2016) from the greatest drop height of 0.45 m. Calculating a resultant of displacements in the three separately reported planes resulted in a shank wobbling mass displacement limit of 38 mm. As with the spring-dampers at the foot-ground interface, a penalty of 0.1 was added to the score function for each mm of displacement beyond this limit in any simulation.

A comparison between the above limit, determined from a thorough segment-specific investigation of fifty-six markers, and the displacement of three reflective markers positioned over the shank soft tissue during the experimental trials of the present thesis (Section 3.4.2) would provide a scale factor that could be used to convert measured marker displacements at the thigh and trunk into maximum possible segmental soft tissue mass centre displacements. It was therefore necessary to conduct an analysis of the retroreflective markers positioned over the soft tissue in all three of these areas during the experimental drop landing trials.

Resultant soft tissue marker displacements from two dimensions (longitudinal and perpendicular) were calculated in the local coordinate system of the rigid segment relative to their position in static standing trials (Figure 7.13). It was noted that the soft tissue and hence these retroreflective markers move relative to the underlying rigid segment during a very slow and controlled squatting movement with no impact force or shock wave present due to gravitational and inertial effects. Furthermore, the fact that these markers had not been filtered (Section 7.3.1), or indeed gap filled, meant that the presence of high frequency noise within the marker displacement

signals remained. Thus, it was necessary to separate out the marker displacement in the rigid segment's coordinate system due to the impact shock wave from that due to voluntary movement, electrical noise, or tracking errors. As such, a power spectral density analysis was performed on the displacement data, following the same procedure as for accelerometer data in Section 4.3.2, and when determining filtering cut-off frequencies in Section 7.3.1. From the frequency-amplitude (Figure 7.14) and power spectral density (Figure 7.15) plots it was decided to band-pass filter the resultant displacements between 9 and 23 Hz in an attempt to remove the influence of voluntary movement, electrical noise, or tracking errors (Figure 7.16).

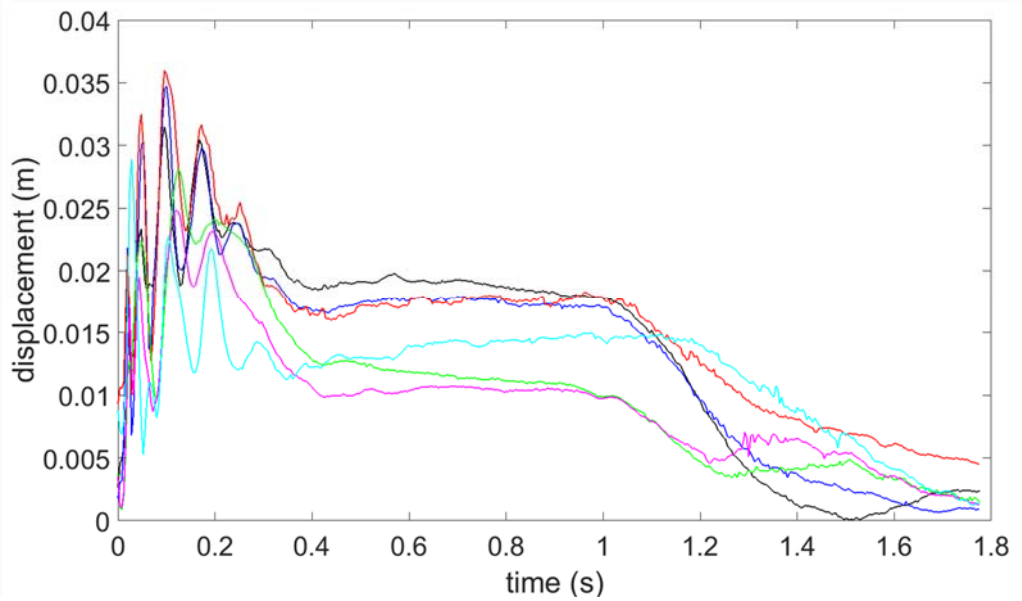

Figure 7.13. Resultant shank and thigh wobbling mass marker displacements relative to underlying segment for a drop landing from 0.74 m. Black = lateral posterior shank; dark blue = posterior shank; red = medial posterior shank; green = anterior thigh; pink = lateral thigh; light blue = posterior thigh.

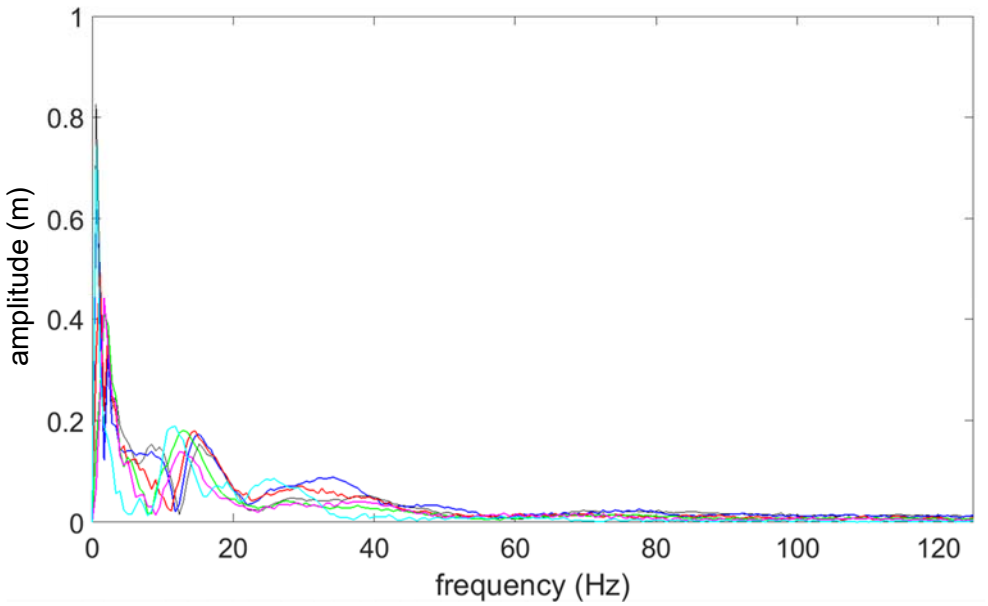

Figure 7.14. Frequency-amplitude plot of resultant shank and thigh wobbling mass marker displacements relative to underlying segment for a drop landing from 0.74 m. Black = latero-posterior shank; dark blue = posterior shank; red = medio-posterior shank; green = anterior thigh; pink = lateral thigh; light blue = posterior thigh.

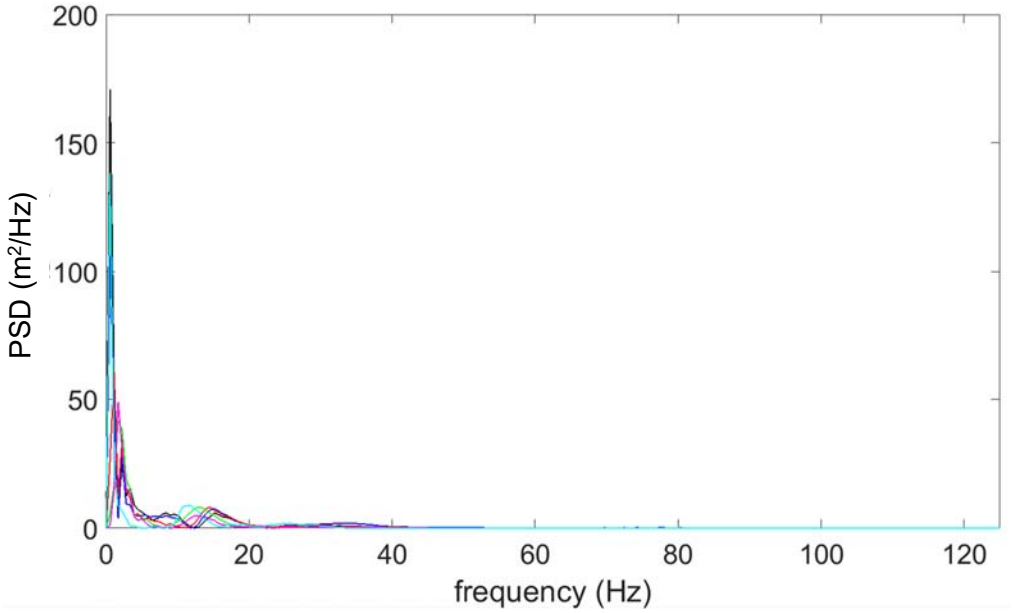

Figure 7.15. Power spectral density plot of resultant shank and thigh wobbling mass marker displacements relative to underlying segment for a drop landing from 0.74 m. Black = latero-posterior shank; dark blue = posterior shank; red = medio-posterior shank; green = anterior thigh; pink = lateral thigh; light blue = posterior thigh.

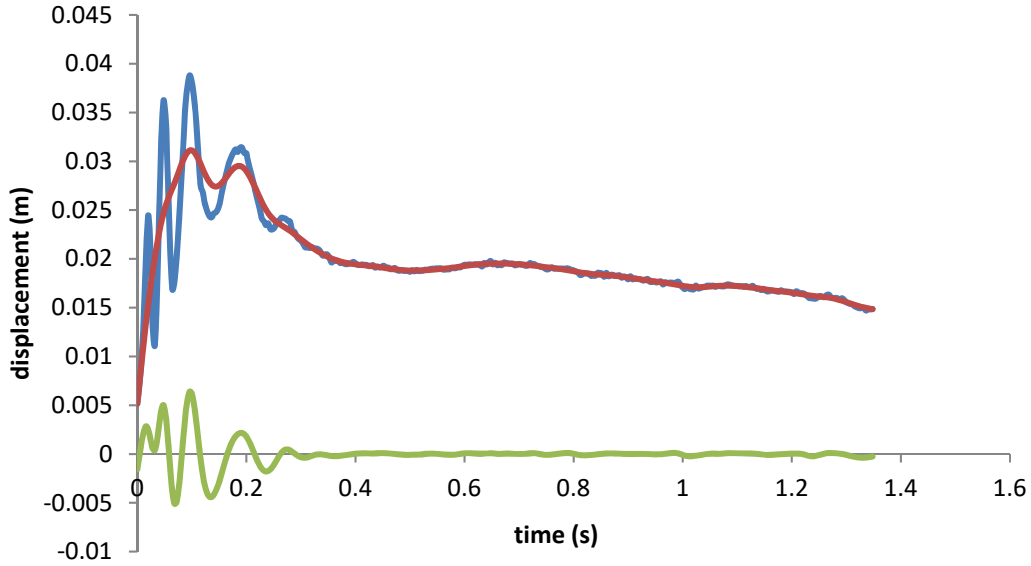

Figure 7.16. Raw posterior shank marker displacement relative to underlying segment (blue) and isolated voluntary movement (red) and impact shock wave (green) related components during a drop landing from 0.74 m.

The blue line on Figure 7.16 highlights the presence of a noisy raw resultant marker displacement. Low-pass filtering at a cut-off frequency of 9 Hz (red line) removes the high frequency noise, seen most clearly in the later part of the signal when the subject is stationary, and also the 'wobble' shortly after landing. This red line shows how the marker would have displaced relative to the underlying segment due to the active movement of the subject alone without the presence of a prior 0.74 m drop landing. Band-pass filtering between 9 and 23 Hz (green line) shows that most of the post-impact 'wobble' was due to frequency components within this range due to the impact shock wave, as with accelerometer data in Chapter 4. Once this component has been damped, the low-pass filtered component follows a similar path to the raw data. The peak impact-related 'additional' displacement, over and above what would have been present without an impact, after band-pass filtering was 9.3 mm at the shank, 12.1 mm at the thigh, 9.5 mm at the abdomen, and 10.0 mm at the chest. Only weak correlations were observed between peak resultant ground reaction force and wobbling mass displacement, with little difference also between drop landings and drop jumps. It was therefore decided to use the above absolute maximum observed displacements in the 9 to 23 Hz range

regardless of the magnitude of impact force experienced. As there was very little difference between the stomach and chest in the present lean subject, the slightly higher stomach value was chosen to represent the entire trunk muscle and adipose mass.

The shank mas centre maximal displacement of 3.8 cm compared with the impact shock wave related 0.9 cm determined above were used to scale the maximal mass centre displacements at the thigh and trunk to 4.9 cm and 4.0 cm respectively. At the trunk, however, it was also necessary to incorporate internal viscera displacement. The assumption of trunk viscera mass as 0.14 x unshod body mass (Ciba Geigy, Scientific Tables; Minetti & Belli, 1994) gave a subject-specific trunk viscera mass of 12.4 kg. Subtracting this from the trunk wobbling segment total mass gave a trunk muscle and adipose mass of 17.5 kg. As discussed in Section 2.4.1, a viscera displacement with a vertical range of 5 cm – 8 cm (Minetti & Belli, 1994) will not displace the entire trunk wobbling mass by 8 cm and will likely be out of sync with the muscle and adipose tissue oscillation. For that reason, the lower value of 5 cm will be used for maximum viscera displacement. A weighted average of 5.0 cm viscera displacement and 4.0 cm muscle/adipose displacement according to their relative masses gives a combined maximal trunk wobbling mass segment displacement of 4.4 cm. As with the shank, each millimetre of wobbling mass displacement beyond 4.9 cm at the thigh and/or 4.4 cm at the trunk will result in a penalty of 0.1 being added to the score function for that simulation.

Compliant joint deformation penalty

The spring-damper at the ankle joint was included to represent in vivo compliance within both the joint itself and the medial longitudinal arch of the foot (Section 2.4.1). Of the studies, discussed in Section 2.4.1, investigating navicular drop and medial longitudinal arch compliance, the greatest observed navicular drop that was calculated in such a way as to not incorporate the effects of heel pad deformation was the 13.4 mm reported by Nielsen et al. (2009). Fragomen et al. (2014) reported that for nine specimens, an average of 4.9 mm of distraction would be required at the ankle joint to provide total unloading during full weight-bearing (700 N). The maximum value for any of the nine specimens was 7.0 mm, although it was

acknowledged by the authors that in vivo, the dynamic load placed on the ankle joint by the tendons, including ankle dorsi flexors and plantar flexors, may increase the load and require greater distraction to unload the joint. The same could be said for greater loads during activities other than ambulation. However, because this value does not relate directly to the magnitude of compression and compliance within the joint, the 7.0 mm was taken as a crude surrogate measure for maximal compression at the joint, with the acknowledgement that the spring-dampers within joints in the simulation model will necessarily incorporate all forms of compliance not included elsewhere at the foot-ground interface or wobbling masses. As such, the 13.4 mm due to the medial longitudinal arch and the 7 mm at the ankle joint resulted in an ankle joint spring-damper deformation limit of 20.4 mm, beyond which a penalty value of 0.1 was added to the objective score function for every further mm of deformation.

Again, little literature is available with regards to the magnitudes of possible compression in and around the knee and hip joints during a high impact. Recognising the fact that the model is necessarily a simplification of reality and each spring-damper will have to accommodate some local compliance that is unaccounted for in the system, joint space measures from the literature were used as a crude surrogate measure for possible compliance. Deep et al. (2003) found a maximum medial tibiofemoral joint space of 7 mm and a maximum lateral tibiofemoral joint space of 8 mm regardless of joint angle. The mean limit of 7.5 mm was used as a threshold value for maximal permissible deformation at the knee and hip joints, with each further mm at either joint again independently resulting in a penalty value of 0.1.

For the spring-damper at the mid-trunk level, Bostock's (2009) method was repeated for the present thesis' experimental data to represent spinal compression. The resultant vector length change between the C7 and L5 vertebra markers was determined for each drop landing and drop jump trial. Bostock (2009) calculated compression as the difference in distance between markers when in a natural standing position and the minimum distance after impact. However, because a standing static trial does not represent true unloaded conditions due to the ground reaction force of one bodyweight, compression was expressed relative to the time frame immediately before impact in the present study. The resultant length change

in three dimensions was used to represent the full extent of spinal compliance and not be distorted by any small out of plane movements. Markers had been filtered prior to this analysis (Section 7.3.1) and so any effects of signal noise or suboptimal marker tracking were minimised. The mean length change in all trials was 17.4 mm, with a standard deviation of 9.4 mm. The maximum observed length change was 31.2 mm during a drop landing from 0.30 m. Values of 29.8 mm and 29.0 mm in a 0.74 m drop landing and a 0.445 m drop jump respectively show that this maximum value was not an outlier, and so 31.2 mm was used as the threshold for the application of penalties. As at other spring-dampers, each further mm of deformation resulted in a penalty of 0.1 being applied.

The spring-damper at the shoulder differed to those at the other joints in that rather than compression within a joint, it represented a passive depression / elevation movement of the shoulder girdle following the impact with the ground. Limits for the displacement of this spring-damper were determined based on experimental data of drop landings and drop jumps collected in Chapter 3 of the present thesis. Firstly, the resultant hip joint centre to shoulder joint centre distance was calculated for each time point during ground contact (Figure 7.17) of each trial, again in three dimensions to represent the true magnitude of displacement and to not be affected by any small out of plane movements. It was necessary to consider the voluntary flexion or extension of the shoulder occurring simultaneously with any passive movement. Therefore, utilising frequency-amplitude (Figure 7.18) power spectral density plots (Figure 7.19), determined as above for the wobbling mass displacements and as with accelerometer signals in Section 4.3.2, it was decided to low-pass filter the hip-to-shoulder distance at a cut off frequency of 5 Hz to isolate low frequency voluntary movement (Figure 7.17).

The maximum offset between overall recorded hip-to-shoulder joint distance, and the low-pass filtered hip-to-shoulder joint distance representative of voluntary displacements only (Figure 7.17) was 10.6 mm during a drop landing from the highest height of 0.74 m. As such this 10.6 mm offset was used as the limit for shoulder spring-damper deformation prior to the application of a 0.1 penalty for each further millimetre of deformation.

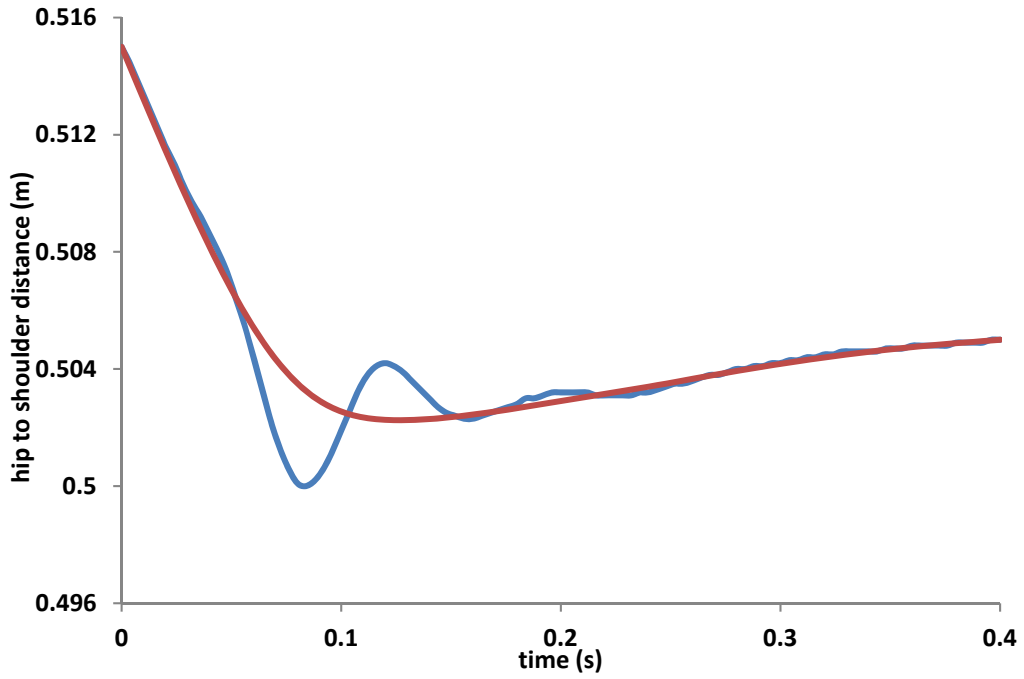

Figure 7.17. Post-impact hip to shoulder distance before (blue) and after filtering to isolate voluntary movement related shoulder displacement (red).

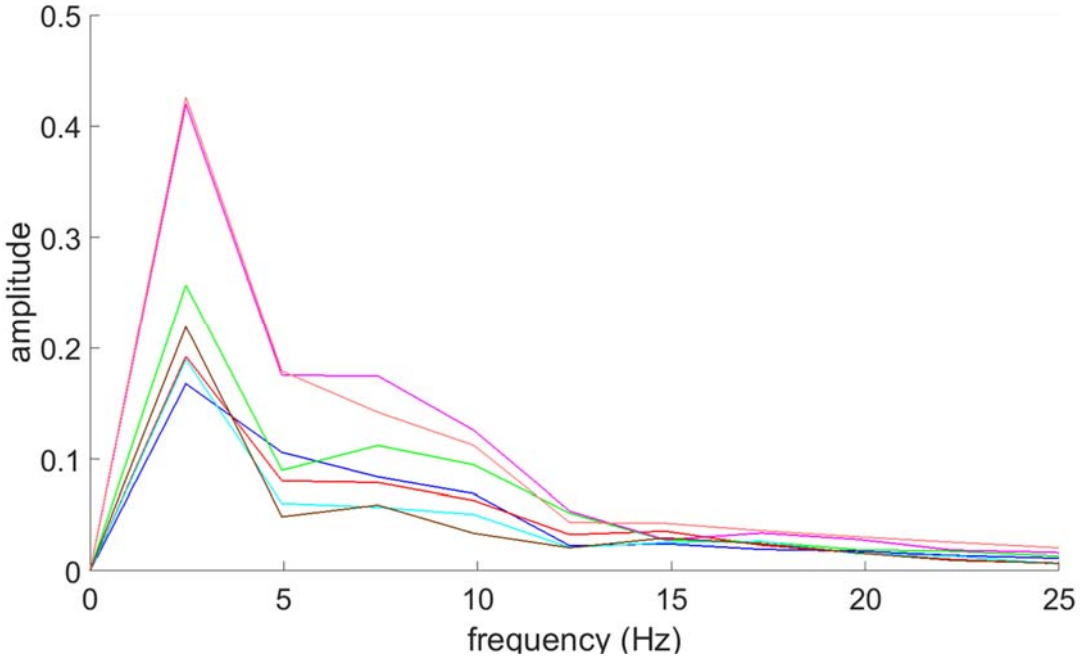

Figure 7.18. Frequency-amplitude plot for hip to shoulder distance during ground contact. Each line represents a different trial.

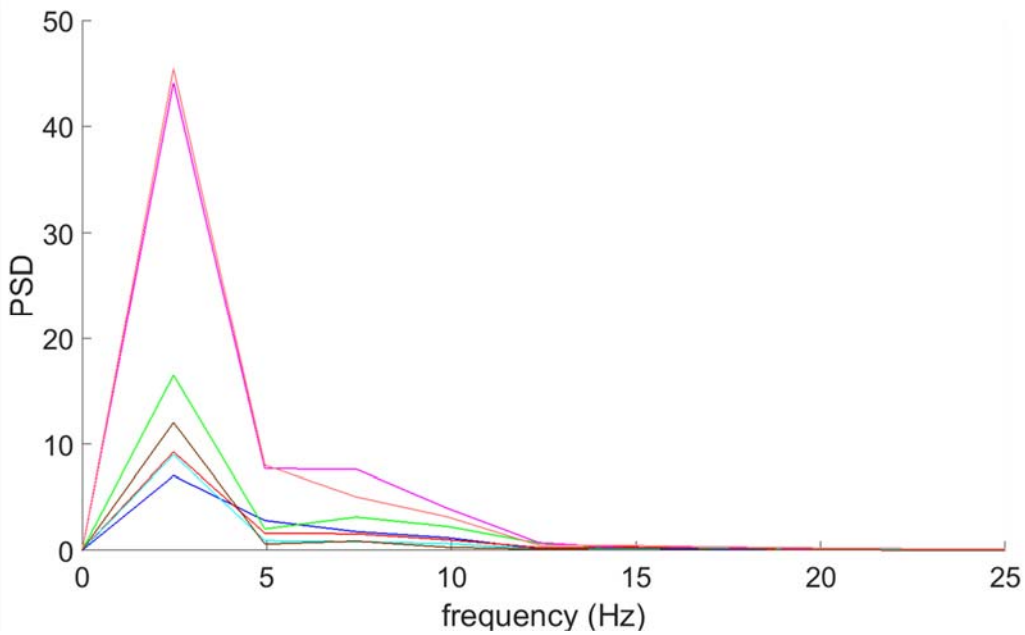

Figure 7.19. Power spectral density plot for hip to shoulder distance during ground contact. Each line represents a different trial.

7.6 JOINT COMPLIANCE FREE MODEL

To evaluate the effects of incorporating compliance within joint structures on simulation model performance and ability to match experimental data, an equivalent model was evaluated without compliance at the joints. This second model was constructed in the same way (Section 5.4), with the same inputs and work flow (Section 7.4), and with parameters determined in the same way (Section 7.5) using the same objective score function (Section 7.5.3). The only difference was that the compliant joint stiffness parameters were set to a number approaching infinite stiffness, and the damping parameters were set to zero. This represented the performance of an equivalent model constructed using frictionless pin joints in the traditional manner, but with the same realistic limits placed on spring-damper deformations elsewhere in the system (Section 7.5.4).

7.7 RESULTS

The genetic algorithm generated an optimal match between the simulation featuring compliant joint structures and 0.595 m drop jump experimental performance data with a final objective score of 3.7% (Table 7.6).

Table 7.6. Optimal compliant simulation objective score function components relative to 0.595 m drop jump experimental performance

component	score (%)
orientation angle RMS difference	2.34
joint angles RMS difference	5.47
ground contact duration difference	0.30
jump height difference	2.34
ground reaction force score	5.08
total score	**3.66**

Experimental and simulation orientation angle time histories are displayed in Figure 7.20. The individual joint angle RMS differences ranged from 2.5° at the knee to 8.0° at the MTP joint (Table 7.7; Figures 7.21 to 7.26). Had the MTP joint not been included in the joint angles score calculation then the score for that component would have been reduced from 5.47° to 4.81°.

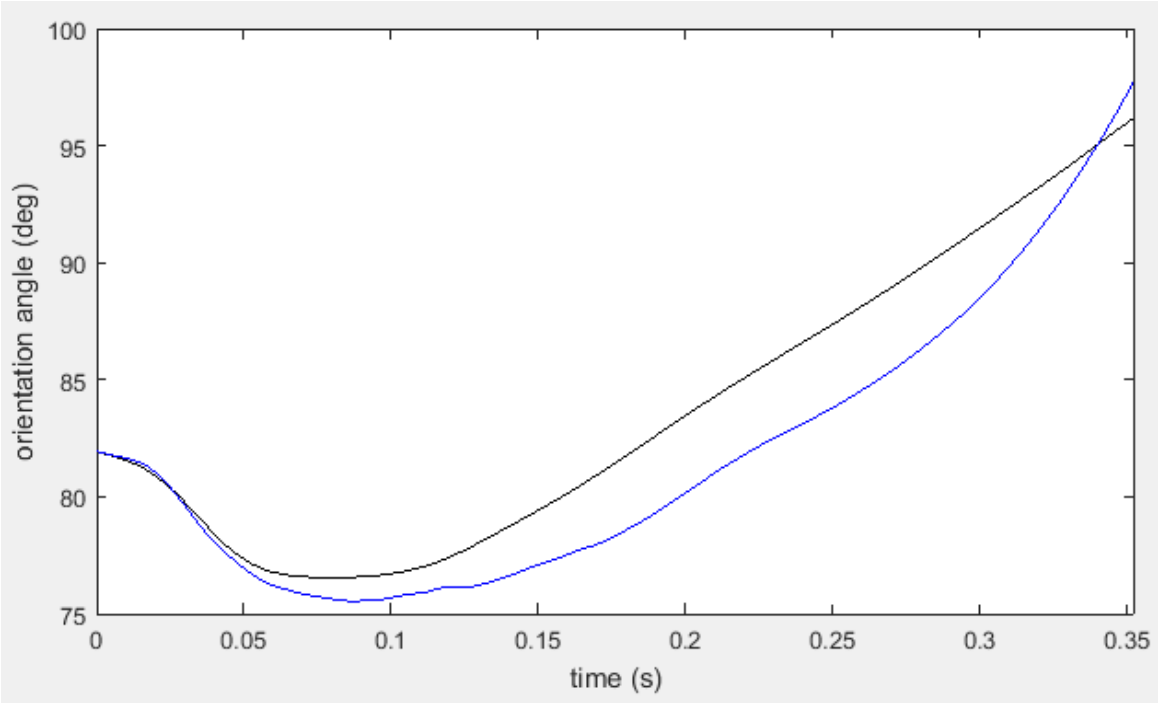

Figure 7.20. Simulation (blue) and experimental (black) orientation angle

Table 7.7. Individual joint angle RMS differences

joint	RMS difference (°)
MTP	8.01
ankle	6.08
knee	2.54
hip	5.38
shoulder	5.41
elbow	3.74
total joint angle RMS score	**5.47**

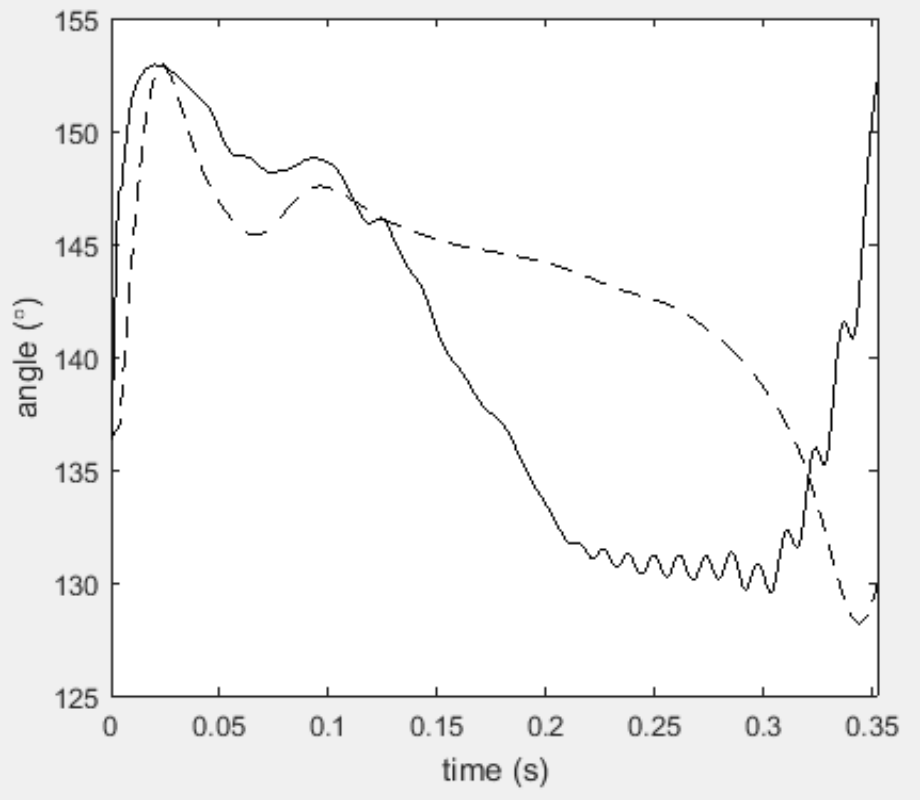

Figure 7.21. Simulation (solid line) and experimental (dashed line) MTP joint angle

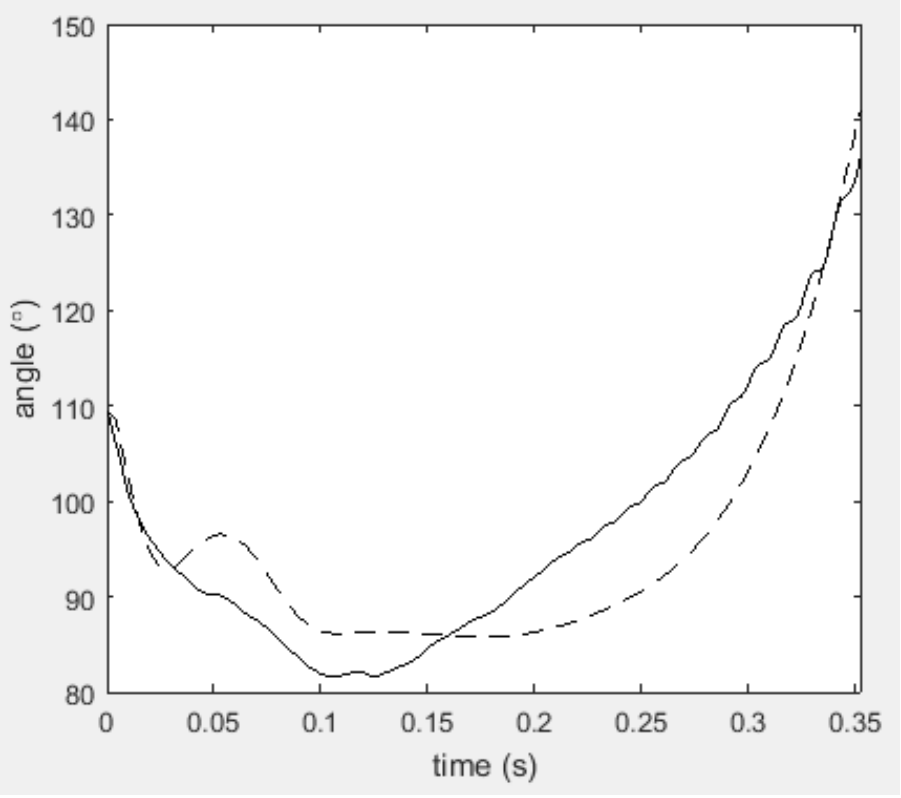

Figure 7.22. Simulation (solid line) and experimental (dashed line) ankle joint angle

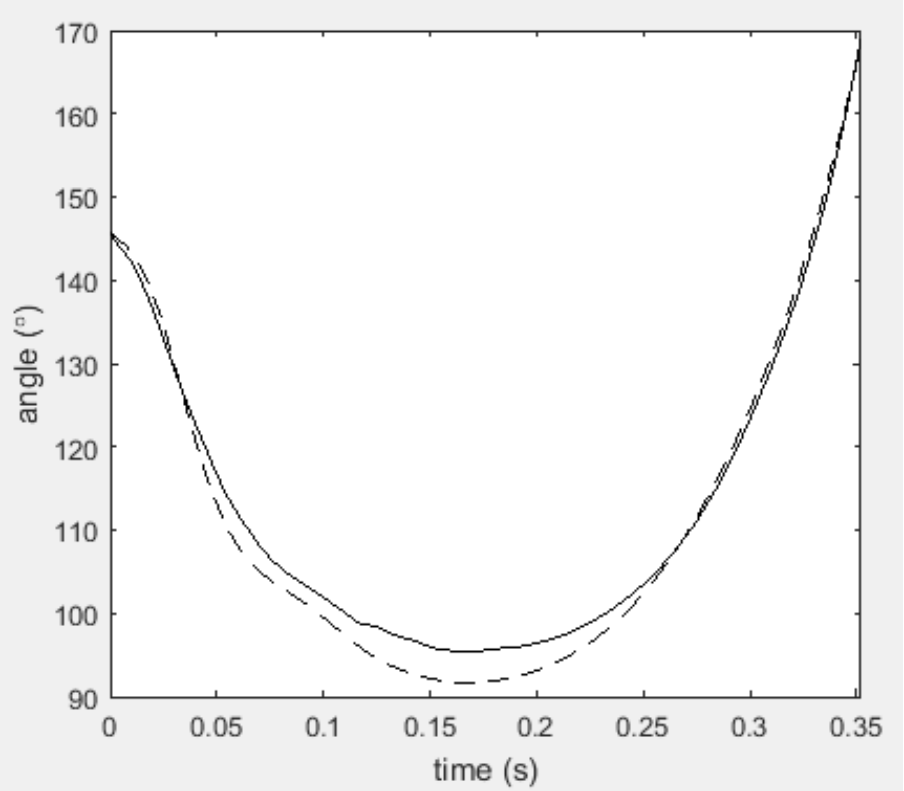

Figure 7.23. Simulation (solid line) and experimental (dashed line) knee joint angle

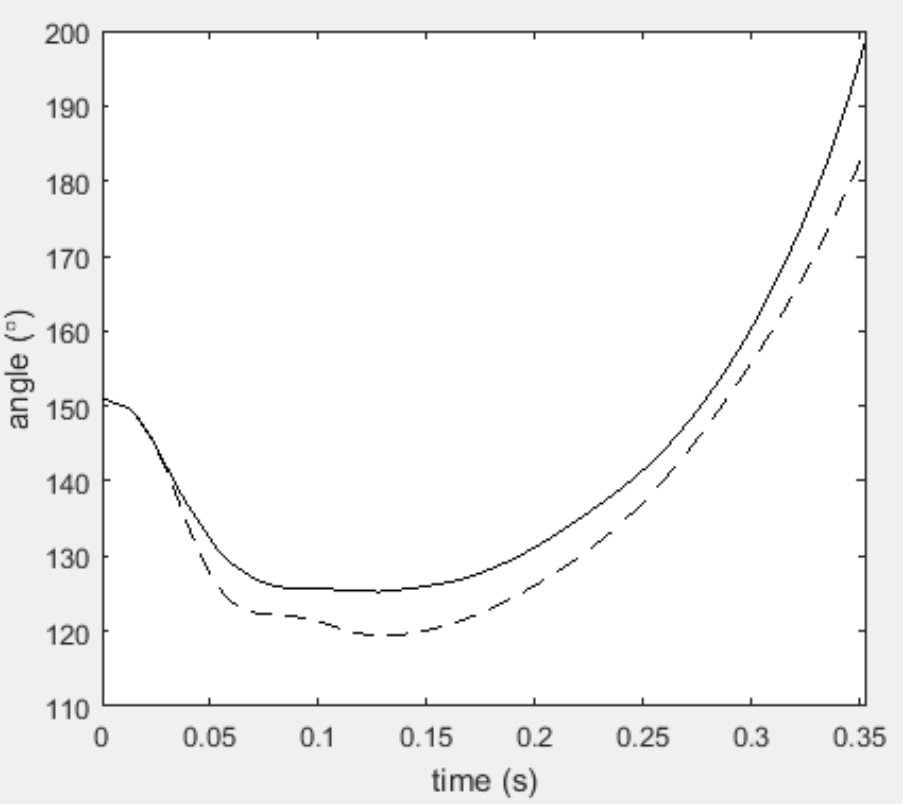

Figure 7.24. Simulation (solid line) and experimental (dashed line) hip joint angle

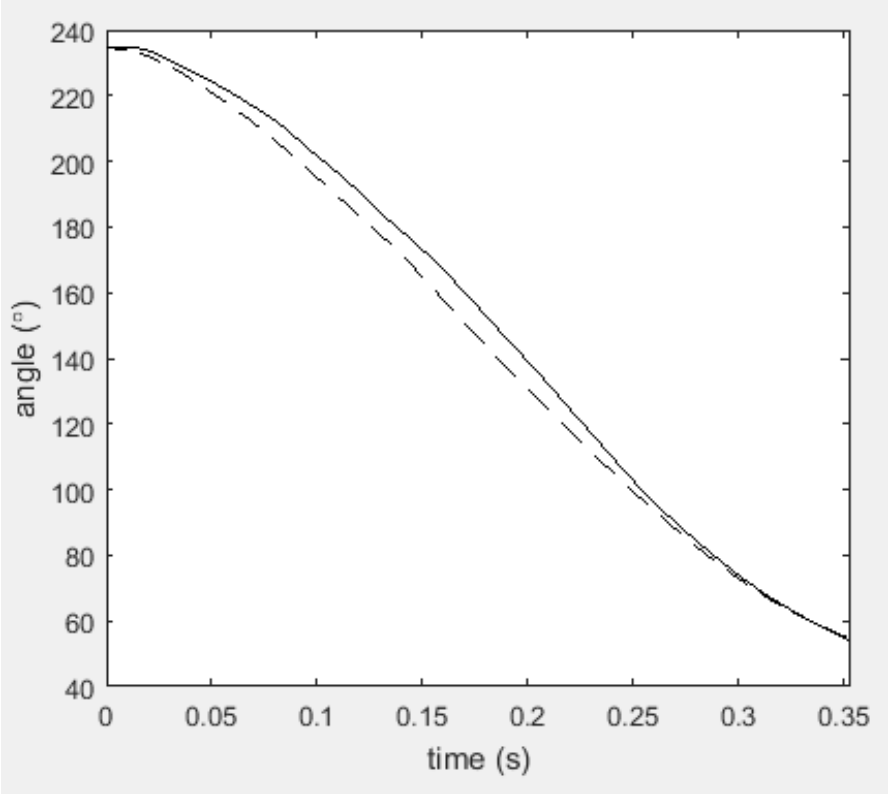

Figure 7.25. Simulation (solid line) and experimental (dashed line) shoulder joint angle

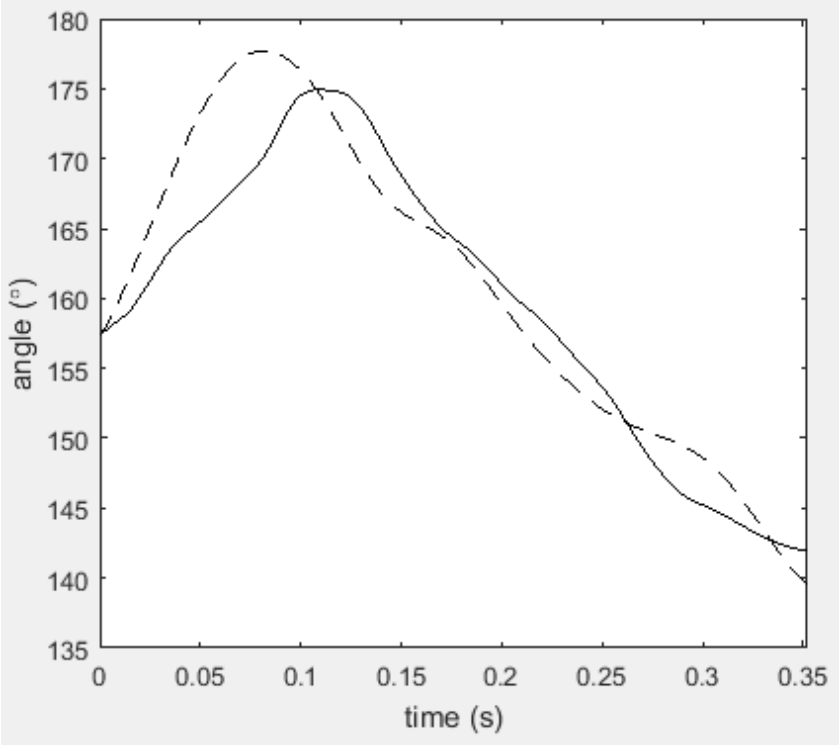

Figure 7.26. Simulation (solid line) and experimental (dashed line) elbow joint angle

Simulation ground contact duration was 0.353 s, only 3 ms shorter than the experimental 0.356 ms. Simulation jump height was 0.676 m, compared with an experimental jump height of 0.699 m.

The ground reaction force score of 5.07% consisted of an anterior-posterior ground reaction force RMS of 3.84% (Figure 7.27) and a vertical ground reaction force RMS difference of 8.53% (Figure 7.28), peak force difference of 0.6%, and timing of peak force difference of 0.011 s.

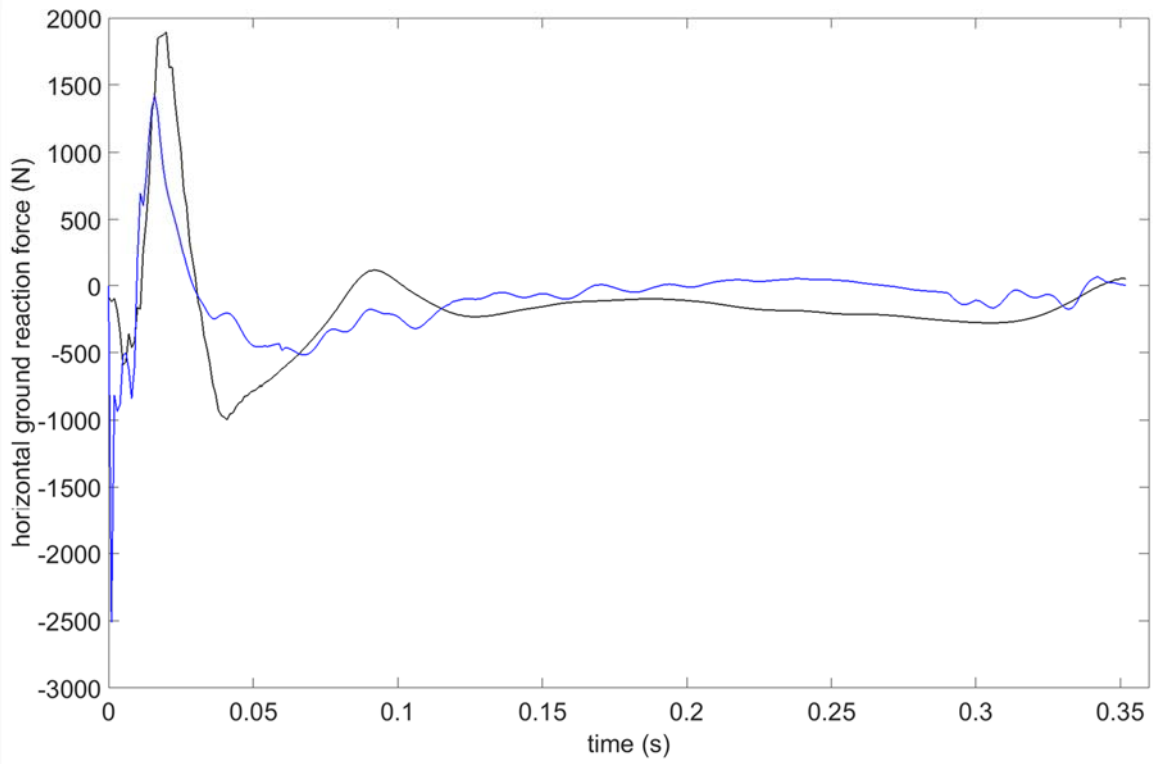

Figure 7.27. Simulation (blue) and experimental (black) horizontal ground reaction force

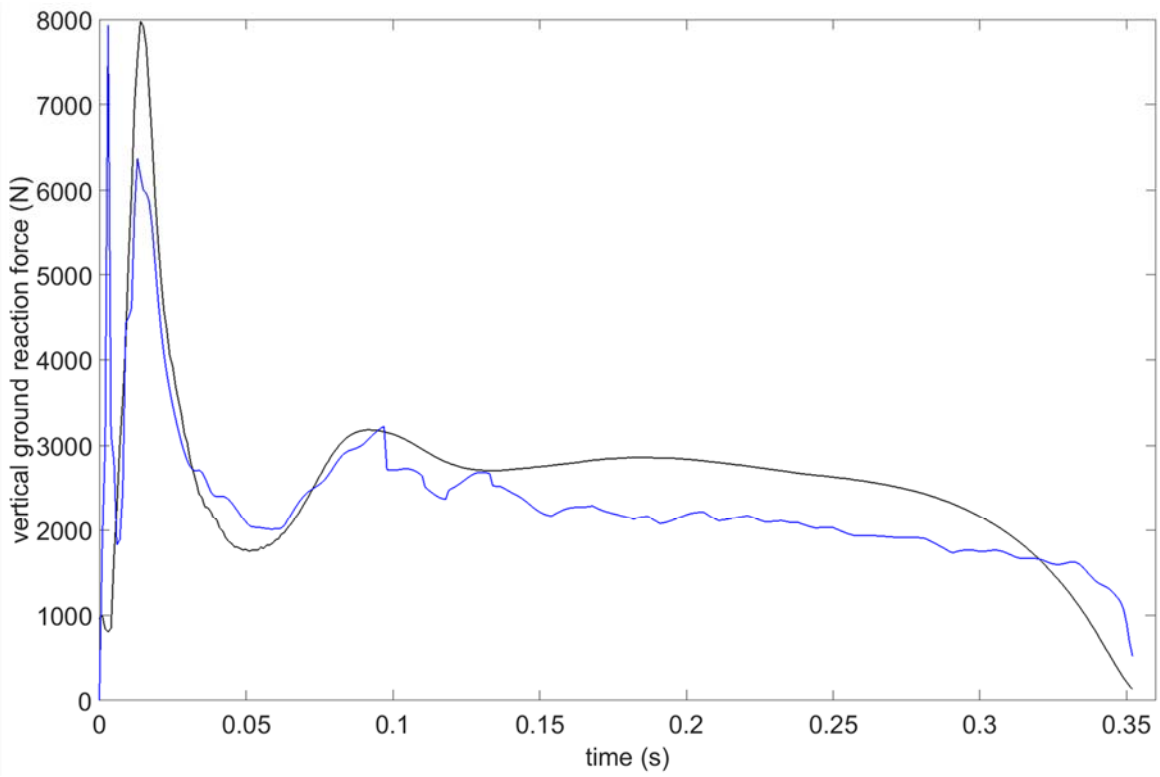

Figure 7.28. Simulation (blue) and experimental (black) vertical ground reaction force

The whole-body configurations of both the subject's experimental performance and the simulation model can be seen and compared periodically throughout the ground contact period in Figure 7.29.

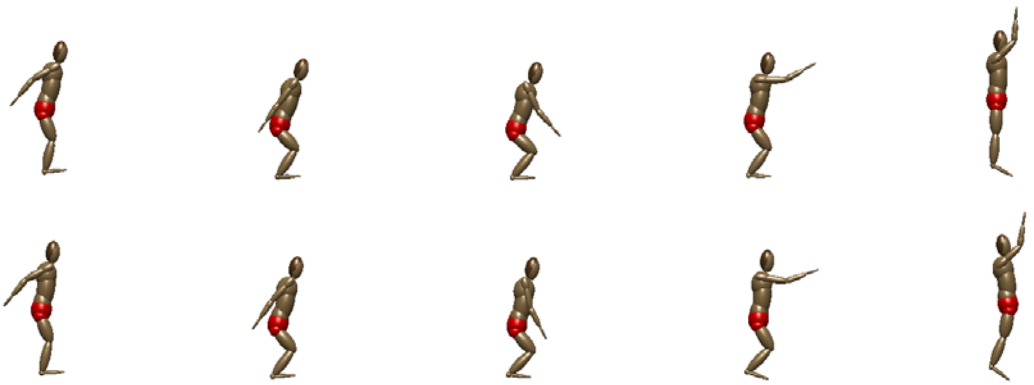

Figure 7.29. Experimental (top) and simulation (bottom) whole-body configuration throughout the period of ground contact.

No penalties were incurred by the optimal matched simulation (Table 7.8), meaning that all spring-damper displacements were within limits (Section 7.5.4; Figures 7.30 and 7.31) and all joints remained within their anatomical ranges of motion (Figures 7.21 to 7.26). Likewise, the foot remained in contact with the ground until the moment of take off.

Table 7.8. Penalty thresholds and simulation values

penalty component	penalty limit (cm)	simulation maximum (cm)
toe horizontal displacement	2.65	0.04
toe vertical compression	1.15	1.15
MTP horizontal displacement	2.65	1.99
MTP vertical compression	1.15	1.04
heel horizontal displacement	2.65	0.00
heel vertical compression	2.42	1.91
ankle deformation	2.04	1.67
knee deformation	0.75	0.57
hip deformation	0.75	0.70
mid-trunk deformation	3.10	2.63
shoulder deformation	1.10	0.86
shank wobbling displacement	3.80	1.47
thigh wobbling displacement	4.90	1.97
trunk wobbling displacement	4.40	3.67

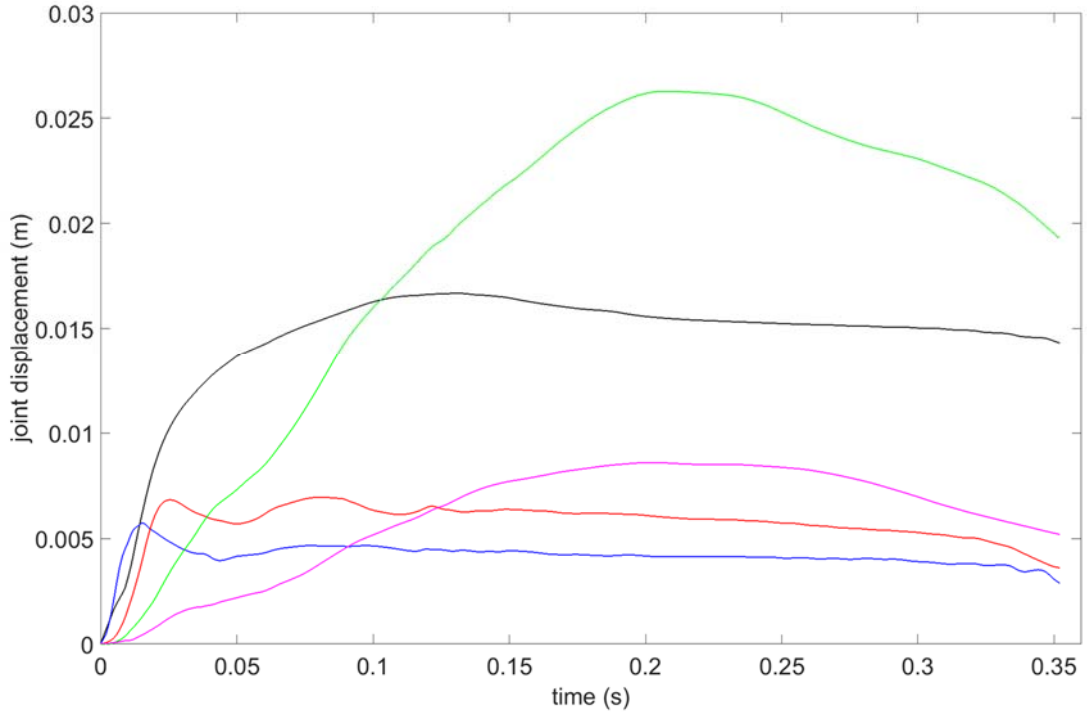

Figure 7.30. Simulation ankle (black), knee (blue), hip (red), mid-trunk (green), and shoulder (pink) spring-damper stretch magnitudes

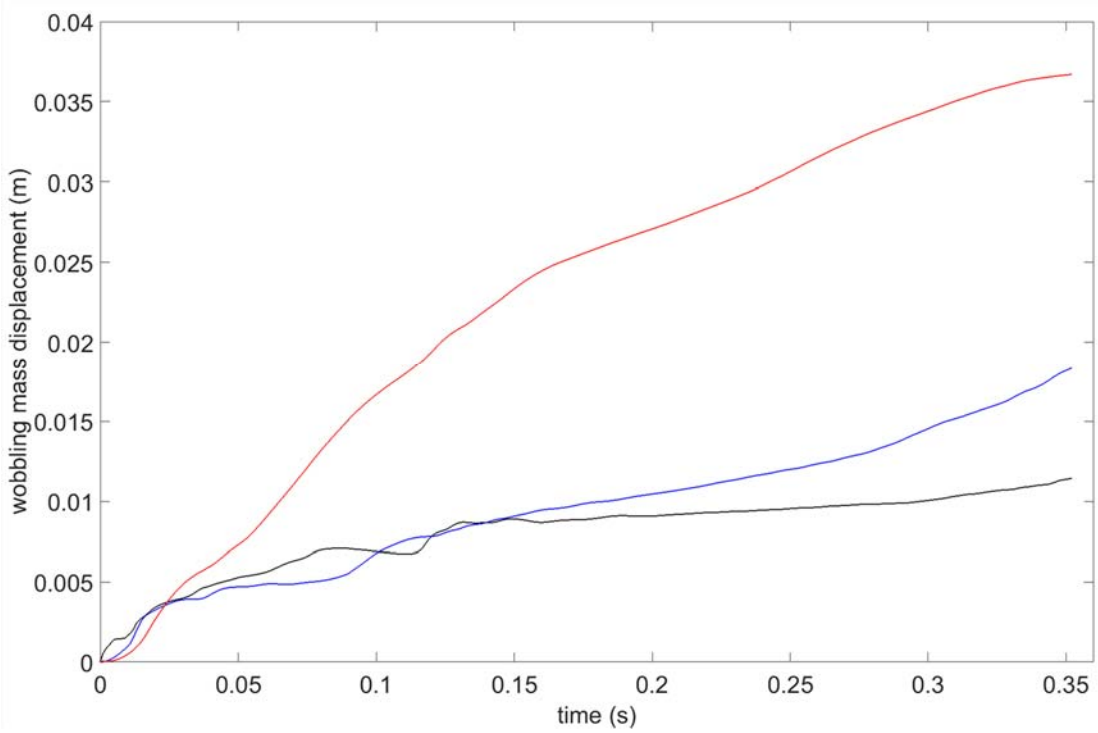

Figure 7.31. Simulation shank (black), thigh (blue), and trunk (red) wobbling mass spring-damper stretch magnitudes

Although not included in the objective score function, the following figures display a comparison of experimental and simulation whole-body centre of mass trajectories (Figure 7.32) and anterior-posterior centre of pressure (Figure 7.33). Simulation joint torque generator activation profiles are displayed in Figures 7.34 to 7.39, whilst Figure 7.40 presents resultant accelerations output by the simulation model for the first 50 ms at the same measured locations as the accelerometers positioned in Chapter 3's experimental trials and analysed in Chapter 4. Table 7.9 contains the relative magnitudes of peak resultant accelerations at each of these positions.

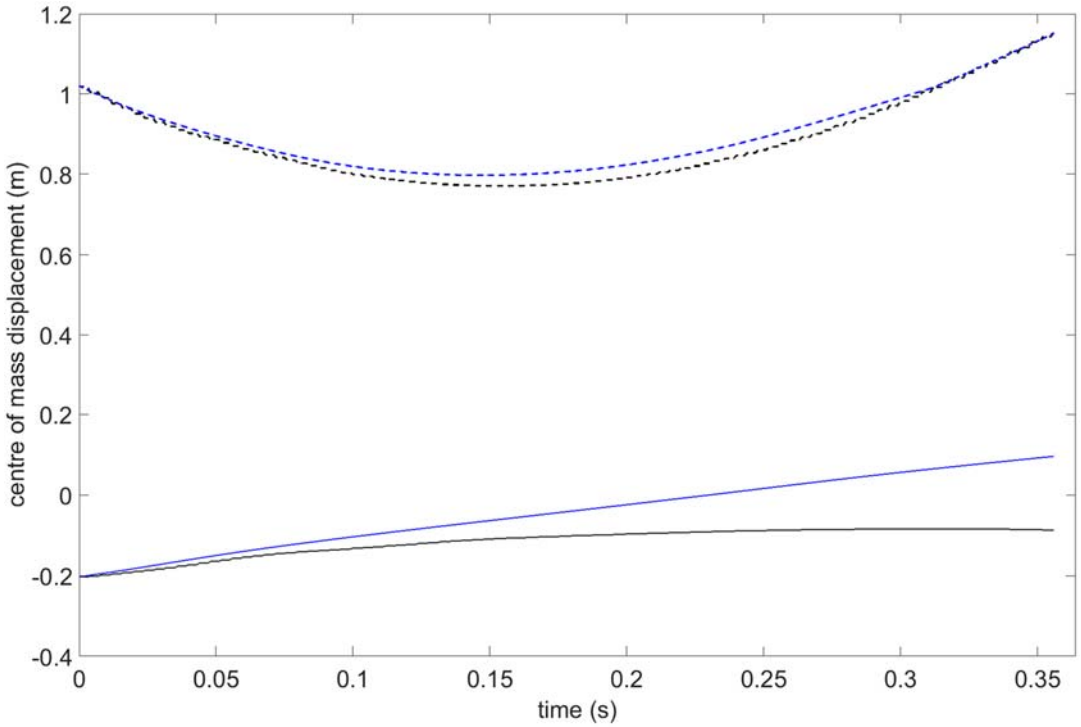

Figure 7.32. Simulation (blue) and experimental (black) vertical (dashed lines) and horizontal (solid lines) centre of mass time histories.

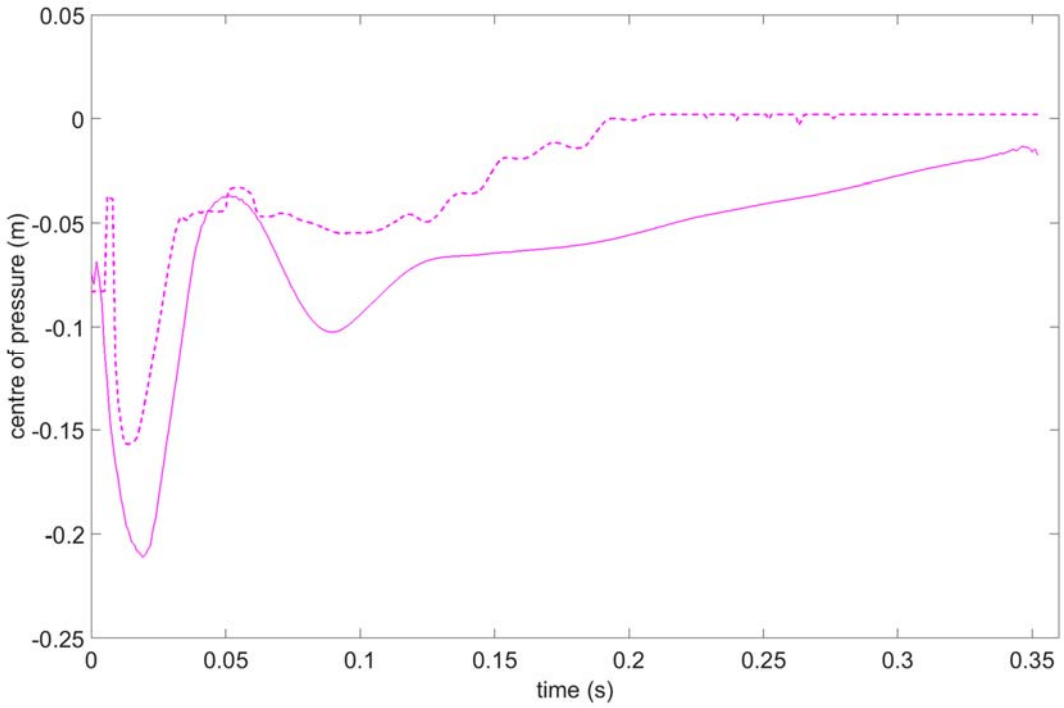

Figure 7.33. Simulation (dashed line) and experimental (solid line) anterior-posterior centre of pressure.

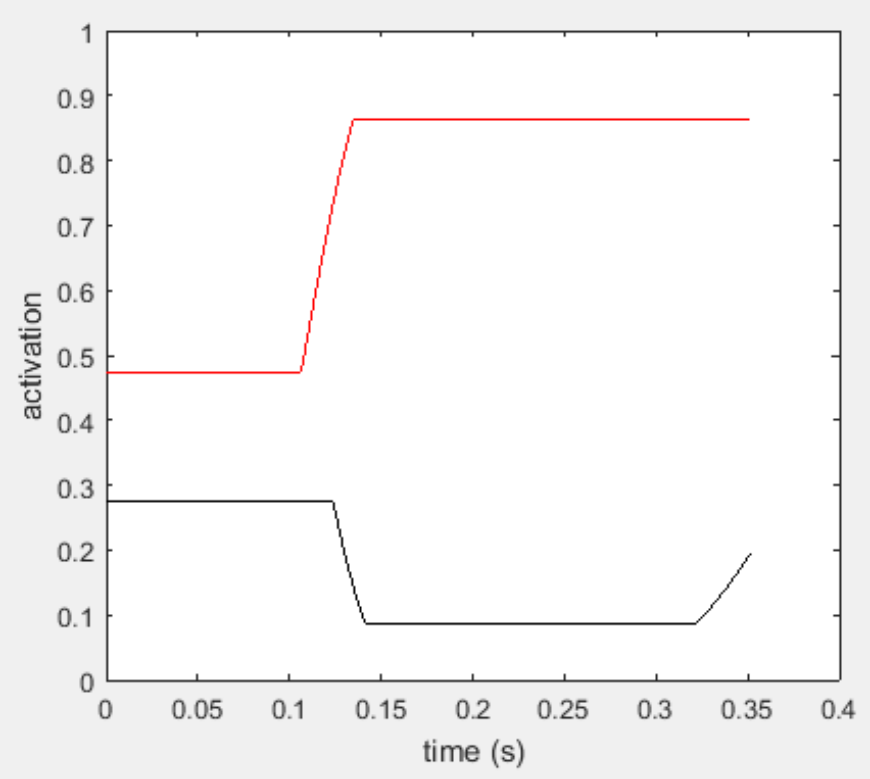

Figure 7.34. Simulation MTP joint torque generator flexion (black) and extension (red) activation profiles

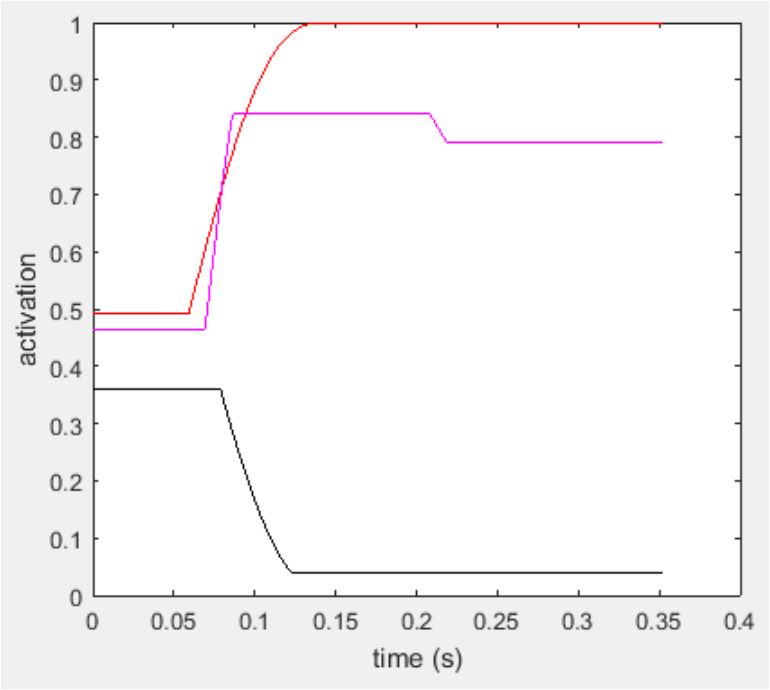

Figure 7.35. Simulation ankle joint torque generator dorsi flexion (black), monoarticular plantar flexion (red), and biarticular plantar flexion (pink) activation profiles

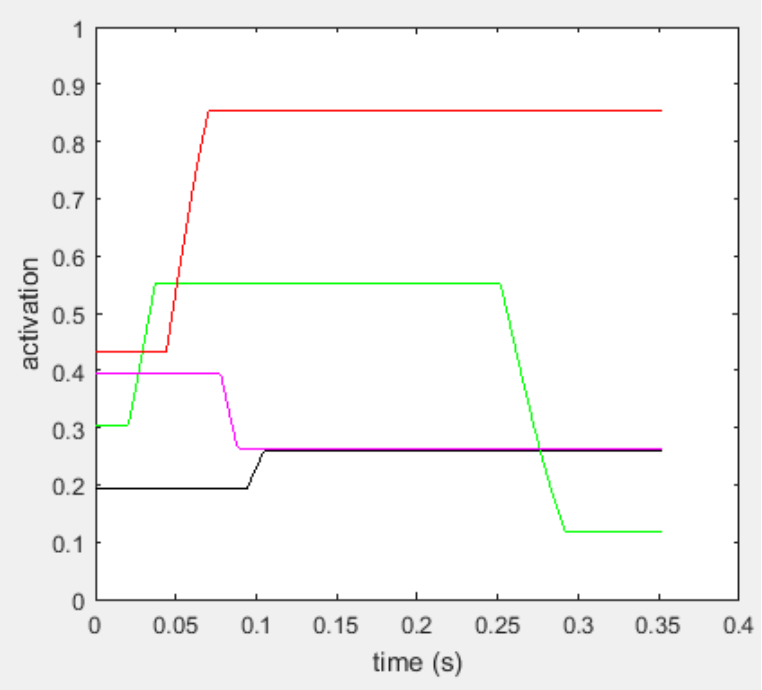

Figure 7.36. Simulation knee joint torque generator monoarticular flexion (black), biarticular flexion (green), monoarticular extension (red), and biarticular extension (pink) activation profiles

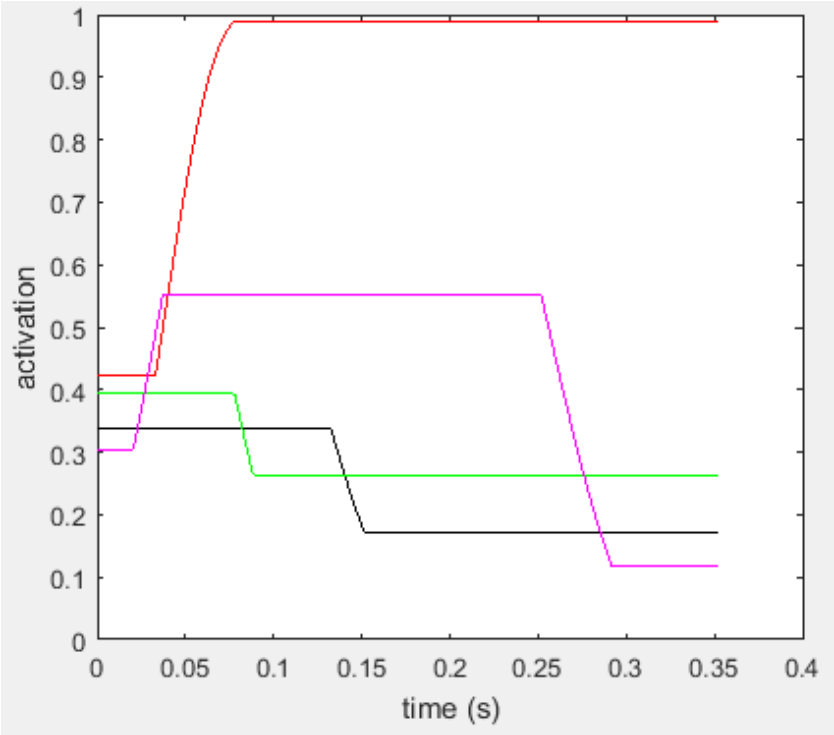

Figure 7.37. Simulation hip joint torque generator monoarticular flexion (black), biarticular flexion (green), monoarticular extension (red), and biarticular extension (pink) activation profiles

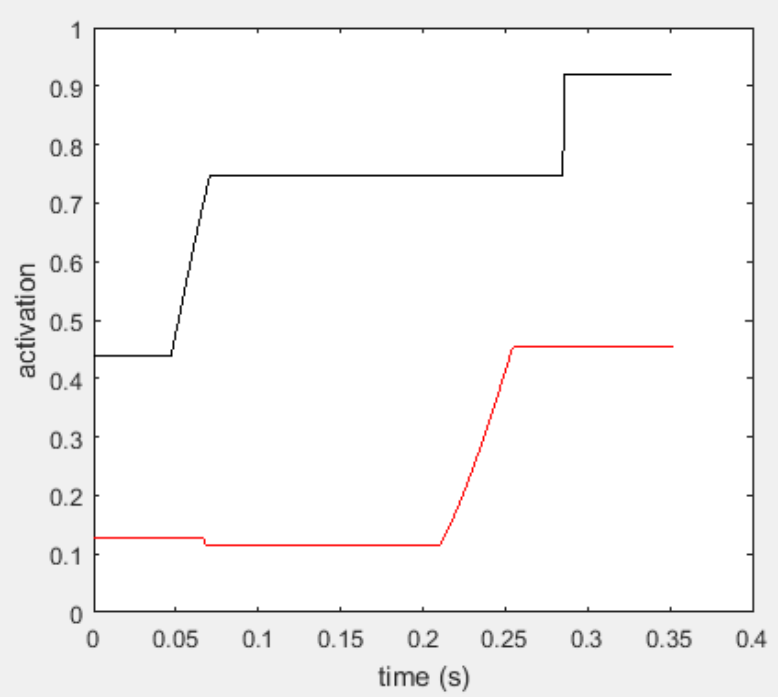

Figure 7.38. Simulation shoulder joint torque generator flexion (black) and extension (red) activation profiles

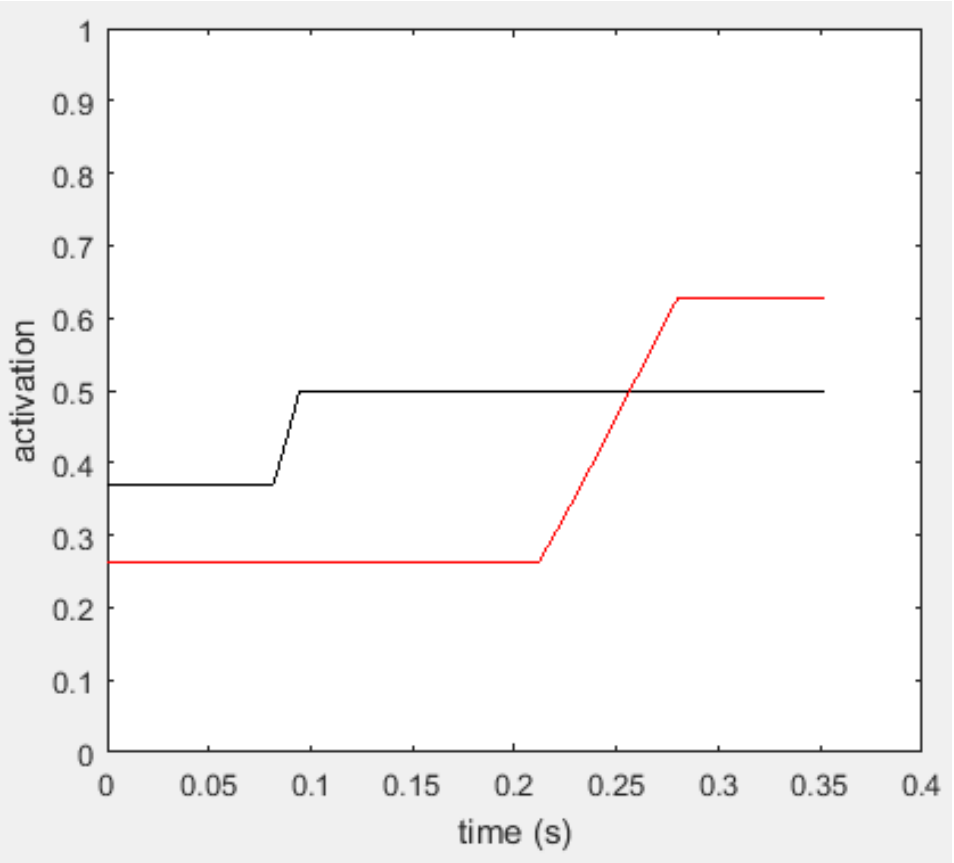

Figure 7.39. Simulation elbow joint torque generator flexion (black) and extension (red) activation profiles

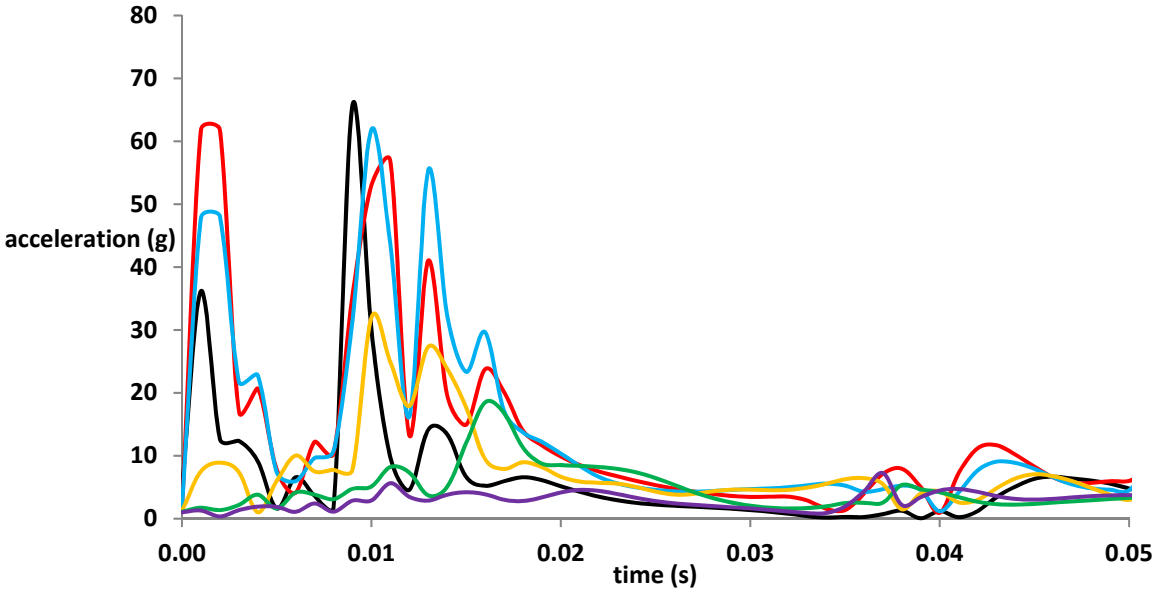

Figure 7.40. Simulation resultant accelerations at experimental accelerometer positions of MTP (black), distal shank (red), proximal shank (blue), distal thigh (orange), L5 (green), and C7 (purple) levels

Table 7.9. Relative magnitudes of peak resultant acceleration in each position relative to that at the MTP for simulation and experimental data

position	experimental peak acceleration (% of MTP)	simulation peak acceleration (% of MTP)
distal shank	79	94
proximal shank	57	94
distal thigh	65	49
L5	24	28
C7	13	11

The parameters for the simulation model determined within the genetic algorithm optimisation procedure are presented in Table 7.10. All joint torque generator activation parameters for the matched simulation are listed in Appendix 5.

Table 7.10. Simulation model parameters determined within the matching optimisation.

parameter	units	value
toe and MTP vertical linear stiffness	N m^{-1}	2.9 x 10^{4}
toe and MTP vertical non-linear stiffness	N m^{-2}	1.7 x 10^{5}
toe and MTP vertical damping	N s m^{-1}	3.8 x 10^{6}
heel vertical linear stiffness	N m^{-1}	1.0 x 10^{5}
heel vertical non-linear stiffness	N m^{-2}	9.4 x 10^{5}
heel vertical damping	N s m^{-1}	3.4 x 10^{5}
foot-ground horizontal linear stiffness	N m^{-1}	19
foot-ground horizontal non-linear stiffness	N m^{-2}	3623
foot-ground horizontal damping	N s m^{-1}	1.1 x 10^{5}
ankle non-linear stiffness	N m^{-3}	5.6 x 10^{8}
ankle damping	N s m^{-1}	1.0 x 10^{4}
knee non-linear stiffness	N m^{-3}	2.6 x 10^{10}
knee damping	N s m^{-1}	2001
hip non-linear stiffness	N m^{-3}	6.5 x 10^{9}
hip damping	N s m^{-1}	3239
mid-trunk non-linear stiffness	N m^{-3}	4.9 x 10^{7}
mid-trunk damping	N s m^{-1}	3622
shoulder non-linear stiffness	N m^{-3}	9.1 x 10^{8}
shoulder damping	N s m^{-1}	5093
shank wobbling mass non-linear stiffness	N m^{-3}	1.6 x 10^{7}
shank wobbling mass damping	N s m^{-1}	3505
thigh wobbling mass non-linear stiffness	N m^{-3}	6.7 x 10^{5}
thigh wobbling mass damping	N s m^{-1}	5881
trunk wobbling mass non-linear stiffness	N m^{-3}	1.3 x 10^{6}
trunk wobbling mass damping	N s m^{-1}	5214

7.7.1 PIN-JOINT MODEL

When the compliance within joint structures was removed, the genetic algorithm generated an optimal match between simulation and 0.595 m drop jump experimental performance data with a final objective score of 44.1%, due largely to an inability to match experimental jump height. This was despite activation of the monoarticular ankle plantarflexor and hip extensor torque generators ramping up to the maximum possible level of 1.00. Activation of these torque generators had similarly reached 1.00 and 0.99 respectively in the matched simulation model incorporating joint compliance. It is likely that when the energy dissipative abilities of the viscoelastic joint springs were removed, the negative work that must be performed by the torque generators increased. The torque generators did not have additional strength capabilities to meet this increased demand and so the model was no longer able to match the experimentally recorded jump height.

Subsequently, the jump height difference was replaced in the objective score function (Section 7.5.3) with an RMS of both vertical and horizontal whole-body centre of mass position RMS differences. The genetic algorithm then generated an optimal match between simulation and performance data with a final objective score of 10.96% (Table 7.11). The function of the optimisation algorithm is to reduce the objective score function to the lowest value possible within the parameter bounds specified, with no subjective knowledge of the task being simulated. In the case of the present model without viscoelastic joint springs, this was achieved through a solution in which the model left the ground prematurely, incurring a high ground contact duration difference value. This did, however, enable relatively lower score values for kinematic differences during the countermovement, or downward, phase of the jump whilst avoiding the subsequent inevitably high kinematic difference values for the propulsion, or upward, phase of the jump that would occur due to the above-mentioned strength limitations. Therefore, whilst general conclusions can be drawn from the poor ability of the pin-joint model to match the experimental performance data, the specific time-domain kinematic differences are a function of the objective score function selected.

Table 7.11. Optimal pin-joint simulation objective score function components for non-compliant model relative to 0.595 m drop jump experimental performance

component	score (%)
orientation angle RMS difference	1.90
joint angles RMS difference	14.98
ground contact duration difference	7.30
mass centre RMS differences	2.78
ground reaction force score	12.09
total score	**10.96**

The individual joint angle RMS differences ranged from 4.96° at the hip to 27.95° at the knee joint (Table 7.12).

Table 7.12. Individual joint angle RMS differences for the non-compliant model

joint	RMS difference (°)
MTP	5.26
ankle	17.21
knee	27.95
hip	4.96
shoulder	11.7
elbow	8.94
total joint angle RMS score	**14.98**

Simulation ground contact duration was 0.283 s, 73 ms shorter than the experimental 0.356 ms. The ground reaction force score of 12.09 consisted of an anterior-posterior ground reaction force RMS of 11.19% (Figure 7.41) and a vertical ground reaction force RMS difference of 18.10% (Figure 7.42), peak force difference of 3.49%, and timing of peak force difference of 0.010 s.

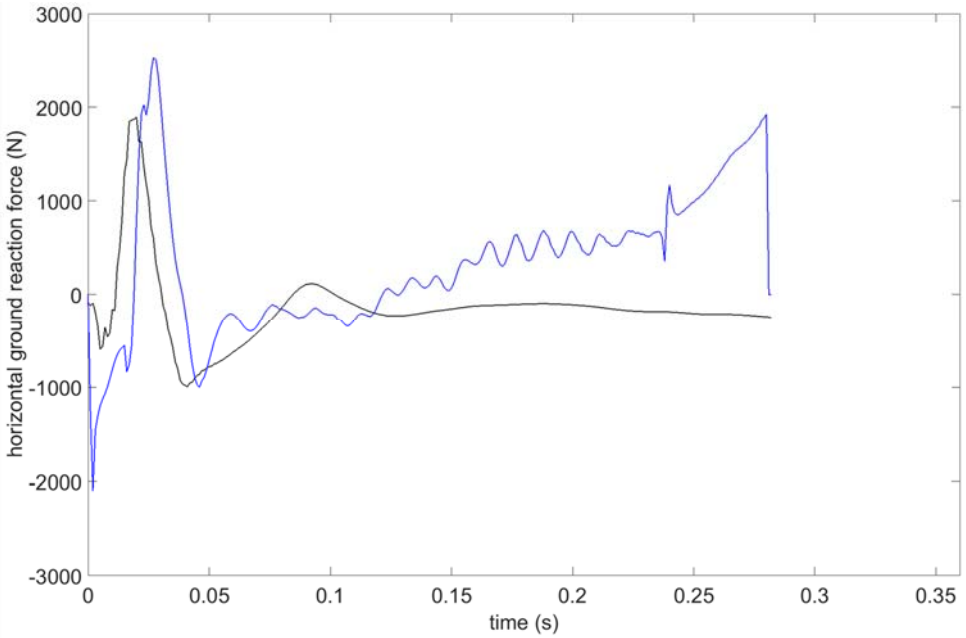

Figure 7.41. Non-compliant simulation (blue) and experimental (black) horizontal ground reaction force

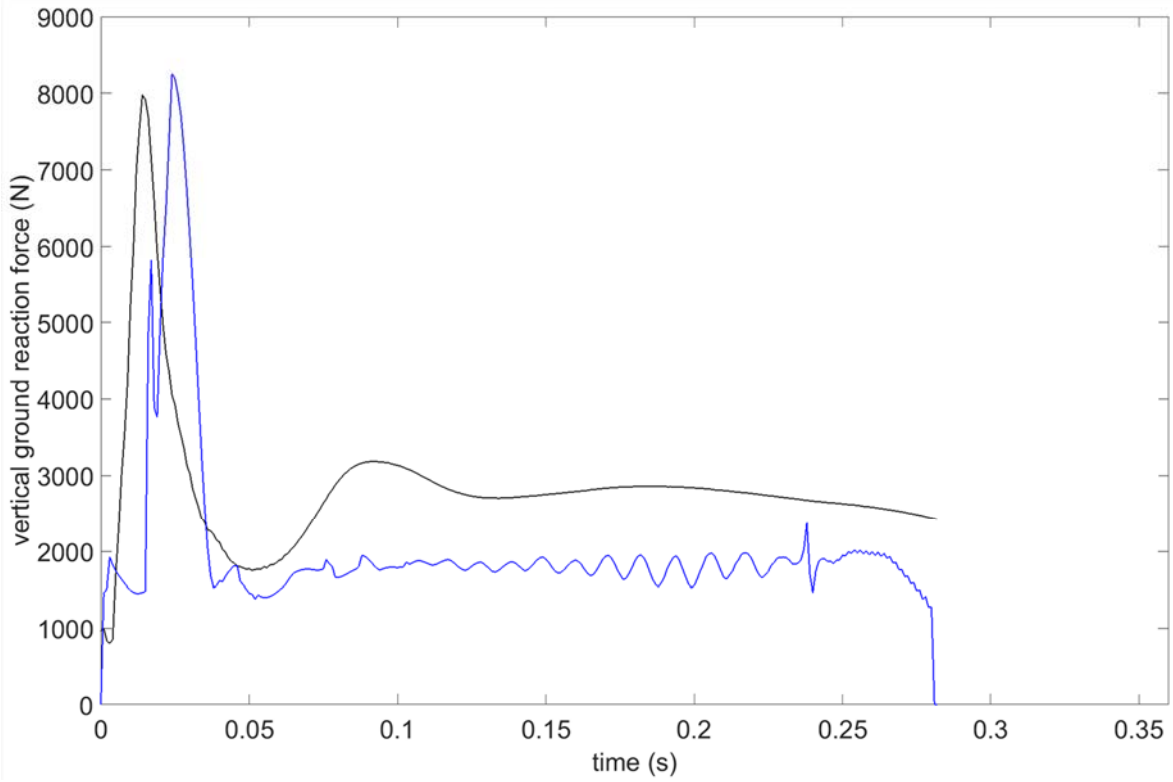

Figure 7.42. Non-compliant simulation (blue) and experimental (black) vertical ground reaction force

The whole-body configurations of both the subject's experimental performance and the non-compliant simulation model can be seen and compared periodically throughout the ground contact period in Figure 7.43.

Figure 7.43. Experimental (top) and non-compliant simulation (bottom) whole-body configuration throughout the period of ground contact.

As with the compliant model, no penalties were incurred by the optimal matching simulation, meaning that all spring-damper displacements were within limits (Section 7.5.4) and all joints remained within their anatomical ranges of motion. Likewise, the foot remained in contact with the ground until the moment of take off. Except for the horizontal ground-contact spring-dampers, all other (vertical ground-contact and wobbling mass) spring-dampers approached the limits of their respective penalty threshold displacements. Figure 7.44 displays a comparison of experimental and non-compliant simulation whole-body centre of mass trajectory, whilst Figure 7.45 presents resultant accelerations output by the simulation model for the first 50 ms at the same measured locations as the accelerometers positioned in Chapter 3's experimental trials and analysed in Chapter 4. Table 7.13 contains the relative magnitudes of peak resultant acceleration at each of these positions.

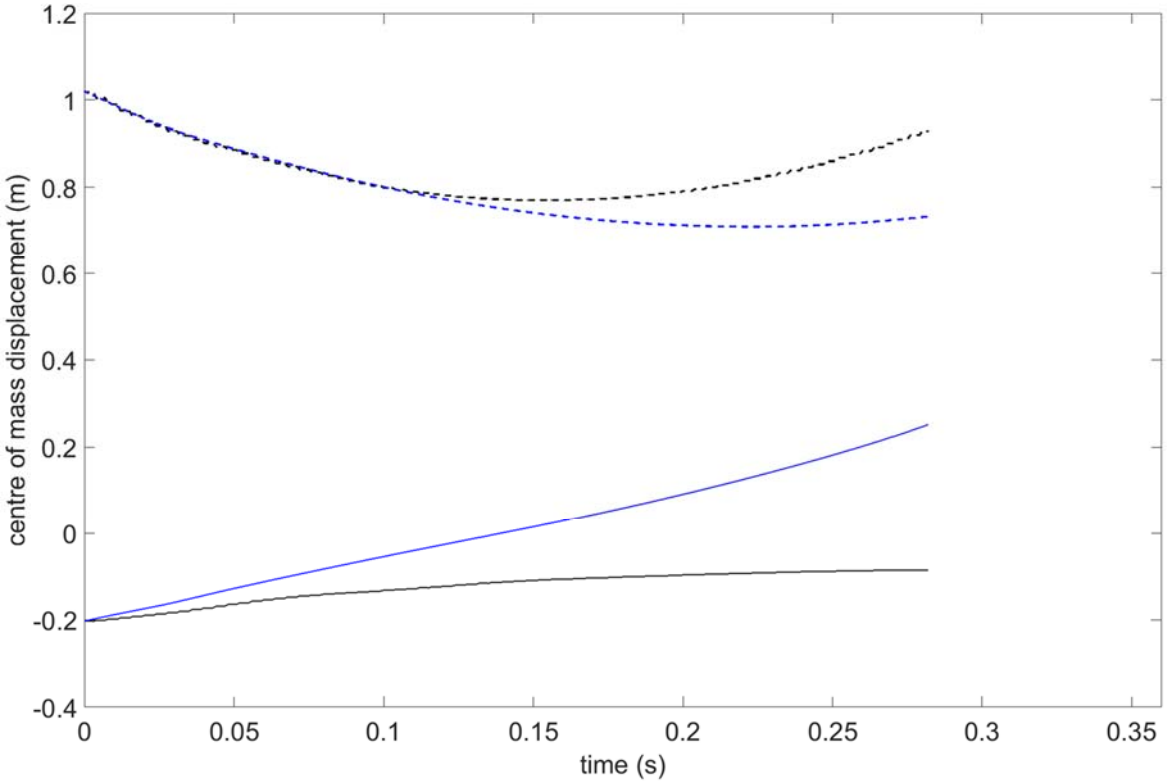

Figure 7.44. Non-compliant simulation (blue) and experimental (black) vertical (dashed lines) and horizontal (solid lines) centre of mass time histories.

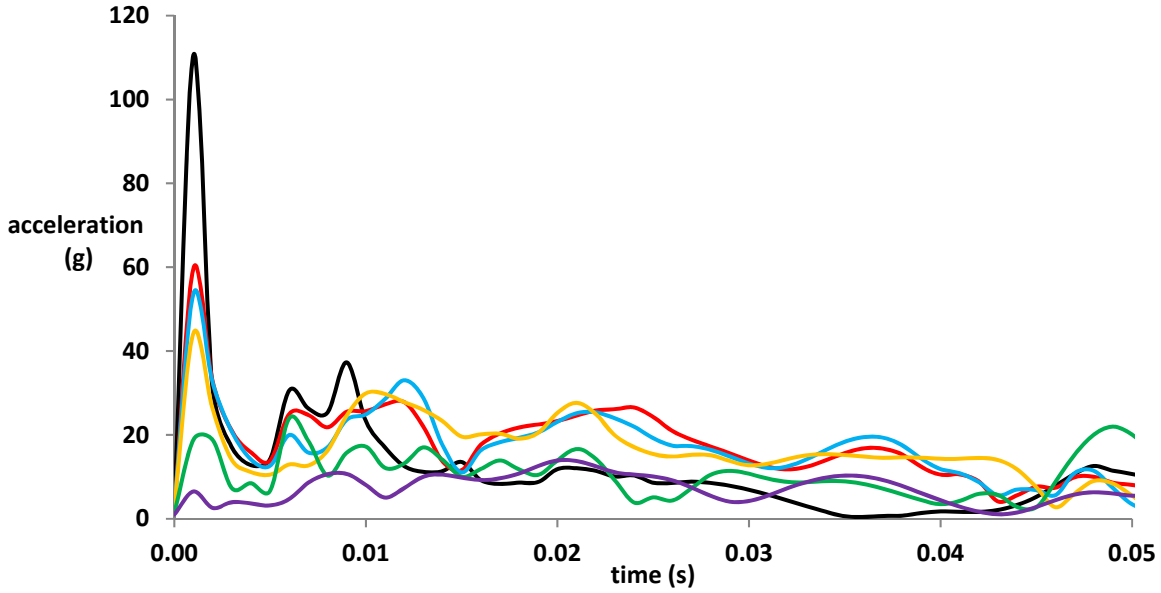

Figure 7.45. Non-compliant simulation resultant accelerations at experimental accelerometer positions of MTP (black), distal shank (red), proximal shank (blue), distal thigh (orange), L5 (green), and C7 (purple) levels

Table 7.13. Relative magnitudes of peak resultant acceleration in each position relative to that at the MTP for non-compliant simulation and experimental data

position	experimental peak acceleration (% of MTP)	simulation peak acceleration (% of MTP)
distal shank	79	54
proximal shank	57	49
distal thigh	65	40
L5	24	21
C7	13	13

7.8 CHAPTER SUMMARY

In this chapter, the determination of simulation model parameters has been discussed alongside the evaluation of the model. Realistic limits for displacement at each spring-damper within the model were determined, prior to the matching of the model, and an equivalent model without compliant joint structures, against experimental performance data collected in Chapter 3. In the next chapter these simulation model evaluation results are analysed and discussed with specific reference to the research questions posed at the start of the thesis in Chapter 1.

CHAPTER 8

DISCISSION AND CONCLUSIONS

8.1 CHAPTER OVERVIEW

This chapter will summarise the previous seven chapters by addressing each of the research questions posed in Section 1.4 in turn. The answers to these questions will draw upon the existing literature reviewed in Chapter 2, the experimental data collected as outlined in Chapter 3, the accelerometer-based results from Chapter 4, the simulation model constructed in Chapter 5, the subject-specific torque profiles determined in Chapter 6, and the results of the evaluation of the simulation model in the previous chapter.

8.2 RESEARCH QUESTION ONE

Q1. What contribution does spinal and joint compression make to the attenuation of ground reaction forces during impact landings?

8.2.1 PREVIOUS RESEARCH

Humans can experience extremely large ground reaction forces during foot-ground impacts which lead to an impact shock wave, and yet direct transmission of the resulting kinetic energy to vital internal organs in the torso and crucially the head is avoided. Various mechanisms within the body contribute to this dissipation of energy, including but not limited to shoe compression, heel pad deformation, foot arch compliance, lower limb joint compliance, soft tissue movement, spinal compression, and voluntary movement. The net effect of these combined mechanisms has previously been studied in activities including drop landings (Zhang et al., 2008) and treadmill running (Shorten & Winslow, 1992) using accelerometers placed on the shank and head of subjects. Consequently, we know the frequency characteristics of the impact shock wave, and the considerable

attenuation in acceleration signals between these points at opposite ends of the human body. However, little is known of the relative contributions of the various structures and mechanisms to this attenuation effect.

Furthermore, recent computer simulation work has speculated at the potential need to incorporate compliance at sites on the body other than either at the foot-ground interface or through the displacement of soft tissue relative to the underlying bone. In their investigation into the necessary compliance within simulation models to match experimental ground reaction forces, Allen et al. (2012) concluded that the future calculation of accurate internal forces would require the incorporation of compliance elsewhere in the rigid system. Thus, it was necessary to determine whether compression within articulating joints and the spine contribute to the observed attenuation of the impact shock wave accelerations.

8.2.2 EXPERIMENTAL PROTOCOL

One subject performed two drop landings and two maximal effort drop jumps from each of 0.30 m, 0.445 m, 0.595 m, and 0.74 m onto a force platform, with lightweight accelerometers strapped firmly to the MTP, distal shank, proximal shank, distal thigh, L5 vertebra level on the back, and C6 vertebra level on the neck.

8.2.3 ACCELERATION ATTENUATION

Peak accelerations tended to decrease progressively up the body. This ensured that the peak accelerations close to vital organs were less than 25% of those at the MTP joint. The effects of the lower limbs, both voluntary and passive, therefore act to reduce the risk of serious injury to these organs.

In drop landings in Chapter 4, peak accelerations at the distal femur were non-significantly greater than those at the proximal tibia. This difference was negligible on average in the drop jumps. A subsequent spectral analysis revealed that power spectra contained two major components, corresponding to the active voluntary movement (2 – 14 Hz) and impact shock wave (16 – 26 Hz) related phases of the time-domain signals. Transfer functions demonstrated progressive acceleration

attenuation from the MTP towards the C6 vertebra within the 16 – 26 Hz frequency component in almost all conditions. The transfer function between the proximal tibia and distal femur included signal attenuation in the range of frequencies associated with the impact shock wave. It can therefore be said that the mechanical features of the knee joint contribute to attenuation of the impact shock wave, with lower acceleration within the relevant frequency range experienced directly above the joint compared with directly below. Unlike between accelerometer positions such as the distal and proximal shank, there is negligible soft tissue movement between the proximal tibia and distal femur. Thus, it is most likely that compliance and/or viscosity within the joint structure is responsible for the dissipation of energy and hence attenuation in shock wave acceleration. Previous research using cadaveric knees has shown that removal or damage of meniscus, articular cartilage, and subchondral bone causes sequential increases in the magnitudes of forces transmitted through the knee (Hoshino & Wallace, 1987). These features explain the attenuation in impact shock wave acceleration observed across the knee joint in the present study.

Such compliance elsewhere within the human musculoskeletal system is likely to have a similar effect on the passive transmission of energy throughout the system. Although no accelerometer was positioned directly below the hip joint, it can be assumed that compliance within this joint, along with soft tissue displacement within the thigh, contributed partly to the attenuation between distal thigh and L5 accelerometer signals. Likewise, compliance within the ankle will have contributed to attenuation between the MTP and distal tibia.

Furthermore, the accelerations towards the top of the spine were even lower than those towards its base. Thus, it can be said that the spine itself, as well as other features within the torso such as soft tissue displacement, protect the brain and vestibular organs from damage by further dissipating energy from an impact. Indeed, peak acceleration occurred later at C6 level than at any other measured site on the body and was the only peak acceleration not correlated to peak resultant ground reaction force. Correlations, as shown in Figure 4.5, suggest that acceleration at all other positions, particularly during the more passive drop landings, will increase with each increase in magnitude of distal impact force experienced. However, the human body is capable of further dissipating the

resulting kinetic energy to ensure that greater impact forces do not lead to greater shock at the head. This agrees with the findings of Hamill et al. (1995), which showed unchanged peak head accelerations across running speeds. Likewise, Shorten and Winslow (1992) found that during treadmill running, impact attenuation between the tibia and the head increased with increases in running speeds.

On average 11% of the reduction in peak acceleration compared with the MTP occurred between the base and top of the spine, with this value as high as 20% for the more passive drop landing conditions. Transfer functions highlighted greater magnitudes of attenuation within the impact-related frequency range from L5 to C6 than between any other pair of adjacent accelerometer positions. Thus, the compliance within the trunk should not be ignored. Researchers should not assume that all of the energy dissipation occurs within the lower limbs or incorporate compliant representations at the lower extremities of the body only. It remains true that a certain proportion of this dissipation may be brought about through the effects of soft tissue displacement within the trunk, but in lean individuals such as the subject in the present study, this will be limited. Thus, compliance within the spine itself, namely the flattening of its curved shape, quantified at up to 3.1 cm during Chapter 3's experimental trials (determined as a limit of spinal compliance for simulation model parameter determination in Chapter 7), is likely to contribute greatly. Further support for this argument can be found in Helliwell's (1989) comparison of subjects with and without ankylosing spondylitis, a condition involving fusion of the spine and thus minimal spinal compliance. The control group, but not the ankylosing spondylitis group, exhibited the ability to attenuate shock at frequencies above 15 Hz, similar to the 16 – 26 Hz range identified in Chapter 4 of the present thesis. Spinal compliance may also explain the fact that acceleration at the neck did not increase in the present study with increases in ground reaction force, despite increases in peak acceleration at every other measured position below the base of the spine. Thus, it can be said that the final phase of post-impact energy dissipation prior to the shock wave reaching the head is spinal column compliance and as such this dissipative ability is of high importance.

8.2.4 ADDRESSING THE RESEARCH QUESTION

As discussed above, the mechanical features such as compliance and viscosity within the lower-limb joints contributed to post-impact energy dissipation and attenuation of the impact shock wave, ensuring that the peak accelerations close to vital organs were less than 25% of those at the MTP joint. In drop landings, 20% of the reduction in peak acceleration compared with the MTP joint occurred between the base and top of the spine, attributable in part to up to 3.1 cm of compliance within the spine. Transfer functions highlighted greater magnitudes of attenuation within the impact-related frequency range from L5 to C6 than between any other two adjacent accelerometer positions. Thus, spinal and joint compression contribute greatly to the dissipation of energy during impact landings and should not be ignored in models of human impacts.

8.2.5 IMPLICATIONS

The observed attenuation of impact accelerations across joint structures has implications for both experimental and theoretical investigations. The assumption that the distal end of one body segment shares a common point with the proximal end of the connecting segment neglects the influence of compliance within joint structures and the subsequent effects on the kinetics and kinematics within the human musculoskeletal system. Attenuation between sites above the MTP joint or between which there is little soft tissue highlights the fact that not all compliance within an accurate model of the human musculoskeletal system can be placed at the foot-ground interface or within wobbling masses. Likewise, the summed dissipative effects of these compliant features explain why previous simulation modelling investigations have been unable to successfully predict ground reaction forces in their absence and have required the arbitrary addition of extra compliance (Allen et al., 2012). Thus, it can be said that such effects of compliance within the spine and lower-limb joint structures should be considered when representing the connection between adjacent body segments in a theoretical investigation.

8.2.6 LIMITATIONS AND FUTURE DEVELOPMENTS

A potential limitation of the present study when it comes to identifying the relative contributions of various joints to impact shock wave attenuation is the lack of direct measures. Accelerometers provide a good estimate of the shock wave characteristics and can highlight areas and magnitudes of differences, particularly when combined with a spectral analysis as in Chapter 4. However, future studies should seek to quantify magnitudes of compression within the joint structures using techniques such as high-speed x-ray imaging under various levels of realistic and dynamic high impact loading. Likewise, internal direct force measurements, rather than indirect surface accelerations, will provide accurate quantification of the forces acting at each joint and the dissipation of energy across various structures.

8.3 RESEARCH QUESTION TWO

Q2. Is it necessary to represent compression within the spinal column and ankle, knee, hip and shoulder joints in planar whole-body simulation models of drop jumping?

8.3.1 PREVIOUS RESEARCH

Previous whole-body forward-dynamics simulation models of sporting activities have been unable to accurately reproduce experimentally measured ground reaction forces without the application of excessive compliance at both the foot-ground interface and the attachments between wobbling mass and rigid body segments, far greater than those seen experimentally in the reviewed literature of Chapter 2. Indeed, Allen et al. (2012) investigated the effects of varying foot-ground compliance limits on the ability of a whole-body forward-dynamics simulation model of triple jumping to match experimentally recorded performances and ground reaction forces. When foot spring compression was limited to 20 mm, which already exceeds realistic limits determined in Chapter 7 (toe and MTP: 11.5 mm; heel: 26.5 mm) at sites other than the heel, the simulation model was only able to match experimental ground reaction forces to a 48% difference. Compression of 40 mm

enabled a more acceptably matched ground reaction force, with a 16% difference, and the difference was reduced to 12.4% with the removal of all foot-ground compression constraints. This final condition saw compressions of between 43 mm and 56 mm obtained in the three phases of the action, and yet there were still large noticeable differences in the force-time histories. Whole-body mass centre position was within 4 mm of the experimental position at the times of these unrestricted maximum compressions, further supporting the argument that excessive foot-ground compression was replacing compression from elsewhere in the human body.

8.3.2 SIMULATION MODEL CONSTRUCTION

Chapters 5 to 7 of the present thesis investigated the effects of incorporating compliance within joint structures on the ability of a whole-body forward-dynamics simulation model to match experimentally recorded kinematics and kinetics. In addition, this was done alongside realistic limits for compliance throughout the system, determined in Chapter 7 from a combination of experimental data collected in Chapter 3 and the available scientific literature reviewed in Chapter 2.

A planar nine-segment simulation model of drop jumping was constructed, with subject-specific joint torque generators incorporated at the MTP, ankle, knee, hip, shoulder, and elbow joints. Maximal strength at each of these joints was determined from maximal effort isovelocity dynamometer measures made on the subject and analysed in Chapter 5 to obtain subject-specific torque-joint angle and torque-joint angular velocity relationships. For ankle plantar flexion and flexion and extension at the knee and hip, joint torques were determined based not only upon kinematics at that joint but also at a secondary joint, resulting in biarticular joint torque actuators.

Spring-dampers were modelled at the toe, MTP joint, and heel, as well as connecting rigid segments to wobbling masses at the shank, thigh, and trunk. Displacements at each of these spring-dampers was limited to realistic bounds, which were considerably lower than those in all similar previous whole-body forward-dynamics simulation models of human sporting movements. With excessive compliance therefore removed from the model, additional compliance was added at the sites where it is known to exist in vivo (see literature review of

Chapter 2). Indeed, the accelerometer analysis of Chapter 4 highlighted the need for compliance within the spine and lower-limb joint structures to be considered when representing the connection between adjacent body segments in such a theoretical investigation. Non-linear spring-dampers were therefore incorporated connecting adjacent segments at the ankle, knee, hip, mid-trunk, and shoulder.

8.3.3 SIMULATION MODEL PERFORMANCE

To match the model to Chapter 3's experimental performance data for a representative 0.595 m drop jump trial, a genetic algorithm was used to vary the joint torque generator activation parameters, minimising an objective score function of differences between simulation and experimental data. This resulted in an optimum simulation 3.7% different to the experimental data. The root mean square differences for ground reaction forces were 3.8% anterior-posteriorly, and 8.5% vertically. This would give a combined RMS of those differences of 6.6% or a ground reaction force score of 5.1% once timing and magnitude of peak vertical ground reaction force were included. These differences are considerably lower than for previous torque-driven whole-body forward-dynamics computer simulation models of sporting impacts (Allen et al., 2012; Felton, 2014; King et al., 2006).

As discussed above, Allen et al. (2012) required 56 mm of compression at the foot-ground interface to match ground reaction forces to 12.4%, albeit for a higher impact activity in triple jumping. The simulation model featuring joint compliance evaluated in Chapter 7 only compressed the foot-ground interface by 11.5, 10.4, and 19.1 mm at the toe, MTP joint, and heel respectively. Wobbling mass displacements were equally well within realistic limits and less than those in most previous similar models. It can therefore be assumed that the overall magnitude of compliance within the system was not a limiting factor in the ability of this simulation model to match kinetic and kinematic experimental performance data. Finally, resultant accelerations at the same positions on the model as the accelerometers on the subject in Chapter 3 and 4 revealed decreases with every increase in height on the body, as observed in Chapter 4. Although peak accelerations at the MTP, distal shank, and proximal shank were very similar, those higher up mirrored experimental reductions closely (distal thigh 49% of that at MTP compared with 65%

experimentally; L5 28% of that at MTP compared with 24% experimentally; C6 11% of that at MTP compared with 13% experimentally). Thus, the incorporation of spring-dampers at joints in the simulation model had a positive effect on all aspects of the model's ability to more closely represent reality.

8.3.4 COMPARISON TO A MODEL WITHOUT COMPLIANT JOINTS

It cannot be seen from this model alone to what extent the results are a consequence of the compliant joint structures. Therefore, a second simulation model was matched to the same experimental data in the same way, this time with joint spring-dampers approaching infinite stiffness and zero damping to reflect a traditional frictionless pin joint model. A comparison of the evaluation results for this model against those for the model with compliant joints would isolate the effects of those features.

This second model was unable to match performance data to less than 44%. However, this was largely due to an inability to match the experimental jump height due to insufficient strength to match the increased demand for negative work by the torque generators given the lack of energy dissipation elsewhere (as discussed in Section 7.7.1). To prevent the inability to achieve high vertical mass centre velocities during the push off phase from distorting the ability to match other aspects of performance, jump height was replaced by an RMS of mass centre position in the objective score function. The overall difference was then 11.0%, including a ground reaction force score difference of 12.1%. Vertical ground reaction force RMS difference was 18.1% and horizontally this was 11.2%, which would give a combined 15.0% difference in ground reaction force time histories. The kinematics of the model were noticeably much worse than the more compliant model, with joint angles RMS differences of 15.0° rather than 5.5°. As discussed in Section 7.7.1, a premature take off ended the simulation as these differences were increasing, and so had the ground contact duration been matched then the differences would likely have been even greater.

8.3.5 DISCUSSION

The results described above suggest that not only does incorporating joint compliance allow a closer match between experimental and simulation performances than has been possible in many previous studies, but that without this joint compliance, a whole-body model is unable to match realistic kinetics or kinematics if compliance elsewhere in the system is constrained to realistic limits. Indeed, the fact that spring-damper displacements approached their respective pre-specified limits (Section 7.5.4) suggests that the overall magnitude of compliance within the system was a limiting factor in the absence of spring-dampers at joints. It should be noted, however, that it is possible to achieve similar or even better kinematic matches using excessive compliance at the ground and at wobbling masses (Allen, 2010; Lewis, 2011; Felton, 2014) if this does not weaken the ability to answer the specific research questions of a study. As noted by Allen et al. (2012) when suggesting the future inclusion of joint compliance within such models, excessive ground compliance may be acceptable to generate accurate kinematics, but that accurate internal kinetics may require compliance elsewhere in the system.

Furthermore, peak simulation model resultant accelerations at the experimental accelerometer positions were very similar between compliant and non-compliant models, likely due to the approximately equal stepwise increases in mass and distance from the ground. Indeed, peak acceleration at C6 level, and so that reaching the neck and head was 11% of peak MTP acceleration in the compliant model, 13% in the non-compliant model, and averaged 13% experimentally. The main difference in acceleration-time histories between the two models though was in the time duration of impact shock wave transmission. In a traditional model without compliance at the joints, the main impact peak in acceleration occurred at the same time point at all six positions in the body, suggesting instantaneous transmission of impact accelerations from the foot straight up to the head. Whilst other features within the model were able to reduce the magnitude of experienced acceleration, they were not able to delay its transmission. In the compliant model, however, the acceleration time histories far more closely resembled those time domain acceleration signals seen experimentally in Chapter 4. That is, there was a

presence of multiple peaks at some positions, as well as a latency as the impact shock wave was seemingly transmitted from inferior towards superior segments of the body. Perhaps, therefore, one further benefit of compliance within simulation model joint structures is the potential for future applications of more realistic energy transmission throughout the body.

8.3.6 LIMITATIONS

Although the simulation model featuring spring-dampers at joints was able to match experimentally recorded ground reaction forces more closely than previous whole-body forward-dynamics computer simulation models of sporting activities, it is not clear how closely the non-compliant model would have matched experimental performance data had excessively compliant wobbling masses and foot-ground interfaces been enabled as in previous investigations. Research suggests that the kinematic root mean square differences may have more closely resembled those in the compliant model (Allen et al., 2012). The ground reaction force differences, however would likely still have remained larger than when spring-dampers are included at joints.

8.3.7 RELEVANCE AND FUTURE DEVELOPMENTS

Increased accuracy of internal energy transmission presents the possibility for future forward-dynamics whole-body simulation research to utilise similar methodologies to those employed in this thesis in an attempt to calculate realistic approximations of internal joint reaction forces. Realistic magnitudes of joint reaction force may necessitate the use of a ‘lumped’ muscle-driven model, whereby the joint torque calculated in the same way as the present study can be applied instead as a net muscle force at a combined, equivalent insertion distance from the joint (Mills et al., 2008).

The relationships between technique factors and injury risk could then be investigated theoretically without the need for potentially injurious experimental procedures. Likewise, the likelihood of acute or chronic musculoskeletal injuries

could be considered alongside performance measures when determining the optimum technique for a specific individual through subject-specific modelling approaches. An attempt should be made to identify how successfully the parameters determined within Chapter 7 for this model can be applied to similar models of alternative activities to improve ground reaction force replication.

8.3.8 ADDRESSING THE RESEARCH QUESTION

As with all simulation modelling investigations, the decision regarding which features to incorporate or to neglect should be specific to the research question being answered and should be based upon an appropriate trade off between model complexity and simplicity for processing time and ease of use. Taking this into consideration, it is necessary to represent compression within joints including the spinal column and ankle, knee, hip, and shoulder joints in planar whole-body simulation models of drop jumping when one or more of the following criteria are met:

- it is desirable to generate realistic whole-body kinematics alongside realistic foot-ground and wobbling mass displacements;
- accurate ground reaction force replication is a priority;
- impact shock wave transmission must be non-instantaneous.

8.4 CONCLUSION

The purpose of this thesis was to investigate the effect of incorporating joint compliance on the ability of a subject-specific computer simulation model to accurately predict ground reaction forces during dynamic jumping activities. Compliance within joint structures is an important contributor to the attenuation of the impact shock wave, and the incorporation of viscoelastic elements at key joints enables accurate replication of experimentally recorded ground reaction forces within realistic whole-body kinematics. This also removes the previous need for excessively compliant wobbling masses and/or foot-ground interfaces and enables non-instantaneous shock wave transmission within the simulation model.

REFERENCES

Aerts, P., Clercq, D.D. (1993). Deformation characteristics of the heel region of the shod foot during a simulated heel strike: the effect of varying midsole hardness. *Journal of Sports Sciences*, **11**, 449-461.

Aerts, P., Ker, R.F., De Clercq, D., Ilsley, D.W., Alexander, R.M. (1995). The mechanical properties of the human heel pad: a paradox resolved. *Journal of biomechanics*, **28**, 1299-1308.

Alexander, R.M. (1989). Sequential joint extension in jumping. *Human Movement Sciences*. **8**, 339-345.

Alexander, R.M. (1990). Optimum take-off techniques for high and long jumps. *Philosophical Transactions of the Royal Society of London*. **B329**, 3-10.

Alexander, R.M., 1992. Simple models of walking and jumping. *Human Movement Science*. **11**(1-2), 3-9.

Alexander, R.M., Bennett, M.B., KER, R.F. (1986). Mechanical properties and function of the paw pads of some mammals. *Journal of Zoology*, London, A209, 405-419.

Allen, S.J. (2010). Optimisation of performance in the triple jump using computer simulation. *Unpublished Doctoral Thesis*, Loughborough University.

Allen, S.J., King, M.A., Yeadon, M.R. (2012). Models incorporating pin joints are suitable for simulating performance but unsuitable for simulating internal loading. *Journal of Biomechanics*. **45**, 1430-1436.

Amadio, A.C. (1985). *Biomechanische analyse des dreisprungs*. Deutsche Sporthochschule, Koln.

Amiridis, I.G., Martin, A., Morlon, B., Martin, L., Cometti, G., Pousson, M., van Hoecke, J. (1996). Co-activation and tension-regulating phenomena during isokinetic knee extension in sedentary and highly skilled humans. *European Journal of Applied Physiology*, **73**, 149-156.

Anderson, F.C., Pandy, M.G. (1999). A dynamic optimization solution for vertical jumping in three dimensions. *Computer Methods in Biomechanics and Biomedical Engineering*. **2**, 201-231.

Andersson, E., Sward, L., Thorstensson, A. (1988). Trunk muscle strength in athletes. *Medicine and Science in Sports and Exercise*. **20**, 587-593.

Arampatzis, A., Schade, F., Walsh, M., Brüggemann, G-P. (2001). Influence of leg stiffness and its effect on myodynamic jumping performance. *Journal of Electromyography and Kinesiology*, **11**, 355-364.

Ashby, B.M., Delp, S.L. (2006). Optimal control simulations reveal mechanisms by which arm movement improves standing long jump performance. *Journal of biomechanics*. **39**,1726-1734.

Bandholm, T., Boysen, L., Haugaard, S., Zebis, M.K., Bencke, J. (2008). Foot medial longitudinal-arch deformation during quiet standing and gait in subjects with medial tibial stress syndrome. *The Journal of Foot and Ankle Surgery*, **47**, 89-95.

Bennett, M.B., & Ker, R.F. (1990). The mechanical properties of the human subcalcaneal fat pad in compression. *Journal of anatomy*, **171**, 131.

Billis, E., Katsakiori, E., Kapodistrias, C., Kapreli, E. (2007). Assessment of foot posture: Correlation between different clinical techniques. *The foot*, **17**(2), 65-72.

Blache, Y., Monteil, K. (2014). Influence of lumbar spine extension on vertical jump height during maximal squat jumping. *Journal of Sports Sciences*, **32**, 642-651.

Bobbert, M.F. (2001). Dependence of human squat jump performance on the series elastic compliance of the triceps surae: a simulation study. *Journal of Experimental Biology*. **204**, 533-542.

Bobbert, M.F., Casius, L.J.R. (2005). Is the effect of a countermovement on jump height due to active state development? *Medicine and Science in Sports and Exercise*. **37**, 440-446.

Bobbert, M.F., Casius, L.J.R., Sijpkens, I.W.T., Jaspers, R.T. (2008). Humans adjust control to initial squat depth in vertical squat jumping. *Journal of Applied Physiology*. **105**, 1428-1440.

Bobbert, M.F., Gerritsen, K.G., Litjens, M.C., Van Soest, A.J. (1996). Why is countermovement jump height greater than squat jump height? *Medicine and Science in Sports and Exercise.* **28**, 1402-1412.

Bobbert, M.F., Houdijk, H., de Koning, J.J., de Groot, G. (2002). From a one-legged vertical jump to the speed-skating push-off: a simulation study. *Journal of Applied Biomechanics*. **18**, 28-45.

Bobbert, M.F., Huijing, P.A., van Ingen Schenau, G.J. (1987a). Drop jumping. I. The influence of jumping technique on the biomechanics of jumping. *Medicine and Science in Sports and Exercise*, **19**, 332-338.

Bobbert, M.F., Huijing, P.A., van Ingen Schenau, G.J. (1987b). Drop jumping. II. The influence of dropping height on the biomechanics of drop jumping. *Medicine and Science in Sports and Exercise*, **19**, 339-346.

Bobbert, M.F., van Ingen Schenau, G.J. (1988). Coordination in vertical jumping. *Journal of Biomechanics*, **21**, 249-262.

Bobbert, M.F., van Soest, A.J. (1994). Effects of muscle strengthening on vertical jump height: a simulation study. *Medicine and Science in Sports and Ecercise*, **26**, 1012-1020.

Bobbert, M.F., Van Soest, A.J. (2001). Why do people jump the way they do? *Exercises and Sports Sciences Reviews*. **29**(3), 95-102.

Bobbert, M.F., van Zandwijk, J.P. (1999). Dynamics of force and muscle stimulation in human vertical jumping. *Medicine and Science in Sports and Exercise*, **31**, 303-310.

Boocock, M.G., Garbutt, G., Linge, K., Reilly, T., Troup, J.D.G. (1990). Changes in stature following drop jumping and post-exercise gravity inversion. *Medicine and Science in Sport and Exercise*, **22**, 385-390.

Bostock, S.L. (2009). Spinal compression during drop jump landings. *Unpublished MSc Thesis*, Loughborough University.

Brewin, M.A., Yeadon, M.R., Kerwin, D.G. (2000). Minimising peak forces at the shoulders during backward longswings on rings. *Human Movement Sciences*. **19**, 717-736.

Brody, D. (1982). Techniques in the evaluation and treatment of the injured runner. *Orthopedic Clinics of North America*. **13**, 542-558.

Caldwell, G.E. (2004). Muscle m,odeling (Eds. G.E. Robertson, G.E. Caldwell, J. Hamill, G. Kamen, S.N. Whittlesey*). Research Methods in Biomechanics*. Champaign: Human Kinetics.

Camosso, M.E., Marotti, G. (1962). The mechanical behaviour of articular cartilage under compressive stress. *Journal of Bone and Joint Surgery*. **44**, 699-709.

Carroll, D. L. (2001). FORTRAN genetic algorithm (GA) driver. http://cuaerospace. com/carroll/gatips. html.

Cashmere, T., Smith, R., Hunt, A. (1999). Medial longitudinal arch of the foot: stationary versus walking measures. *Foot and Ankle International*. **20**, 112-118.

Cavanagh, P.R., Valiant, G.A., Misevich, K.W. (1984). Biological aspects of modeling shoe/foot interaction during running. *In: Frederick, E.C. (Ed.), Sports Shoes and Playing Surfaces*. Human Kinetics Publishers, Champaign, IL, pp. 24–46.

Chandler, R.F., Clauser, C.E., McConville, J.T., Reynolds, H.M., Young, J.W. (1975). Investigation of inertial properties of the human body. AMRL-TR-74-137, AD-A016-485, DOT-HS-801-430. *Aerospace Medical Research Laboratories*, Wright-Patterson Air Force Base, Ohio

Chapman, A.E. (1985). The mechanical properties of human muscle. (Ed. R.L. Terjung). *Exercise and Sport Sciences Reviews*. **13**, 443-501. London: MacMillan.

Chow, J.W. (2001). Isokinetic exercise and knee joint forces during isokinetic knee extensions. *Proceedings of the 25th Annual Meeting of the American Society of Biomechanics*, pp127-128.

Chow, J.W., Darling, W.G., Hay, J.G. (1997). Mechanical characteristics of knee extension exercise performed on an isokinetic dynamometer. *Medicine and Science in Sports and Exercise*. **29**, 794-803.

Clarke, T.E., Cooper, L.B., Clark, D.E., Hamill, C.L. (1985). The effect of increased running speed upon peak shank deceleration during ground contact. *In D. Winter, R. Normal, R. Wells, K. Hayes, & A. Patla (Eds.), Biomechanics IX-B*, pp. 101-105. Champaign, E Human Kinetics.

Clarys, J.P., Marfell-Jones, M.J. (1986). Anthropometric prediction of component tissue masses in the minor limb segments of the human body. *Human Biology*, **58**, 761-769.

Clarys, J.P., Martin, A.D., Drinkwater, D.T. (1984). Gross tissue weights in the human body by cadaver dissection. *Human Biology*. **54**, 459-473.

Corana, A., Marchesi, M., Martini, C., Ridella, S. (1987). Minimizing multimodal functions of continuous variables with the "simulated annealing" algorithm. *ACM Transactions on Mathematical Software*. **13**, 262-280.

Coventry, E., O'Connor, K.M., Hart, B.A., Earl, J.E., Ebersole, K.T. (2006). The effect of lower extremity fatigue on shock attenuation during single-leg landing. *Clinical Biomechanics*. **21**, 1090-1097.

Dai, X.Q., Li, Y., Zhang, M., Cheung, J.T.M. (2006). Effect of sock on biomechanical responses of foot during walking. *Clinical Biomechanics*, **21**, 314-321.

Dapena, J. (1981). Simulation of modified human airborne movements. *Journal of Biomechanics*. **14**, 81-89.

Dapena, J. (1999). A biomechanical explanation of the effect of arm actions on the vertical velocity of a standing vertical jump. *Proceedings of the XVIIth Congress of the International Society of Biomechanics*.

Davis, R. B., Ounpuu, S., Tyburski, D., Gage, J. R. (1991). A gait analysis data collection and reduction technique. *Human Movement Science*, **10**, 575-587.

De Clercq, D., Aerts, P., Kunnen, M. (1994). The mechanical characteristics of the human heel pad during foot strike in running: an in vivo cineradiographic study. *Journal of Biomechanics*, **27**, 1213-1222.

Deep, K., Norris, M., Smart, C., Senior, C. (2003). Radiographic measurement of joint space height in non-osteoarthritic tibiofemoral joints. *Bone & Joint Journal*, **85**, 980-982.

Dempster, W.T. (1955). Space requirements of the seated operator. *Rpt-55-159. Wright-Patterson Air Force Base*: WADC.

Denoth, J. (1986) Load on the human locomotor system and modelling. Biomechanics of Running Shoes (Edited by Nigg, B. M.) pp. 63-l16. Human Kinetics, Champaign, IL.

Denoth, J., Nigg, B. M. (1981). The influence of various sports floors on the load on the lower extremities. *In Biomechanics VII-B (ed. A. Moreki, K. Fidelus, K. Kedzior, A. Wit)*, pp. 100-105. Baltimore, Maryland: University Park Press.

Derrick, T.R. (2004). The effects of knee contact angle on impact forces and accelerations. *Medicine and science in sports and exercise*, **36**, 832-837.

Devita P, Skelly W. (1992). Effect of landing stiffness on joint kinetics and energetics in the lower extremity. *Medicine and Science in Sports and Exercise*. **24**, 108-15.

Duda, G. N., Brand, D., Freitag, S., Lierse, W., Schneider, E. (1996). Variability of femoral muscle attachments. *Journal of Biomechanics*. **29**, 1185-1190.

Duda, G.N., Schneider, E., Chao, E.Y. (1997). Internal forces and moments in the femur during walking. *Journal of Biomechanics*. **30**, 933-941.

Dudley, G.A., Harris, R.T., Duvoisin, M.R., Hather, B.M. & Buchanan, P. (1990). Effect of voluntary vs. artificial activation on the relationship of muscle torque to speed. *Journal of Applied Physiology*. **69**, 2215-2221.

Durnin, J.V., Womersley, J.V.G.A. (1974). Body fat assessed from total body density and its estimation from skinfold thickness: measurements on 481 men and women aged from 16 to 72 years. *British Journal of Nutrition*, **32**(1), 77-97.

Edwards, J. (1966). Paper 6: Physical Characteristics of Articular Cartilage. *In Proceedings of the Institution of Mechanical Engineers, Conference Proceedings* **181**(10), 16-24. Sage UK: London, England: SAGE Publications.

Edwards, S., Steele, J.R., McGhee, D.E. (2010). Does a drop landing represent a whole skill landing and is this moderated by fatigue? *Scandinavian Journal of Medicine and Science in Sports*, **20**, 516-523.

Felton, P.J. (2014). Factors limiting fast bowling performance in cricket. Unpublished Doctoral Thesis, Loughborough University.

Finni, T., Komi, P.V. (2002). Two methods for estimating tendinous tissue elongation during human movement. *Journal of Applied Biomechanics*, **18**, 180-188.

Fiolkowski, P., Brunt, D., Bishop, M., Woo, R., Horodyski, M. (2003). Intrinsic pedal musculature support of the medial longitudinal arch: an electromyography study. *The Journal of foot and ankle surgery*, **42**, 327-333.

Forrester, S.E., Yeadon, M.R., King, M.A., Pain, M.T.G. (2011). Comparing different approaches for determining joint torque parameters from isovelocity dynamometer measurements. Journal of Biomechanics. **44**, 955-961.

Fragomen, A.T., McCoy, T.H., Meyers, K.N., Rozbruch, S.R. (2014). Minimum distraction gap: how much ankle joint space is enough in ankle distraction arthroplasty?. *HSS Journal*, **10**, 6-12.

Frederick, E.C. (1986). Kinematically mediated effects of sport shoe design: A review. *Journal of sports sciences*, **4**, 169-184.

Freund, H.J., Büdingen, H.J. (1978). The relationship between speed and amplitude of the fastest voluntary contractions of human arm muscles. *Experimental Brain Research*. **31**, 1-12.

Furlong, L.A.M., Kong, P.W., Pain, M.T. (2016). Soft tissue movement in the lower limb during drop jumps. *In ISBS-Conference Proceedings Archive*. **34**.

Gerritsen, K.G.M., van den Bogert, A.J., Nigg, B.M. (1995). Direct dynamics simulation of the impact phase in heel-toe running. *Journal of Biomechanics*. **28**, 661-668.

Gray, H. (1918). *Anatomy of the human body*. Philadelphia: Lea & Febiger.

Grieve, D. W., Pheasant, S., Cavanagh, P. R. (1978). Prediction of gastrocnemius length from knee and ankle joint posture. University Park Press, Baltimore, 405-412.

Gross, T.S., Nelson, R.C. (1988). The shock attenuation role of the ankle during landing from a vertical jump. *Medicine and Science in Sports and Exercise*. **20**, 506-514.

Gruber, K., Denoth, J., Stuessi, E., Ruder, H. (1987). The wobbling mass model. *In: Jonsson, B. (Ed.), Biomechanics X-B.* Human Kinetics Publishers, Champaign, pp. 1095-1105.

Gruber, K., Ruder, H., Denoth, J., Schneider, K. (1998). A comparative study of impact dynamics: wobbling mass model versus rigid body models. *Journal of Biomechanics*. **31**, 439-444.

Hageman, E.R., Hall, M., Sterner, E.G., Mirka, G.A. (2011). Medial longitudinal arch deformation during walking and stair navigation while carrying loads. *Foot & ankle international*, **32**, 623-629.

Hamill, J., Derrick, T.R., Holt, K.G. (1995). Shock attenuation and stride frequency during running. *Human Movement Science*. **14**, 45-60.

Hatze, H. (1981). A comprehensive model for human motion simulation and its application to the take-off phase of the long jump. *Journal of Biomechanics*. **3**, 135-142.

Headlee, D.L., Leonard, J.L., Hart, J M., Ingersoll, C.D., & Hertel, J. (2008). Fatigue of the plantar intrinsic foot muscles increases navicular drop. *Journal of Electromyography and Kinesiology,* **18**, 420-425.

Helliwell, P.S., Smeathers, J.E., Wright, V. (1989). Shock absorption by the spinal column in normal and in ankylosing spondylitis. *Proceedings of the Institute of Mechanical Engineers*, **203**, 187-190.

Hiley, M.J., Yeadon, M.R. (2003). The margin for error when releasing the high bar for dismounts. *Journal of Biomechanics*. **36**, 313-319.

Hill, A.V. (1938). The heat of shortening and the dynamic constants of muscle. *Proceedings of the Royal Society of London. Series B, Biological Sciences.* **126**(843), 136-195.

Hirsch, C. (1944) A contribution to the pathogenesis of chondromalacia of the patella. Acta Chirurgica Scandinavica. Supplementum, 83.

Holland, J.H. (1975). Adaptation in natural and artificial systems. *First edn*. Ann Arbor: University of Michigan Press.

Hoshino, A., Wallace, W.A. (1987). Impact-absorbing properties of the human knee. *British Editorial Society of Bone and Joint Surgery*. **69**, 807-811.

Huang, C., Kitaoka, H., An, K., Chao, E. (1993). Biomechanical evaluation of longitudinal arch stability. *Foot and Ankle International*. **14**, 353-357.

Huiskes, R. (1990). The various stress patterns of press-fit, ingrown, and cemented femoral stems. *Clinical Orthopaedics and Related Research*, **261**, 27-38.

Huxley, A.F. (1957). Muscle structure and theories of contraction. *Progress in Biophysics and Biophysical Chemistry*. **7**, 255-318.

Jackson, M.I. (2010). The mechanics of the table contact phase of gymnastics vaulting. *Unpublished Doctoral Thesis*, Loughborough University.

Jackson, M.I., Hiley, M.J., Yeadon, M.R. (2011). A comparison of Coulomb and pseudo-Coulomb friction implementations: applications to the table contact phase of gymnastics vaulting. *Journal of Biomechanics*. **44**, 2706-2711.

Jaiganesh, V., Dhileep Kumar, J., & Girija Devi, J. (2015). Replacement of intervertebral disc in spine by Poly (ethylene glycol) – diacrylate (PEGDA) material through Stereolithography. *Biomedical Research*, **26**, S22-25.

Jørgensen, U., Bojsen-Møller, F. (1989). Shock absorbency of factors in the shoe/heel interaction—with special focus on role of the heel pad. *Foot & ankle*, **9**(6), 294-299.

Ker, R.F., Bennett, M.B., Alexander, R.M., & Kester, R.C. (1989). Foot strike and the properties of the human heel pad. *Proceedings of the Institution of Mechanical Engineers, Part H: Journal of Engineering in Medicine*, **203**, 191-196.

King, M.A. (1998). Contributions to performance in dynamic jumps. *Unpublished Doctoral Thesis*, Loughborough University.

King, M.A., Yeadon, M.R. (2002). Determining subject specific torque parameters for use in a torque driven simulation model of dynamic jumping. *Journal of Applied Biomechanics*. **18**, 207-217.

King, M.A., Yeadon, M.R. (2004). Maximising somersault rotation in tumbling. *Journal of Biomechanics*. **37**, 471-477.

King, M.A., Wilson, C., Yeadon, M.R. (2006). Evaluation of a torque-driven model of jumping for height. *Journal of Applied Biomechanics*. **22**, 264-274.

King, M.A., Lewis, M.G.C., Yeadon, M.R. (2012). Is it necessary to include biarticular effects within joint torque representations of knee flexion and knee extension? *International Journal for Multiscale Computational Engineering*. **10**, 117-130.

Kinoshita, H., Ogawa, T., Kuzuhara, K., Ikuta, K. (1993). In vivo examination of the dynamic properties of the human heel pad. *International Journal of Sports Medicine*, **14**, 312-319

Kirkpatrick, S., Gelatt, C.D., Vecchi, M.P. (1983). Optimization by simulated annealing. *Science*. **220**(4598), 671-680.

Klein, P., Mattys, S., Rooze, M. (1996). Moment arm length variations of selected muscles acting on talocrural and subtalar joints during movement: An in vitro study. *Journal of Biomechanics*. **1**, 21-30.

Kong, P.W. (2005). Computer simulation of the take-off in springboard diving. *Unpublished Doctoral Thesis*, Loughborough University.

Kristianslund, E., Krosshaug, T., Van den Bogert, A.J. (2012). Effect of low pass filtering on joint moments from inverse dynamics: implications for injury prevention. *Journal of Biomechanics*, **45**, 666-671.

Kristianslund, E., Krosshaug, T., Van Den Bogert, A.J. (2013). Artefacts in measuring joint moments may lead to incorrect clinical conclusions: the nexus between science (biomechanics) and sports injury prevention!. . *British Journal of Sports Medicine*. **47**, 470-473.

Lafortune, M.A., Cavanagh, P.R., Sommer III, H.J., Kalenak, A. (1992). Three-dimensional kinematics of the human knee during walking. *Journal of Biomechanics*. **25**, 347-357.

Lafortune, M.A., Lake, M.J., Hennig, E.M. (1996). Differential shock transmission response of the human body to impact severity and lower limb posture. *Journal of biomechanics*, **29**, 1531-1537.

Langenderfer, J., Jerabek, S. A., Thangamani, V. B., Kuhn, J. E., Hughes, R. E. (2004). Musculoskeletal parameters of muscles crossing the shoulder and elbow and the effect of sarcomere length sample size on estimation of optimal muscle length. *Clinical Biomechanics*. **19**, 664-670.

Levine, W.S., Zajac, F.E., Cho, Y.M., Zomlefer, M.R. (1987). The bang-bang phase of maximal height jumps by humans. *IFAC Proceedings Volumes*, **20**(5), 31-36.

Lewis, M.G.C. (2011). Are torque-driven simulation models limited by an assumption of monoarticularity. *Unpublished Doctoral Thesis*, Loughborough University.

Lewis, M.G.C., King, M.A., Yeadon, M.R., Conceição, F. (2012). Are joint torque models limited by an assumption of monoarticularity? *Journal of Applied Biomechanics*. **28**, 520-529.

Light, L.H., McLellan, G.E., Klenerman, L. (1980). Skeletal transients on heel strike in normal walking with different footwear. *Journal of biomechanics*, **13**, 477-480.

Locatelli, M. (2000). Simulated annealing algorithms for continuous global optimization: convergence conditions. *Journal of Optimization Theory and Applications*. **104**, 121-133.

Madsen, O.R. (1996). Trunk extensor and flexor strength measured by the Cybex 6000 dynamometer. Assessment of short-term and long-term reproducibility of several strength variables. *Spine*. **21**, 2770-2776.

Marshall, B.M., Moran, K.A. (2013). Which drop jump technique is most effective at enhancing countermovement jump ability, “countermovement” drop jump or “bounce” drop jump? *Journal of Sports Sciences*, **31**, 1368-1374.

McConville, J.T., Clauser, C.E., Churchill, T.D., Cuzzi, J., Kaleps, I. (1980). Anthropometric relationships of body and body segment moments of inertia. Technical Report AFAMRL-TR-80-119. *Air Force Aerospace Medical Research Laboratory*, Wright-Patterson AFB, Ohio.

McCutchen, C. W. (1962). The frictional properties of animal joints. *Wear*, **5**(1), 1-17.

Mercer, J.A., Bates, B.T., Dufek, J.S., Hreljac,A. (2003). Characteristics of shock attenuation during fatigued running. *Journal of Sports Science*, **21**, 911-919.

Miller, D.I. (1971). A computer simulation of the airborne phase of diving. *In Selected Topics on Biomechanics (Ed. J.M. Cooper)*, pp. 207-215. Chicago: Athletic Institute.

Mills, C., Pain, M.T., Yeadon, M.R. (2008). The influence of simulation model complexity on the estimation of internal loading in gymnastics landings. *Journal of Biomechanics*, **41**, 620-628.

Minetti, A.E., & Belli, G. (1994). A model for the estimation of visceral mass displacement in periodic movements. *Journal of Biomechanics*, **27**, 97-101.

Mizrahi, J., Verbitsky, O., & Isakov, E. (2000). Shock accelerations and attenuation in downhill and level running. *Clinical Biomechanics*, **15**, 15-20.

Moran, K.A., Marshall, B.M. (2006). Effect of fatigue on tibial impact accelerations and knee kinematics in drop jumps. *Medicine and science in sports and exercise*, **38**, 1836-1842.

Muramatsu, T., Muraoka, T., Takeshita, D., Kawakami, Y., Hirano, Y., & Fukunaga, T. (2001). Mechanical properties of tendon and aponeurosis of human gastrocnemius muscle in vivo. *Journal of Applied Physiology*, **90**, 1671-1678.

Newland, D.E. (1984). Random vibrations and spectral analysis (2nd ed.). New York: Longman.

Nielsen, R.G., Rathleff, M.S., Simonsen, O.H., Langberg, H. (2009). Determination of normal values for navicular drop during walking: a new model correcting for foot length and gender. *Journal of foot and ankle research*, **2**, 12.

Nigg, B. M. & Denoth, J. (1980). Sportplatzbeldge. Zfurich: Juris Verlag.

Noe, D.A., Voto, S.J., Hoffmann, M.S., Askew, M.J., & Gradisar, I.A. (1993). Role of the calcaneal heel pad and polymeric shock absorbers in attenuation of heel strike impact. *Journal of biomedical engineering*, **15**, 23-26.

Oliver, J., Middleditch, A. (1991). Functional anatomy of the spine. *Elsevier Health Sciences.*

Osternig, L.R., Sawhill, J.A., Bates, B.T., Hamill, J. (1982). A method for rapid collection and processing of isokinetic data. *Research Quarterly for Exercise and Sport*. **53**, 252-256.

Out, L., Vrijkotte, T.G.M., van Soest, A.J., Bobbert, M.F. (1996). Influence of the parameters of a human triceps surae muscle model on the isometric torque-angle relationship. *Journal of Biomechanical Engineering*. **118**, 17-25.

Owen, B.M., Lee, D.N. (1986). Establishing a frame of reference for action. *In: M.G. Wade, H.T.A. Whiting (Eds.) Motor development in children: Aspects of coordination and control. NATO ASI_series D:34.* Dordrecht: Martimus Nyhoff.

Pain, M.T.G., Challis, J.H. (2001). The role of the heel pad and shank soft tissue during impacts: a further resolution of a paradox. *Journal of Biomechanics*. **34**, 327-333.

Pain, M.T., & Challis, J.H. (2002). Soft tissue motion during impacts: their potential contributions to energy dissipation. *Journal of Applied Biomechanics*, **18**, 231-242.

Pain, M. T., Challis, J. H. (2006). The influence of soft tissue movement on ground reaction forces, joint torques and joint reaction forces in drop landings. *Journal of Biomechanics*, **39**, 119-124.

Pandy, M.G. (2001). Computer modelling and simulation of human movement. *Annual Reviewsin Biomedical Engineering*. **3**, 245-273.

Pandy, M.G., Zajac, F.E. (1991). Optimal muscular coordination strategies for jumping. *Journal of Biomechanics*. **24**, 1-10.

Pandy, M.G., Zajac, F.E., Hoy, M.G., Topp, E.L., Tashman, S., Stevenson, P.J, ... & Levine, W.S. (1988). Sub-Optimal Control of a Maximum Height, Countermovenment Jump. *In Modeling and Control Issues in Biomechanical Systems, Proceedings of the ASME Winter Annual Meeting*, pp. 27-44.

Pandy, M.G., Zajac, F.E., Sim, E., Levine, W.S. (1990). An optimal control model for maximum-height human jumping. *Journal of Biomechanics*, **23**, 1185-1198.

Paul, I.L., Munro, M.B., Abernethy, P.J., Simon, S.R., Radin, E.L., Rose, R.M. (1978). Musculo-skeletal shock absorption: relative contribution of bone and soft tissues at various frequencies. *Journal of biomechanics*, **11**, 237-239.

Pavol, M. J., Grabiner, M. D. (2000). Knee strength variability between individuals across ranges of motion and hip angles. *Medicine and Science in Sports and Exercise*. **5**, 985-992.

Pierrynowski, M.R., 1995. Analytic representation of muscle line of action and geometry. *In: P. Allard, I.A.F. Stokes, J. Blanchi (eds), Three- Dimensional*

Analysis of Human Movement. Champaign, IL: Human Kinetics, pp. 215-256.

Pozzo, T.A., Berthoz, A., Lefort, L., Vitte, E. (1991). Head stabilisation during various locomotor tasks in humans. I. Patients with bilateral vestibular deficits. *Experimental Brain Research*. **85**, 208-217.

Prendergast, P.J., Taylor, D. (1990). Stress analysis of the proximo-medial femur after total hip replacement. *Journal of Biomedical Engineering*, **12**, 379-382.

Radin, E.L., Paul, I.L., Lowy, M. (1970). A comparison of the dynamic force transmitting properties of subchondral bone and articular cartilage. *The Journal of Bone and Joint Surgery*. **52**, 444-456.

Ranson, C., King, M., Burnett, A., Worthington, P., & Shine, K. (2009). The effect of coaching intervention on elite fast bowling technique over a two year period. *Sports Biomechanics*, **8**, 261-274.

Refshauge, K.M., Chan, R., Taylor, J.L., McCloskey, D.I. (1995). Detection of movements imposed on human hip, knee, ankle and toe joints. *The Journal of Physiology*, **488**, 231-241.

Riddick, R.C., & Kuo, A.D. (2016). Soft tissues store and return mechanical energy in human running. *Journal of Biomechanics*, **49**, 436-441.

Roosen, A. (2007). Skill reproduction in a reduced time-frame by martial athletes *Unpublished Doctoral Thesis*, Loughborough University.

Roughley, P.J., & White, R.J. (1980). Age-related changes in the structure of the proteoglycan subunits from human articular cartilage. *Journal of Biological Chemistry*, **255**(1), 217-224.

Rugg, S.G., Gregor, R.J., Mandelbaum, B.R., Chius, L. (1990). In vivo moment arm calculations at the ankle using magnetic resonance imaging (MRI). *Journal of Biomechanics*. **23**, 495-501.

Scovil, C. Y., Ronsky, J. L. (2006). Sensitivity of a Hill-based muscle model to perturbations in model parameters. *Journal of Biomechanics*. **39**, 2055-2063.

Selbie, W.S., Caldwell, G.E. (1996). A simulation study of vertical jumping from different starting postures. *Journal of Biomechanics*. **29**, 1137-1146.

Shorten, M.R., Winslow, D.S. (1992). Spectral analysis of impact shock during running. *International Journal of Sport Biomechanics*, **8**, 288-304.

Simkin, A., Leichter, I., Giladi, M., Stein, M., Milgrom, C. (1989). Combined effect of foot arch structure and an orthotic device on stress fractures. *Foot and Ankle*. **10**, 25-29.

Smeathers, J.E. (1984). Some time dependent properties of the intervertebral joint when under compression. *Engineering in Medicine*, **13**, 83-87.

Smeathers, J.E., Joanes, D.N. (1988). Dynamic compressive properties of human lumbar intervertebral joints: a comparison between fresh and thawed specimens*. Journal of Biomechanics*, **21**, 425-433.

Snook, A.G. (2001). The relationship between excessive pronation as measured by navicular drop and isokinetic strength of the ankle musculature. *Foot & ankle international*, **22**, 234-240.

Spoor, C. W., van Leewun, J. L., Meskers, C. G., Titulaer, A. F., Huson, A. (1990). Estimation of instantaneous moment arms of the lower-leg muscles. *Journal of Biomechanics*. **12**, 1247-1259.

Taylor, M.E., Tanner, K.E., Freeman, M.A.R., Yettram, A.L. (1996). Stress and strain distribution within the intact femur: compression or bending?. *Medical Engineering & Physics*, **18**, 122-131.

Tensi, H.M., Gese, H., Ascherl, R. (1989). Non-linear three-dimensional finite element analysis of a cementless hip endoprosthesis. *Proceedings of the Institution of Mechanical Engineers, Part H: Journal of Engineering in Medicine*, **203**, 215-222.

Umberger, B. R., Gerritsen, K. G., Martin, P. E. (2006). Muscle fiber type effects on energetically optimal cadences in cycling. *Journal of Biomechanics*. **8**, 1472-1479.

Valiant, G.A. (1990). Transmission and attenuation of heelstrike acceleration. *In: P.R. Cavanagh (Ed.), Biomechanics of distancerunning*. Champaign, IL: Human Kinetics, pp. 228-229.

Valiant, G.A. & Cavanagh, P.R. (1984). An (in vivo) determinantion of the mechanical characteristics of the human heel pad. *Proceedings of the American Society for Biomechanics*, pp. 61-62. Tucson, Arizona.

Valiant, G.A., & Cavanagh, P.R. (1985). An in vivo determination of the mechanical characteristics of the human heel pad. *Journal of Biomechanics*, **18**, 242.

Valiant, G.A., McMahon, T.A., Frederick, E.C. (1987). A new test to evaluate the cushioning properties of athletic shoes. I*n B. Jonsson (Ed.), Biomechanics X-B*, pp. 937-941. Champaign, IL: Human Kinetics.

Van den Bogert, A.J., De Koning, J.J. (1996). On optimal filtering for inverse dynamics analysis. *In Proceedings of the IXth biennial conference of the Canadian society for biomechanics,* pp. 214-215. Vancouver: Simon Fraser University.

Van der Helm, F.C. (1994). Analysis of the kinematic and dynamic behavior of the shoulder mechanism. *Journal of Biomechanics*, **27**, 527-550.

Van Soest, A.J., Bobbert, M.F. (1993). The contribution of muscle properties in the control of explosive movements. *Biological Cybernetics*. **69**, 195-204.

Van Soest, A.J., Casius, L.J.R. (2003). The merits of a parallel genetic algorithm in solving hard optimisation problems. *Journal of Biomechanical Engineering*. **125**, 141-146.

Van Soest, A.J., Schwab, A.L., Bobbert, M.F., Van Ingen Schenau, G.J. (1993). The influence of the biarticularity of the gastrocnemius muscle on vertical-jumping achievement. *Journal of Biomechanics*. **26**, 1-8.

Vanrenterghem, J., Bobbert, M.F., Casius, L.J.R., De Clercq, D. (2008). Is energy expenditure taken into account in human sub-maximal jumping? – A simulation study. *Journal of Electromyography and Kinesiology*. **18**(1), 108-115.

Verdejo, R., Mills, N. J. (2004). Heel–shoe interactions and the durability of EVA foam running-shoe midsoles. *Journal of Biomechanics*, **37**, 1379-1386.

Verdonschot, N., Huiskes, R., Freeman, M.A.R. (1993). Pre-clinical testing of hip prosthetic designs: a comparison of finite element calculations and laboratory tests. *Proceedings of the Institution of Mechanical Engineers Part H - Journal of Engineering in Medicine.* **207**, 149-154.

Visser, J. J., Hoogkamer, J. E., Bobbert, M. F., Huijing, P. A. (1990). Length and moment arm of human leg muscles as a function of knee and hip-joint angles. *European Journal of Applied Physiology and Occupational Physiology*. **61**, 453-460.

Webber, S., Kriellers, D. (1997). Neuromuscular factors contributing to in vivo eccentric moment generation. *Journal of Applied Physiology*. **83**, 40-45.

Wilson, C. (2003). Optimisation of performance in running jumps. *Unpublished Doctoral Thesis*, Loughborough University.

Wilson, C., King, M.A., Yeadon, M.R. (2006). Determination of subject-specific model parameters for visco-elastic elements. *Journal of Biomechanics*. **39**, 1883-1890.

Winter, D. A. (1990). Biomechanics and motor control of human movement. Wiley, New York.

Wood, G.A., Jennings, L.S. (1979). On the use of spline functions for data smoothing. *Journal of Biomechanics*. **12**, 477-479.

Wright, I.C., Neptune, R.R., van den Bogert, A.J., Nigg, B.M. (1998). Passive regulation of impact forces in heel-toe running. *Clinical Biomechanics*. **13**, 521-531.

Yamada, K., Healey, R., Amiel, D., Lotz, M., Coutts, R. (2002). Subchondral bone of the human knee joint in aging and osteoarthritis. *Osteoarthritis and Cartilage*. **10**, 360–369.

Yang, G., Reinstein, L.E., Pai, S., Xu, Z., Carroll, D.L. (1998). A new genetic algorithm technique in optimization of permanent 125I prostate implants. *Medical Physics*, **25**, 2308-2315.

Yeadon, M. R. (1990). The simulation of aerial movement - II. A mathematical inertia model of the human body. *Journal of Biomechanics*. **23**, 67-74.

Yeadon, M.R., Atha, J., Hales, F.D. (1990). The simulation of aerial movement – IV: A computer simulation model. *Journal of Biomechanics.* **25**, 85-89.

Yeadon, M.R., Hiley, M.J. (2000). The mechanics of the backward giant circle on the high bar. *Human Movement Sciences*. **19**, 153-173.

Yeadon, M.R., King, M.A. (2002). Evaluation of a torque-driven simulation model of tumbling. *Journal of Applied Biomechanics*. **18**, 195-206.

Yeadon, M.R., King, M.A. (2008). *Biomechanical simulation models of sports activities, In Handbook of Biomechanics and Human Movement Science, Hong, Y., Bartlett, R.M. (eds)*. Routledge, Oxford, UK, 367-382.

Yeadon, M.R., King, M.A., Forrester, S.E., Caldwell, G.E., Pain, M.T.G. (2010). The need for muscle co-contraction prior to a landing. *Journal of Biomechanics.* **43**, 364-369.

Yeadon, M.R., King, M.A., Wilson, C. (2006). Modelling the maximum voluntary joint torque/angular velocity relationship in human movement. *Journal of Biomechanics*. **39**, 476-482.

Young, W.B., Pryor, J.F., Wilson, G.J. (1995). Effect of instructions on characteristics of countermovement and drop jump performance. Journal of Strength and Conditioning Research, 9, 232-236.

Zajac, F.E., Wicke, R.W., Levine, W.S. (1984). Dependence of jumping performance on muscle properties when humans use only calf muscles for propulsion. *Journal of Biomechanics*. **17**(7), 513-523.

Zhang,S-N., Bates, B.T., Dufek, J.S. (1998). Contributions of lower extremity joints to energy dissipation during landings. *Medicine and Science in Sports and Exercise*. **32**, 812-819.

Zhang, S., Derrick, T.R., Evans, W., Yu, Y.-J. (2008). Shock and impact reduction in moderate and strenuous landing activities. *Sports Biomechanics*. **7**, 296-309.

Ziegert, J.C., Lewis, J.L. (1979). The effect of soft tissues on measurements of vibrational bone motion by skin-mounted accelerometers. *Journal of Biomechanical Engineering*. **101**, 218-220.

APPENDIX 1: PARTICIPANT INFORMATION SHEET

The effect of joint compliance within rigid whole-body computer simulations of impacts

Participant Information Sheet

Main investigator: Mr Stuart McErlain-Naylor, S.A.McErlain-Naylor@lboro.ac.uk
Supervisors: Dr Mark King, M.A.King@lboro.ac.uk
Dr Sam Allen, S.J.Allen@lboro.ac.uk

What is the purpose of the study?

To investigate the effect of incorporating joint compliance on the ability of a computer simulation model to accurately predict ground forces during dynamic jumping activities. Furthermore, the study aims to utilise this simulation model to investigate the complex relationships between strength, technique, and variability in dynamic jumping performance.

Impact forces of up to 13 times bodyweight have been observed in dynamic jumping activities such as the triple jump. It has long been accepted that the human skeletal system is capable of damping such impact shock waves and avoiding direct transmission of impact forces to internal structures. The force attenuating mechanisms responsible, however, have previously been overlooked in whole-body computer simulation modelling in aid of simplistic representations. This has led to unrealistic transfer of force and acceleration throughout the body and hence difficulty in accurately reproducing experimentally measured forces at the ground. This study will provide information regarding the required model complexity for accurate ground reaction force prediction during dynamic jumps.

Who is doing this research and why?

This study is part of a PhD research project supported by Loughborough University. The testing will be run by Stuart McErlain-Naylor (Sports Biomechanics PhD student at the School of Sport, Exercise and Health Sciences, Loughborough University) under the supervision of Dr Mark King and Dr Sam Allen.

Are there any exclusion criteria?

You must not present any medical complaints that may prevent you from safely and successfully completing the physical tests. Any subjects with existing musculoskeletal injuries will be excluded. You are required to complete a full health screen questionnaire prior to the start of the study.

Once I take part, can I change my mind?

Yes! After you have read this information and asked any questions you may have you will be asked to complete an Informed Consent Form. However if at any time, before, during or after the sessions you wish to withdraw from the study please just contact the main investigator. You can withdraw at any time, for any reason and you will not be asked to explain your reasons for withdrawing. If you are a student at the University, your decision to withdraw will not have any bearing on your academic progress.

Will I be required to attend any sessions and where will these be?

You will be required to attend a laboratory in the Performance Centre on one occasion, followed by a laboratory in the Wavy Top building on two occasions. These will involve 1) maximal dynamic jumping (drop jumps; and running jumps for height and distance) performances in the Performance Centre; and 2) maximal ankle, knee, hip, shoulder, and elbow strength testing in the Wavy Top building.

How long will it take?

It will take approximately 2 hours for the first session in the Performance Centre and around 2.5 hours for each session in the Wavy Top building. The total time requirement of participation will therefore be approximately 7 hours in total.

Is there anything I need to do before the sessions?

Participants are required to be prepared and in condition for maximum physical effort. The requirements are therefore as follows: 1) refrain from atypical or strenuous exercise for 12 hours prior to each session; and 2) have eaten, drunk and slept normally in the previous 24 hours.

Is there anything I need to bring with me?

No.

What type of clothing should I wear?

You are required to wear shorts during all testing sessions, and your typical trainers for the dynamic jumps in the first session. Shorts will be provided should you not have any that are appropriate. You will be required to be topless for the duration of the first testing session.

What will I be asked to do?

At the first testing session you will be required to complete a health screen questionnaire and provide written consent prior to your participation in the study. You will then have a number of measurements taken. These involve measuring the length and circumference, etc. of different parts of your body (the four limbs, for example). You will then have a number of small reflective markers placed over specific points on the body (mainly key joint centres). The locations of these markers will be tracked by an automatic motion capture system. Six lightweight accelerometers will also be taped to your body. You will be required to perform two drop landings and two maximal effort vertical drop jumping trials from a range of four

drop heights (0.30 – 0.75 m) as well as three running jumps for each of maximal height and distance. A photographic example of the marker locations is displayed below:

At the second and third testing sessions you will be asked to perform strength testing (Session two: knee and hip; Session three: ankle; shoulder; and elbow) on a dynamometer (a device for measuring force, torque, or power; below). All trials will involve maximum effort; these may be isometric force application (no movement at the joint) or isovelocity (constant velocity movement over a range of velocities within normal physical function). Isometric trials will last 3 seconds and isovelocity trials up to 10 seconds. A recovery period of no less than 60 seconds will be given between trials.

What personal information will be required from me?

Basic descriptive data including your age, height and body mass will be collected. You will also be asked to complete a very brief questionnaire detailing your health status.

Are there any risks in participating?

Repeating maximal voluntary contractions involves physical effort that can cause sensations of fatigue. Any associated discomfort would be minor and short-term, with any delayed muscle soreness lasting no longer than 2-3 days. Maximal voluntary contractions also cause a brief increase in blood pressure, as is the case for any forceful muscle contraction. For healthy individuals this is not regarded as dangerous in any way. There is a potential, however unlikely, risk of muscle strain during the maximal contractions. Should a participant perceive excessive discomfort at any point, appropriate rest or treatment will be organised and participants are free to withdraw at any time.

Will my taking part in this study be kept confidential?

All data will be computerised and will be stored and processed in accordance with the Data Protection Act 1998. The data will be classified alphanumerically, rather than by name, for confidentiality purposes. Individual participants will not be referred to directly in any written pieces and participant details will be provided anonymously. Participants' confidentiality will not be breached.

What will happen to the results of the study?

The results will be submitted as part of a PhD thesis supported by Loughborough University and the key results submitted for publication in peer reviewed journals. Information regarding individual participants will remain confidential.

What do I get for participating?

If interested, you may receive information regarding the maximum strength profile at the joints tested and/or 3D motion capture feedback of your dynamic jumping performances. Persons participating in the pilot study have commented on the particularly enjoyable experience of the first testing session. Finally, university students may gain valuable experience of involvement in a research project.

I have some more questions. Who should I contact?

Any further questions should be directed in the first instance to Stuart McErlain-Naylor (Main Investigator). All contact details are provided on the first page.

What if I am not happy with how the research was conducted?

If you are not happy with how the research was conducted, please contact Mrs Zoe Stockdale, the Secretary for the University's Ethics Approvals (Human Participants) Sub-Committee:

Mrs Z Stockdale, Research Office, Rutland Building, Loughborough University, Epinal Way, Loughborough, LE11 3TU. Tel: 01509 222423. Email: Z.C.Stockdale@lboro.ac.uk

The University also has a policy relating to Research Misconduct and Whistle Blowing which is available online at:
http://www.lboro.ac.uk/admin/committees/ethical/Whistleblowing(2).htm.

APPENDIX 2: HEALTH SCREEN QUESTIONNAIRE

Loughborough University

Name .....

Health Screen Questionnaire for Study Volunteers

As a volunteer participating in a research study, it is important that you are currently in good health and have had no significant medical problems in the past. This is (i) to ensure your own continuing well-being and (ii) to avoid the possibility of individual health issues confounding study outcomes.

Please complete this brief questionnaire to confirm your fitness to participate:

1. **At present,** do you have any health problem for which you are:

(a)	on medication, prescribed or otherwise	Yes ☐	No ☐
(b)	attending your general practitioner.....	Yes ☐	No ☐
(c)	on a hospital waiting list	Yes ☐	No ☐

2. **In the past two years,** have you had any illness which required you to:

(a)	consult your GP	Yes ☐	No ☐
(b)	attend a hospital outpatient department.....	Yes ☐	No ☐
(c)	be admitted to hospital	Yes ☐	No ☐

3. **Have you ever** had any of the following:

(a)	Convulsions/epilepsy	Yes ☐	No ☐
(b)	Asthma	Yes ☐	No ☐
(c)	Eczema	Yes ☐	No ☐
(d)	Diabetes	Yes ☐	No ☐

(e)	A blood disorder	Yes		No	
(f)	Head injury	Yes		No	
(g)	Digestive problems	Yes		No	
(h)	Heart problems	Yes		No	
(i)	Problems with bones or joints	Yes		No	
(j)	Disturbance of balance/coordination	Yes		No	
(k)	Numbness in hands or feet	Yes		No	
(l)	Disturbance of vision	Yes		No	
(m)	Ear / hearing problems	Yes		No	
(n)	Thyroid problems	Yes		No	
(o)	Kidney or liver problems	Yes		No	
(p)	Allergy to nuts	Yes		No	

4. **Has any,** otherwise healthy, member of your family under the age of 35 died suddenly during or soon after exercise? ..... Yes ☐ No ☐

If YES to any question, please describe briefly if you wish (eg to confirm problem was/is short-lived, insignificant or well controlled.)

.....

.....

.....

5. **Allergy Information**

(a)	are you allergic to any food products?	Yes		No	
(b)	are you allergic to any medicines?	Yes		No	
(c)	are you allergic to plasters?	Yes		No	

If YES to any of the above, please provide additional information on the allergy

……

……

6. Please provide contact details of a suitable person for us to contact in the event of any incident or emergency.

Name: …….

Telephone Number: ……..

Work ☐ Home ☐ Mobile ☐

Relationship to

Participant:……

Are you currently involved in any other research studies at the University or elsewhere?

Yes ☐ No ☐

If yes, please provide details of the study

APPENDIX 3: INFORMED CONSENT FORM

Loughborough University

The effect of joint compliance within rigid whole-body computer simulations of impacts

INFORMED CONSENT FORM

(to be completed after Participant Information Sheet has been read)

The purpose and details of this study have been explained to me. I understand that this study is designed to further scientific knowledge and that all procedures have been approved by the Loughborough University Ethical Approvals (Human Participants) Sub-Committee.

I have read and understood the information sheet and this consent form.

I have had an opportunity to ask questions about my participation.

I understand that I am under no obligation to take part in the study.

I understand that I have the right to withdraw from this study at any stage for any reason, and that I will not be required to explain my reasons for withdrawing.

I understand that all the information I provide will be treated in strict confidence and will be kept anonymous and confidential to the researchers unless (under the statutory obligations of the agencies which the researchers are working with), it is judged that confidentiality will have to be breached for the safety of the participant or others.

I agree to participate in this study.

Your name _____

Your signature _____

Signature of investigator _____

Date _____

APPENDIX 4: SIMULATION MODEL AUTOLEV™ CODE

```
%% TD_v2.al
%% ======================================================
%%
%% Stuart McErlain-Naylor (2016)
%% ======================================================
%%
%% torque-driven full-body simulation model,
%% incorporating compliance within joints (2-part feet; 2-part back)
%% 9 rigid segments
%% 3 wobbling masses
%% accelerometer points
%% springs at floor, ankles, knees, hips, mid-spine, and shoulders
%% shoulders that moves along upper trunk according to shoulder angle
% ======================================================
%
% INITIAL DECLARATIONS
% ======================================================
newtonian n
% this defines a newtonian reference frame, with 3 orthogonal axes
% (n1,n2,n3) where n1 is right, n2 is up, and n3 is 'n1 about n2'
autoz on
% uses z notation; simplifies the output equations
% ======================================================
%
% DEFINING RIGID SEGMENTS
% ======================================================
bodies a %% right toes
bodies c %% right rear-foot
bodies e %% right shank
bodies g %% right thigh
bodies i %% lower trunk
bodies j %% upper trunk
bodies k %% head & neck
bodies l %% right upper arm
bodies r %% right forearm & hand; n,o,p,q used elsewhere / confusing
% form triangular rear-foot segments:
frames framerf %% reference frame for right triangular foot
% ======================================================
%
% DEFINING WOBBLING MASS SEGMENTS
% ======================================================
bodies ew %% right shank wobbling mass
bodies gw %% right thigh wobbling mass
bodies ijw %% trunk wobbling mass
% ======================================================
%
% DEFINING POINTS - ORIGIN, RIGID BODY, CENTRE OF MASS
% ======================================================
points o %% origin
points p1 %% right toe
```

```
points p3 %% right MTP
points p5 %% right heel
points p7 %% right inferior ankle
points p9 %% right superior ankle
points p11 %% right inferior knee
points p13 %% right superior knee
points p15 %% inferior hip
points p16 %% superior hip
points p17 %% inferior mid-trunk
points p18 %% superior mid-trunk
points p19 %% neck
points p20 %% head
points p21 %% right shoulder insertion on trunk
points p23 %% right shoulder joint (proximal upper arm)
points p25 %% right elbow
points p27 %% right wrist
points CM %% centre of mass
points co1,co2 %% define the two rear-foot CoM components (along ankle to MTP and
along heel to MTP) as points
% ======================================================
%
% DEFINING POINTS - ACCELEROMETER POSITIONS
% ======================================================
points p29 %% right MTP accelerometer position
points p30 %% right distal shank accelerometer position
points p31 %% right proximal shank accelerometer position
points p32 %% right distal thigh accelerometer position
points p33 %% lower back accelerometer position
points p34 %% lower neck accelerometer position
% ======================================================
%
% DEFINING POINTS - WOBBLING MASSES
% ======================================================
points p35 %% distal right shank wobbling mass
points p37 %% proximal right shank wobbling mass
points p39 %% distal right thigh wobbling mass
points p41 %% proximal right thigh wobbling mass
points p43 %% lower end of trunk wobbling mass
points p44 %% upper end of trunk wobbling mass
% ======================================================
%
% DECLARE MASSES - RIGID BODIES
% ======================================================
mass a = ma
mass c = mc
mass e = me
mass g = mg
mass i = mi
mass j = mj
mass k = mk
mass l = ml
mass r = mr
```

```
% ======================================================
%
% DECLARE MASSES - WOBBLING MASSES
% ======================================================
mass ew = mew
mass gw = mgw
mass ijw = mijw
% ======================================================
%
% DECLARE MASSES – WHOLE-BODY MASS
% ======================================================
mWB = ma + mc + me + mg + mi + mj + mk + ml + mr + mew + mgw + mijw
% ======================================================
%
% DECLARE MOMENTS OF INERTIA - RIGID BODIES
% ======================================================
inertia a,0,0,ia
% e.g. body a has moments of inertia about a1>, a2>, and a3> of 0,0, and ia
respectively (it is 2D)
inertia c,0,0,ic
inertia e,0,0,ie
inertia g,0,0,ig
inertia i,0,0,ii
inertia j,0,0,ij
inertia k,0,0,ik
inertia l,0,0,il
inertia r,0,0,ir
% ======================================================
%
% DECLARE MOMENTS OF INERTIA - WOBBLING MASSES
% ======================================================
inertia ew,0,0,iew
inertia gw,0,0,igw
inertia ijw,0,0,iijw
%
================================================================================
%
% DEFINE SEGMENT LENGTHS AND CENTRE OF MASS DISTANCES FROM THE PROXIMAL JOINT -
RIGID BODIES
%
================================================================================
constants la,lao %% e.g. la = right toe segment length; lao = CoM distance from
MTP (proximal)
constants lc1,lco1 %% along the line from inferior ankle to MTP
constants lc2,lco2 %% along the line from heel to MTP
constants thetarfoot %% angle of right rear-foot segment
constants le,leo
constants lg,lgo
constants li,lio
constants lj,ljo
constants lk,lko
constants ll,llo
```

```
constants lr,lro
% ============================================================
%
% DEFINE SEGMENT LENGTHS AND CENTRE OF MASS DISTANCES FROM THE PROXIMAL JOINT -
WOBBLING MASSES
% ============================================================
constants lew,lewo
constants lgw,lgwo
% trunk wobbling mass length will vary as the distance between the ends of the
upper and lower trunk segments (calculated (specified) later on)
% these will vary in distance apart due to the spring between the two segments
% trunk wobbling mass centre of mass distance to vary as a percentage of the
distance along the wobbling segment (lijwopercent as a constant used to calculate
(specify) lijwo later on)
constants lijwopercent
% ============================================================
%
% DEFINE ACCELEROMETER POSITION DISTANCES FROM THE PROXIMAL JOINT
% ============================================================
constants lacc1 %% 1MTP from ankle towards MTP
constants lacc2 %% distal shank from knee towards ankle
constants lacc3 %% proximal shank from knee towards ankle
constants lacc4 %% distal thigh from hip towards knee
constants lacc5 %% lower back from hip towards mid-trunk
constants lacc6 %% lower neck from neck towards head
% ============================================================
%
% DEFINE GROUND CONTACT PARAMETERS - HORIZONTAL
% ============================================================
constants ksy1,ksy2,kdy1 %% stiffness and damping (like vertical - to represent
foot-in-shoe and shoe-on-ground (same parameters at all points)
variables ry1,ry3,ry5 %% horizontal GRF exerted at points 1,3,5
variables GRFyr, GRFy %% total horizontal GRF at right foot, overall (equals
right foot when only one leg)
% ============================================================
%
% DEFINE GROUND CONTACT PARAMETERS - VERTICAL
% ============================================================
constants ks1,kd1,ks17 %% shoe and plantar soft tissue
% non-linear: ks1 = linear stiffness; kd1 = damping; ks17 = non-linear stiffness
constants ks2,ks3,kd2 %% heel pad - ks2 = linear stiffness; ks3 = non-linear
stiffness; kd2 = damping
variables rz1,rz3,rz5 %% spring vertical GRF at R toe (1), R MTP (3), R heel(5)
variables PEs1,PEs3,PEs5 %% spring potential energy (PEs) at R toe (1), R MTP
(3), R heel(5)
variables GRFzr,GRFz %% total vertical GRF at right foot, overall (equals right
foot when only one leg)
variables GRFresr,GRFres %% resultant GRF at right foot, overall (equals right
foot when only one leg)
variables CoPr,COP %% centre of pressure right, overall (equals right foot when
only one leg)
% ============================================================
```

```
%
% DEFINE SPRING PARAMETERS - WOBBLING MASSES
% ============================================================
constants ks6,kd6 %% both shanks (both limbs and both ends equal parameters)
constants ks7,kd7 %% both thighs
constants ks8,kd8 %% trunk
variables rs1,rs3,rs5,rs7,rs9,rs10 %% spring force (rs) for R distal shank wm
(1), R proximal shank wm (3), R distal thigh wm (5), R proximal thigh wm (7),
proximal trunk wm (9), distal trunk wm (10)
variables PEsew,PEsgw,PEsijw %% potential energy (PE) for the wobbling bodies (in
springs)
specified stretch{1:10}',velocity{1:10} %% 1-6 stretch and velocity for each
wobbling mass spring, listed and specified later %% 7-10 stretch and velocity for
R ankle, R knee, hip, shoulder listed and specified later
% ============================================================
%
% DEFINE SPRING PARAMETERS - COMPLIANT JOINTS
% ============================================================
constants ks9,kd9,ks11,kd11,ks13,kd13,ks15,kd15,ks16,kd16 %% non-linear, similar
to wobbling masses; along unit vectors (like wobbling masses); ks = stiffness
(^3); kd = damping; numbered locations below)
% 9 - ankles (unit vector)
% 11 - knees (unit vector)
% 13 - hips (unit vector)
% 15 - mid trunk (longitudinal along lower trunk)
% 16 - shoulders (unit vector)
variables rsy11,rsy13,rsy15,rs16,rsz17 %% force (rs) of springs at numbered
locations below
variables PEsy11,PEsy13,PEsy15,PEs16,PEsz17 %% potential energy (PEs) of springs
at numbered locations below
% y11 - right ankle
% y12 - left ankle
% y13 - right knee
% y14 - left knee
% y15 - hip
% 16 - mid trunk longitudinal
% z17 - right shoulder
% z18 - left shoulder
% ============================================================
%
% DEFINE TOTAL ENERGIES
% ============================================================
variables PEsT %% total PE in springs
variables PECM %% potential energy of centre of mass
variables PEtot %% total potential energy of system
variables KECM %% total kinetic energy of centre of mass
variables TENERGY %% total system energy
% kinetic energy of different bodies:
variables kea,kec,kee,keg,kei,kej,kek,kel,ker,keew,kegw,keijw
% potential energy of different bodies:
variables pea,pec,pee,peg,pei,pej,pek,pel,per,peew,pegw,peijw
% ============================================================
```

```
%
% DEFINE GRAVITY
% ============================================================
constants g %% gravity
%
================================================================================
%
% DECLARE GENERALISED DEGREES OF FREEDOM (E.G., DISPLACEMENTS) AND THEIR TIME
DERIVATIVES (angle inputs to be edited in fortran)
%
================================================================================
variables q{1:27}'
variables ACA,AEC,AGE,AIG,ALJ,ARL,LTWM,LTWMCM,SHDIST
variables AVCA,AVEC,AVGE,AVIG,AVLJ,AVRL
ACA=q22
AEC=q23
AGE=q24
AIG=q25
ALJ=q26
ARL=q27
constant AKJ
% q1 and q2 are the position of p1 (right toe) in the n1> and n2> directions
respectively - right toe coordinates
% q3 is the orientation angle of the trunk about the world n3> (anticlockwise) -
orientation angle
% ACA is the angular displacement of the right rear-foot (c) about the right toes
a3> (anticlockwise) - right MTP
% AEC is the angular displacement of the right shank (e) about the right foot c3>
(anticlockwise) - right ankle
% AGE is the angular displacement of the right thigh (g) about the right shank
e3> (anticlockwise) - right knee
% AIG is the angular displacement of the lower trunk (i) about the right thigh
g3> (anticlockwise) - right hip
% AKJ is the angular displacement of the head & neck (k) about the upper trunk
j3> (anticlockwise) - neck
% ALJ is the angular displacement of the right upper arm (l) about the upper
trunk j3> (anticlockwise) - right shoulder
% ARL is the angular displacement of the right forearm & hand (r) about the right
upper arm l3> (anticlockwise) - right elbow
% q4 is the angular displacement of the right shank wobbling mass (ew) about the
right shank e3> (anticlockwise) - right shank wobbling mass
% q5 is the angular displacement of the right thigh wobbling mass (gw) about the
right thigh g3> (anticlockwise) - right thigh wobbling mass
% q6 is the angular displacement of the trunk wobbling mass (ijw) about the trunk
i3> (anticlockwise) - trunk wobbling mass
% q7 is the right shank wobbling mass perpendicular spring displacement - distal
% q8 is the right shank wobbling mass longitudinal spring displacement - distal
% q9 is the right thigh wobbling mass perpendicular spring displacement - distal
% q10 is the right thigh wobbling mass longitudinal spring displacement - distal
% q11 is the trunk wobbling mass perpendicular spring displacement - proximal
% q12 is the trunk wobbling mass longitudinal spring displacement - proximal
% q13 is the right ankle horizontal spring displacement
```

```
% q14 is the right ankle vertical spring displacement
% q15 is the right knee horizontal spring displacement
% q16 is the right knee vertical spring displacement
% q17 is the hip horizontal spring displacement
% q18 is the hip vertical spring displacement
% q19 is the mid-trunk longitudinal spring displacement
% q20 is the right shoulder horizontal spring displacement
% q21 is the right shoulder vertical spring displacement
% q22 = MTP angle
% q23 = ankle angle
% q24 = knee angle
% q25 = hip angle
% q26 = shoulder angle
% q27 = elbow angle
% LTWM is the trunk wobbling mass length
% LTWMCM is the trunk wobbling mass centre of mass distance from the hip along
the segment
% SHDIST is the right shoulder insertion distance along the upper trunk from
superior mid-trunk towards neck
%
==========================================================================
%
% DECLARE CONSTANT ANGLE BETWEEN THE TWO TRUNK SEGMENTS (180 DEG OR PI RAD)
%
==========================================================================
constants trunkang %% the angular displacement of upper trunk (j) about lower
trunk i3> (anticlockwise) - constant at 180 deg or pi radians (straight line with
longitudinal only spring
%
==========================================================================
%
% DECLARE DIFFERENTIALS OF GENERALISED DEGREES OF FREEDOM (E.G., VELOCITIES) AND
THEIR TIME DERIVATIVES
%
==========================================================================
variables u{1:27}' %% differentials (u's) of the degrees of freedom (q's) listed
above
AVCA=u22
AVEC=u23
AVGE=u24
AVIG=u25
AVLJ=u26
AVRL=u27
%
==========================================================================
%
% KINEMATIC DIFFERENTIAL EQUATIONS RELATING TIME DERIVATIVES OF GENERALISED
DEGREES OF FREEDOM TO THE MOTION VARIABLES
%
==========================================================================
q1'=u1 %% u1 is the first derivative of q1 with respect to time
q2'=u2
```

```
q3'=u3
q4'=u4
q5'=u5
q6'=u6
q7'=u7
q8'=u8
q9'=u9
q10'=u10
q11'=u11
q12'=u12
q13'=u13
q14'=u14
q15'=u15
q16'=u16
q17'=u17
q18'=u18
q19'=u19
q20'=u20
q21'=u21
q22'=u22
q23'=u23
q24'=u24
q25'=u25
q26'=u26
q27'=u27
% ============================================================
%
% CREATE VARIABLES FOR 2D COORDINATES, VELOCITIES, AND ACCLERATIONS
% ============================================================
% 2D coordinates of each of the points in the modelL
variables
poCMy,poCMz,pop1y,pop1z,pop3y,pop3z,pop5y,pop5z,pop7y,pop7z,pop9y,pop9z,pop11y,po
p11z,pop13y,pop13z,pop15y,pop15z,pop16y,pop16z
variables
pop17y,pop17z,pop18y,pop18z,pop19y,pop19z,pop20y,pop20z,pop21y,pop21z,pop23y,pop2
3z,pop25y,pop25z,pop27y,pop27z,pop29y,pop29z,pop30y,pop30z,pop31y,pop31z
variables
pop32y,pop32z,pop33y,pop33z,pop34y,pop34z,pop35y,pop35z,pop37y,pop37z,pop39y,pop3
9z,pop41y,pop41z,pop43y,pop43z,pop44y,pop44z
variables
poaoy,poaoz,pocoy,pocoz,poeoy,poeoz,pogoy,pogoz,poioy,poioz,pojoy,pojoz,pokoy,pok
oz,poloy,poloz,poroy,poroz,poewoy,poewoz,pogwoy,pogwoz,poijwoy,poijwoz
% centre of mass linear velocities and accelerations:
variables vocmy,vocmz,aocmy,aocmz
% foot point vertical velocities (for spring equations):
variables vop1z,vop3z,vop5z,vop1y,vop3y,vop5y
% accelerations of the accelerometer points (resultants):
variables aop29,aop30,aop31,aop32,aop33,aop34
%
================================================================================
%
```

```
% SPECIFY THE ANGLES WHICH DRIVE THE MODEL (3RD ORDER, TO BE EDITED IN FORTRAN
CODE)
%
================================================================================
% to be overwritten in fortran code:
% ACA=t^3
% AEC=t^3
% AGE=t^3
% AIG=t^3
% ALJ=t^3
% ARL=t^3
% ============================================================
%
% FORM DIRECTION COSINE MATRICES - ROTATION OF SEGMENTS
% ============================================================
simprot (n,i,3,q3) %% orientation of i (lower trunk) in global reference frame n
about its third axis by an amount q3 (now assigned q3)
simprot (a,c,3,ACA) %% right rear-foot rotated about right toes
simprot (c,framerf,3,thetarfoot) %% orientation of triangle in reference frame of
right foot (c)
simprot (c,e,3,AEC) %% right shank rotated about right rear-foot
simprot (e,g,3,AGE) %% right thigh rotated about right shank
simprot (g,i,3,AIG) %% lower trunk rotated about right thigh
simprot (i,j,3,trunkang) %% this angle (between the two trunk segments is fixed
at 180 deg or pi radians (specified below - 'trunkang')
simprot (j,k,3,AKJ)
simprot (j,l,3,ALJ)
simprot (l,r,3,ARL)
% wobbling segment angles relative to parent segment:
simprot (e,ew,3,q4)
simprot (g,gw,3,q5)
simprot (i,ijw,3,q6)
%
================================================================================
%
% SPECIFY THE TORQUES WHICH DRIVE THE MODEL (3RD ORDER, TO BE EDITED IN FORTRAN
CODE)
%
================================================================================
% net joint torque - to be overwritten in fortran code:
rmtptq=T^3
ranktq=T^3
rknetq=T^3
rhiptq=T^3
rshotq=T^3
relbtq=T^3
% flexion and extension torques:
specified
rmtptqf,rmtptqe,ranktqf,ranktqe,rknetqf,rknetqe,rhiptqf,rhiptqe,rshotqf,rshotqe,r
elbtqf,relbtqe
%
================================================================================
```

```
%
% SPECIFY THE FUNCTION TO DRIVE THE VARIABLE HIP TO SHOULDER INSERTION LENGTH
%
==========================================================================
SHDIST = (-0.009156*ALJ^3+0.044942*ALJ^2-0.005912*ALJ+0.491396) - li %% right
% right/left shoulder insertion points determined by cubic function of right/left
shoulder angle respectively - from superior mid-trunk so subtract lower trunk
length
%
==========================================================================
%
% SPECIFY THE FUNCTIONS FOR TRUNK WOBBLING MASS LENGTH AND MASS CENTRE LOCATION
%
==========================================================================
LTWM = ((pop19y-pop16y)^2+(pop19z-pop16z)^2)^0.5 %% resultant distance between
two ends of trunk
LTWMCM = LTWM * lijwopercent %% trunk wobbling mass CoM is a fixed proportion
(lijwopercent) along the segment (body ijw of length LTWM)
%
==========================================================================
%
% FORM POSITION VECTORS
%
==========================================================================
%
% right toe segment:
p_o_p1> = q1*n1> + q2*n2> %% defines the position vector from o to p1 along the
horizontal and vertical global axes
pop1y=dot(p_o_p1>,n1>) %% y coordinate of point for output
pop1z=dot(p_o_p1>,n2>)
p_p1_ao> = (la-lao)*a1> %% defines position of segment centre of mass along the
segment (subtracted to convert from 'from proximal end' to 'from distal end')
p_o_ao> = p_o_p1> + p_p1_ao> %% defines position of points relative to origin for
output
poaoy=dot(p_o_ao>,n1>)
poaoz=dot(p_o_ao>,n2>)
p_p1_p3> = la*a1> %% defines length of segment along the segment
p_o_p3> = p_o_p1> + p_p1_p3>
pop3y=dot(p_o_p3>,n1>)
pop3z=dot(p_o_p3>,n2>)
%
% right rear-foot segment:
p_p3_p7> = lc1*c1> %% MTP to ankle along main foot length (that line)
p_o_p7> = p_o_p3> + p_p3_p7>
pop7y=dot(p_o_p7>,n1>)
pop7z=dot(p_o_p7>,n2>)
p_p3_co1> = (lc1-lco1)*c1> %% rear-foot centre of mass along that line
p_o_co1> = p_o_p3> + p_p3_co1>
p_p3_p29> = (lc1-lacc1)*c1> %% 1MTP accelerometer along that line
p_o_p29> = p_o_p3> + p_p3_p29>
pop29y=dot(p_o_p29>,n1>)
pop29z=dot(p_o_p29>,n2>)
```

```
p_p3_p5> = lc2*framerf1> %% MTP to heel along the rear-foot triangle frame I
created above that is rotated by thetarfoot about the main rear-foot line (c)
p_o_p5> = p_o_p3> + p_p3_p5>
pop5y=dot(p_o_p5>,n1>)
pop5z=dot(p_o_p5>,n2>)
p_p3_co2> = (lc2-lco2)*framerf1> %% rear-foot centre of mass along the second
line
p_o_co2> = p_o_p3> + p_p3_co2>
p_p3_co> = (p_p3_co1> + p_p3_co2>)/2
p_o_co> = p_o_p3> + p_p3_co>
pocoy=dot(p_o_co>,n1>)
pocoz=dot(p_o_co>,n2>)
%
% right ankle spring:
p_p7_p9> = q13*n1> + q14*n2> %% defines separation between two ends of spring by
the spring lengths (q13 and q14)
p_o_p9> = p_o_p7> + p_p7_p9>
pop9y=dot(p_o_p9>,n1>)
pop9z=dot(p_o_p9>,n2>)
%
% right shank segment:
p_p9_p11> = le*e1> %% right shank rigid length
p_o_p11> = p_o_p9> + p_p9_p11>
pop11y=dot(p_o_p11>,n1>)
pop11z=dot(p_o_p11>,n2>)
p_p9_p30> = (le-lacc2)*e1> %% distal shank accelerometer
p_o_p30> = p_o_p9> + p_p9_p30>
pop30y=dot(p_o_p30>,n1>)
pop30z=dot(p_o_p30>,n2>)
p_p9_p31> = (le-lacc3)*e1> %% proximal shank accelerometer
p_o_p31> = p_o_p9> + p_p9_p31>
pop31y=dot(p_o_p31>,n1>)
pop31z=dot(p_o_p31>,n2>)
p_p9_eo> = (le-leo)*e1> %% right shank centre of mass
p_o_eo> = p_o_p9> + p_p9_eo>
poeoy=dot(p_o_eo>,n1>)
poeoz=dot(p_o_eo>,n2>)
p_p9_p35> = q7*e2> + q8*e1> %% perpendicular and longitudinal spring
displacements
p_o_p35> = p_o_p9> + p_p9_p35>
pop35y=dot(p_o_p35>,n1>)
pop35z=dot(p_o_p35>,n2>)
p_p35_p37> = lew*ew1> %% wobbling right shank length
p_o_p37> = p_o_p35> + p_p35_p37>
pop37y= dot(p_o_p37>,n1>)
pop37z=dot(p_o_p37>,n2>)
p_p35_ewo> = (lew-lewo)*ew1> %% wobbling mass centre of mass
p_o_ewo> = p_o_p35> + p_p35_ewo>
poewoy=dot(p_o_ewo>,n1>)
poewoz=dot(p_o_ewo>,n2>)
%
% right knee spring:
```

```
p_p11_p13> = q15*n1> + q16*n2> %% defines separation between two ends of spring
by the spring lengths (q15 and q16)
p_o_p13> = p_o_p11> + p_p11_p13>
pop13y=dot(p_o_p13>,n1>)
pop13z=dot(p_o_p13>,n2>)
%
% right thigh segment:
p_p13_p15> = lg*g1> %% right thigh rigid length
p_o_p15> = p_o_p13> + p_p13_p15>
pop15y=dot(p_o_p15>,n1>)
pop15z=dot(p_o_p15>,n2>)
p_p13_p32> = (lg-lacc4)*g1> %% distal thigh accelerometer
p_o_p32> = p_o_p13> + p_p13_p32>
pop32y=dot(p_o_p32>,n1>)
pop32z=dot(p_o_p32>,n2>)
p_p13_go> = (lg-lgo)*g1> %% right thigh centre of mass
p_o_go> = p_o_p13> + p_p13_go>
pogoy=dot(p_o_go>,n1>)
pogoz=dot(p_o_go>,n2>)
p_p13_p39> = q9*g2> + q10*g1> %% perpendicular and longitudinal spring
displacements (at distal end)
p_o_p39> = p_o_p13> + p_p13_p39>
pop39y=dot(p_o_p39>,n1>)
pop39z=dot(p_o_p39>,n2>)
p_p39_p41> = lgw*gw1> %% wobbling right thigh length
p_o_p41> = p_o_p39> + p_p39_p41>
pop41y=dot(p_o_p41>,n1>)
pop41z=dot(p_o_p41>,n2>)
p_p39_gwo> = (lgw-lgwo)*gw1> %% wobbling mass centre of mass
p_o_gwo> = p_o_p39> + p_p39_gwo>
pogwoy=dot(p_o_gwo>,n1>)
pogwoz=dot(p_o_gwo>,n2>)
%
% hip spring:
p_p15_p16> = q17*n1> + q18*n2> %% defines separation between two ends of spring
by the spring lengths (q17 and q18)
p_o_p16> = p_o_p15> + p_p15_p16>
pop16y=dot(p_o_p16>,n1>)
pop16z=dot(p_o_p16>,n2>)
%
% lower trunk segment:
p_p16_p17> = li*i1>
p_o_p17> = p_o_p16> + p_p16_p17>
pop17y=dot(p_o_p17>,n1>)
pop17z=dot(p_o_p17>,n2>)
p_p16_io> = lio*i1> %% from proximal end is now from the 'bottom' of the segment
as past the centre of mass
p_o_io> = p_o_p16> + p_p16_io>
poioy=dot(p_o_io>,n1>)
poioz=dot(p_o_io>,n2>)
p_p16_p33> = lacc5*i1> %% lower back accelerometer
p_o_p33> = p_o_p16> + p_p16_p33>
```

```
pop33y=dot(p_o_p33>,n1>)
pop33z=dot(p_o_p33>,n2>)
%
% mid-trunk spring:
p_p17_p18> = q19*i1> %% two segments have zero perpendicular separation - only
separated longitudinally
p_o_p18> = p_o_p17> + p_p17_p18>
pop18y=dot(p_o_p18>,n1>)
pop18z=dot(p_o_p18>,n2>)
%
% upper trunk segment:
p_p18_p19> = lj*j1>
p_o_p19> = p_o_p18> + p_p18_p19>
pop19y=dot(p_o_p19>,n1>)
pop19z=dot(p_o_p19>,n2>)
p_p18_jo> = ljo*j1>
p_o_jo> = p_o_p18> + p_p18_jo>
pojoy=dot(p_o_jo>,n1>)
pojoz=dot(p_o_jo>,n2>)
p_p18_p21> = SHDIST*j1> %% right shoulder insertion point - moves up and down the
segment as a function of shoulder angle (specified above)
p_o_p21> = p_o_p18> + p_p18_p21>
pop21y=dot(p_o_p21>,n1>)
pop21z=dot(p_o_p21>,n2>)
%
% trunk wobbling mass segment:
p_p16_p43> = q11*i2> + q12*i1> %% perpendicular and longitudinal spring
displacements
p_o_p43> = p_o_p16> + p_p16_p43>
pop43y=dot(p_o_p43>,n1>)
pop43z=dot(p_o_p43>,n2>)
p_p43_p44> = LTWM*ijw1> %% trunk wobbling mass length (LTWM - varies due to the
spring mid-way up the trunk - specified above)
p_o_p44> = p_o_p43> + p_p43_p44>
pop44y=dot(p_o_p44>,n1>)
pop44z=dot(p_o_p44>,n2>)
p_p43_ijwo> = LTWMCM*ijw1> %% trunk wobbling mass centre of mass position (fixed
proportion of segment length but absolute distance varies with segment length
(specified above)
p_o_ijwo> = p_o_p43> + p_p43_ijwo>
poijwoy=dot(p_o_ijwo>,n1>)
poijwoz=dot(p_o_ijwo>,n2>)
%
% head and neck segment:
p_p19_p20> = lk*k1>
p_o_p20> = p_o_p19> + p_p19_p20>
pop20y=dot(p_o_p20>,n1>)
pop20z=dot(p_o_p20>,n2>)
p_p19_ko> = lko*k1> %% centre of mass
p_o_ko> = p_o_p19> + p_p19_ko>
pokoy=dot(p_o_ko>,n1>)
pokoz=dot(p_o_ko>,n2>)
```

```
p_p19_p34> = lacc6*k1>
p_o_p34> = p_o_p19> + p_p19_p34>
pop34y=dot(p_o_p34>,n1>)
pop34z=dot(p_o_p34>,n2>)
%
% right shoulder spring:
p_p21_p23> = q20*n1> + q21*n2> %% defines separation between two ends of spring
by the spring lengths (q20 and q21)
p_o_p23> = p_o_p21> + p_p21_p23>
pop23y=dot(p_o_p23>,n1>)
pop23z=dot(p_o_p23>,n2>)
%
% right upper arm segment:
p_p23_p25> = ll*l1>
p_o_p25> = p_o_p23> + p_p23_p25>
pop25y=dot(p_o_p25>,n1>)
pop25z=dot(p_o_p25>,n2>)
p_p23_lo> = llo*l1> %% centre of mass
p_o_lo> = p_o_p23> + p_p23_lo>
poloy=dot(p_o_lo>,n1>)
poloz=dot(p_o_lo>,n2>)
%
% right forearm and hand segment:
p_p25_p27> = lr*r1>
p_o_p27> = p_o_p25> + p_p25_p27>
pop27y=dot(p_o_p27>,n1>)
pop27z=dot(p_o_p27>,n2>)
p_p25_ro> = lro*r1> %% centre of mass
p_o_ro> = p_o_p25> + p_p25_ro>
poroy=dot(p_o_ro>,n1>)
poroz=dot(p_o_ro>,n2>)
% ============================================================
%
% WHOLE-BODY CENTRE OF MASS
% ============================================================
p_o_CM>=CM(o) %% position of centre of mass with respect to the origin
poCMy=dot(p_o_CM>,n1>)
poCMz=dot(p_o_CM>,n2>)
% ============================================================
%
% ANGULAR VELOCITIES - FOR TORQUES
% ============================================================
w_i_n> = u3*i3> %% angular velocity of lower trunk (i) about reference frame (n)
in the global coordinate system
w_c_a> = AVCA*c3>  %% for torques
w_framerf_c> = 0> %% foot base remains a set angle (thetarfoot) from line of MTP
to ankle, therefore w is zero.
w_e_c> = AVEC*e3> %% for torques
w_g_e> = AVGE*g3> %% for torques
w_i_g> = AVIG*i3> %% for torques
w_j_i> = 0> %% fixed at 180 degrees or pi radians - only longitudinal movement
between the segments
```

```
% w_k_j> = AKJ'*k3> + u35*k3> %% constant neck angle - determined from
experimental trials
w_k_j> = 0>
w_l_j> = AVLJ*l3> %% for torques
w_r_l> = AVRL*r3> %% for torques
% wobbling segment angles relative to parent segment:
w_ew_e> = u4*ew3>
w_gw_g> = u5*gw3>
w_ijw_i> = u6*ijw3>
% ================================================================
%
% ANGULAR ACCELERATIONS
% ================================================================
alf_i_n> = u3'*i3> %% angular acceleration of lower trunk (i) about reference
frame (n) in the global coordinate system
alf_c_a> = u22'*c3> %% right rear-foot about right toes
alf_framerf_c> = 0> %% foot base remains a set angle (thetarfoot) from line of
MTP to ankle, therefore w and alf are both zero.
alf_e_c> = u23'*e3>
alf_g_e> = u24'*g3>
alf_i_g> = u25'*i3>
alf_j_i> = 0> %% constant angle so w and alf = 0
alf_k_j> = 0> %% constant angle so w and alf = 0
alf_l_j> = u26'*l3>
alf_r_l> = u27'*r3>
% wobbling segment angles relative to parent segment:
alf_ew_e> = u4'*ew3>
alf_gw_g> = u5'*gw3>
alf_ijw_i> = u6'*ijw3>
% ================================================================
%
% LINEAR VELOCITIES
% ================================================================
v_o_n> = 0> %% origin has zero velocity in global reference frame (n)
v_p1_n> = dt(p_o_p1>,n) %% linear velocity of point p1 in reference frame n
(differentiated position with respect to time)
v2pts(n,a,p1,ao) %% velocity of ao on same body (a) as p1 in reference frame n
v2pts(n,a,p1,p3)
v2pts(n,c,p3,p29)
v2pts(n,c,p3,p7)
v_p5_n> = dt(p_o_p5>,n)
v_p9_n> = dt(p_o_p9>,n)
v2pts(n,e,p9,p30)
v2pts(n,e,p9,p31)
v2pts(n,e,p9,eo)
v2pts(n,e,p9,p11)
v_p35_n> = dt(p_o_p35>,n)
v2pts(n,ew,p35,ewo)
v2pts(n,ew,p35,p37)
v_p13_n> = dt(p_o_p13>,n)
v2pts(n,g,p13,p32)
v2pts(n,g,p13,go)
```

```
v2pts(n,g,p13,p15)
v_p39_n> = dt(p_o_p39>,n)
v2pts(n,gw,p39,gwo)
v2pts(n,gw,p39,p41)
v_p16_n> = dt(p_o_p16>,n)
v2pts(n,i,p16,p17)
v2pts(n,i,p16,io)
v2pts(n,i,p16,p33)
v_p18_n> = dt(p_o_p18>,n)
v2pts(n,j,p18,p19)
v2pts(n,j,p18,jo)
v2pts(n,j,p18,p21)
v_p43_n> = dt(p_o_p43>,n)
v2pts(n,ijw,p43,p44)
v2pts(n,ijw,p43,ijwo)
v2pts(n,k,p19,p20)
v2pts(n,k,p19,ko)
v2pts(n,k,p19,p34)
v_p23_n> = dt(p_o_p23>,n)
v2pts(n,l,p23,p25)
v2pts(n,l,p23,lo)
v2pts(n,r,p25,p27)
v2pts(n,r,p25,ro)
v_co_n> = dt(p_o_co>,n)
v_CM_n> = dt(p_o_CM>,n) %% centre of mass
vocmy=dot(v_CM_n>,n1>)
vocmz=dot(v_CM_n>,n2>)
% vertical velocity of foot points for ground contact springs:
vop1z=dot(v_p1_n>,n2>)
vop3z=dot(v_p3_n>,n2>)
vop5z=dot(v_p5_n>,n2>)
vop1y=dot(v_p1_n>,n1>)
vop3y=dot(v_p3_n>,n1>)
vop5y=dot(v_p5_n>,n1>)
% ============================================================
%
% LINEAR ACCELERATIONS
% ============================================================
a_o_n> = 0> %% origin has zero velocity or acceleration in global reference frame
(n)
a_p1_n> = dt(v_p1_n>,n) %% linear acceleration of point p1 in reference frame n
(differentiated velocity with respect to time)
a2pts(n,a,p1,ao) %% acceleration of ao on same body (a) as p1 in reference frame
n
a2pts(n,a,p1,p3)
a2pts(n,c,p3,p29)
a2pts(n,c,p3,p7)
a_p5_n> = dt(v_p5_n>,n)
a_p9_n> = dt(v_p9_n>,n)
a2pts(n,e,p9,p30)
a2pts(n,e,p9,p31)
a2pts(n,e,p9,eo)
```

```
a2pts(n,e,p9,p11)
a_p35_n> = dt(v_p35_n>,n)
a2pts(n,ew,p35,ewo)
a2pts(n,ew,p35,p37)
a_p13_n> = dt(v_p13_n>,n)
a2pts(n,g,p13,p32)
a2pts(n,g,p13,go)
a2pts(n,g,p13,p15)
a_p39_n> = dt(v_p39_n>,n)
a2pts(n,gw,p39,gwo)
a2pts(n,gw,p39,p41)
a_p16_n> = dt(v_p16_n>,n)
a2pts(n,i,p16,p17)
a2pts(n,i,p16,io)
a2pts(n,i,p16,p33)
a_p18_n> = dt(v_p18_n>,n)
a2pts(n,j,p18,p19)
a2pts(n,j,p18,jo)
a2pts(n,j,p18,p21)
a_p43_n> = dt(v_p43_n>,n)
a2pts(n,ijw,p43,p44)
a2pts(n,ijw,p43,ijwo)
a2pts(n,k,p19,p20)
a2pts(n,k,p19,ko)
a2pts(n,k,p19,p34)
a_p23_n> = dt(v_p23_n>,n)
a2pts(n,l,p23,p25)
a2pts(n,l,p23,lo)
a2pts(n,r,p25,p27)
a2pts(n,r,p25,ro)
a_co_n> = dt(v_co_n>,n)
a_CM_n> = dt(v_CM_n>,n) %% centre of mass
aocmy=dot(a_CM_n>,n1>)
aocmz=dot(a_CM_n>,n2>)
% accelerometer points - resultant accelerations:
aop29=mag(a_p29_n>)
aop30=mag(a_p30_n>)
aop31=mag(a_p31_n>)
aop32=mag(a_p32_n>)
aop33=mag(a_p33_n>)
aop34=mag(a_p34_n>)
% ============================================================
%
% SPRING POSITION VECTORS AND VELOCITIES
% ============================================================
% spring stretch:
stretch1=mag(p_p9_p35>)-1.0e-08 %% right shank wobbling mass distal spring
stretch2=mag(p_p11_p37>)-1.0e-08 %% right shank wobbling mass proximal spring
stretch3=mag(p_p13_p39>)-1.0e-08 %% right thigh wobbling mass distal spring
stretch4=mag(p_p15_p41>)-1.0e-08 %% right thigh wobbling mass proximal spring
stretch5=mag(p_p16_p43>)-1.0e-08 %% trunk wobbling mass proximal spring
stretch6=mag(p_p19_p44>)-1.0e-08 %% trunk wobbling mass distal spring
```

```
stretch7=mag(p_p7_p9>)-1.0e-08 %% right ankle spring
stretch8=mag(p_p11_p13>)-1.0e-08 %% right knee spring
stretch9=mag(p_p15_p16>)-1.0e-08 %% hip spring
stretch10=mag(p_p21_p23>)-1.0e-08 %% right shoulder spring
% unit vectors:
uvec1> = unitvec(p_p9_p35>)
uvec2> = unitvec(p_p11_p37>)
uvec3> = unitvec(p_p13_p39>)
uvec4> = unitvec(p_p15_p41>)
uvec5> = unitvec(p_p16_p43>)
uvec6> = unitvec(p_p19_p44>)
uvec7> = unitvec(p_p7_p9>)
uvec8> = unitvec(p_p11_p13>)
uvec9> = unitvec(p_p15_p16>)
uvec10> = unitvec(p_p21_p23>)
% spring velocities (rate of change of stretch with respect to time):
velocity1=dt(stretch1)
velocity2=dt(stretch2)
velocity3=dt(stretch3)
velocity4=dt(stretch4)
velocity5=dt(stretch5)
velocity6=dt(stretch6)
velocity7=dt(stretch7)
velocity8=dt(stretch8)
velocity9=dt(stretch9)
velocity10=dt(stretch10)
% ============================================================
%
% SPECIFY FORCES
% ============================================================
gravity(g*n2>) %% gravity acting in the n2> direction
%
% edit the fortran code so that all ground contact forces are only applied when
in contact with the ground
% forces acting at the foot-heel-shoe interface:
rz1 = -ks1*pop1z -ks17*pop1z^3 +kd1*vop1z*abs(pop1z)
rz3 = -ks1*pop3z -ks17*pop3z^3 +kd1*vop3z*abs(pop3z)
rz5 = -ks2*pop5z -ks3*pop5z^3 +kd2*vop5z*abs(pop5z)
GRFzr = rz1+rz3+rz5 %% right
GRFz = GRFzr %% total
%
% horizontal ground reaction forces:
ry1=-rz1*(ksy1*pop1y +ksy2*pop1y^3 -kdy1*vop1y*pop1y)
ry3=-rz3*(ksy1*pop3y +ksy2*pop3y^3 -kdy1*vop3y*pop3y)
ry5=-rz5*(ksy1*pop5y +ksy2*pop5y^3 -kdy1*vop5y*pop5y)
GRFyr = ry1+ry3+ry5
GRFy = GRFyr
GRFresr = (GRFyr^2+GRFzr^2)^0.5
GRFres = (GRFy^2+GRFz^2)^0.5 %% resultant ground reaction force
%
% apply ground reaction forces to the foot-heel-shoe:
force(p1,ry1*n1>+rz1*n2>)
```

```
force(p3,ry3*n1>+rz3*n2>)
force(p5,ry5*n1>+rz5*n2>)
%
% calculate centre of pressure:
CoPr = (rz1*pop1y + rz3*pop3y + rz5*pop5y) / GRFzr
CoP = CoPr
%
% forces between wobbling and rigid segments:
% distal right shank:
rs1 = -ks6*stretch1^3-kd6*velocity1
force(p9/p35,rs1*uvec1>)
% proximal right shank:
rs3 = -ks6*stretch2^3-kd6*velocity2
force(p11/p37,rs3*uvec2>)
% distal right thigh:
rs5 = -ks7*stretch3^3-kd7*velocity3
force(p13/p39,rs5*uvec3>)
% proximal right thigh:
rs7 = -ks7*stretch4^3-kd7*velocity4
force(p15/p41,rs7*uvec4>)
% lower trunk:
rs9 = -ks8*stretch5^3-kd8*velocity5
force(p16/p43,rs9*uvec5>)
% upper trunk:
rs10 = -ks8*stretch6^3-kd8*velocity6
force(p19/p44,rs10*uvec6>)
%
% forces at compressive joint springs:
% right ankle:
rsy11 = -ks9*stretch7^3-kd9*velocity7
force(p7/p9,rsy11*uvec7>)
% right knee:
rsy13 = -ks11*stretch8^3-kd11*velocity8
force(p11/p13,rsy13*uvec8>)
% hips:
rsy15 = -ks13*stretch9^3-kd13*velocity9
force(p15/p16,rsy15*uvec9>)
% mid trunk:
rs16 = -ks15*q19^3-kd15*u19
force(p17/p18,rs16*i1>)
% right shoulder:
rsz17 = -ks16*stretch10^3-kd16*velocity10
force(p21/p23,rsz17*uvec10>)
%
% calculate joint torques:
torque(c/a,rmtptq*c3>) %% right MTP
torque(e/c,ranktq*e3>) %% right ankle
torque(g/e,rknetq*g3>) %% right knee
torque(i/g,rhiptq*i3>) %% right hip
torque(l/j,rshotq*l3>) %% right shoulder
torque(r/l,relbtq*r3>) %% right elbow
%
```

```
%% ============================================================
%
% ENERGY
% ============================================================
% kinetic energy (all bodies combined --> total):
KECM=KE(a,c,e,g,i,j,k,l,r,ew,gw,ijw)
% kinetic energy of individual bodies:
kea=ke(a)
kec=ke(c)
kee=ke(e)
keg=ke(g)
kei=ke(i)
kej=ke(j)
kek=ke(k)
kel=ke(l)
ker=ke(r)
keew=ke(ew)
kegw=ke(gw)
keijw=ke(ijw)
% potential energy - CoM and segments:
PECM = -1*mWB*g*pocmz %% negative to cancel out the negative gravity
pea = -1*ma*g*poaoz
pec = -1*mc*g*pocoz
pee = -1*me*g*poeoz
peg = -1*mg*g*pogoz
pei = -1*mi*g*poioz
pej = -1*mj*g*pojoz
pek = -1*mk*g*pokoz
pel = -1*ml*g*poloz
per = -1*mr*g*poroz
peew = -1*mew*g*poewoz
pegw = -1*mgw*g*pogwoz
peijw = -1*mijw*g*poijwoz
% wobbling mass springs:
PEsew = 0.25*ks6*(stretch1^4+stretch2^4) %% right shank - remember energy will be
lost due to damping
PEsgw = 0.25*ks7*(stretch3^4+stretch4^4) %% right thigh
PEsijw = 0.25*ks8*(stretch5^4+stretch6^4) %% trunk
% compliant joint springs:
PEsy11 = 0.25*ks9*stretch7^4
PEsy13 = 0.25*ks11*stretch8^4
PEsy15 = 0.25*ks13*stretch9^4
PEs16 = 0.25*ks15*q19^4
PEsz17 = 0.25*ks16*stretch10^4
% ground springs:
PEs1 = 0.5*ks1*pop1z^2 + 0.25*ks17*pop1z^4 + 0.5*ksy1*pop1y^2 + 0.25*ksy2*pop1y^4
PEs3 = 0.5*ks1*pop3z^2 + 0.25*ks17*pop3z^4 + 0.5*ksy1*pop3y^2 + 0.25*ksy2*pop3y^4
PEs5 = 0.5*ks2*pop3z^2 + 0.25*ks3*pop3z^4 + 0.5*ksy1*pop5y^2 + 0.25*ksy2*pop5y^4
% total potential energy in springs:
PEst = (PEsew+PEsgw+PEsijw) + (PEsy11+PEsy13+PEsy15+PEs16+PEsz17) +
(PEs1+PEs3+PEs5)
% total potential energy:
```

```
PEtot = PECM + PEst
% total energy:
TENERGY = KECM + PEtot
% ============================================================
%
% FOOT FLAGS TO BE EDITED IN FORTRAN – TAKE OFF WHEN BOTH OFF GROUND
% ============================================================
variables footflagr
footflagr=0
% ============================================================
%
% ANGULAR AND LINEAR MOMENTUM
% ============================================================
AMOM>=momentum(angular,CM) %% angular momentum
ZAMOM=dot(AMOM>,n3>) %% angular momentum about global axis
LMOM>=momentum(linear) %% linear momentum
YMOM=dot(LMOM>,n1>) %% horizontal linear momentum
ZMOM=dot(LMOM>,n2>) %% vertical linear momentum
% ============================================================
%
% FORM EQUATIONS OF MOTION
% ============================================================
zero = fr() + frstar() % the structure of calculation is Kanes method
% ============================================================
%
% INPUTS
% ============================================================
input tinitial = 0, tfinal = 0.274
% will change tfinal at a later point to 0.4 and then stop when feet leave floor
in fortran using flags for ground contact
input integstp = 0.0001, printint = 10 % can change if necessary, printint will
now match force data and splines, etc (printing every ten steps - 0.001 s)
input abserr = 1.0E-08, relerr = 1.0E-07 % absolute and relative error
%
% rigid body masses:
input ma = 0.476556 %% double mass as both sides of body combined
input mc = 2.293174
input me = 2.620873
input mg = 2.872105
input mi = 3.773762
input mj = 1.643121
input mk = 5.611179
input ml = 6.322968
input mr = 3.709966
%
% wobbling body masses:
input mew = 7.921398
input mgw = 22.200949
input mijw = 29.875970
%
% rigid moments of inertia:
```

```
input ia = 0.000308 %% double inertia as both sides of body combined (double from
exact value, not 6 d.p.)
input ic = 0.005920
input ie = 0.045220
input ig = 0.048319
input ii = 0.057412
input ij = 0.005609
input ik = 0.034402
input il = 0.058772
input ir = 0.056782
%
% wobbling moments of inertia:
input iew = 0.109014
input igw = 0.372387
input iijw = 0.628658
%
% rigid and wobbling segment lengths ('l_') and rigid and wobbling centre of mass
distances from proximal joint ('l_o'):
input la = 0.084500
input lao = 0.035314
input lc1 = 0.139000
input lco1 = 0.062610
input lc2 = 0.180500
input lco2 = 0.081302
input thetarfoot = 0.888189
input le = 0.452500
input leo = 0.226250
input lg = 0.446500
input lgo = 0.223250
input li = 0.418000
input lio = 0.209000
input lj = 0.182000
input ljo = 0.091000
input lk = 0.269000
input lko = 0.136210
input ll = 0.323000
input llo = 0.138057
input lr = 0.469000
input lro = 0.167803
input lew = 0.452500
input lewo = 0.180040
input lgw = 0.446500
input lgwo = 0.184596
input lijwopercent = 0.654681
%
% accelerometer position distances from proximal joint:
input lacc1 = 0.016000
input lacc2 = 0.368750
input lacc3 = 0.073750
input lacc4 = 0.394500
input lacc5 = 0.004000
input lacc6 = 0.035000
```

```
%
% ground contact parameters:
input ksy1 = 50
input ksy2 = 50
input kdy1 = 10
input ks1 = 1000
input ks17 = 1000000
input kd1 = 100
input ks2 = 50
input ks3 = 0
input kd2 = 0
%
% wobbling mass parameters:
input ks6 = 1000000
input kd6 = 1000
input ks7 = 1000000
input kd7 = 1000
input ks8 = 1000000
input kd8 = 1000
%
% compliant joint parameters:
input ks9 = 10000000
input kd9 = 1000
input ks11 = 10000000
input kd11 = 1000
input ks13 = 10000000
input kd13 = 1000
input ks15 = 10000000
input kd15 = 1000
input ks16 = 10000000
input kd16 = 1000
%
% gravity:
input g = -9.817180
%
% constant angle between two trunk segments:
input trunkang = 3.141592654 %% change to exactly pi in fortran
% constant neck angle between upper trunk and head segments:
input AKJ = 2.654652
%
% initial centre of mass velocity and acceleration:
% input vocmy = 0.744833 % give initial velocity in fortran
% input vocmz = -3.354867 % give initial velocity in fortran
%
% initial conditions for generalised degrees of freedom and time derivatives:
input q1 = 0.0, u1 = 0.608900
input q2 = 0.0, u2 = -3.681800
input q3 = 1.4302, u3 = -0.5252
input q4 = 0.0, u4 = 0.0
input q5 = 0.0, u5 = 0.0
input q6 = 0.0, u6 = 0.0
input q7 = 1.0e-05, u7 = 0.0
```

```
input q8 = 0.0, u8 = 0.0
input q9 = 1.0e-05, u9 = 0.0
input q10 = 0.0, u10 = 0.0
input q11 = 1.0e-05, u11 = 0.0
input q12 = 0.0, u12 = 0.0
input q13 = 1.0e-05, u13 = 0.0
input q14 = 0.0, u14 = 0.0
input q15 = 1.0e-05, u15 = 0.0
input q16 = 0.0, u16 = 0.0
input q17 = 1.0e-05, u17 = 0.0
input q18 = 0.0, u18 = 0.0
input q19 = 0.0, u19 = 0.0
input q20 = 1.0e-05, u20 = 0.0
input q21 = 1.0e-05, u21 = 0.0
input q22 = 0.0, u22 = 0.0
input q23 = 0.0, u23 = 0.0
input q24 = 0.0, u24 = 0.0
input q25 = 0.0, u25 = 0.0
input q26 = 0.0, u26 = 0.0
input q27 = 0.0, u27 = 0.0
% ============================================================
%
% OUTPUTS
% ============================================================
% coordinates and CoM velocity and acceleration:
output t,poCMy,poCMz,vocmy,vocmz,aocmy,aocmz
output
t,pop1y,pop1z,pop3y,pop3z,pop5y,pop5z,pop7y,pop7z,pop9y,pop9z,pop11y,pop11z,pop13
y,pop13z,pop15y,pop15z,pop16y,pop16z
output
t,pop17y,pop17z,pop18y,pop18z,pop19y,pop19z,pop20y,pop20z,pop21y,pop21z,pop23y,po
p23z,pop25y,pop25z,pop27y,pop27z
output
t,pop29y,pop29z,pop30y,pop30z,pop31y,pop31z,pop32y,pop32z,pop33y,pop33z,pop34y,po
p34z
output
t,pop35y,pop35z,pop37y,pop37z,pop39y,pop39z,pop41y,pop41z,pop43y,pop43z,pop44y,po
p44z
output
t,poaoy,poaoz,pocoy,pocoz,poeoy,poeoz,pogoy,pogoz,poioy,poioz,pojoy,pojoz,pokoy,p
okoz,poloy,poloz,poroy,poroz,poewoy,poewoz,pogwoy,pogwoz,poijwoy,poijwoz
% angles:
output t,q3,ACA,AEC,AGE,AIG,AKJ,ALJ,ARL,q4,q5,q6,trunkang
% ground reaction forces:
output
t,GRFres,GRFy,GRFz,COP,ry1,ry3,ry5,rz1,rz3,rz5,pop1z,pop3z,pop5z,vop1z,vop3z,vop5
z
% total energy:
output t,TENERGY,KECM,PEtot,PECM,PEsT
% potential energy:
```

```
output
t,PEtot,PECM,PEsT,PEs1,PEs3,PEs5,PEsew,PEsgw,PEsijw,PEsy11,PEsy13,PEsy15,PEs16,PE
sz17,pea,pec,pee,peg,pei,pej,pek,pel,per,peew,pegw,peijw
% kinetic energy:
output t,KECM,YMOM,ZMOM,ZAMOM,kea,kec,kee,keg,kei,kej,kek,kel,ker,keew,kegw,keijw
% wobbling mass forces:
output
t,rs1,rs3,rs5,rs7,rs9,q7,q8,q9,q10,q11,q12,u7,u8,u9,u10,u11,u12,LTWM,LTWMCM
% joint spring forces:
output
t,rsy11,rsy13,rsy15,rs16,rsz17,stretch7,stretch8,stretch9,stretch10,velocity7,vel
ocity8,velocity9,velocity10,SHDIST
% accelerometer accelerations:
output t,aop29,aop30,aop31,aop32,aop33,aop34
% joint torques and forces:
output t,rmtptq,ranktq,rknetq,rhiptq,rshotq,relbtq
% ============================================================
%
% UNITS
% ============================================================
units t=s
units [ma,mc,me,mg,mi,mj,mk,ml,mr,mew,mgw,mijw,mWB]=kg
units [ia,ic,ie,ig,ii,ij,ik,il,ir,iew,igw,iijw]=kg.m^2
units [q{1:2}]=m
units [q{7:21}]=m
units [LTWM,LTWMCM]=m
units [stretch{1:10}]=m
units
[la,lao,lc1,lco1,lc2,lco2,le,leo,lg,lgo,li,lio,lj,ljo,lk,lko,ll,llo,lr,lro,lew,le
wo,lgw,lgwo,lacc1,lacc2,lacc3,lacc4,lacc5,lacc6,CoPr,COP,poCMy,poCMz,pop1y,pop1z,
pop3y,pop3z,pop5y,pop5z,pop7y,pop7z,pop9y,pop9z,pop11y,pop11z,pop13y,pop13z,pop15
y,pop15z,pop16y,pop16z,pop17y,pop17z,pop18y,pop18z,pop19y,pop19z,pop20y,pop20z,po
p21y,pop21z,pop23y,pop23z,pop25y,pop25z,pop27y,pop27z,pop29y,pop29z,pop30y,pop30z
,pop31y,pop31z,pop32y,pop32z,pop33y,pop33z, &
pop34y,pop34z,pop35y,pop35z,pop37y,pop37z,pop39y,pop39z,pop41y,pop41z,pop43y,pop4
3z,pop44y,pop44z,poaoy,poaoz,pocoy,pocoz,poeoy,poeoz,pogoy,pogoz,poioy,poioz,pojo
y,pojoz,pokoy,pokoz,poloy,poloz,poroy,poroz,poewoy,poewoz,pogwoy,pogwoz,poijwoy,p
oijwoz]=m
units [thetarfoot,trunkang]=rad
units [q{3:6}]=rad
units [q{22:27}]=rad
units [ACA,AEC,AGE,AIG,AKJ,ALJ,ARL]=rad
% units
[ry1,ry3,ry5,GRFyr,GRFy,rz1,rz3,rz5,GRFzr,GRFz,GRFresr,GRFres,rs1,rs3,rs5,rs7,rs9
,rsy11,rsy13,rsy15,rs16,rsz17]=N
units
[ry1,ry3,ry5,GRFyr,GRFy,rz1,rz3,rz5,GRFzr,GRFz,GRFresr,GRFres,rs1,rs3,rs5,rs7,rs9
,rsy11,rsy13,rsy15,rs16,rsz17]=N
units
[lijwopercent,ksy1,ksy2,kdy1,ks1,kd1,ks17,ks2,ks3,kd2,ks6,kd6,ks7,kd7,ks8,kd8,ks9
,kd9,ks11,kd11,ks13,kd13,ks15,kd15,ks16,kd16,footflagr]=units
```

```
units
[PEs1,PEs3,PEs5,PEsew,PEsgw,PEsijw,PEsy11,PEsy13,PEsy15,PEs16,PEsz17,PEsT,PECM,PE
tot,KECM,TENERGY,kea,kec,kee,keg,kei,kej,kek,kel,ker,keew,kegw,keijw,pea,pec,pee,
peg,pei,pej,pek,pel,per,peew,pegw,peijw]=J
units [velocity{1:10}]=m/s
units [u{1:2}]=m/s
units [u{7:21}]=m/s
units [vocmy,vocmz,vop1z,vop3z,vop5z]=m/s
units [g,aocmy,aocmz,aop29,aop30,aop31,aop32,aop33,aop34]=m/s^2
units [u{3:6}]=rads/s
units [u{22:27}]=rads/s
units [rmtptq,ranktq,rknetq,rhiptq,rshotq,relbtq]=Nm
units [ZAMOM]=kg.m^2/s
% ============================================================
%
% SAVE AND CODE
% ============================================================
save TD_v2.all % saves .al code and responses from Autolev
code dynamics() TD_v2.for, subs % export fortran script
% ============================================================
% To compile go to standard screen and type 'g77 -o  TD_v2 TD_v2.for'
% After it is compiled type 'TD_v2' to run
```

APPENDIX 5: JOINT TORQUE GENERATOR ACTIVATION PARAMETERS

Table A5.1. Joint torque generator activation parameters for simulation matched to experimental data.

joint torque generator	a_0	a_1	a_2	ts_1	tr_1	tp	tr_2
MTP flexion	0.276	0.088	0.428	0.047	0.123	0.074	0.332
MTP extension	0.475	0.863	0.962	0.047	0.121	0.364	0.109
ankle dorsi flexion	0.361	0.038	0.235	-0.021	0.174	0.169	0.211
ankle monoarticular plantar flexion	0.491	0.999	0.673	-0.025	0.170	0.256	0.220
ankle biarticular plantar flexion	0.464	0.841	0.790	0.032	0.077	0.009	0.302
knee monoarticular flexion	0.193	0.258	0.346	0.014	0.247	0.124	0.293
knee biarticular flexion	0.304	0.552	0.117	-0.028	0.123	0.085	0.152
knee monoarticular extension	0.431	0.855	0.379	-0.005	0.106	0.216	0.209
knee biarticular extension	0.393	0.264	0.657	-0.001	0.141	0.220	0.170
hip monoarticular flexion	0.339	0.172	0.586	0.027	0.180	0.189	0.307
hip monoarticular extension	0.424	0.990	0.629	-0.01	0.103	0.280	0.277
shoulder flexion	0.439	0.746	0.920	-0.017	0.137	0.165	0.143
shoulder extension	0.127	0.116	0.454	0.003	0.088	0.066	0.205
elbow flexion	0.370	0.499	0.605	0.003	0.183	0.208	0.091
elbow extension	0.261	0.629	0.825	0.087	0.339	0.159	0.203